CONTINUOUS-WAVE LIGHT MODULATION USING STIMULATED RAMAN SCATTERING

by

Joshua Joseph Weber

A dissertation submitted in partial fulfillment of
the requirements for the degree of

Doctor of Philosophy

(Physics)

at the

UNIVERSITY OF WISCONSIN–MADISON

2014

Date of final oral examination: August 8, 2014

The dissertation is approved by the following members of the Final Oral Committee:

Deniz D. Yavuz, Associate Professor, Physics

James E. Lawler, Professor, Physics

Mark Saffman, Professor, Physics

Thad G. Walker, Professor, Physics

Randall H. Goldsmith, Assistant Professor, Chemistry

Dedicated to My Family and Friends

ACKNOWLEDGMENTS

First of all, I would like to thank my advisor, Deniz Yavuz. I could not have asked for a better advisor. Deniz is an excellent scientist, and he is enthusiastic about his work. He shares his excitement about physics, and is great at explaining concepts. He was always very patient with me, and he was always willing to talk about anything that I was struggling with regarding physics or my career. He always listened and valued my point of view, no matter how much I thought my contributions were trivial. I will miss my regular conversations with Deniz. He is a great advisor, and a great human being. He made graduate school fun. He always tolerated our nonsense, and he let me stay in the lab group even after I knocked him out of the department ping pong tournament.

I would like to thank my thesis committee: Deniz, Mark Saffman, Thad Walker, Jim Lawler, and Randy Goldsmith. I appreciate their time and effort reviewing my thesis and defense. Special thanks to Mark Saffman for introducing me to atomic physics in my first summer at UW-Madison.

I would like to thank all of the current and past members of Yavuz Lab. Our lab is a fun, supportive place to work. I would like to thank Daniel Sikes and Nick Proite for their advice and help during my earlier years in the group. I especially want to thank Tyler Green, from whom I inherited my research project, for all of his help over the years. It was always fun to work with Tyler. Both Tyler and Nick have continued to give useful advice to me even after they graduated. I would also like to thank Larry Isenhower for all of his help and advice over the years. Even though he was not in our group, he was an invaluable source of help over the years.

I also want to thank the current members of the group. It has been fun working (and not working) with Zach Simmons, Jared Miles, and Nick Brewer. They have helped out a lot with research, and they have tolerated my goofiness and complaining. We had a great group of people in Yavuz Lab. It has been fun seeing the next generation, David Gold and Dipto Das, starting their

work in Yavuz Lab. I have enjoyed working with David on the modulation project, and I feel that I am leaving the project in good hands.

I would like to thank the other graduate students in AMO physics from our class year. Zack DeLand, Kara Maller, and Marty Lichtman have all contributed to my research and to the fun I have had in graduate school.

I would like to thank Sujeev Wickramasekara, my undergraduate advisor at Grinnell College, for all of his support and advice during graduate school. Without Sujeev, I would not have majored in physics, let alone continued on to graduate school. Professors at Grinnell like Sujeev and Paul Tjossem, with their knowledge of physics, excellent teaching skills, and friendly demeanors, have greatly influenced my decision to pursue a career in physics education.

I would also like to thank the staff of the Physics Department at UW-Madison. They do so much to keep everything in the department running smoothly, and their work is largely underappreciated. In particular, I would like to thank Ann Austin, Aimee Lefkow , Renee Lefkow, Dave Lockman, and Brett Unks for all of their help over the last five years.

Although it is not discussed in this thesis, a significant portion of my time at UW-Madison has been spent teaching and learning about physics education. I would like to thank the many people who I have had the pleasure to work with on teaching and physics education issues. It is heartening to be around people who care so much about physics *and* education. The staff of the Physics Learning Center, especially Susan Nossal, Amihan Huesmann, and Larry Watson, has been very supportive of me, and I have enjoyed working with them. I would like to thank Jim Reardon for his help and interesting discussions about teaching and education over the years. I would also like to thank Don Gillian-Daniel and everyone with the Delta Program for supporting my efforts to become a better educator. Special thanks to Peter Timbie for working with me as a faculty mentor on my Delta internship project.

There are too many to list them all here, but I would also like to thank all of my friends from my years in Madison. I want to thank everyone from the UW Physics / Bye Week / Magnetic Monopoles / Baltimore Factorioles softball team for all of the fun. I especially want to thank Mike Wood, who has been a great co-co-manager and a great friend. Again, although I cannot

thank everyone, and I am sure I am unintentionally leaving someone out here, I want to be sure to thank Dan Fiorino, Jenna Ryon, Alyssa Frey, Kenny Rudinger, Claire Murray, David French, David Wake, Chris Bard, Bob Wyllie, Jake King, and Guilhem Ribeill (as well as my other friends already mentioned) for all the fun times weve shared. Outside of Madison, I want to thank Emily Metzger and Ann Murray for all of their support during my time at UW-Madison. Emily especially has put up with a lot of me being stressed out in these last couple of months. She is the best.

Without all of these great friends, I almost certainly would have accomplished more in graduate school, but it definitely would not have been nearly as much fun.

Most importantly, I would like to thank my family. Their love and support throughout my life has made everything that I have done possible. My mom, Karen Weber, and my dad, Nick Weber, have always been supportive of whatever I have done. My brother, Zack Weber, and my stepmom, Leigh Weber, have also been incredibly encouraging and supportive. My grandparents, aunts, uncles, and cousins have also always been there for me. I could not have asked for a better family, and I cannot explain all the wonderful things that they have done for me.

I would like to especially thank my dad, David Gold, and Zach Simmons for their help in editing this document. This thesis was significantly improved by their careful reading and insightful suggestions.

Finally, I would like to acknowledge the funding sources that made this work possible. My graduate work has been funded by the National Science Foundation and the Wisconsin Alumni Research Foundation.

TABLE OF CONTENTS

Page

LIST OF FIGURES

Figure Page

Figure Page

Figure Page

Figure Page

Figure Page

Figure Page

Figure Page

Figure Page

Figure Page

Figure Page

Figure Page

Figure Page

Figure Page

Figure Page

Figure Page

Figure Page

Figure Page

Figure Page

Figure Page

Abstract

Continuous-Wave Light Modulation Using Stimulated Raman Scattering

Joshua J. Weber

Under the supervision of Associate Professor Deniz D. Yavuz

At the University of Wisconsin - Madison

This thesis focuses on the development of a device that modulates light at molecular frequencies. The purpose of this molecular modulator is to generate a broad, continuous-wave laser spectrum. Our novel approach is based on stimulated Raman scattering in a high-finesse cavity. Using high-intensity intracavity fields, we drive ro-vibrational Raman transitions in a low-density gas of molecular deuterium (or hydrogen). This builds up a molecular coherence between ro-vibrational energy levels. This molecular coherence is then used to modulate a laser beam, generating sidebands that are spaced from the original frequency by multiples of the Raman frequencies, which can exceed 100 THz. The sidebands form a broad, coherent spectrum. Such a spectrum has numerous potential applications including ultrashort pulse generation, precision spectroscopy, and coherent control.

To our knowledge, the spectra produced by our molecular modulator are the broadest coherent spectra ever produced in the continuous-wave domain. This thesis describes the generation of a spectrum that has over fifteen spectral components that cover nearly two octaves of optical bandwidth, a wavelength range from 800 nm to 3100 nm. In contrast to molecular modulation methods that are based on pulsed lasers, our continuous-wave approach ensures that each spectral component has a narrow frequency linewidth. In addition to the generation of broad spectra, this thesis describes work that demonstrates the broadband capabilities of molecular modulation and computational work that suggests promising applications for our modulator.

Introduction

Imagine that you want to photograph something that is moving quickly, like the swing of a baseball bat or a speeding car. If your shutter speed is too slow, the moving object in your photo will be blurred. In order to capture a crisp image of the action, you need your shutter to move quickly enough that your subject does not have time to noticeably move while the shutter is open. In other words, you need the duration of the pulse of light that hits the film (or the charge-coupled device sensor) to be shorter than the timescale of action that you want to capture.

More generally, in order to optically examine a transient phenomenon, you need a pulse of light with duration shorter than the timescale of the action. This principle holds on timescales that are well beyond the capabilities of even the fastest camera shutters. This thesis focuses on the development of a device that could permit the exploration of action that happens on sub-femtosecond timescales. Recall that a femtosecond is 10^{-15} seconds, or one millionth of a billionth of a second. The ratio of one femtosecond to one second is roughly the same as the ratio of seven and a half minutes to the age of the universe. To give some perspective, here are a few processes that last on the order of a femtosecond: the classical Kepler orbital period of an electron around a nucleus, the oscillation period for visible light, and the reaction time of some of the fastest chemical reactions [1].

Because a femtosecond is much faster than any shutter, exploration of such phenomena on sub-femtosecond timescales requires alternative methods of generating ultrashort pulses of light (or, more generally, electromagnetic radiation). Several methods of creating ultrashort pulses have been developed including mode-locked lasers [2], high harmonic generation [3], free electron lasers [4], optical parametric amplifiers [5, 6], non-linear fibers [7, 8, 9], and molecular modulation [10, 11].

This thesis focuses on this last approach, which so far has been able to produce the shortest pulses in the optical region of the spectrum. Molecular modulation is the shifting of the frequency of light through laser-molecule interactions. In these interactions, the molecules can gain (or lose)

quanta of energy. The laser photons, which lose (or gain) this energy in the exchange, thus experience a corresponding downward (or upward) shift in frequency. Because it stems from the energy quanta of the molecules, the magnitude of this frequency shift is determined by the molecular properties. The original frequency and the shifted frequencies, which are called *sidebands*, together form a spectrum of lasers.

A broad, coherent generated spectrum is the key to ultrashort pulse generation through molecular modulation. *Coherent* here means that all of the components of the spectrum have a definite phase relationship with one another. Suppose the phases of the components begin in such a way that all of the different frequencies in the spectrum have their maxima aligned. At this time, the components add constructively, and the overall intensity of the light is high. However, because all of the components oscillate at different frequencies, the peaks will not stay aligned. This means that the components start to add destructively, and the overall intensity of the light is lower. After a number of oscillations, the maxima will be aligned (or nearly aligned) again. Thus, there is again constructive interference and higher intensity. This cycle repeats, forming a temporal pattern of intensity maxima and minima. With enough frequencies, the destructive interference dominates for most of the period, yielding long intervals of darkness interrupted by brief flashes of light from constructive interference. These brief flashes are the ultrashort pulses. See Figure 0.1.

The ultrashort pulses generated by broadband spectra allow the exploration of ultrafast phenomena [1], but that is not the limit of the utility of broadband spectra. In addition, broadband sources have applications in precision spectroscopy [12] and quantum control of atoms and molecules [13, 14, 15]. Each frequency in a spectrum is a unique laser, so a broadband spectrum serves as a versatile spectroscopy toolbox. This wide selection of frequencies also makes a broadband source ideal for coherently probing a wide range of electronic, rotational, and vibrational excitations in molecules. This is normally challenging, as these excitations vary in energy by orders of magnitude. If the frequencies of the components are precisely determined, a broadband spectrum could also allow for the construction of precise optical clocks in different regions of the spectrum [16]. The spectrum could also serve as a broad absolute frequency reference with components covering much of the optical region [17]. Furthermore, each frequency in the spectrum

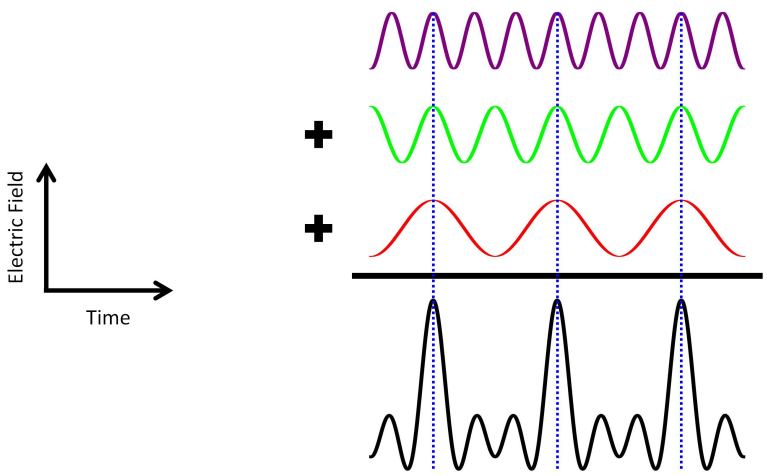

Figure 0.1 *Pulse Generation* This figure illustrates pulse generation with a spectrum containing only three frequencies. The violet, green, and red electric fields interfere to create the pulse structure of the total black field, a superposition of the other three. The vertical blue dotted lines mark the bright pulses, times of constructive interference. In between the bright pulses, destructive interference causes the total field to be smaller in magnitude, and the light is dimmer.

is like a Fourier component, so with appropriate phase and amplitude control, one can combine the pulses to form arbitrary optical waveforms, like with an electronic radio-frequency synthesizer, but at optical frequencies. These Fourier synthesized waveforms can be used to probe and also to manipulate processes that happen on ultrashort timescales [18, 19]. Such an arbitrary optical waveform generator would be a powerful tool in ultrafast science.

This thesis describes important steps towards using molecular modulation to produce a broadband coherent spectrum suitable for use in an arbitrary optical waveform generator.

Chapter 1 provides an introduction to the concept of light modulation. We discuss the process of sideband generation through phase modulation, and then we examine different methods of light modulation with a special emphasis on molecular modulation.

Chapter 2 explores molecular modulation with more mathematical rigor. The Hamiltonian that governs the molecular interaction is presented along with the relevant eigenstates and eigenvalues. We also discuss the propagation equation that describes the generation of sidebands in Raman media.

Chapter 3 describes relevant previous work in the field of molecular modulation. We review the first proposals for molecular modulation and early progress in the field with pulsed lasers. We then discuss experiments with continuous-wave molecular modulation and recent developments in the field.

Chapter 4 is a brief overview of the experimental arrangement for our molecular modulator.

Chapter 5 provides details on a particular aspect of our experiment: resonance and laser locking. We begin with an overview of the concept of resonance and then discuss the generation of an error signal. We close with a discussion of the specifics of the locking system used in our experiment.

Chapter 6 discusses another aspect of our experiment: optical cavities. We discuss Gaussian beam propagation and mode-matching Gaussian beams to optical cavities. We then discuss the optical cavity used in our experiments, including a discussion of the effects of cooling it to liquid nitrogen temperatures.

Chapter 7 is an overview of previous progress from our research group. We begin with an experiment with continuous-wave rotational Raman generation in molecular deuterium. We then discuss vibrational Raman generation and the coherence of the resulting spectrum. An experiment demonstrating multiple-order rotational Raman generation closes the chapter.

Chapter 8 is a description of the broadband spectrum that we generate with our molecular modulator. We describe the spectrum, which spans nearly two octaves of optical bandwidth and contains up to thirty spectral components. We demonstrate that the spectral components have narrow frequency linewidths and Gaussian spatial profiles.

Chapter 9 focuses on the capability of our modulator to modulate an independent mixing beam. We demonstrate molecular modulation at a modulation frequency of 17.6 THz for a mixing beam that makes a single pass through our system. We also discuss the broadband modulation capabilities of our modulator.

Chapter 10 features numerical simulations that suggest that molecular modulator could be used as a source of coherent terahertz radiation. We propose two schemes based on realistic experimental parameters. Our calculations suggest that both would be capable of producing radiation in a hard-to-access region of the spectrum with an unprecedented combination of power and tunability.

Chapter 11 concludes the work. We examine our on-going experiments involving an independent Stokes laser and modulation of an independent mixing beam at a modulation frequency of 89.6 THz. We also briefly discuss possible future directions for our research.

Chapter 1

Light Modulation

The goal of this project is to develop an efficient molecular modulator, so we will begin with a discussion of light modulation. In this context, to *modulate* a light beam means to shift its frequency. An optical modulator, as illustrated in Figure 1.1, is a device that takes monochromatic laser light of a certain frequency ω_0 and shifts the frequency of some of that light to other frequencies. The shifted frequencies are spaced from the original frequency by integer multiples of the modulation frequency, ω_m, which is set by properties of the optical modulator. This frequency shift can be understood in the time domain as the laser intensity or frequency varying with time.

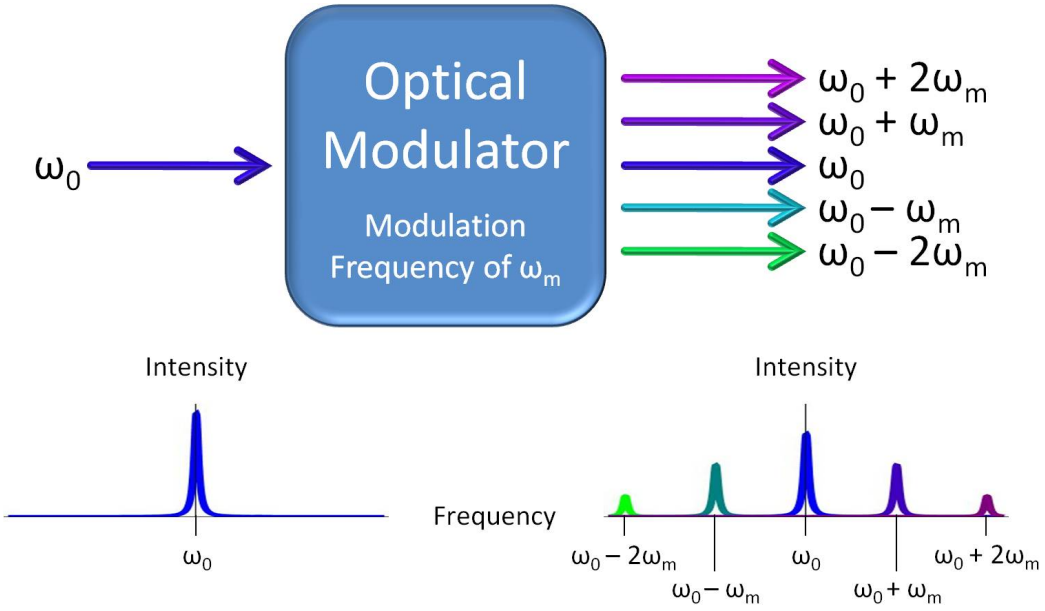

Figure 1.1 *Optical Modulator* An optical modulator with modulation frequency ω_m takes light at a frequency ω_0 and shifts the frequency of some of the light to frequencies $\omega_0 + n\omega_m$, where n is an integer.

1.1 Phase Modulation and Sideband Generation

The mechanism for the frequency shift in optical modulators is a time-varying index of refraction. In Section 1.2 we will discuss how such a time-varying index can occur. First, let us discuss why a time-varying index of refraction yields a frequency shift.

Suppose we have a monochromatic laser at some frequency ω_0. We can write its electric field as

$$E(t) = E_0 e^{j\omega_0 t}, \tag{1.1}$$

where we have explicitly separated the time-dependent phase, $e^{j\omega_0 t}$, from the rest of the complex field E_0. j is the imaginary unit, and t is time.

Now suppose that this monochromatic laser propagates in a material with a refractive index $n(t)$ that consists of a constant component n_0 and a small sinusoidal time variation,

$$n(t) = n_0 + \delta n \cdot sin(\omega_m t), \tag{1.2}$$

where $\delta n \ll n_0$.

The index of refraction of a material is inversely proportional to the velocity at which light travels through it,

$$n = \frac{c}{v}, \tag{1.3}$$

so the sinusoidal time-varying component of the index yields a time-varying component of the velocity. Furthermore, since the phase delay that light experiences in a material is directly proportional to its velocity, this means that there is also a sinusoidal time variation in the phase of the light.

$$\phi(t) = \phi_0 + \delta\phi \cdot sin(\omega_m t), \tag{1.4}$$

Note that we again have a constant term ϕ_0 and a small time-varying term that varies with the same frequency as the index of refraction variation. Again, the constant term dominates: $\delta\phi \ll \phi_0$.

Including this phase delay in the electric field above (Equation 1.1) yields

$$\begin{aligned} E(t) &= E_0 e^{j(\omega_0 t + \phi(t))} \\ &= E_0 e^{j(\omega_0 t + \phi_0 + \delta\phi \cdot sin(\Omega t))}. \end{aligned} \tag{1.5}$$

We can absorb the time-independent phase $e^{j\phi_0}$ into the time-independent complex field and call this new time-independent leading term E_0', which allows us to rewrite our electric field (Equation 1.5) as

$$\begin{aligned} E(t) &= E_0' e^{j(\omega_0 t + \delta\phi \cdot sin(\omega_m t))} \\ &= E_0' e^{j\omega_0 t} e^{j\delta\phi \cdot sin(\omega_m t)}, \end{aligned} \tag{1.6}$$

in which the time-dependence is entirely contained in the last two terms.

Now let us examine the time-dependence of this phase. Because the variation $\delta\phi$ is small, we can approximate the latter half of the exponential using a Taylor expansion

$$e^{j\delta\phi \cdot sin(\omega_m t)} \approx 1 + j\delta\phi \cdot sin(\omega_m t), \tag{1.7}$$

which yields

$$E(t) \approx E_0' e^{j\omega_0 t} (1 + j\delta\phi \cdot sin(\omega_m t)). \tag{1.8}$$

Next from Euler's formula, we can rewrite the sine term as the difference of two complex exponentials,

$$\begin{aligned} j\delta\phi \cdot sin(\omega_m t) &= j\delta\phi \cdot \frac{1}{2j}\left(e^{j\omega_m t} - e^{-j\omega_m t}\right) \\ &= \frac{\delta\phi}{2}\left(e^{j\omega_m t} - e^{-j\omega_m t}\right). \end{aligned} \tag{1.9}$$

Making this substitution into Equation 1.8 gives us

$$\begin{aligned} E(t) &\approx E_0' e^{j\omega_0 t}\left(1 + \frac{\delta\phi}{2}\left(e^{j\omega_m t} - e^{-j\omega_m t}\right)\right) \\ &= E_0' e^{j\omega_0 t} + \frac{\delta\phi}{2} E_0' e^{j\omega_0 t}\left(e^{j\omega_m t} - e^{-j\omega_m t}\right) \\ &= E_0' e^{j\omega_0 t} + \frac{\delta\phi}{2} E_0'\left(e^{j(\omega_0+\omega_m)t} - e^{j(\omega_0-\omega_m)t}\right). \end{aligned} \tag{1.10}$$

The electric field now is oscillating at three different frequencies; it now has components at $\omega_0 + \omega_m$ and $\omega_0 - \omega_m$ as well as at the original ω_0. The fields at these new frequencies are called *sidebands*. Notice that their amplitude is decreased by a factor of the small $\delta\phi$. The sideband that is shifted down in frequency is called the *Stokes* sideband, while the sideband that is shifted

up in frequency is called the *anti-Stokes* sideband. It is important to note that there are only three frequencies because we only included the first two terms in the Taylor expansion of our exponential. Had we included more terms, we would have seen more frequencies at $\omega_0 - q\omega_m$ and $\omega_0 + q\omega_m$ (with q as a positive integer). These are called *higher-order Stokes and anti-Stokes sidebands*. (The higher-orders sidebands have smaller amplitudes due to increasing powers of $\delta\phi$.) This process of sideband generation is called *phase modulation*. Although it will not be discussed here, it can be shown in a similar manner that a time-varying amplitude will also produce frequency sidebands.

1.2 Methods of Optical Modulation

There are several approaches that can be used to produce a time-varying index of refraction and thus to modulate light. The two most commonly used methods of frequency modulation are acousto-optic and electro-optic modulation. We will briefly discuss these common types of modulation before moving on to discuss molecular modulation, which is the focus of this thesis. (See the beginning of Chapter 9 for an additional comparison of these three types of modulation.)

1.2.1 Acousto-Optic Modulation

Acousto-optic modulators (AOMs) create a time-varying index of refraction using mechanical waves in a crystalline structure. As illustrated in Figure 1.2, a periodic driving force, such as one provided by a piezoelectric transducer, creates pressure waves inside an acousto-optic crystal. Acousto-optic crystals, such as quartz, fused silica, or tellurium dioxide, are materials whose index of refraction changes with compression and expansion of the crystalline lattice. In an AOM, the piezoelectric transducer is driven with a radio frequency (RF) signal, and the refractive index of the crystal varies with this same frequency. Thus, when light passes through this vibrating crystal, it is modulated and sidebands are formed by the process described above.

Another way to think about AOMs is to consider the interaction between the photons and the phonons of the oscillating crystalline structure. As the light passes through the crystal, its photons can exchange momentum with the crystalline phonons. This exchange of momentum has two main

effects on the photons. The first is that an exchange of momentum is also an exchange of energy. If momentum is transferred from a phonon to a photon, the energy of the photon increases, and thus its frequency is shifted upward. If the relative propagation direction of the compression waves is reversed, momentum can be transferred from a photon to a phonon. This leads to the photon frequency being shifted downward. The second consequence of the momentum transfer is that, in order to conserve momentum, the photons are diffracted from their original trajectories. Thus, the frequency-shifted light is spatially separated from the original beam.

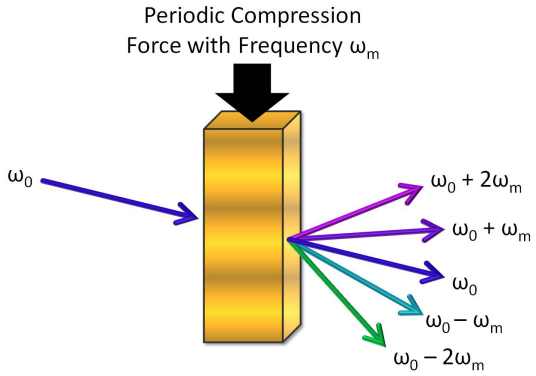

Figure 1.2 *Acousto-Optic Modulator* An acousto-optic modulator uses pressure waves to create a time-varying index of refraction in a crystalline structure. This time-varying index can be used to modulate the frequency of laser light. The frequency shift is the result of an exchange of momentum between phonons in the crystal and incident photons.

1.2.2 Electro-Optic Modulation

Electro-optic modulators (EOMs) create a time-varying index of refraction using time-varying electric fields. As depicted in Figure 1.3, a time-varying voltage is applied across a capacitor whose parallel plates are separated by an electro-optic crystal. The indices of refraction of electro-optic crystals, such as lithium niobate ($LiNbO_3$) or gallium arsenide (GaAs), change in the presence of an applied electric field. Due to the applied field, the atoms in the crystal feel an electric force, which distorts the crystalline structure, changing the index of refraction. When the relationship between applied field strength and refractive index is linear, as is the case with lithium niobate and gallium arsenide, the effect is called the *Pockels effect*. (The linear Pockels effect, which is relatively strong

and only present in crystalline materials that lack inversion symmetry, can be contrasted with the *Kerr effect*, a more widely exhibited, but usually weaker nonlinear electro-optic response.) With a parallel plate capacitor, the electric field between the plates is directly proportional to the applied voltage. Thus, a sinusoidal time variation of the voltage produces a sinusoidally-varying electric field on the crystal, which in turn creates a sinusoidally-varying index of refraction due to the Pockels effect. As with an AOM, this variation generates frequency sidebands on light passing through the crystal. Unlike with an AOM, however, the sidebands propagate collinearly with the original frequency.

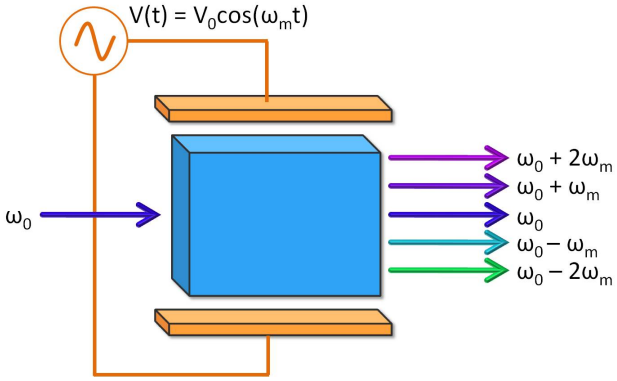

Figure 1.3 *Electro-Optic Modulator* An electro-optic modulator uses an alternating electric field to create a time-varying index of refraction in a crystalline structure. This time-varying index can be used to modulate the frequency of laser light. The alternating electric field is provided by an alternating voltage across parallel plate capacitors surrounding an electro-optic crystal.

1.2.3 Molecular Modulation

This thesis focuses on a third type of modulator: molecular modulators. As shown in Figure 1.4, molecular modulators create a time-varying index of refraction with coherently rotating or vibrating molecules. Lasers of the appropriate frequencies incident on a molecular gas can induce rotations and vibrations in the molecules. When the driving laser fields are strong enough, the molecules all vibrate (or rotate) in unison. This coherent, periodic molecular motion yields a time-varying index of refraction.

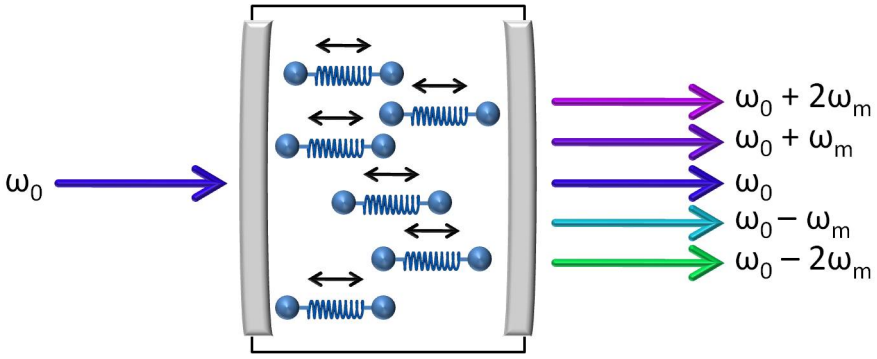

Figure 1.4 *Molecular Modulator* A molecular modulator uses coherently vibrating (or rotating) molecules to create a time-varying index of refraction in a molecular gas. This time-varying index can be used to modulate the frequency of laser light. As discussed in more detail in following sections, the coherent motion of the molecules is stimulated by lasers with frequencies corresponding to particular molecular resonances.

The diatomic molecules shown in Figure 1.5 provide a simplified, semi-classical explanation of the source of the time-varying index of refraction in rotating and vibrating molecules. For vibrations, when the molecular bonds are stretched, there is more space between the atoms, and the index of refraction is lower than when the bonds are compressed and the atoms are close together. For rotations, when the molecules are oriented perpendicular to the propagation direction of the driving fields, the index of refraction is lower than when the molecules are oriented parallel to the fields. In both cases, this time-varying index of refraction generates frequency sidebands on light passing through the molecular gas, just as with AOMs and EOMs.

For a single molecule, the index change illustrated in Figure 1.5 is a negligible effect. For an ensemble of randomly vibrating and rotating molecules, the different molecules oscillate with different phases and orientations. The individual contributions wash out, and the net effect is small. However, if we have an ensemble of molecules oscillating in unison, the contributions from each molecule add *coherently*, and the net effect can be significant. The net effect of this *coherent* oscillation is a time-varying index of refraction. *Coherence* is the key mechanism for molecular modulation. Increased coherence yields an increase in efficiency for the modulator. (As discussed later in Section 2.3, this coherence is related to the density matrix of the molecular system. See the discussion above Equation 2.45.)

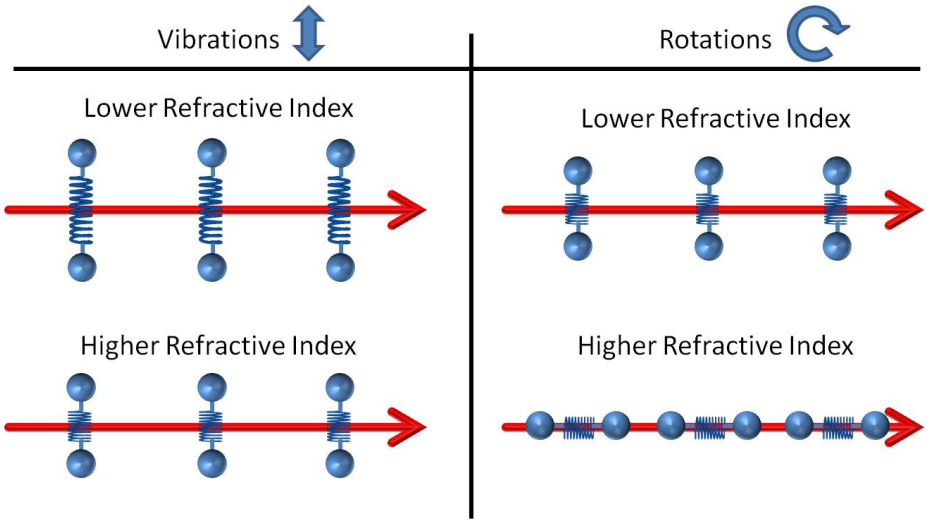

Figure 1.5 *Index of Refraction Variation* As molecules vibrate and rotate, their indices of refraction change. Semi-classically, this variation can be understood as a changing density seen by an incident laser. The laser experiences a higher index of refraction when the molecules are compressed or oriented so as to increase the optical density.

Another way to view the frequency shift in molecular modulation is to consider Raman scattering. Raman scattering is an inelastic collision, an energy exchange, between light and matter. When an incident photon collides with a molecule, the photon can give energy to the molecule, exciting a vibration or rotation in the molecule. The photon loses energy in the collision and thus exits with a lower frequency. (As in an EOM, the frequency shifted photon continues on its original path.) An inelastic collision can also cause an upward shift in frequency if the photon gains energy from a rotating or vibrating molecule (which then rotates or vibrates at a slower rate). The inelastic collisions of Raman scattering can be contrasted with the elastic collisions of Rayleigh scattering. In Rayleigh scattering, the collisions are elastic and no energy is exchanged between the photon and the molecule, so no frequency shift occurs. Rayleigh scattering, as well as the two inelastic Raman scattering processes, is illustrated in Figure 1.6.

In order to understand this process more completely, we will examine scattering from a quantum point of view. We can view both Raman and Rayleigh scattering as two-photon processes, with an incident photon and a scattered photon. The energy difference between the photons corresponds to the energy splitting between ro-vibrational energy levels of the molecules. (*Ro-vibrational* here

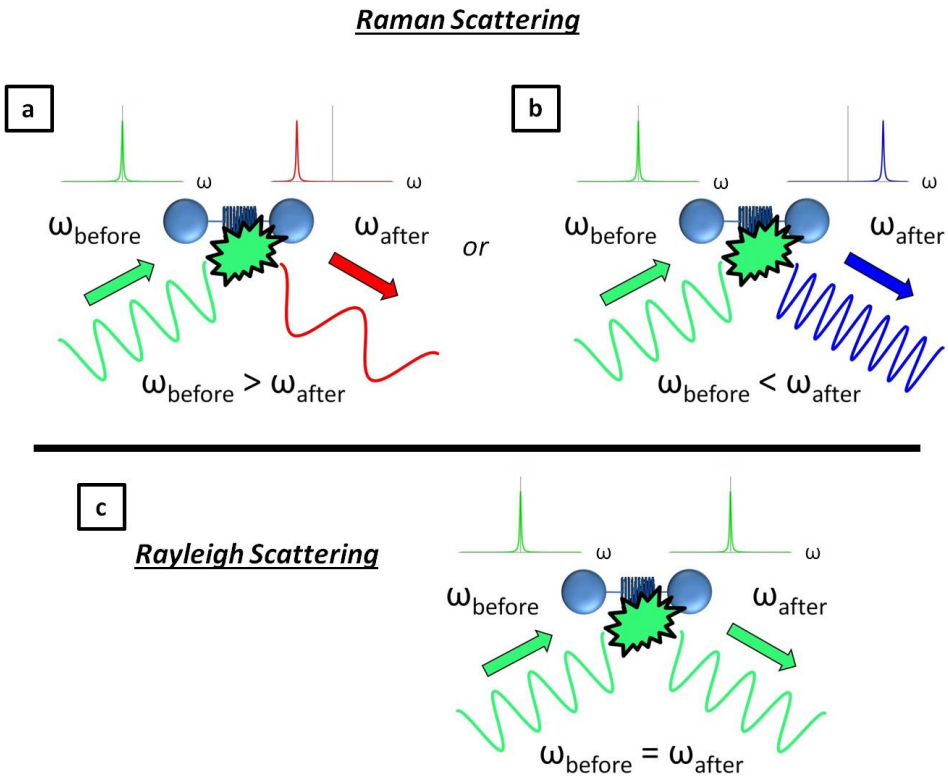

Figure 1.6 *Raman and Rayleigh Scattering* In Raman scattering events, the collision between the photon and the molecule is inelastic. (a.) The photon can give energy to the molecule, exciting the molecule and leaving with less energy and thus a lower frequency. (b.) The photon can also gain energy from the molecule, de-exciting the molecule and leaving with more energy and thus a higher frequency. (c.) In contrast, Rayleigh scattering is an elastic collision. The molecule remains in the same state and the photon retains the same frequency. In each case, the plots illustrate the frequency, ω, of the photon both before and after the collision.

refers to the quantum mechanical energy state of a molecule, which includes both rotational and vibrational components. Throughout this thesis, all ro-vibrational states mentioned are in the electronic ground state unless explicitly stated otherwise.)

Consider a molecule with ro-vibrational states $|a\rangle$ and $|b\rangle$, as well as excited electronic-ro-vibrational states $|i\rangle$ that are much higher in energy. (Single-photon transitions from $|a\rangle$ to $|b\rangle$ are dipole forbidden, but single-photon transitions from either $|a\rangle$ or $|b\rangle$ to the upper states $|i\rangle$ are allowed.) Such a system is shown below in Figure 1.7. Note that excited states $|i\rangle$ are so much higher in energy that they are not shown. The energy splitting between the lower two states will

determine the modulation frequency of the molecular modulator:

$$\begin{aligned} E_b - E_a &= |\hbar\omega_{inc} - \hbar\omega_{sc}| \\ &= \hbar\omega_m, \end{aligned} \tag{1.11}$$

in which E_a and E_b are the energies of states $|a\rangle$ and $|b\rangle$, ω_{inc} and ω_{sc} are the frequencies of the incident and scattered photons, $\omega_m \equiv |\omega_{inc} - \omega_{sc}|$ is the modulation frequency, and $\hbar$ is the reduced Planck's constant.

Suppose we begin with the molecule in state $|a\rangle$. An incident photon excites the molecule to a so-called *virtual state*. This transition to a virtual state is actually a very-far-detuned transition to one of the excited states $|i\rangle$. This detuning is so great that the virtual state is not stable; another transition must occur to connect to a stable energy state. (This large detuning from the excited state means that there is essentially no resonance condition for this transition to a virtual state. The scattering process is weak, but a broad range of frequencies can excite the molecule to the virtual state. This is key to the broadband modulation capability of our molecular modulator. See the discussion around Figure 9.5.) In the case of Rayleigh scattering, our incident and scattered photons have the same energy, so this two-photon transition connects back to the original state $|a\rangle$, and there is no change in energy.

To examine a Raman transition, again suppose we start in state $|a\rangle$. The incident photon, now called the *pump* photon, again excites the molecule to a virtual state. This time, however, the photon gives energy to the molecule, so the scattered photon is lower in energy. The molecules is excited to state $|b\rangle$ by the two-photon transition illustrated in Figure 1.8. This type of Raman scattering, in which the scattered photon is lower in both energy and frequency than the incident pump photon, is called a *Stokes* transition, and the scattered photon is a *Stokes* photon.

Raman transitions can also occur if we begin with the molecule in the excited state $|b\rangle$. The incident pump photon again excites the molecule to a (perhaps different) virtual state, but this time the molecule gives energy to the photon, and the scattered photon is higher in energy and in frequency than the incident photon. This two-photon process results in the molecule transitioning to the lower energy state $|a\rangle$, as shown in Figure 1.8. This process is called an *anti-Stokes* Raman

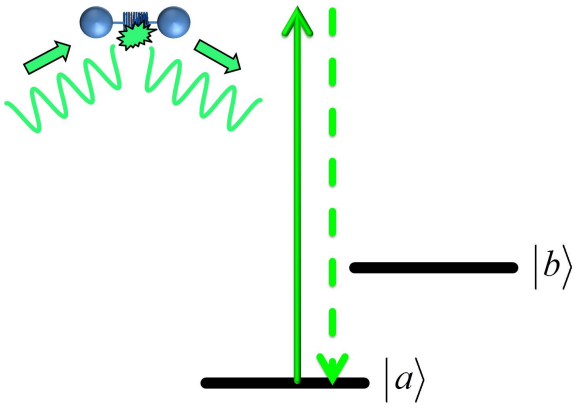

Figure 1.7 *Rayleigh Scattering* Rayleigh scattering is an elastic process that results in no change in frequency for the photon nor change in energy for the molecule. The molecule is excited to a virtual state by the incident photon (solid arrow), but it quickly returns to its original state and the photon leaves (dotted arrow) without a change in frequency.

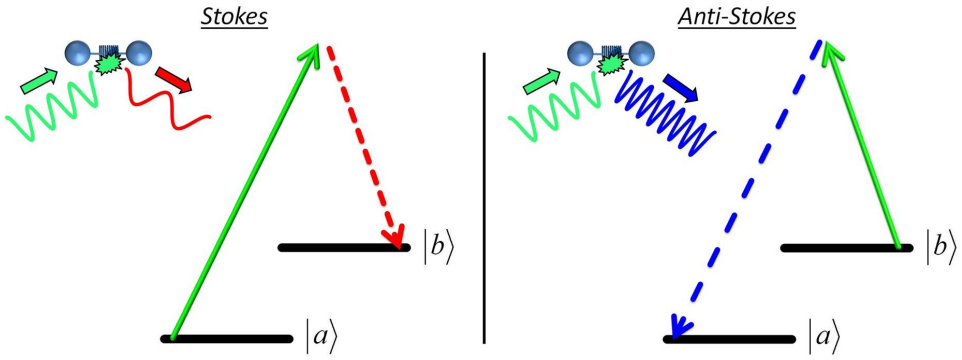

Figure 1.8 *Raman Scattering* Raman scattering is a two-photon inelastic process that results in a frequency shift for the photon and a change in energy for the molecule. The molecule is first excited to a virtual state by an incident pump photon (solid green arrow). It then transitions to a second energy state and the scattered photon (dashed arrow) is shifted in frequency. This Raman scattering is called a Stokes transition if the molecule gains energy and the photon is shifted to a lower frequency. It is called an anti-Stokes transition if the molecule loses energy and the photon is shifted to a higher frequency.

transition, and the higher-frequency scattered photon is called an *anti-Stokes* photon. (Most anti-Stokes photons in our experiment are produced through four-wave mixing. See Figure 7.2.)

For both Stokes and anti-Stokes processes, the scattered photons can be scattered again, leading to further frequency shifts as shown in Figure 1.9. The resulting photons are called *higher-order*

Stokes and anti-Stokes photons, and their frequencies are spaced from the original frequency by integer multiples of the modulation frequency: $\omega_q = \omega_0 + q \cdot \omega_m$, where q is an integer.

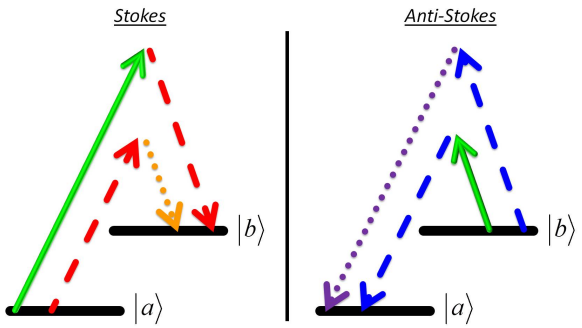

Figure 1.9 *Second-Order Raman Scattering* Both Stokes and anti-Stokes photons can themselves experience Raman scattering, and this frequency shift generates higher-order Stokes and anti-Stokes photons. First- and second-order Raman scattering processes are shown in this figure. In both scenarios the incident pump photon is the solid green arrow. This photon then scatters as part of a two-photon transition, generating the first-order Stokes (red) and anti-Stokes (blue) photons, which are represented with dashed arrows. These first-order photons are then themselves scattered, generating the second-order Stokes (orange) and anti-Stokes (purple) photons, illustrated with dotted-line arrows.

Rayleigh scattering occurs much more frequently than Raman scattering. That is, most scattered light is not frequency shifted. If we seek to efficiently shift the frequency of light through this normally weak process, we must stimulate Raman scattering. Stimulated Raman scattering, a $\chi^{(3)}$ nonlinear process, occurs when we first use resonant driving lasers to "prime" the molecules. That is, resonant lasers build up molecular coherence by driving two-photon Raman transitions. This driving process reinforces itself; when there is more Raman scattering, Raman scattering is more likely to occur. This again highlights the importance of coherence for molecular modulation, and it provides another way to view coherence. Building up coherence can be understood as making a connection between ro-vibrational energy states (between states $|a\rangle$ and $|b\rangle$ above). This is key to efficient Raman scattering. When more molecules oscillate in unison, or when the connection between ro-vibrational states is stronger, modulation is more effective. (Note that significant stimulated Raman scattering occurs only with coherent light. Without a coherent source, scattered

photons lack a definite phase relationship, and thus do not add constructively.) Chapter 2 explores stimulated Raman scattering in more detail.

Chapter 2

Raman System Formalism

In order to understand stimulated Raman scattering, we will now examine the Raman system described in Chapter 1 in more rigorous mathematical detail. Consider a system with the energy level scheme shown in Figure 2.1. States $|a\rangle$ and $|b\rangle$ are the ro-vibrational ground and excited states, respectively, of the Raman transition. States $|i\rangle$ are higher energy electronic ro-vibrational states. Single-photon transitions from $|a\rangle$ to $|b\rangle$ are electric dipole forbidden, but single-photon transitions from either Raman state to $|i\rangle$ are allowed. We will examine the interaction of this molecular system and Raman sideband beams of complex amplitudes E_q and angular frequencies ω_q, where q is an integer. E_0 is the incident pump beam, and E_{-1} is then the Stokes beam. Not shown is E_1, the anti-Stokes beam. Higher-order beams are also not shown, but E_{-2} and E_2 are the second-order Stokes and anti-Stokes beams, and so on for higher q.

Note that since

$$\omega_i \gg \omega_a, \omega_b, \tag{2.1}$$

we use $\delta\omega$ for all single-photon detunings from states $|i\rangle$;

$$\begin{aligned} \omega_i - \omega_a &\approx \omega_i - \omega_b \\ &\equiv \delta\omega. \end{aligned} \tag{2.2}$$

Furthermore, let $\Delta\omega$ be the frequency detuning from the two-photon Raman resonance. This two-photon detuning is defined as

$$\Delta\omega \equiv (\omega_b - \omega_a) - (\omega_0 - \omega_{-1}), \tag{2.3}$$

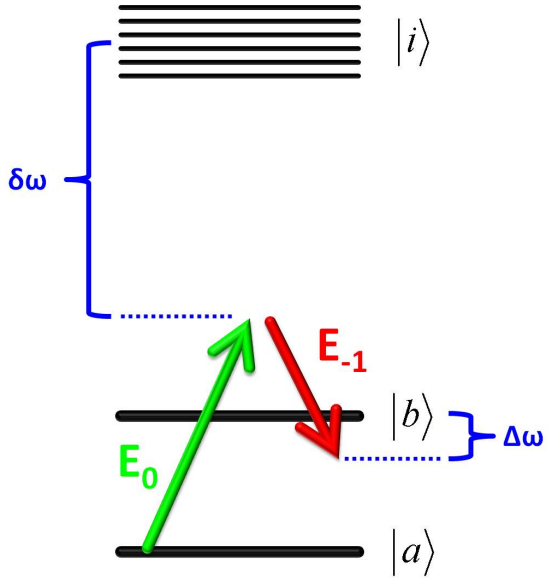

Figure 2.1 *Raman System* This simplified molecular Raman system serves as the basis for our molecular modulator. States $|a\rangle$ and $|b\rangle$ are the ro-vibrational ground and excited states, respectively, of the Raman transition. States $|i\rangle$ are higher energy electronic ro-vibrational states. The molecular system interacts with Raman sidebands. E_0 is the incident pump beam, and E_{-1} is the Stokes beam. The single- and two-photon detunings are given by $\delta\omega$ and $\Delta\omega$, respectively.

where $\omega_b - \omega_a$ is the frequency difference between the Raman energy states, and $\omega_0 - \omega_{-1}$ is the frequency difference between the pump and the Stokes lasers. Note that Figure 2.1 is *not* to scale; $\delta\omega \gg \Delta\omega$. We will also assume that the two-photon detuning is small compared to the frequency of the Raman transition;

$$\omega_{Raman} \equiv \omega_b - \omega_a \gg \Delta\omega. \tag{2.4}$$

In contrast, we assume that the $\delta\omega$ is large. In our system, the single-photon detuning is more than an order of magnitude larger than our photon frequencies and more than seven orders of magnitude larger than the two-photon detuning. Despite the fact that the large $\delta\omega$ puts $|i\rangle$ well outside any single-photon (or two-photon) resonance, these upper level states are necessary for the Raman process, as we will see below when we examine the Hamiltonian of the system. The discussion on the Hamiltonian is modeled after work from Grischkowsky and colleagues and the Harris and Yavuz groups [20, 21, 22, 23, 24, 25].

This significant single-photon detuning results in inefficient Raman scattering, as the Raman coupling between the states $|a\rangle$ and $|b\rangle$ is (very nearly) inversely proportional to the single-photon detuning. However, the Raman coupling is also proportional to the product of the two driving electric fields of the two-photon transition. (Both of these facts will be discussed further in the next section.) By increasing the intensity of the lasers, we can *stimulate* scattering and increase the efficiency of the Raman process. In the next section, we will examine in more detail the Hamiltonian of the Raman system, which will demonstrate the importance of the driving fields for coherence and for efficient Raman generation.

2.1 Effective Hamiltonian

The molecular wavefunction $|\psi\rangle$ is governed by the Schrödinger equation,

$$j\hbar\frac{d\left|\psi\right\rangle}{dt} = \hat{H}\left|\psi\right\rangle, \tag{2.5}$$

where j is the imaginary unit and $\hat{H}$ is the Hamiltonian of the system. We can write the Hamiltonian for the molecule-laser interaction as the sum of an unperturbed Hamiltonian $\hat{H}_0$ and an interaction Hamiltonian $\hat{H}_I$;

$$\hat{H} \equiv \hat{H}_0 + \hat{H}_I. \tag{2.6}$$

The wavefunction $|\psi(t)\rangle$ is defined as follows:

$$|\psi(t)\rangle \equiv c_a(t)\, e^{-j\omega_a t}\,|a\rangle + c_b(t)\, e^{-j\omega_b t}\,|b\rangle + \sum_i c_i(t)\, e^{-j\omega_i t}\,|i\rangle\,. \tag{2.7}$$

$c_n(t)$ and $\omega_n = \frac{E_n}{\hbar}$ are the coefficient and frequency associated with molecular state $|n\rangle$.

We will make the reasonable approximation that the only non-negligible interaction between the electric field and the molecule is the electric dipole interaction. If we also ignore insignificant interactions between (largely unpopulated) upper ro-vibrational states $|i\rangle$, this dipole approximation yields unperturbed and interaction Hamiltonians as follows:

$$\hat{H}_0 \equiv \hbar\omega_a\,|a\rangle\langle a| + \hbar\omega_b\,|b\rangle\langle b| + \sum_i \hbar\omega_i\,|i\rangle\langle i|\,, \tag{2.8}$$

and

$$\begin{aligned}\hat{H}_I \equiv -E(t)\,\hat{P} = &- E(t)\sum_i \mu_{ai}\,|a\rangle\langle i| - E(t)\sum_i \mu_{bi}\,|b\rangle\langle i| \\ &- E^*(t)\sum_i \mu^*_{ai}\,|i\rangle\langle a| - E^*(t)\sum_i \mu^*_{bi}\,|i\rangle\langle b|\,,\end{aligned} \tag{2.9}$$

where $E(t)$ is the electric field, $\hat{P}$ is the electric dipole moment operator, and μ_{nm} is the matrix element between states $|n\rangle$ and $|m\rangle$. * denotes a complex conjugate. The total (physical and therefore real) electric field, $E(t)$, is given by the sum of the Raman sidebands:

$$E(t) = \frac{1}{2}\sum_q E_q e^{j(\omega_q t - k_q z)} + \frac{1}{2}\sum_q E^*_q e^{-j(\omega_q t - k_q z)} \tag{2.10}$$

where $k_q \equiv \frac{\omega_q}{c}$ is the wave number (with c as the speed of light), t is time, and z is the displacement along the direction of propagation. The sums include all Raman sidebands, that is, all integer values of q. By applying Equation 2.9 to Equation 2.10, we can construct an effective Hamiltonian for the system:

$$\hat{H} = -\frac{\hbar}{2}\begin{bmatrix} A & B \\ C & D - 2\Delta\omega \end{bmatrix}. \tag{2.11}$$

In this Hamiltonian, we have used the following variables:

$$A \equiv \sum_q a_q\,|E_q|^2 \tag{2.12}$$

$$B \equiv \sum_q b_q E_q E^*_{q-1} \tag{2.13}$$

$$C \equiv \sum_q b^*_q E^*_q E_{q-1} = B^* \tag{2.14}$$

$$D \equiv \sum_q d_q\,|E_q|^2 \tag{2.15}$$

These variables contain the dispersion constants defined as

$$a_q \equiv \frac{1}{2\hbar^2}\sum_i |\mu_{ai}|^2\left[\frac{1}{(\omega_i - \omega_a) - \omega_q} + \frac{1}{(\omega_i - \omega_a) + \omega_q}\right] \tag{2.16}$$

and

$$d_q \equiv \frac{1}{2\hbar^2}\sum_i |\mu_{bi}|^2\left[\frac{1}{(\omega_i - \omega_b) - \omega_q} + \frac{1}{(\omega_i - \omega_b) + \omega_q}\right], \tag{2.17}$$

and the coupling constant

$$b_q \equiv \frac{1}{2\hbar^2} \sum_i \mu_{ai}\mu_{bi}^* \left[\frac{1}{(\omega_i - \omega_a) - \omega_q} + \frac{1}{(\omega_i - \omega_b) + \omega_q} \right]. \tag{2.18}$$

A detailed derivation of the effective Hamiltonian can be found in Appendix A. Note that in arriving at this result, in addition to the aforementioned assumptions and approximations, we have assumed that we are close to a two-photon resonance, so we have used the rotating wave approximation to eliminate terms that oscillate rapidly. We have also assumed that all probability amplitudes vary slowly compared to $\frac{1}{\delta\omega}$ and that the transition linewidths are arbitrarily small.

The first thing to note about this Hamiltonian is that it is a 2×2 matrix; the complex molecular interaction is effectively a two-level system. Appreciable probability amplitudes exist only in states $|a\rangle$ and $|b\rangle$.

Now examine the form of the Hamiltonian in more detail. Note that every term (with the exception of the detuning term $\Delta\omega$) contains a coupling or dispersion constant: a_q, b_q, or d_q. These constants all feature terms of the form $\frac{1}{(\omega_i - \omega_a) \pm \omega_q}$ or $\frac{1}{(\omega_i - \omega_b) \pm \omega_q}$. As discussed earlier, the large single-photon detuning means that $\omega_i - \omega_a \approx \omega_i - \omega_b \equiv \delta\omega$. Also, the detuning is much greater than the photon frequency: $\delta\omega \gg \omega_q$. Therefore, $\frac{1}{(\omega_i - \omega_a) \pm \omega_q} \approx \frac{1}{(\omega_i - \omega_b) \pm \omega_q} \approx \frac{1}{\delta\omega}$. Each of the constants A, B, and D is then roughly proportional to the inverse of the single-photon detuning;

$$A, B, D \sim \frac{1}{\delta\omega}. \tag{2.19}$$

The effective Hamiltonian also shows how the upper ro-vibrational states $|i\rangle$ play an necessary role in the transition, even though their probability amplitudes are negligibly small. In addition to the appearance of ω_i in the detuning expressions, the terms of the effective Hamiltonian all depend on a product of μ_{ai} and μ_{bi}, the matrix elements of the transition.

Also note that all terms in the Hamiltonian depend on some product of the electric fields of the lasers, E_q and E_{q-1}. This indicates that, perhaps unsurprisingly, when the fields are more intense, more interaction occurs. Moreover, the dependence of the off-diagonal terms on the product $E_q E_{q-1}^*$ (or its conjugate) highlights the fact that the coupling between states $|a\rangle$ and $|b\rangle$ is proportional to both fields in the two-photon transition (as opposed to, for example, being a sum of

independent contributions from each field). The coupling is driven by the product of the pump and the Stokes beams (or by any pair of consecutive sidebands).

Note that the terms A and D have the form of a second-order perturbation theory calculation of the product of the electric field, E_q, and the electric dipole moment, μ_{mn}. Thus, we can understand the physical meaning of the A and D terms in the Hamiltonian; they are proportional to the AC Stark shift of the states $|a\rangle$ and $|b\rangle$ due to the laser fields. The off-diagonal terms B and C are related to the coupling of the molecular states. They each have the product of $E_q \cdot \mu_{ai}$ (from the first photon) and $E_{q-1} \cdot \mu_{bi}$ (from the second photon). These single-photon Rabi frequencies are divided by the detunings of the transitions. Such a product of single-photon Rabi frequencies over a detuning yields a term proportional to the two-photon Rabi frequency. Therefore, B and C are proportional to the two-photon Rabi frequency.

2.2 Eigenstates and Eigenvectors

The eigenstates of the effective Hamiltonian are calculated to be

$$|\pm\rangle = 2B\,|a\rangle + \left[-\left(A - D + 2\Delta\omega\right) \mp \sqrt{\left(A - D + 2\Delta\omega\right)^2 + 4\,|B|^2}\right] |b\rangle \tag{2.20}$$

with eigenvalues

$$E_\pm = -\frac{\hbar}{4}\left[\left(A + D - 2\Delta\omega\right) \mp \sqrt{\left(A - D + 2\Delta\omega\right)^2 + 4\,|B|^2}\right]. \tag{2.21}$$

See Appendix B for detailed calculations.

We focus on the lower energy state, $|-\rangle$, because it is smoothly connected to the unperturbed ground state, $|a\rangle$. This is assured by the adiabatic theorem. The adiabatic theorem states that a system remains in its original eigenstate when perturbed if the perturbation is slow compared to the characteristic frequency of the system [26]. In the case of our experiment, the perturbations to the Hamiltonian of the Raman system come from the applied laser fields. The time scale of these perturbations is set by how quickly the fields build up in the cavity and by the fluctuations in the cavity fields over time. In both cases, the fastest fluctuations occur on the order of the time that the

light spends in the cavity,

$$t_{perturbations} \sim t_{round-trip} \cdot n = \frac{2L}{c} \cdot \mathcal{F}, \tag{2.22}$$

where $t_{perturbations}$ is the characteristic timescale of the perturbations, $t_{round-trip}$ is the time light takes to go twice L (the length of the cavity), c is the speed of light in the cavity, n is the average number of round trips that the light makes before being transmitted, and $\mathcal{F}$ is the finesse of the cavity. (Finesse can be thought of here as how well a cavity holds light. A high finesse means that light reflects many times on the mirrors before being transmitted. See Section 6.2 for a more complete discussion of finesse.) In our experiment, $t_{perturbations} \sim 0.1$ ms.

The characteristic time scale of the Raman system comes from the energy difference between the eigenstates of the system. This splitting is given by the energy difference between the eigenvalues (Equation 2.21):

$$\begin{aligned}
\Delta E &= E_+ - E_- \\
&= -\frac{\hbar}{4}\left[(A+D-2\Delta\omega) - \sqrt{(A-D+2\Delta\omega)^2 + 4\left|B\right|^2}\right] \\
&\quad -\left(-\frac{\hbar}{4}\left[(A+D-2\Delta\omega) + \sqrt{(A-D+2\Delta\omega)^2 + 4\left|B\right|^2}\right]\right) \\
&= \frac{\hbar}{2}\sqrt{(A-D+2\Delta\omega)^2 + 4\left|B\right|^2}.
\end{aligned} \tag{2.23}$$

As discussed at the end of Section 2.1, A, B, and D are roughly proportional to $\frac{1}{\delta\omega}$ and to the product of the electric fields of the Raman sidebands. Thus, if we take the applied fields to be weak, the fact that $\delta\omega$ is large means that A, B, and D are very small, and

$$\begin{aligned}
\Delta E &= E_+ - E_- \\
&= -\frac{\hbar}{4}\left[(A+D-2\Delta\omega) - \sqrt{(A-D+2\Delta\omega)^2 + 4\left|B\right|^2}\right] \\
&\quad -\left(-\frac{\hbar}{4}\left[(A+D-2\Delta\omega) + \sqrt{(A-D+2\Delta\omega)^2 + 4\left|B\right|^2}\right]\right) \\
&= \frac{\hbar}{2}\sqrt{(A-D+2\Delta\omega)^2 + 4\left|B\right|^2} \\
&\approx \frac{\hbar}{2}\sqrt{(2\Delta\omega)^2} \\
&= \hbar\Delta\omega.
\end{aligned} \tag{2.24}$$

Thus, the characteristic time scale of the Raman system would be

$$t_{characteristic} \sim \frac{1}{\Delta\omega}. \tag{2.25}$$

For our experiment, this characteristic time is $t_{characteristic} \sim 10$ ns. Therefore, $t_{perturbations} \sim 0.1$ ms $\gg t_{characteristic} \sim 10$ ns. The timescale of the perturbations is much longer than the characteristic timescale of the system, and thus the adiabatic theorem holds.

The lower energy eigenstate $|-\rangle$ (Equation 2.20) is thus connected to the unperturbed ground state. We now rewrite this lower energy state in a more standard form.

$$|-\rangle = 2B\,|a\rangle + \left[-\left(A - D + 2\Delta\omega\right) + \sqrt{\left(A - D + 2\Delta\omega\right)^2 + 4\,|B|^2}\right]|b\rangle \tag{2.26}$$

can be written as

$$|-\rangle \equiv |\psi\rangle = \cos\left(\frac{\theta}{2}\right) e^{j\frac{\phi}{2}}\,|a\rangle + \sin\left(\frac{\theta}{2}\right) e^{-j\frac{\phi}{2}}\,|b\rangle\,, \tag{2.27}$$

where we have defined θ and ϕ with the following relationships:

$$\theta = \tan^{-1}\left(\frac{2\,|B|}{A - D + 2\Delta\omega}\right), \tag{2.28}$$

and

$$B = |B|^{j\phi}\,. \tag{2.29}$$

Further discussion of the eigenstates and eigenvalues can be found in Appendix B.

2.3 Electric Field Propagation in the Raman System

We can now examine how the Raman sideband fields E_q propagate through the molecular medium. We begin by calculating the molecular polarization due to the applied fields. The polarization is given by the expectation value for the dipole moment operator $\hat{P}$ with a generic molecular state $|\psi(t)\rangle$:

$$P(t) = \langle\psi(t)|\,\hat{P}\,|\psi(t)\rangle\,, \tag{2.30}$$

with

$$\hat{P} \equiv \sum_i \mu_{ai}\,|a\rangle\,\langle i| + \sum_i \mu_{bi}\,|b\rangle\,\langle i| + \sum_i \mu_{ai}^*\,|i\rangle\,\langle a| + \sum_i \mu_{bi}^*\,|i\rangle\,\langle b|\,. \tag{2.31}$$

and, as above,

$$|\psi(t)\rangle \equiv c_a(t)\, e^{-j\omega_a t}\,|a\rangle + c_b(t)\, e^{-j\omega_b t}\,|b\rangle + \sum_i c_i(t)\, e^{-j\omega_i t}\,|i\rangle\,. \tag{2.32}$$

In these expressions, $c_n(t)$ and $\omega_n = \frac{E_n}{\hbar}$ are the coefficient and frequency associated with molecular state $|n\rangle$. μ_{nm} is the dipole matrix element between states $|n\rangle$ and $|m\rangle$.

Using the calculated polarization and the assumption that the two-photon detuning $\Delta\omega$ is small compared to the frequencies of the fields and of the transitions, we find the following propagation equation for the Raman sidebands in the molecular medium:

$$\frac{\partial E_q}{\partial z} = -j\eta\hbar\omega_q N\left[|\tilde{c}_a|^2 E_q a_q + |\tilde{c}_b|^2 E_q d_q + \tilde{c}_a^*\tilde{c}_b E_{q+1} b_{q+1} + \tilde{c}_a\tilde{c}_b^* E_{q-1} b_q^*\right], \tag{2.33}$$

where E_q and ω_q are the electric field and frequency of the qth sideband, $\tilde{c}_n$ is a phase-transformed coefficient of state $|n\rangle$, and a_q, b_q, and d_q are the coupling and dispersion constants defined above (Equations 2.16, 2.17, and 2.18). z is the propagation direction, and N is the number of molecules per unit volume. $\tilde{c}_n$ is the phase-transformed coefficient of the molecular state $|n\rangle$, and

$$\eta \equiv \sqrt{\frac{\mu}{\varepsilon_0}}. \tag{2.34}$$

See Appendix C for more details.

In the derivation of the propagation equation, we have used the slowly-varying envelope approximation to Maxwell's equations. This approximation is based on two main assumptions. The first is that the temporal variations of the light envelope are small compared to the frequencies of light interacting with the system. The second is that the spatial variations on the envelope of the light are small compared to the wavelengths of the light. The slowly varying envelope approximation yields a fairly accurate description of the molecular interaction [27]. Note that we have also assumed that diffraction effects are negligible, so we have dropped a second-order term in the transverse directions.

The form of Equation 2.33 reveals two vital features of the interaction of the light and the molecular system. The first is the interaction and interdependence of the Raman beams. The equation explicitly shows how the propagation of the qth sideband, $\frac{\partial E_q}{\partial z}$, depends not only on the qth electric field, but also on the $(q-1)$th and $(q+1)$th sidebands, E_{q-1} and E_{q+1}.

Moreover, the form of Equation 2.33 demonstrates the importance of the coefficients c_a and c_b in determining the strength of this interaction, which determines the efficiency of the Raman scattering. As mentioned in Chapter 1, semi-classically, the key to efficient Raman scattering is having all molecules coherently rotating or vibrating. Quantum mechanically, this uniform ro-vibrational motion corresponds to the molecules being in a (near) equally-weighted superposition of states $|a\rangle$ and $|b\rangle$. That is, the molecules are in a state

$$|\psi\rangle = c_a |a\rangle + c_b |b\rangle \tag{2.35}$$

such that

$$|c_a| \approx |c_b| . \tag{2.36}$$

The Raman interaction is stronger, and thus the molecular modulation is more efficient, when the molecules are in such a mixed state. A density matrix approach helps to quantify this mixture. We can define a density matrix for our system as follows:

$$\rho \equiv \begin{bmatrix} \rho_{aa} & \rho_{ab} \\ \rho_{ab}^* & \rho_{bb} \end{bmatrix} = \begin{bmatrix} |c_a|^2 & c_a^* c_b \\ c_a c_b^* & |c_b|^2 \end{bmatrix} . \tag{2.37}$$

In this density matrix, the diagonal elements ρ_{aa} and ρ_{bb} give the fractional populations of states $|a\rangle$ and $|b\rangle$. The off-diagonal element ρ_{ab} is called the *coherence* of the molecular system. This is a quantitative expression of the same coherence that was discussed in Chapter 1 in terms of uniform oscillations of molecules and in terms of connections between ro-vibrational states. Here we see that the coherence (along with its conjugate) determines the extent of the mixing between the quantum states $|a\rangle$ and $|b\rangle$. The mixing stemming from this coherence is the key to molecular modulation.

For the eigenstate that is smoothly connected to the ground state (Equation 2.27), the density matrix elements are given by

$$\rho_{aa} = \cos^2\left(\frac{\theta}{2}\right) , \tag{2.38}$$

$$\rho_{bb} = \sin^2\left(\frac{\theta}{2}\right) , \tag{2.39}$$

and

$$\rho_{ab} = \frac{1}{2}\sin(\theta)\, e^{j\phi}, \tag{2.40}$$

where θ and ϕ are defined as above (Equations 2.28 and 2.29).

In the regime where the molecular states are weakly coupled, we can rewrite these matrix elements as follows:

$$\rho_{ab} \approx \frac{B}{A - D + 2\Delta\omega}, \tag{2.41}$$

$$\rho_{aa} \approx 1 - |\rho_{ab}|^2, \tag{2.42}$$

and

$$\rho_{bb} \approx |\rho_{ab}|^2, \tag{2.43}$$

where A, D, and $2\Delta\omega$ are defined as in the effective Hamiltonian above (Equation 2.11). More details can be found in Appendix D.

Finally, using the density matrix definitions, we can rewrite Equation 2.33 as

$$\frac{\partial E_q}{\partial z} = -j\eta\hbar\omega_q N\left[\rho_{aa}E_q a_q + \rho_{bb}E_q d_q + \rho_{ab}^* E_{q+1} b_{q+1} + \rho_{ab}E_{q-1}b_q^*\right]. \tag{2.44}$$

This form of the propagation equation highlights the pivotal role of the coherence in the creation (and interaction) of the Raman sidebands. The coherence couples the electric fields of different sidebands, and this allows for the generation of new sidebands. Through the coherence, the $(q+1)$th and the $(q-1)$th sidebands contribute to the propagation of the qth sideband. Thus, for example, the presence of a $(q-1)$th field can generate a previously non-existent qth field. The efficiency of this process is tied to the coherence. When the magnitude of ρ_{ab} increases, the connection between Raman sidebands increases, and molecular modulation is more efficient. Much of our research is devoted to efforts to increase ρ_{ab} in our molecular system to a value closer to the maximal coherence value of

$$|\rho_{ab}^{max}| = 0.5, \tag{2.45}$$

which corresponds to half of the molecular population being coherently transferred from the lower Raman state $|a\rangle$ to the upper Raman state $|b\rangle$.

Note that Equation 2.44 is true for a generic field E_q; this E_q need not be the same as the E_q used to build up the coherence. This is extremely important because it means that *almost any* beam can be modulated by the Raman system. Strong beams can be used to drive the coherence, while an arbitrary, independent beam can mix with that coherence and be modulated. An experimental realization of such an independent mixing beam scheme is discussed in Chapter 9.

A final quick aside about the two-photon detuning and its connection to phase: In Raman systems with large single-photon detunings such as this system, the Stark shift terms A and D will be roughly equal. Thus, the denominator of θ (Equation 2.28) is

$$A - D + 2\Delta\omega \approx 2\Delta\omega, \tag{2.46}$$

and its sign (and thus the sign of θ) is determined by the sign of $\Delta\omega$. If $\Delta\omega$ (and thus θ) is positive, then the coherence

$$\rho_{ab} = \frac{1}{2}\sin(\theta)\, e^{j\phi} \tag{2.47}$$

will have the phase $e^{j\phi}$. Because of how we defined ϕ (Equation 2.29), this is the same phase as B, the coupling term from the driving fields. Thus, if the two-photon detuning $\Delta\omega$ is positive, the coherence has the same phase as the driving field coupling term, and we say that it is a *phased eigenstate*. On the other hand, if $\Delta\omega$ (and thus θ) is negative, then the coherence effectively picks up a negative sign, as $\sin(-x) = -\sin(x)$.

$$\begin{aligned} \rho_{ab} &= \frac{1}{2}\sin(\theta)\, e^{j\phi} \\ &= -\frac{1}{2}\sin(|\theta|)\, e^{j\phi} \end{aligned} \tag{2.48}$$

This is equivalent to a π phase shift, as $-e^{j\phi} = e^{j(\phi+\pi)}$.

Thus, the phase of the coherence is now π out of phase with the driving field term B, which has phase ϕ.

$$\rho_{ab} = \frac{1}{2}\sin(|\theta|)\, e^{j(\phi+\pi)} \tag{2.49}$$

Therefore, if the two-photon detuning $\Delta\omega$ is negative, it is called an *anti-phased eigenstate*.

In both the phased and anti-phased cases, the phase of the coherence compared to the driving fields is well-defined, and the contributions from all the molecules add together in phase. (This is

true assuming that the two-photon detuning is large enough that all molecules have the same sign for the detuning. With a small detuning, inhomogeneous broadening or a driving laser with a large frequency bandwidth could lead to some molecules with a positive $\Delta\omega$ and some with a negative $\Delta\omega$. This would result in different molecules experiencing differently-phased coherences, and the effects would not add constructively.)

Chapter 3

An Overview of Molecular Modulation Research

Our work with molecular modulation is motivated by promising past work in the field. This chapter provides a brief overview of stimulated Raman scattering and molecular modulation research.

3.1 Early Pioneering Research

The ideas behind molecular modulation began to come together in the early 1990s. In 1993, Imasaka and colleagues put forth one of the first proposals for molecular modulation using Raman scattering [28]. They used computer simulations to show how a spectrum generated through Raman scattering in molecular hydrogen could be used to generate ultrashort optical pulses. Soon after in 1994, Kaplan suggested a similar technique using cascaded stimulated Raman scattering to produce trains of sub-femtosecond pulses [29].

Within a decade, experiments were demonstrating the feasibility and power of molecular modulation. In 1999, Kawano *et al*. demonstrated stimulated Raman scattering in gaseous hydrogen [30]. They observed both vibrational and rotational Raman scattering, including higher-order beams generated through four-wave mixing. The Harris group used two driving lasers to stimulate Raman transitions in molecular hydrogen [31, 32]. In the first few years of the 2000s, they used coherently oscillating molecules to create both frequency- and amplitude-modulated light from a generated spectrum ranging from 195 nm to 2.94 μm in wavelength. In 2002, Losev *et al*. further demonstrated the usefulness of molecular modulation with the development of a broadband multi-frequency shifter [33]. This device generated many orders of frequency-shifted sidebands

through molecular modulation in a cell of hydrogen using a multi-pass geometry. In 2003, the Harris group used adiabatic molecular modulation to generate approximately 200 Raman sidebands, and they showed that these sidebands had mutually coherent phases [34]. In 2005, Shverdin *et al*. demonstrated the utility of the technique for ultrashort pulse generation when they used a modulation generated spectrum to synthesize a light pulse with the duration of a single optical cycle [35]. Zhavoronkov and Korn have extended the technique of ultrashort pulse generation by means of molecular modulation [36]. In 2002, they moved from the adiabatic regime to the impulsive regime, in which the driving laser pulse has a duration shorter than the inverse of the molecular frequency. In this technique, the strong driving pulses prepare the molecular coherence. Detrimental effects from these strong pulses dissipate before the arrival of a later, weaker pulse that is modulated by the remaining coherence.

3.2 Recent Developments

Molecular modulation research continues to expand and reach new milestones. There have been developments in both the generation of Raman spectra and in the manipulation of such spectra towards waveform synthesis. In 2008, the Kung group used molecular modulation to generate a Raman spectrum capable of generating sub-single-optical-cycle pulses with duration less than 0.5 fs [37]. This work is set apart from previous work because their driving laser frequencies were selected to be exact multiples of their modulation frequency, and thus the generated sidebands were all harmonics of a common fundamental frequency (the modulation frequency). Therefore, rather than having the peak pulse location vary with respect to the peak of the carrier envelope, the sub-cycle pulses generated by this spectrum have a constant carrier-envelope phase. In 2012, the Imasaka group was able to generate a broad example of such a harmonic spectrum, with high-order Raman scattering generating a spectrum ranging from the ultraviolet to the near infrared [38]. In 2008, Suzuki and colleagues performed detailed phase measurements on the components of a generated Raman spectrum [39]. This helped to reveal the temporal structure of ultrashort pulses generated from the spectrum, and the definite phase relationship suggests the feasibility of using such a spectrum for Fourier synthesis of waveforms. In 2009, the Kung group demonstrated the

ability to manipulate the carrier envelope phase of pulses generated through molecular modulation [40]. Two years later, they further demonstrated the ability to synthesize sawtooth, square, and triangular waves using phase and amplitude control of Raman spectra [41]. The ability to synthesize arbitrary optical waveforms is powerful, as it allows for the exploration and coherent manipulation of molecules with unprecedented control and resolution. For recent developments in coherent control, see the work of Gandman and colleagues [15]. For an overview of coherent control, see the review article by Shapiro and Brumer [14].

3.3 Limitations of Past Work

These pioneering experiments, along with others, demonstrated the viability of molecular modulation. They also had one important thing in common; all of the experiments described above were accomplished using pulsed driving lasers to stimulate Raman scattering. Q-switched pulsed pump and Stokes lasers were loosely focused on a Raman cell filled with low-pressure molecular gas. The ultrafast pulses from these lasers were typically 10s of mJ in energy and on the order of 10 ns in duration.

As discussed in Chapter 2, the coherence of a Raman system is proportional to the product of the lasers that drive the two-photon transition. To get near-maximal coherence and thus efficient molecular modulation, strong driving fields are required. Preparation of near-maximal molecular coherence requires laser intensities approaching 1 GW/cm^2 [42]. Pulsed lasers are capable of producing these intense fields, and that is why most early molecular modulation experiments used pulsed lasers.

There are drawbacks to using pulsed lasers in molecular modulation experiments that have limited their utility, and these shortcomings have motivated our research. First of all, pulsed molecular modulation cannot be used with CW laser sources. (Particularly relevant is the incompatibility of pulsed modulation with CW titanium-sapphire lasers. See Chapter 11.) Furthermore, while they are capable of producing the high fields necessary to achieve near-maximal coherence, pulsed lasers are fundamentally limited in their frequency linewidths. Pulsed laser linewidths cannot be arbitrarily narrow; the frequency spread $\Delta\nu$ is roughly inversely proportional to the pulse duration

t_{pulse}:

$$\Delta\nu \sim \frac{1}{t_{pulse}}. \tag{3.1}$$

Note that ν is the frequency, rather than the angular frequency, ω, which we used in previous chapters. From this point on, we will often discuss frequency rather than angular frequency. The two are related in the usual way as shown in Equation 3.2.

$$\omega = 2\pi\nu \tag{3.2}$$

The relationship between linewidth and pulse duration of Equation 3.1 limits the frequency linewidth of Raman sidebands produced through molecular modulation with pulsed lasers. For a pulse with $t_{pulse} \sim 10$ ns, this implies a frequency linewidth of $\Delta\nu \sim 100$ MHz. Thus, sidebands from the generated spectrum have too wide of a frequency linewidth to be used in precision spectroscopy or other applications that require narrow linewidth lasers.

3.4 Continuous-Wave Molecular Modulation

The frequency linewidth limitation on pulsed lasers has motivated our pursuit of molecular modulation based on stimulated Raman scattering with *continuous-wave* (CW) lasers. CW lasers have no pulse duration, so the relationship of Equation 3.1 places no lower bound on the frequency linewidth. Narrow linewidth CW lasers routinely have full-width-half-maximum linewidths on the order of 100s of Hz to 100s of kHz. (The CW lasers in our experiment have full-width-half-maximum linewidths around 10 kHz.) Although there are certainly technical challenges, in principle, CW lasers can have frequency linewidths on the order of 1 Hz. If the lasers that drive the Raman process have very stable, precisely known frequencies, then the modulation frequency will also be very stable and precisely known. Therefore, the same will be true for all of the sidebands. This stability and precision could be accomplished by locking the driving lasers to a stable frequency reference, like one of the teeth of a frequency comb. Such references have been shown to have frequency precision better than 1 part in 10^{15} [43, 17].

CW lasers also avoid the pulsed laser problems of low duty cycles and pulse-to-pulse inconsistencies in timing and intensity. The low duty cycles of pulsed lasers, usually less than 1 part in

10^7, severely restricts data rates in pulsed experiments, and the pulse-to-pulse inconsistencies are detrimental to experimental repeatability.

The benefits of CW lasers must be weighed against the significant challenge of a decrease in intensity. As mentioned above, the coherence of a Raman system is proportional to the product of the driving laser fields. CW lasers cannot provide the high intensities achieved at the peak of laser pulses, and thus CW lasers are much less efficient at stimulating Raman scattering. As proposed by Yavuz and by Shinzen *et al.* in the 2000s, this limitation can be overcome [44, 45]. CW lasers can be used for molecular modulation if the scattering occurs inside a high-finesse optical cavity, which increases the laser intensity seen by the molecules. (It should be noted that this also adds the experimental complexities associated with high-finesse cavities. See the discussion below and also Chapter 6 for further discussion of optical cavities.)

This idea of CW molecular modulation was motivated by earlier successes of Raman scattering in a high-finesse cavity. The Carlsten group first demonstrated a CW Raman laser (a laser based on stimulated Raman scattering rather than stimulated emission) using hydrogen molecules in a high-finesse cavity in the late 1990s [46]. Carlsten and colleagues also developed and explored the theory behind Raman lasing [47]. Further experiments in the early 2000s demonstrated the power of stimulated Raman scattering inside a high-finesse cavity. Tunable Raman lasers were developed that were capable of generating both Stokes and anti-Stokes sidebands off of vibrational and rotational molecular transitions [48, 49, 50]. In the middle of the decade, simulations and experiments from the Imasaka group demonstrated that the spectra generated from such CW Raman scattering were coherent and suitable for generating ultrashort pulses [45, 51].

As an aside, note that the addition of a cavity places restrictions on the frequencies of the Raman lasers, and it slightly alters the energy level scheme discussed in Chapters 1 and 2. (For example, see the energy level scheme of Figure 2.1.) As shown in Figure 3.1, the addition of a cavity means that the lasing is restricted to cavity resonances, which are represented by purple dotted lines. Thus, the two-photon detuning and the Stokes frequencies are limited to a set of discrete values set by these resonances. However, the cavity resonances can be modified by slightly tuning the pump frequency or the cavity length.

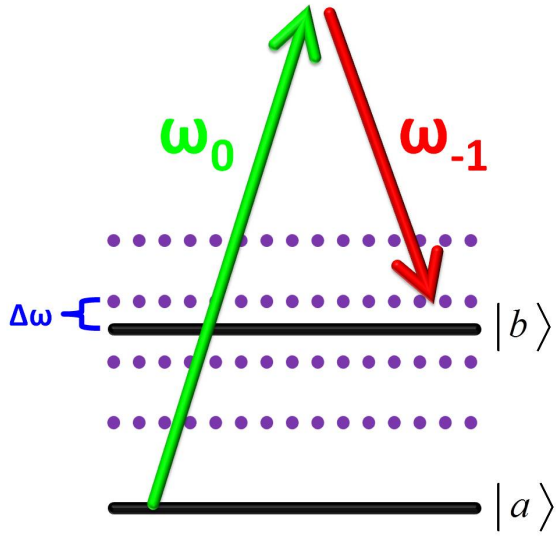

Figure 3.1 *Raman System in a Cavity* The addition of a cavity modifies the energy level diagram of the Raman system. The Raman frequencies are limited by the requirement that they be resonant with the cavity. The cavity resonances are marked with dotted purple lines. $|a\rangle$ and $|b\rangle$ are ro-vibrational states of the molecule. ω_0 and ω_{-1} are the frequencies of the pump and Stokes photons, respectively, that drive the two-photon Raman process. $\Delta\omega$ is the two-photon detuning, the difference between the Raman frequency ($\omega_b - \omega_a$) and the frequency difference of the driving photons ($\omega_0 - \omega_{-1}$). In this case, $\Delta\omega$ is the difference between the frequency of state $|b\rangle$ and that of the cavity resonance on which the Stokes beam is lasing. The cavity resonances, and thus $\Delta\omega$, can be changed by adjusting the cavity length or pump laser frequency.

A significant advance made by Yavuz in 2007 was to propose to use this stimulated Raman scattering in a high-finesse cavity as a molecular modulator for an *independent* laser beam [44]. In this proposal, it was no longer necessary for a beam to be resonant with the cavity in order to be modulated. The idea is that the driving lasers are resonant with the cavity, and their strong fields build up coherence in the molecular medium. An independent mixing beam then passes through the cavity, mixes with the established coherence, and its frequency is modulated in a single pass. The lack of a resonance requirement for the mixing beam greatly increases the versatility of the modulator. Although there are technical limitations from the optics used, this method can be used to develop a broadband modulator, one capable of modulating any laser in the optical range of

the spectrum (roughly 100 nm - 10 μm). (See Chapter 9 for further discussion of broadband modulation.)

Experimental progress with CW molecular modulation continues to the present. In 2009, the Yavuz group demonstrated experimental progress towards the proposed goal of a broadband modulator, developing a CW Raman laser inside a high-finesse cavity that will serve as the basis for the proposed modulator [52]. (See Chapter 7.) The Yavuz modulator operates at higher laser powers, lower molecular pressures, and colder temperatures than other molecular modulators. The high-power work in the Yavuz group is motivated by the fact that in 2004, the Carlsten group demonstrated high-power Raman lasing, a necessary step towards a high-power molecular modulator [53]. (The Imasaka group also continues to work with continuous-wave stimulated Raman scattering, but they have focused on phase matching of Raman components in a dispersion-compensated cavity rather than modulation of an independent mixing beam [54, 55].) The research covered in this thesis builds upon and expands this early continuous-wave molecular modulation work of the Yavuz group.

As a last note before discussing our research in detail, it is important to acknowledge that there are other Raman-based modulation methods that will not be discussed in this thesis. Both our work and the experiments discussed above are based on Raman scattering in molecular gases. However, there are other Raman media that can be used for molecular modulation. Molecular modulation techniques have been developed using diverse media such as solid hydrogen [56], photonic crystal fibers [57], Raman-active crystals [58, 59], and phonons in semiconductors [60].

Chapter 4

Molecular Modulation Experiment Overview

Before discussing our results, we present a detailed description of our experiment. The basic components of our experiment are shown in Figure 4.1. Chapters 5 and 6 provide more details on the locking circuitry and high-finesse cavity.

Our laser system begins with a custom-built external cavity diode laser (ECDL) at a wavelength of 1064 nm that serves as our Raman pump laser. The external cavity is formed by a grating in the Littrow configuration that provides optical feedback. The grating is mounted on a piezoelectric transducer (PZT) and on actuators to allow for frequency tunability. We can choose the lasing frequency by using the grating and the PZT to selectively feed that frequency back to the laser. The optical power of the ECDL is around 20 mW, and its free-running full-width-half-maximum linewidth is around 0.5 MHz. The ECDL beam goes through a Faraday isolator (not shown in the figure) to prevent frequency-disrupting optical feedback, and then it is sent through an electro-optic modulator (EOM). The EOM modulates the phase of the beam at 50 MHz. (The resulting frequency sidebands are roughly 5 - 10 % of the intensity of the main beam.) This phase modulation is used to lock the laser to a high-finesse cavity (HFC). The beam is then used to seed a ytterbium fiber amplifier (Yb FA) from IPG Photonics. The Yb FA amplifies the 5 mW of seed power to 30 W of continuous-wave (CW) power. (See note at the end of this chapter.) The Yb FA output is single mode spatially, single mode in frequency, and linearly polarized. After it passes through another Faraday isolator (also not shown), a series of mode-matching lenses (MML, represented by a single lens in the schematic) shape the amplified beam to match the fundamental Gaussian mode (TEM_{00}) of the HFC. The HFC contains the dilute (0.1 - 0.5 atm) molecular gas

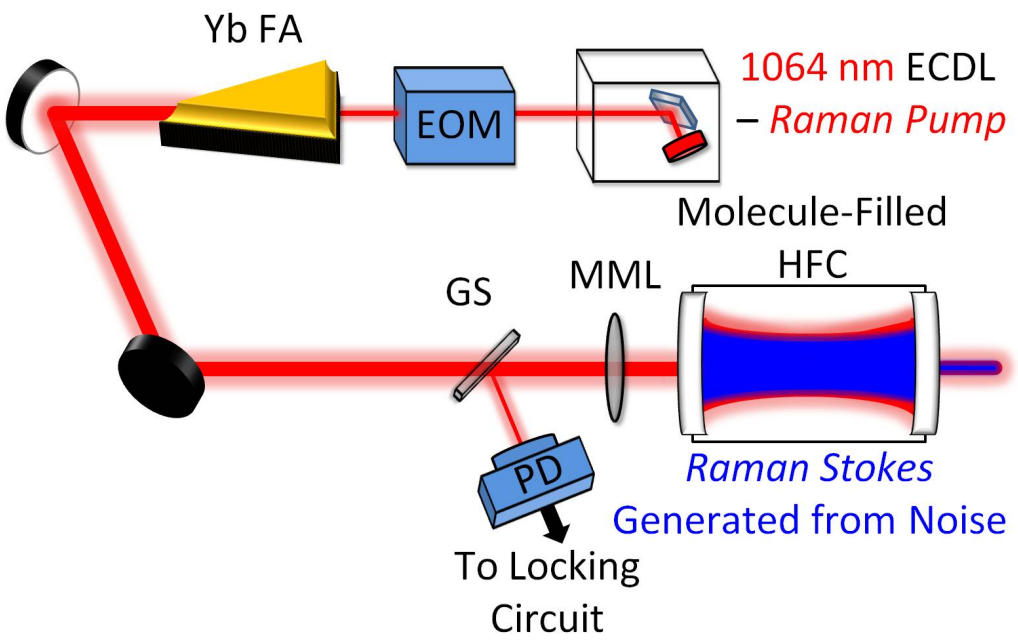

Figure 4.1 *Experiment Schematic* We seed our experiment with a custom-built external cavity diode laser (**ECDL**). The continuous-wave (CW) beam is modulated by an electro-optic modulator (**EOM**) so that it can be used in a Pound-Drever-Hall locking scheme. The ECDL output is on the order of 10 mW, and this seeds a ytterbium fiber amplifier (**Yb FA**). The output of the Yb FA is up to 30 W of CW power in a single spatial mode and a single frequency mode. The Yb FA output is coupled to a high-finesse cavity (**HFC**) using a mode-matching lens (**MML**). Raman scattering in the HFC generates a Raman Stokes beam, which also resonates in the HFC. A glass slide (**GS**) picks off part of the reflection from the cavity and sends the signal to the locking circuit through a photodiode (**PD**). Further details are in the main text.

that serves as the Raman medium for our molecular modulator. Our Raman Stokes laser is generated from noise through stimulated Raman scattering of the pump beam inside the cavity. We use the Pound-Drever-Hall (PDH) technique to lock the laser to one of the longitudinal modes of the HFC [61]. In locking the laser to the cavity, we are effectively comparing the laser to a time-average of itself (over the time it spends circulating in the cavity), and using feedback to keep the laser self-consistent in the face of perturbations [62]. This locking keeps the laser on resonance with the cavity, narrows its frequency linewidth, and allows for the build-up of the intense fields

that are required to stimulate Raman scattering. A glass slide (GS) picks off part of the reflection from the input cavity mirror and sends it to a photodiode (PD). This signal is then sent to the locking circuit. The following chapters describe the locking circuitry and the HFC in more detail.

Notes on Fiber Amplifier Power

Although the amplifier has a maximum output of 30 W, we cannot exceed 20 W for experiments using linearly polarized light. With linearly polarized light, the optics must withstand *twice* the output power of the fiber amplifier: both the incident beam and the beam reflected by the front mirror of the cavity. Due to the high reflectivity of the cavity mirrors, this reflected beam is nearly the same power as the incident beam. Our high-power Faraday isolator cannot handle the intensity of two passes of a 30 W focused beam, so we must run our amplifier at a lower power.

When we use a circularly polarized beam, we use a quarter-wave plate right in front of the cavity to circularly polarize the linear output of the amplifier. The reflected beam thus passes through the quarter-wave plate twice. After this, the reflected beam is linearly polarized in a direction perpendicular to the incident beam. This allows us to separate out this reflected beam with polarization-dependent optics before it reaches the isolator. The isolator can withstand a single pass of 30 W, so we can use full power for experiments with circularly polarized light.

As a final note, we have found that the output of the fiber amplifier changes noticeably depending on the output power. Both the mode quality and beam size change. The coupling to the cavity is extremely sensitive to both of these parameters, so we attempt to keep them constant. To do this, we always run the fiber amplifier at its full 30 W output, and then we cut down the power as necessary. To do this, we use a half-wave plate and a polarizing beam cube to divert the excess power into a high-power beam dump.

Chapter 5

Resonance and Laser Locking

As mentioned in previous chapters, intense fields are required to stimulate the normally weak process of Raman scattering. To get stronger Raman scattering and thus more efficient modulation, CW modulation experiments have molecules inside high-finesse cavities. When light is resonant with a high-finesse cavity, intracavity intensity builds up over time (10s of μs in our experiment), and the field is effectively amplified. In this chapter we will discuss the concepts of resonance and laser *locking*, which is the process of maintaining resonance. Chapter 6 will discuss cavities in more detail.

To understand resonance, let us first consider a basic cavity that consists of two partially-reflective, parallel planar mirrors, as shown in Figure 5.1. Each time a light ray encounters a mirror, some light is transmitted, and some is reflected. The total light at any point is the sum of all of these individual rays. Each ray takes a unique path, and therefore each accumulates a unique phase, ϕ. If the rays are out of phase with one another as they exit the cavity, there can be destructive interference, and thus little transmitted light. Resonance occurs when the phases are such that the rays add constructively, and thus the maximum amount of light is transmitted. (Although this discussion focused on ray optics and planar mirrors, the same principles hold for more realistic Gaussian laser beams and more complicated mirror geometries. Gaussian beams and mode-matching will be discussed in detail in Section 6.2.)

The phase-matching condition for resonance requires that the path difference between the different transmitted beams be equal to an integer number of wavelengths. For visible and near-infrared light, wavelengths are on the order of 1 μm. This means that a change in cavity length of 250 nm (a quarter of a wavelength) changes the round-trip path difference inside the cavity by a

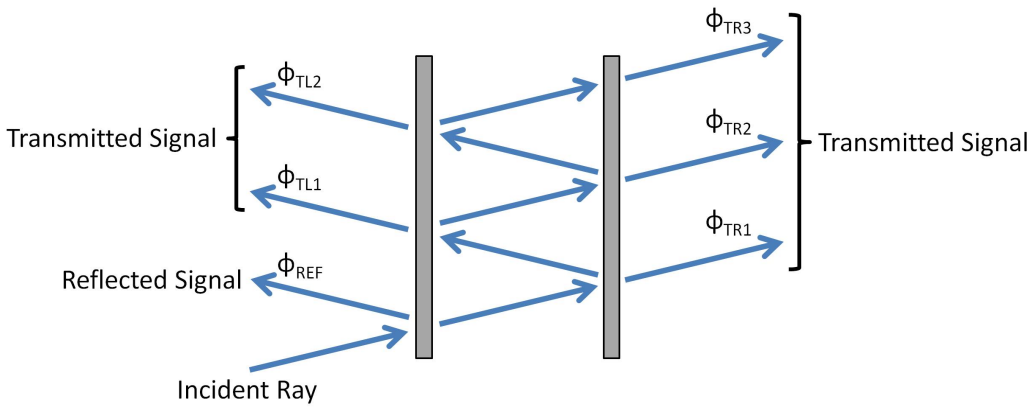

Figure 5.1 *Cavity Resonance* This basic cavity consists of two partially-reflective parallel planar mirrors. With each encounter with a mirror, the ray is partially reflected and partially transmitted. The incident ray is at an angle to make the individual rays easier to distinguish. The rays travel different path lengths, and thus have different phases, ϕ, when they are eventually transmitted through one of the mirrors. Depending on their relative phases, the rays add constructively or destructively. The resonance condition is met when all of the transmitted phases on a side, ϕ_{TR} on the right or ϕ_{TL} on the left, match so as to add constructively and produce the maximum transmitted signal. The significance of the phase of the beam reflected before entering the cavity, ϕ_{REF}, will be considered later; see Figure 5.5 and the surrounding discussion.

half of a wavelength. Such a half-wavelength shift is equivalent to a pi phase shift. This is the difference between perfectly constructive interference and perfectly destructive interference. Thus, a 250 nm shift in cavity length can completely destroy resonance, and depending on the cavity parameters, a much smaller change in length can significantly decrease the amount of transmitted light. Additionally, any drift in laser wavelength over time, perhaps due to fluctuating temperature or current, can take a laser out of resonance with the cavity. Due to the fragile nature of cavity resonances, almost every real laser system requires some sort of feedback mechanism to maintain resonance in spite of vibrations, temperature fluctuations, and other environmental perturbations.

We use the Pound-Drever-Hall technique to lock the pump laser to one of the longitudinal modes of the cavity [61]. (A cavity mode is a laser oscillation that is supported by a cavity resonance. A *longitudinal* mode, as opposed to a *transverse* mode, is a mode along the cavity, along the direction of laser propagation. Chapter 6 discusses transverse cavity modes in more detail.) The

idea behind any feedback technique is to monitor the output of the system, and then use that information to adjust the input to get a more desirable output. With the PDH technique, the reflected (or transmitted) light from the cavity is monitored. There are several possible input parameters one can adjust. In our experiment, we have two feedback loops (which are described in more detail in Section 5.2). One adjusts the current to the seed ECDL to compensate for "fast" fluctuations, in the frequency range of around 100 Hz - 1 MHz. By adjusting the current, we can quickly make slight changes to the laser wavelength, thus keeping it on resonance with the cavity. The other feedback loop adjusts the voltage to a piezoelectric transducer (PZT) on one of the cavity mirrors that makes small adjustments to the length of the resonance cavity. (The total translational range of one of our cavity PZTs is 12 μm. The adjustments made are significantly smaller than this full range.) This covers "slow" frequency fluctuations in the range of roughly DC - 100 Hz. The small changes in cavity length change the resonance frequency of the cavity, again helping to keep the laser on resonance. (Alternatively, we sometimes have our "slow" feedback loop adjust the voltage on the PZT on the grating of our ECDL. This changes the cavity length of the ECDL cavity, shifting the frequency of the laser to keep it on resonance.)

In the following section we will consider some of the concepts behind resonance, locking, and the PDH method. We will conclude the chapter with a discussion of the specifics of our PDH system in Section 5.2.

5.1 Resonance and the Error Signal

The ideas of resonance and the error signal are central to the PDH technique [62, 27]. As discussed above, as we adjust the cavity length, the amount of light transmitted through the cavity varies. Less light is transmitted when the different beams of Figure 5.1 interfere destructively. More light is transmitted when the resonance condition is met and the beams add constructively. Figure 5.2 gives a qualitative plot of cavity transmission as a function of cavity length. Note that because laser frequency also influences the resonance condition, we get a qualitatively similar plot if we plot cavity transmission versus laser frequency. The spacing between resonance peaks is

called the *free spectral range*, ν_{FSR}, of the cavity, and it can be calculated with

$$\nu_{FSR} = \frac{c}{2L}, \tag{5.1}$$

where c is the speed of light in the cavity, and L is the length of the cavity.

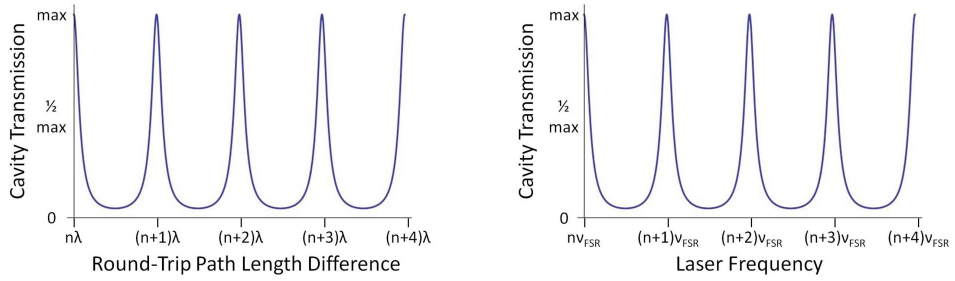

Figure 5.2 *Cavity Resonance Peaks* The plot on the left displays the relationship between cavity transmission and path length difference. Each time the path length difference of beams traveling different number of round trips in the cavity is equal to an integer multiple of the wavelength of the light, λ, the beams interfere constructively, and the cavity transmission reaches a maximum. When the path difference is not an integer multiple of λ, the beams interfere destructively, and less light is transmitted. The plot on the right, a plot of cavity transmission as a function of laser frequency, yields qualitatively similar resonance peaks. n is any positive integer, and ν_{FSR} is the free spectral range of the cavity.

Ideally, we could monitor the transmitted power, and use the feedback loops to ensure that the power level remains constant at its maximum value. When environmental factors cause the laser frequency to drift and resonance is lost, the power level drops. (The idea is exactly the same for a change in cavity length, but for brevity we will discuss only a frequency drift here.) The feedback to the laser current or the cavity PZT could then be adjusted to regain resonance. In practice, however, this is difficult because of an ambiguity that stems from symmetry of the situation. If the laser frequency drifts too high *or* too low, the transmitted power drops. It is unclear whether the frequency needs to be decreased or increased to regain resonance. In order to avoid this ambiguity, instead of monitoring the transmitted power as a function of the laser frequency, we monitor transmitted power as a function of the *derivative* of laser frequency. As shown in Figure 5.3, the derivative, known as the *error signal*, is asymmetric around the cavity resonances. By monitoring this derivative we can tell whether the frequency has drifted too high or too low.

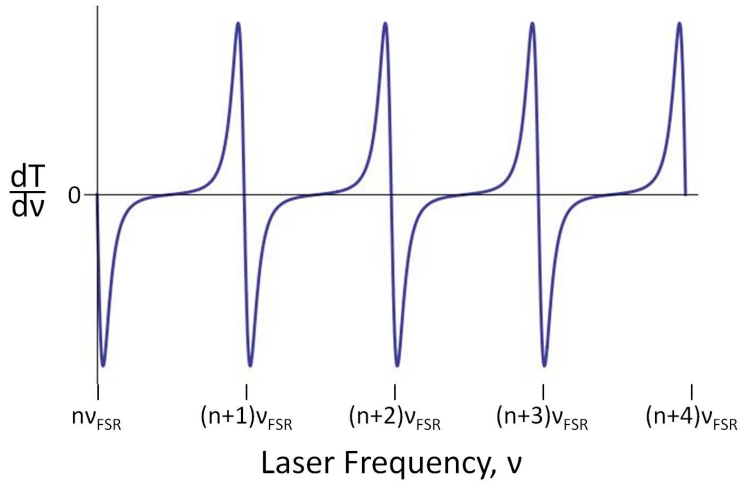

Figure 5.3 *Error Signal* This plot is the derivative of the plot on the right in Figure 5.2. It shows the derivative of cavity transmission with respect to laser frequency, $\frac{dT}{d\nu}$, as a function of laser frequency, ν. This signal, known as the *error signal*, is useful because of its asymmetry around resonances; the error signal indicates whether the laser has drifted to too high or to too low of a frequency. The resonances here are the multiples of the free spectral range of the cavity, ν_{FSR}. n is any positive integer.

To create and monitor the error signal (the derivative of the transmitted power) we slightly vary the frequency periodically with time and see how the transmission responds. The frequency modulation from the EOM mentioned in Chapter 4 is the source of this periodic frequency variation. The error signal is positive at frequencies just below a resonance and negative at frequencies just above a resonance. As shown in Figure 5.4, this means that at frequencies just below a resonance the transmitted intensity will vary in phase with frequency modulation. Just above a resonance, it will vary π out of phase with the frequency modulation. Thus, a comparison of the phase of the transmitted signal and that of the frequency modulation indicates whether the feedback needs to increase or decrease the frequency of the laser to maintain resonance. Figure 5.4 is based on a diagram by Black [62].

Before moving on, we should point out that we do not use exactly the method outlined above in our experiment. We chose to describe the method above because it is a conceptually similar, though perhaps slightly easier to understand, alternative to the method we use. The principles are

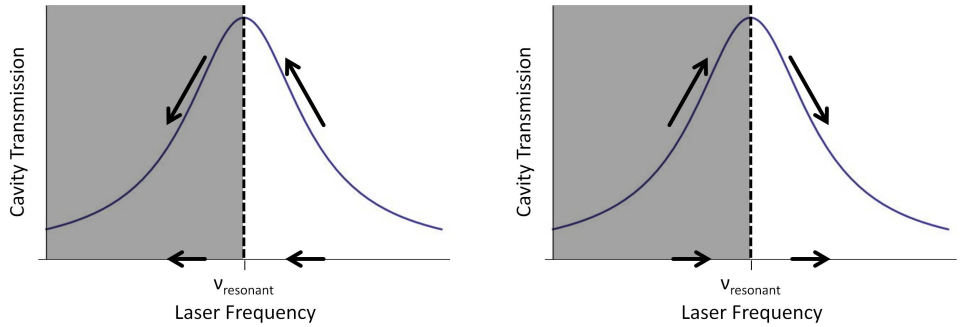

Figure 5.4 *Cavity Response to Frequency Modulation* Depending on whether the frequency is above or below a resonance, the transmission of the cavity responds either in phase or π out of phase with a periodic modulation of the laser frequency. The arrows on the x-axis indicate whether the modulation is decreasing (left plot) or increasing (right plot) the laser frequency. The arrows near the resonance curve indicate the response of the cavity transmission in two regions: when the frequency is below (shaded region) and above (unshaded region) resonance. Below resonance, the response is in phase; when the modulation causes a decrease (an increase) in laser frequency, there is a decrease (an increase) in cavity transmission. Above resonance, however, the response is π out of phase; when the modulation causes a decrease (an increase) in laser frequency, there is an increase (a decrease) in cavity transmission. $\nu_{resonant}$ is one of the laser frequencies that is resonant with the cavity.

the same in both cases, and the conceptual arguments still hold. However, there are two main differences between the method described and our method.

First, instead of monitoring pure cavity transmission (the right side of Figure 5.1), we monitor the light that includes both the cavity transmission and the reflected signal (the left side of Figure 5.1). This changes the sign on a few aspects of the situation. See Figure 5.5 for a simplified version of Figure 5.1 showing only relevant rays. Looking at the light that includes the reflected signal, we observe resonance *dips* instead of resonance peaks. When the resonance condition is met, the beams transmitted out of the left side of Figure 5.5 have traveled an integer number of wavelengths inside the cavity. This means that the path difference adds an integer multiple of 2π to their phase, which does nothing to change their phase relative to the incident ray. Thus, the only phase difference comes from the π phase shift they pick up from a reflection off of the mirror on the right (because $n_{air} < n_{mirror}$). The directly reflected signal experiences no phase difference from its reflection because its reflection is occurring on the right side of the left mirror (*inside* the

mirror substrate), and thus there is no phase shift (because $n_{mirror} > n_{air}$). Thus, on resonance, there is a π phase difference between the promptly reflected beam and the beams transmitted from the cavity. The beams destructively interfere, and there is a dip in the reflected signal. This dip means that the positive and negative signs change in the discussion of phases in Figure 5.4 (because the derivative for a dip is opposite in sign from that of a peak), but otherwise the argument remains the same.

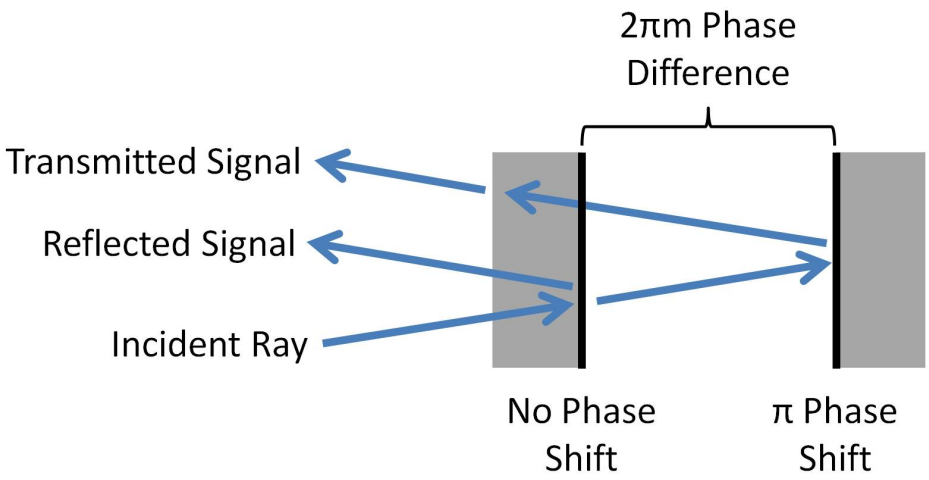

Figure 5.5 *Cavity Resonance and Phase* The simplified resonance diagram explains the phases of the beams on the left side of the cavity. The reflected signal experiences no phase shift from its reflection off of the *right side* of the left mirror (*inside* the mirror substrate) because $n_{mirror} > n_{air}$, so it is in phase with the incident ray. On resonance, the transmitted signal experiences a $2\pi m$ phase shift relative to the reflected signal due to a difference in path length. (m is an integer.) The transmitted signal also experiences a π phase shift from its reflection off of the *left side* of the right mirror because $n_{air} < n_{mirror}$. Thus, the phase of the transmitted signal is $2\pi m + \pi$, that is, π away from the phase of the reflected signal. Therefore, on resonance these two signals interfere destructively and there is a dip in the amount of light on the left side of the cavity.

The second change from the scheme described above and our experiment is that instead of varying the frequency of the beam in time, we modulate the phase of the beam with the EOM to produce frequency sidebands. Let us consider this phase modulation from the EOM in the frequency domain (rather than in the time domain as in Figure 5.4). Small periodic fluctuations of frequency in the time domain are equivalent to adding sidebands in the frequency domain; this is similar to the discussion of time-varying indices of refraction in Section 1.1. We generate the error

signal by looking at the interference of these sidebands with the transmitted signal. The method discussed in Figure 5.4 requires us to know something about the phase of the transmitted beam in order to know whether we are above or below resonance. While we cannot directly measure the phase of the electric field of the transmitted beam, we can measure the phase of the beat signal from the interference of the transmitted beam and the sidebands. From this we can then extract the needed information about the transmitted beam. Figure 5.6 illustrates a frequency space view of how the sideband interference generates the error function.

Our description of the PDH technique has been mostly conceptual. Before moving on to discuss the specifics of our PDH system, we note that a more mathematical description of the error function and further conceptual discussion of the PDH method can be found in a helpful tutorial article by Black [62], a chapter on stabilizing laser diodes to cavities by Fox, Oates, and Holberg [63], and in the thesis of Green [25].

5.2 Our PDH System

Our PDH system uses optical feedback from our HFC to generate the error signal as described in the previous section. We then use two feedback loops to keep the laser resonant with the cavity. The schematic in Figure 5.7 illustrates the important elements of our PDH system.

We begin with a seed ECDL, and we phase modulate the beam using an EOM. This adds frequency sidebands to our laser as shown in the call-outs in Figure 5.7. The EOM is driven by a radio frequency generator (RFG) signal at 50 MHz. After the seed laser is amplified and coupled to the HFC as described in Chapter 4, the reflected beam is sampled by the glass slide (GS), and this signal goes to a photodiode (PD). As described in the previous section, this signal contains the information necessary to create the error signal. The signal from the PD is filtered using a DC block, and then the useful AC signal is amplified using a radio frequency (RF) amplifier. The original RFG signal is split using a splitter; half is sent to the EOM as mentioned above, and the other half is used as a reference. After being appropriately phase-matched using a phase delay line (PDL), this reference signal is compared to the amplified PD signal using a mixer (MIX). (This is the phase comparison discussed conceptually in Figure 5.4.) Our phase delay line is a length

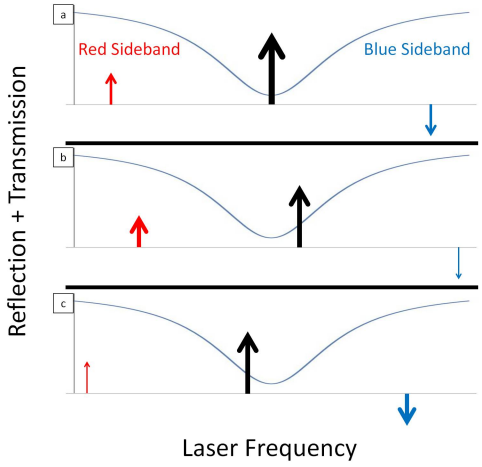

Figure 5.6 *Sideband Interference and Cavity Resonance* This figure suggests how interference between frequency sidebands and the transmitted signal can create the error signal at the beat frequency. (It is important that we are generating the error signal from a beat frequency. This means that the form of the error signal comes only from the frequency drift and not from overall fluctuations in the laser intensity.) The large central arrow in each case is the transmitted beam, while the arrows on the left and right are the red and blue sidebands, respectively. The blue curve shows a resonance dip of the cavity. The horizontal position of the arrow gives the frequency of the beam. The sidebands are spaced from the transmitted beam by the EOM modulation frequency, which is also the beat frequency. An arrow closer to resonance with the cavity is thicker to represent its stronger signal. The direction of the arrow represents its relative phase. An arrow pointing downward represents a π phase shift from an arrow pointing upward. Note that the sidebands are generated with a definite phase relative to the transmitted signal and are π out of phase with one another. (a) When the transmitted signal is on resonance, the red and blue sidebands are of equal strength and π out of phase with one another. The two beat signals (transmitted signal with red sideband and transmitted signal with blue sideband) cancel, yielding zero error signal. (b) When the transmitted signal is slightly too high in frequency, the red sideband is closer to resonance and thus is stronger than the blue. Thus, the *in-phase* red beat signal dominates, meaning that the cavity transmission response is *in phase* with the modulation, and the error signal is positive. (c) When the transmitted signal is slightly too low in frequency, the blue sideband is closer to resonance and thus is stronger than the red. Therefore, the π*-out-of-phase* blue beat signal is stronger, meaning that the cavity response is π *out of phase* with the modulation, and the error signal is negative. Note the sign is different than in Figure 5.3 because we are now looking at a resonance dip (as on the left side of Figure 5.5) rather than a transmission peak.

of BNC cable. Electronic signals travel through BNC at about $\frac{2}{3}$ the speed of light, and thus at a

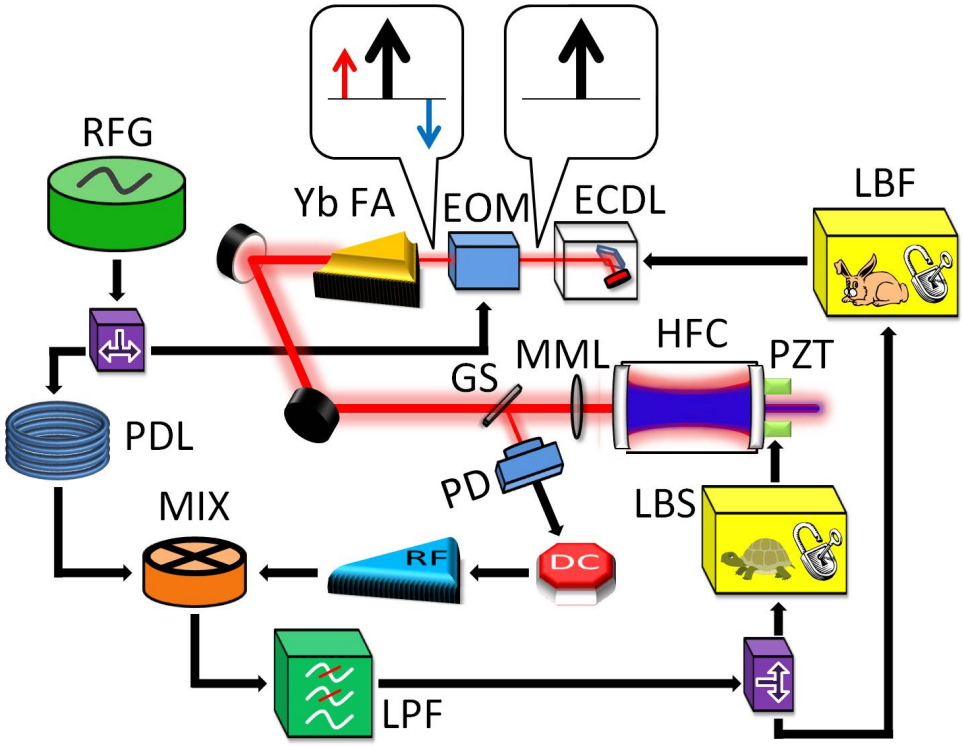

Figure 5.7 *PDH Schematic* This schematic illustrates the important elements of our PDH locking system. See the main text for a description of its function. The glowing red and blue lines are lasers, and the thick black arrows indicated electrical signals. The call-outs with the arrows illustrate how the EOM puts frequency sidebands on the incident beam. To simplify the schematic, optical isolators and additional lenses are not shown. **RFG**: Radio Frequency Generator, **PDL**: Phase Delay Line, **MIX**: Frequency Mixer, **LPF**: Low-Pass Filter, **RF**: Radio Frequency Amplifier, **DC**: Direct Current Block, **PD**: Photodiode, **GS**: Glass Slide, **MML**: Mode-Matching Lens, **HFC**: High-Finesse Cavity, **PZT**: Piezoelectric Transducer, **LBS**: Lock Box for Slow Feedback, **LBF**: Lock Box for Fast Feedback, **ECDL**: External Cavity Diode Laser, **EOM**: Electro-Optic Modulator, **Yb FA**: Ytterbium Fiber Amplifier

frequency of 50 MHz, the wavelength λ of the signal in the cable is

$$\begin{aligned} \lambda &= \frac{v}{f} \\ &\approx \frac{\frac{2}{3}c}{50\ MHz} \\ &\approx 3.8\ m. \end{aligned} \tag{5.2}$$

Using the fact that 3.8 m of BNC is roughly equal to λ or 2π of phase, we can add or subtract length to adjust the phase of the reference signal. This phase control is needed because of the unequal distances traveled by the two signals that are being compared at the mixer. (We optimize this delay by adding and subtracting BNC cables in small increments until we see the error signal take the expected form. See Section 3.2.2 of Green's thesis for more details [25].)

The mixer gives the sum and the difference of its inputs: the amplified PD signal and the reference signal. The difference output contains the beat information needed for locking, and so we filter out the sum output using a low-pass filter (LPF). Thus, the mixer demodulates the reflected beam signal, leaving us with only the useful error signal. This error signal is then sent to the servo locking electronics, the *lock boxes*, to provide two different branches of feedback to keep the laser on resonance with the cavity.

As described earlier in the chapter, one feedback branch handles the *slow* feedback, perturbations from around DC - 100 Hz. This feedback servo (LBS) controls a PZT attached to one of the mirrors of the HFC. It makes slight adjustments to the length of the cavity in order to keep the laser on resonance. (We also occasionally instead use this slow feedback to adjust a PZT that adjusts the length of the cavity in the ECDL. This adjusts the laser frequency, keeping it on resonance. In principle, the HFC would be more stable without a PZT on one of its mirrors. The PZT introduces additional mechanical resonances that must be avoided. However, we have so far found that the ECDL PZT arrangement is not as stable as that with the HFC PZT. For now, the HFC PZT gives us the flexibility we need to maintain resonance. The ECDL PZT is also necessary in experiments in which we are locking two lasers to the cavity, as described in Section 11.1.) The PZT feedback handles perturbations that occur on relatively long time scales, such as those due to temperature drift and some mechanical disturbances and resonances.

The second feedback branch is tuned to provide *fast* feedback, from around 100 Hz - 1 MHz. This servo (LBF) feeds back to the diode of the ECDL to modify its current. By making adjustments to current on these short time scales, the feedback controls the laser frequency, keeping it on resonance with the cavity. The current feedback is designed to deal with perturbations that occur

on very short time scales, such as those due to fluctuations from the laser diode current source, other electrical noise, and some higher frequency mechanical resonances.

In each of these feedback loops, the lock box modifies the input error signal so that the servo responds in an appropriate manner at the design frequencies. The lock boxes adjust the gain and phase of the input error signal, acting as a filter, amplifier, and attenuator. The response must be frequency-dependent, and it must cover a wide range of input frequencies. Lock box design is an involved process, and each feedback loop has different requirements and limitations that require unique design solutions. It is necessary to avoid resonances (electrical and sometimes mechanical) and positive feedback, both of which make it difficult to maintain resonance. Conflicts often arise because multiple parameters must be optimized simultaneously. Successful lock box design often requires much trial and error to discover the circuit parameters that produce the most stable frequency.

The lock boxes used in the experiments described in this thesis were expertly designed and built by Tyler Green. More detailed discussion of locking circuitry, detailed schematics of our PDH circuits, and characterizations of our circuits can be found in Chapter 3 of his thesis [25].

Chapter 6

Optical Cavities

In this chapter, we will examine beam propagation and optical cavities in more detail. In Chapter 5, we examine a basic cavity model using flat mirrors and light rays as shown in Figure 5.1. However, optical cavities are often more complicated than this. In this chapter, we will first briefly overview Gaussian beam propagation and mode-matching to cavities. We will then discuss the details of the custom-built high-finesse cavity used in our experiment.

6.1 Gaussian Beam Propagation

In order to get a more accurate picture of the behavior of laser light, we must move beyond the ray optics description of Chapter 5. If we take into account the wave nature of light and diffraction effects, we arrive at the more accurate representation of light as a Gaussian beam [27]. Gaussian beam propagation is based on the paraxial wave equation, which assumes that light travels roughly like a beam, that it stays reasonably close to some optical axis. For laser light this is almost always a good assumption; the transverse dimensions of the field vary slowly as a function of the propagation distance.

Gaussian beam propagation accounts for the spatial extent and the complex phase of a laser beam. At any given point along the propagation direction z, a Gaussian beam is characterized by a complex radius of curvature, $q(z)$, which takes into account both the transverse beam size $w(z)$ and the radius of curvature of the wavefront $R(z)$.

$$\frac{1}{q(z)} \equiv \frac{1}{R(z)} - j\frac{\lambda}{\pi w^2(z)}, \tag{6.1}$$

where λ is the wavelength of light in the medium and j is the imaginary unit. We call the location where the beam is the smallest the *beam waist*, w_0.

$$w(z)_{min} \equiv w_0 \tag{6.2}$$

Figure 6.1 illustrates the propagation of a Gaussian beam in free space (or another uniform medium). The waist has been marked, and the dotted lines represent the radii of curvature of the wavefront of the beam at various points.

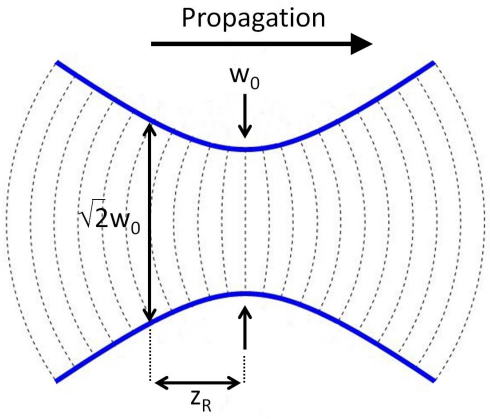

Figure 6.1 *Gaussian Beam Propagation* This figure illustrates the propagation of a Gaussian beam in free space (or another uniform medium). The solid lines mark the $\frac{1}{e^2}$ size of the Gaussian beam, $w(z)$, and the dotted lines show the radius of curvature of the wavefront, $R(z)$, at selected points. The waist, w_0, is the point at which the beam size is smallest. The Rayleigh range, z_R, is the range over which the beam travels before doubling in area.

Note that the radius of curvature of the wavefront is infinite at the beam waist. The *Rayleigh range* of a Gaussian beam, z_R, is the range over which the beam travels before diverging so that its area doubles (or, equivalently its diameter increases by $\sqrt{2}$). The Rayleigh range can be calculated from the laser parameters as follows:

$$z_R \equiv \frac{\pi w_0^2}{\lambda}. \tag{6.3}$$

This definition allows us to describe Gaussian beam propagation in free space with relatively compact relationships. In each case, we define $z = 0$ to be the location of the beam waist.

$$q(z) = z + jz_R \tag{6.4}$$

$$w(z) = w_0\sqrt{1 + \left(\frac{z}{z_R}\right)^2} \tag{6.5}$$

$$R(z) = z + \frac{z_R^2}{z} \tag{6.6}$$

Although these quantities will suffice for our exploration of Gaussian beams, the entire complex field of the Gaussian beam, $U(x, y, z)$, can also be expressed in terms of these variables.

$$U(x, y, z) = \sqrt{\frac{2}{\pi}}\frac{1}{w(z)}e^{-jkz+j\psi(z)}e^{-\frac{x^2+y^2}{w^2(z)}-jk\frac{x^2+y^2}{2R(z)}}, \tag{6.7}$$

where $k = \frac{\omega}{c}$ is the wave number and $\psi(z)$ is defined as

$$\psi(z) \equiv \tan^{-1}\left(\frac{z}{z_R}\right). \tag{6.8}$$

See Chapters 16 and 17 of *Lasers* by Siegman for more details on Gaussian beam propagation [27].

6.2 Optical Cavities and Mode-Matching

The last section discussed Gaussian beams in free space, but often we need to manipulate the size and shape of the beams with optics. In Chapter 5, we discussed the importance of locking for keeping the laser resonant with the cavity. In order to achieve resonance in the first place, we must make our Gaussian beam the correct size and shape to "fit" well with the cavity, that is, to strongly resonate in a cavity mode. The process of achieving this resonance is called *mode-matching*.

As discussed in Figure 5.2, resonance in ray optics requires specific cavity lengths (or, equivalently, laser frequencies). With the more complete Gaussian beam description, we see that there are other requirements as well. In Chapter 5, we discussed resonance in terms of constructive interference. The transmitted beams that travel different numbers of round trips in the cavity must be in phase with one another. This phase requirement can be thought of in terms of the shape of

the laser field. After one full round trip in the cavity, the field must return to its original shape so that it begins its next trip in unison with the light just entering the cavity. In this way, light on its first trip adds constructively with light on its second trip, and its third trip, and so on, and we get constructive interference, resulting in large intracavity fields.

This same resonance requirement holds for Gaussian beams. After each round trip the fields must add constructively, though now we have the added complexity of the Gaussian wavefronts discussed in Section 6.1. In addition to the cavity length requirement, there is now the requirement that the radius of curvature of the mirrors must match the radius of curvature of the wavefront. Matching the mirrors to the wavefront ensures that the beam reflects exactly back on itself after each round trip of the cavity. We call configurations where such constructive interference occurs *cavity modes*. Figure 6.2 illustrates a basic example of cavity resonance with a Gaussian beam.

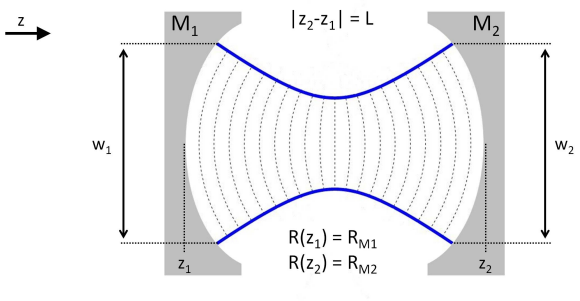

Figure 6.2 *Gaussian Beam in a Cavity* This figure illustrates a Gaussian beam resonating in an optical cavity consisting of two mirrors, M_1 and M_2. At the location of the each mirror, z_1 and z_2, the radius of curvature of the beam, $R(z)$, matches the radius of curvature of the mirror, R_{M1} and R_{M2}. The length of the cavity is L. w_1 and w_2 are the beam sizes at the two mirrors.

As mentioned above, mode-matching can be achieved by matching the cavity mirrors to the radius of curvature of a beam. However, this is often impractical. It is almost always the case that instead the Gaussian beam is manipulated to match a cavity with a predetermined length and mirror radii of curvature. These three cavity parameters completely specify the beam that will best

resonate in a cavity. We combine these parameters to define

$$g_1 \equiv 1 - \frac{L}{R_{M1}} \tag{6.9}$$

and

$$g_2 \equiv 1 - \frac{L}{R_{M2}}. \tag{6.10}$$

These g parameters help to compactly express cavity resonance parameters [27]. First of all, the g parameters specify where along the optical axis the mirrors should be located. The locations are given relative to the cavity waist location, that is, using coordinates with an origin defined by $w(z = 0) = w_0$.

$$z_1 = \frac{g_2(1 - g_1)}{g_1 + g_2 - 2g_1g_2}L \tag{6.11}$$

$$z_2 = \frac{g_1(1 - g_2)}{g_1 + g_2 - 2g_1g_2}L \tag{6.12}$$

The beam size that will best resonate with the cavity can also be described by these parameters. The waist size and the beam size at the two mirrors, w_1 and w_2, can be calculated as shown in Equations 6.13 - 6.15.

$$w_0^2 = \frac{L\lambda}{\pi}\sqrt{\frac{g_1g_2(1 - g_1g_2)}{(g_1 + g_2 - 2g_1g_2)^2}} \tag{6.13}$$

$$w_1^2 = \frac{L\lambda}{\pi}\sqrt{\frac{g_2}{g_1(1 - g_1g_2)}} \tag{6.14}$$

$$w_2^2 = \frac{L\lambda}{\pi}\sqrt{\frac{g_1}{g_2(1 - g_1g_2)}} \tag{6.15}$$

Finally, the Rayleigh range of the resonant beam can also be calculated using

$$z_R^2 = \frac{g_1g_2(1 - g_1g_2)}{(g_1 + g_2 - 2g_1g_2)^2}L^2. \tag{6.16}$$

In Figure 6.2, the cavity was drawn symmetrically, with equally curved mirrors, and this puts the waist in the center of the cavity. This is not the case for all cavities. There are many configurations that support stable cavity modes: asymmetric cavities, cavities with the waist located at one of the mirrors, and even cavities with the waist located outside of the cavity. Figure 6.3 shows a few of the stable linear cavity configurations.

The forms of Equations 6.13 - 6.15 hint at the stability criteria for a stable optical cavity. The term under each radical is positive, and thus the beam sizes are real-valued, only if

$$0 \leq g_1 g_2 \leq 1. \tag{6.17}$$

Equation 6.17 shows the stability criteria for an optical cavity. Note that this equation, and most of the previous discussion of cavities, is specific to *linear* cavities, those with two mirrors facing one another. Although they will not be discussed here, other cavity geometries with more mirrors exist, such as ring cavities [27].

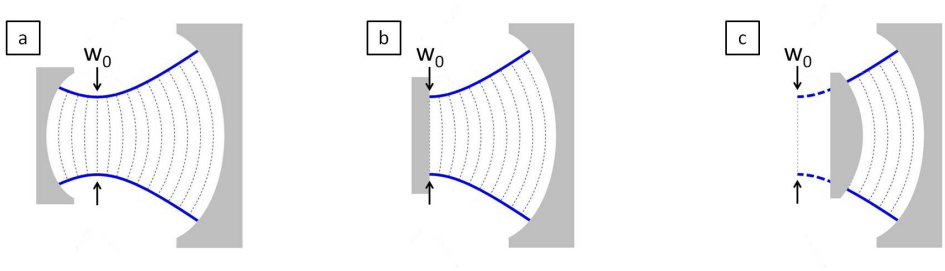

Figure 6.3 *Stable Cavity Configurations* This figure illustrates several stable cavity configurations that support Gaussian beam cavity modes: (a) Asymmetric Cavity, (b) Plano-Concave Cavity, and (c) Convex-Concave Cavity. w_0 indicates the cavity waist in each case. Note that in (b) the waist is located at one of the cavity mirrors, and in (c) the waist is located *outside of* the cavity.

In our experiment, we have a symmetric cavity, which is described in detail in Section 6.3. For this type of cavity, or for any type of stable cavity, we can use the equations above to calculate the profile of a resonant Gaussian beam. The challenge is then to get an arbitrary laser beam to assume the desired form so that it will properly resonate. One way of to change a Gaussian beam size is to use a convex lens to focus it. Concave lenses can also be used to make a beam diverge more quickly. Another parameter that one can change is the distance of propagation between optical elements. By allowing a beam to propagate more or less before it encounters a lens, we can change both the size and the radius of curvature of the incident beam, and this changes the effect the lens has on the beam. There are also prism pairs and cylindrical lenses to change the cross-sectional aspect ratio of beams to make them more (or less) symmetric. Through some combination of lenses and free space propagation, the correct Gaussian profile for a given resonator can usually be

achieved. A final, perhaps subtle note is that the input cavity mirror itself can have a lensing effect on the beam, so it must be included in any mode-matching calculations.

Beam propagation and mode-matching calculations for Gaussian beams are made much easier by the *ABCD* matrix method [27]. Each optical element, interface, or free space propagation distance encountered by a Gaussian beam can be represented by an *ABCD* matrix. The matrix represents how the beam is changed by the encounter. For example, if an incident Gaussian beam with complex radius of curvature q_i encounters an optical element with the following generic *ABCD* matrix:

$$\begin{bmatrix} A & B \\ C & D \end{bmatrix}, \tag{6.18}$$

then the final complex radius of curvature of the beam leaving the optical element, q_f, can be calculated using

$$\frac{q_f}{n_f} = \frac{A\frac{q_i}{n_i} + B}{C\frac{q_i}{n_i} + D}, \tag{6.19}$$

where n_i and n_f are the indices of refraction of the media that the incident and final beams are in.

ABCD matrices for free space propagation and thin lenses are given in Equations 6.20 and 6.21.

Free Space Propagation of Distance d

$$\begin{bmatrix} 1 & d \\ 0 & 1 \end{bmatrix} \tag{6.20}$$

Thin Lens of Focal Length f

$$\begin{bmatrix} 1 & 0 \\ -\frac{1}{f} & 1 \end{bmatrix} \tag{6.21}$$

These matrices assume that the beam is incident at a right angle to the optical element. An article by Massey and Siegman provides *ABCD* matrices for tilted optics [64].

The power of the *ABCD* matrix method comes from its ease of use with complex optical systems. To calculate the net result of the system, the matrices from the individual elements can be multiplied together (with the first element encountered furthest to the left and matrices of the subsequent elements multiplied on the right side), and then use Equation 6.19 with the resulting matrix to get the net effect of the entire optical system.

The *ABCD* matrix method lends itself well to computer calculations. While many programs could be used, we used MathWorks Matlab to develop a program to simulate the Gaussian beam size of a laser as it goes through an optical system. Our program uses the *ABCD* matrix method to calculate $q(z)$ throughout the optical system, and then it plots $w(z)$, the beam size. Figure 6.4 shows a sample output. The goal is to find an optical system that manipulates the beam so as to match it to the ideally resonant cavity mode, as described by Equations 6.13 - 6.15. The free parameters of lens focal lengths and propagation distances between lenses are adjusted until a near match is found. Although we use this program to aid in mode-matching to the cavity, we have found that it is still necessary to make slight adjustments based on empirical evidence in order to optimize coupling.

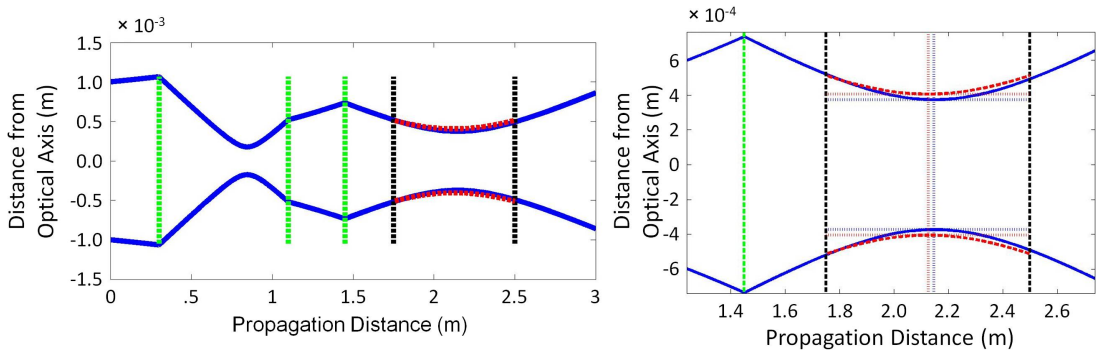

Figure 6.4 ABCD *Matrix Simulation* This figure displays a simulation of Gaussian beam propagation calculated using our *ABCD* matrix Matlab program. The diagram on the left shows the beam being mode-matched to the cavity using several lenses. The diagram on the right is a detailed version of just the region around the cavity. In both diagrams, the blue line indicates the $\frac{1}{e^2}$ beam size of a Gaussian beam. The dashed vertical lines indicate the location of optical elements. The green dashed lines are lenses, and the two black lines on the right of each diagram are the cavity mirrors. The curved dashed red lines indicate the ideal cavity mode for the given cavity. In the drawing on the right, the thin horizontal and vertical dashed lines mark the size of the cavity waist and the location of the cavity waist. The blue dashed lines match up with the calculated beam size, and the red dashed lines match up with the ideal cavity mode. (To make this more apparent, the calculated beam size here is intentionally different from the cavity mode.)

Before moving on to discuss the specifics of our cavity, we will mention two other quantities associated with Gaussian beams in cavities: higher-order transverse Gaussian modes and finesse.

In all of the previous discussion, we have assumed our beam had a Gaussian cross-section in both the transverse directions. However, this is only one solution to the paraxial wave equation. An infinite number of higher-order solutions exist. These higher-order transverse modes are called Hermite-Gaussian modes. (In general, **T**ransverse **E**lectro-**M**agnetic modes are often referred to as TEM modes, with the lowest-order mode being TEM_{00}. See Figure 6.5.) For a beam traveling in the z direction, the general Hermite-Gaussian modes are described as follows [27].

$$E(n,m,x,y,z,\lambda) = u(n,x,z,\lambda)\cdot v(m,y,z,\lambda), \tag{6.22}$$

where

$$u(n,x,z) \equiv \left(\frac{2}{\pi}\right)^{\frac{1}{4}}\left(2^n w(z) n!\right)^{-\frac{1}{2}} H_n\left(\frac{\sqrt{2}x}{w(z)}\right) e^{-\frac{x^2}{w^2(z)}} e^{j\Phi(n,x,z,\lambda)}, \tag{6.23}$$

and $v(m,y,z,\lambda)$ is identical to $u(n,x,z,\lambda)$ with y taking the place of x and m taking the place of n. n and m are indicies that give the order of the Hermite-Gaussian mode in the x and y transverse directions, respectively. $w(z)$ is the beam size at location z along the propagation direction. λ is the wavelength of light. H_n is the nth-order Hermite polynomial, and Φ is a phase term. A few Hermite-Gaussian modes are illustrated in Figure 6.5.

We will continue to look at only the lowest-order transverse mode for the rest of this thesis. The lowest-order beam is desirable for our experiment because it couples best to the cavity. Although the higher-order Gaussian modes are quite interesting, we usually only see them when our lasers are incompletely mode-matched to our cavity. We will not discuss them further here.

We conclude this chapter with a short discussion of *finesse*. Finesse is an important way to characterize an optical cavity. As mentioned in Section 2.2, the finesse of a cavity can be thought of as how well it holds light. Light in a cavity with a high finesse will reflect back and forth for many round trips before it is all transmitted through the cavity mirrors. Roughly, the finesse is how many round trips light makes before exiting the cavity. More specifically, finesse is defined as

$$\mathcal{F} \equiv \frac{\pi\sqrt{g_{rt}}}{1-g_{rt}}, \tag{6.24}$$

where g_{rt} is the round-trip gain in the cavity. The round-trip gain accounts for any gain medium that may be in the cavity, but also for all loss mechanisms, including absorption and light lost through

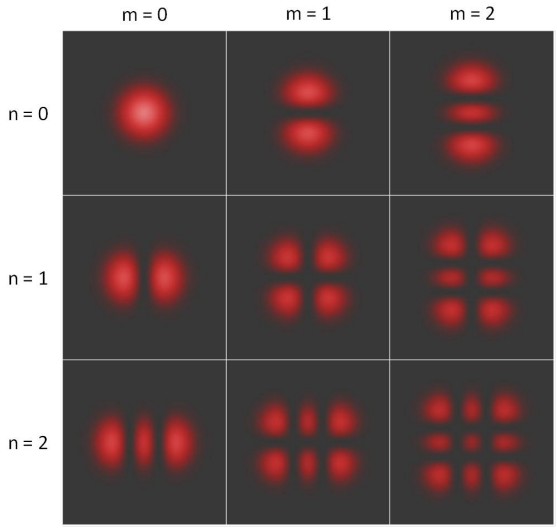

Figure 6.5 *Transverse Electro-Magnetic Modes* This figures shows a cross-sectional view of the lowest-order Gaussian mode ($n = m = 0$) as well as several higher-order Gaussian modes. These **T**ransverse **E**lectro-**M**agnetic modes are often labeled TEM_{nm}. This is a plot of beam intensity, which was obtained by taking the square of the magnitude of the electric field (Equation 6.23). A lighter color indicates a more intense beam. The horizontal and vertical axes of each square are the spatial coordinates in the x and y transverse directions.

transmission through the cavity mirrors. For low-loss cavities with high-reflectivity mirrors such as the one used in our experiment, g_{rt} is very close to 1. Thus, $1 - g_{rt}$ approaches zero, and $\mathcal{F}$ is very large.

The high finesse of our cavity is important because it allows us to build up high-intensity fields. Because our mirrors are highly-reflective and our losses are low, light in the cavity travels many round trips before exiting the cavity. The entire time this light is circulating in the cavity, more light is entering the cavity. Thus, over time (10s of μs), this light builds up, and intense fields circulate in the cavity.

As suggested by Figure 6.6, a very high finesse also means very sharp resonance peaks. A sharp resonance means that there is a very small range of frequencies for which light is resonant with the cavity. This means that cavity modes have narrow frequency linewidths, which is beneficial for producing narrow linewidth lasers. It also means that high performance feedback electronics are

required to maintain resonance, as a slight variation in frequency will cause a significant drop in transmission. (See Chapter 5 for further discussion of locking.)

Finally, we note the connection of finesse to the discussion of resonance of Section 5.1. Another approximately equivalent way of defining finesse is

$$\mathcal{F} \equiv \frac{\nu_{FSR}}{\Delta\nu_{cav}}, \tag{6.25}$$

where ν_{FSR} is the free spectral range of the cavity as defined in Equation 5.1, and $\Delta\nu_{cav}$ is the full-width-half-maximum frequency linewidth of the cavity resonance peaks. (This linewidth is the frequency range around a resonance peak over which a cavity has at least half its maximum transmission.) Figure 6.6 illustrates this view of finesse.

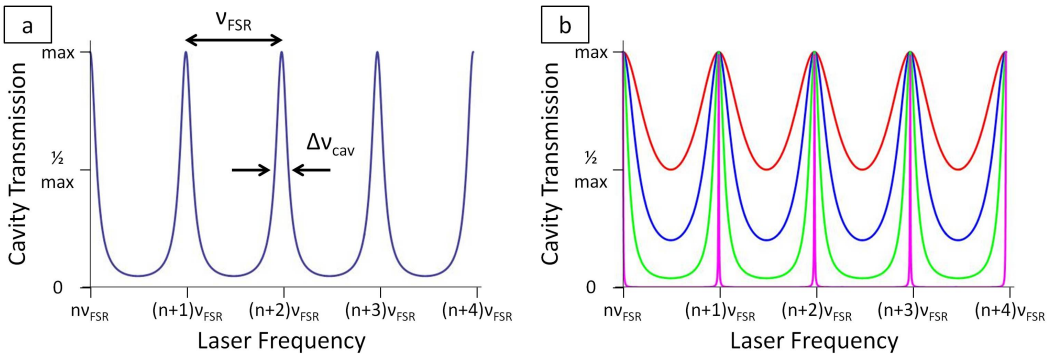

Figure 6.6 *Finesse* Figure (a) illustrates the two quantities that define finesse, $\mathcal{F}$: free spectral range, ν_{FSR}, and full-width-half-maximum cavity linewidth, $\Delta\nu_{cav}$. Figure (b) displays resonance curves for cavities of varying finesse. The cavity represented by the topmost, red curve has a finesse of $\mathcal{F}$. The second-highest, blue curve represents a cavity with a finesse of $2\mathcal{F}$. The second-lowest, green curve represents a cavity that has a finesse of $5\mathcal{F}$. The cavity represented by the lowest, magenta curve has a finesse of $100\mathcal{F}$.

See Chapter 19 of *Lasers* by Siegman for more details on Gaussian beam modes and optical cavities [27].

6.3 Our Liquid-Nitrogen-Cooled HFC

The cavity that serves as the centerpiece of our experiment, our molecular modulator, is a symmetric cavity, similar to the cartoon cavity depicted in Figure 6.2. Both mirrors have a radius

of curvature of 100 cm and the length of the cavity is 75 cm, which yields a free spectral range of 200 MHz. The mirrors, purchased from Precision Photonics, have low-loss, high-reflectivity dielectric coatings. The coatings have a large CW optical damage threshold; they can handle laser intensities exceeding 20 MW/cm^2 before sustaining damage. The mirrors have extremely high reflectivity near the pump (1064 nm) and vibrational Stokes (1560 nm) wavelengths. The reflectivity is 99.99% or higher for wavelength ranges of around 1010 nm - 1150 nm and around 1430 nm - 1620 nm. The manufacturer quotes the absorptive and scattering losses as being at the 100 parts per million (ppm) level for both the pump and the vibrational Stokes wavelengths. We measure the transmittance to be 32 ppm at the pump wavelength and 38 ppm at the vibrational Stokes wavelength. Because there is no gain medium, from these values we can calculate the round-trip gains for both beams in (an empty) cavity.

$$\begin{aligned} g_{rt} &= 1 - losses \\ g_{rt}^{pump} &= 1 - \frac{32}{10^6} - \frac{100}{10^6} \\ g_{rt}^{pump} &= .999868 \end{aligned} \tag{6.26}$$

and

$$\begin{aligned} g_{rt}^{Stokes} &= 1 - \frac{38}{10^6} - \frac{100}{10^6} \\ g_{rt}^{Stokes} &= .999862 \end{aligned} \tag{6.27}$$

With these round-trip gains, we can use Equation 6.24 to calculate the finesse at the two wavelengths.

$$\mathcal{F}_{pump} = 23798 \tag{6.28}$$

$$\mathcal{F}_{Stokes} = 22764 \tag{6.29}$$

Using Equation 6.25 with these finesse values and the aforementioned free spectral range of 200 MHz, we can calculate the full-width-half-maximum cavity linewidths.

$$\begin{aligned} \Delta\nu_{cav} &= \frac{\nu_{FSR}}{\mathcal{F}} \\ \Delta\nu_{cav}^{pump} &= \frac{200\ MHz}{22764} \\ \Delta\nu_{cav}^{pump} &= 8.786\ kHz \end{aligned} \tag{6.30}$$

and

$$\begin{aligned} \Delta\nu_{cav}^{Stokes} &= \frac{200\ MHz}{20942} \\ \Delta\nu_{cav}^{Stokes} &= 9.550\ kHz \end{aligned} \tag{6.31}$$

For comparison, we note that in modulation experiments with optical fibers as the Raman medium, the Stokes sideband often has a bandwidth of order of the full-width-half-maximum linewidth of the Raman transition, about 500 MHz. However, because our Raman medium is inside a HFC, the cavity linewidth acts as a frequency filter, and our Stokes beam has a full-width-half-maximum linewidth on the order of 10 kHz.

As shown in Figure 6.7, the cavity is enclosed inside a custom-made vacuum chamber. The chamber is made of stainless-steel, and the inner tube that contains the cavity and the molecular gas has a diameter of 5 cm. The central 45-cm-long region of the chamber is surrounded by a liquid nitrogen reservoir. The reservoir is wrapped in a 2 cm-thick layer of highly-insulating aerogel to reduce water-vapor condensation on the optics and table and to prevent rapid evaporation of the liquid nitrogen. The chamber has two end pieces that are removable and are designed to mate with standard Kwik-Flange vacuum flanges. These end pieces house the mirrors of the cavity as well as anti-reflection-coated, vacuum-tight windows. One of the mirrors is mounted on a piezoelectric transducer (PZT) that allows slight adjustments of the cavity length. We attach the end pieces to the main chamber with custom end clamps and a Viton o-ring. Six bolts in each clamp allow for precision control of the pitch of the end pieces (and therefore the mirrors) within 1 milliradian. By adjusting the tightness of these bolts, the cavity can be aligned while maintaining the vacuum seal. We have found it necessary to be able to make these pitch adjustments. Although the chamber was accurately machined, cooling the system with liquid nitrogen results in undesired structural

changes for which precision alignment compensation is necessary. See Appendix E for more details on the cavity and chamber.

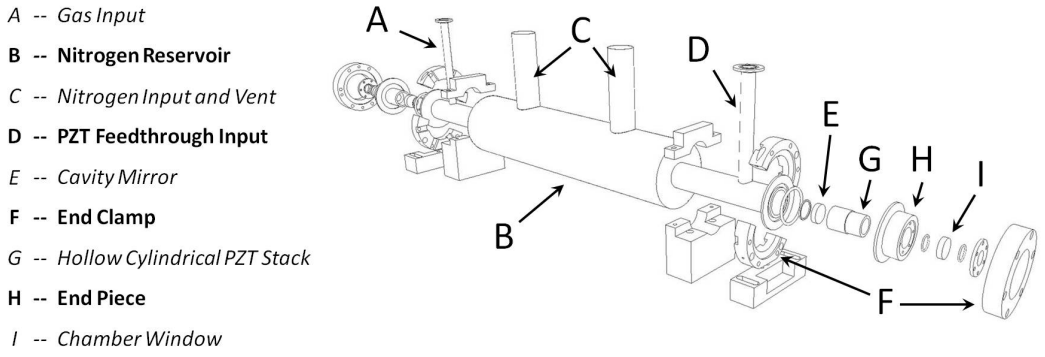

Figure 6.7 *Cavity Diagram* This custom-designed 75-cm-long stainless-steel vacuum chamber houses the high-finesse cavity used in our experiment. (The drawing is to scale). The central cavity contains the cavity mirrors and the molecular gas. Surrounding the cavity there is an insulated 45-cm-long liquid nitrogen reservoir. (The insulation is not shown.) The end clamps hold the end pieces in place, maintaining the vacuum, while the end pieces themselves hold the cavity mirrors and anti-reflection-coated chamber windows. One of the end pieces also houses the piezoelectric transducer (PZT) that allows for slight adjustments of the cavity length. We align the cavity mirrors by making slight adjustments to the six end-clamp-tightening bolts. This allows us to change the pitch of the mirrors while maintaining a vacuum seal. Not shown are the three dial indicators per end piece that record its pitch. See Appendix E for more details.

Inside the cavity, we have a molecular gas (either hydrogen, H_2, or deuterium, D_2), typically with a pressure of 0.1 - 0.5 atm. This pressure is about an order of magnitude lower than the pressures used in previous stimulated Raman scattering experiments [50, 55]. This is notable because dispersion and phase mismatch between Raman sidebands are reduced at such low pressures. The lower pressures also help to reduce significant pressure broadening that could increase the narrow linewidth of the two-photon transition.

Cooling the cavity with liquid nitrogen causes significant difficulties. In addition to the cavity misalignment due to temperature mentioned above, the constant boiling of the nitrogen also causes problems. The constant boiling means not only that the reservoir must be replenished frequently, but also that there is a perpetual source of mechanical perturbations to the cavity, which make it significantly more difficult to keep the laser on resonance with the cavity. Despite these challenges,

it is beneficial to keep the chamber at liquid nitrogen temperatures. The first benefit is due to the Boltzmann distribution of molecular states. In our experiment, we build-up coherence by driving two-photon transitions between the states. For most of our experiments these transitions begin in the ground vibrational or rotational state. We can build a stronger coherence if we cool the molecules so that we begin with a larger percentage of the population in this ground state.

We can find the ratio of populations in two states with energies E_1 and E_2 using the relation

$$\begin{aligned} \frac{P_1}{P_2} &= \frac{g_1 e^{-\frac{E_1}{kT}}}{g_2 e^{-\frac{E_2}{kT}}} \\ &= \frac{g_1}{g_2} e^{\frac{E_2 - E_1}{kT}} \\ &= \frac{g_1}{g_2} e^{\frac{h\Delta\nu}{kT}}, \end{aligned} \tag{6.32}$$

where P_i is the population in the ith state, h is Planck's constant, k is the Boltzmann constant, T is the temperature, g_i is the degeneracy of the ith state, and $\Delta\nu$ is the frequency difference corresponding to the energy splitting between the two levels.

The two Raman media used in our experiment are molecular deuterium (D_2) and molecular hydrogen (H_2). Some relevant frequency separations are shown in Table 6.1. The calculations, which follow those of Herzberg [65], are explained in more detail in Appendix F.

Note that the selection rules for the Raman transitions are [65]

$$\Delta v = \pm 1 \quad \text{and} \quad \Delta J = 0 \ \text{ or } \pm 2. \tag{6.33}$$

Let us return to Equation 6.32 and use the $\Delta\nu$ values from Table 6.1. If we do so, we see that the change from room temperature (300 K) to liquid nitrogen temperature (77 K) is not very important for the vibrational populations. (There is no degeneracy for the vibrational states, so $g_{v=n} = 1$ for all n.) For deuterium molecules in the rotational ground state $J = 0$, the ratio $\frac{P_{v=0}}{P_{v=1}}$ is around 1.7×10^6 at 300 K and 1.8×10^{24} at 77 K. For hydrogen, the ratio is 4.6×10^8 at 300 K and 5.7×10^{33} at 77 K. Although there is definitely a significant difference in the relative populations between the two temperatures, at either temperature the molecules are overwhelmingly in the ground state, $v = 0$. The first excited state, $v = 1$, though it is the second most populated

Molecule	Transition	Transition Type	Transition Frequency, $\Delta\nu$
$\mathbf{D}_2$	$\|v=0, J=0\rangle \rightarrow \|v=1, J=0\rangle$	*vibrational*	89.6 THz
	$\|v=0, J=0\rangle \rightarrow \|v=0, J=2\rangle$	*rotational*	5.4 THz
	$\|v=0, J=1\rangle \rightarrow \|v=0, J=3\rangle$	*rotational*	8.9 THz
$\mathbf{H}_2$	$\|v=0, J=0\rangle \rightarrow \|v=1, J=0\rangle$	*vibrational*	124.7 THz
	$\|v=0, J=0\rangle \rightarrow \|v=0, J=2\rangle$	*rotational*	10.6 THz
	$\|v=0, J=1\rangle \rightarrow \|v=0, J=3\rangle$	*rotational*	17.6 THz

Table 6.1 *Deuterium and Hydrogen Transition Frequencies* This table gives the frequencies $\Delta\nu$ of relevant vibrational and rotational transitions in molecular deuterium (D_2) and hydrogen (H_2). v is the vibrational quantum number, and J is the rotational quantum number. See Appendix F for the details of these calculations.

state, has a comparatively extremely small population at both temperatures for both molecules. Higher-order excited vibrational states have even lower relative populations. Thus, the population is overwhelmingly in the ground state for either room temperature or liquid nitrogen temperature, and the cooling has little noticeable effect on the vibrational quanta.

The same cannot be said about the rotational quanta. As seen in Tables 6.1, F.2, and F.3, the rotational frequency spacings are much smaller than the vibrational spacings. We can use Equation 6.32 and the frequency spacings listed in the tables in Appendix F to calculate the relative populations of the first rotational excited states. This is the same as the above vibrational calculation with one change. With the rotational states, we have to account for the $2J+1$ degeneracy of the Jth rotational level. $g_{J=0} = 1$ and $g_{J=1} = 3$, so we have a factor of $\frac{1}{3}$ when calculating $\frac{P_{J=0}}{P_{J=1}}$. For deuterium, this ratio is around 0.4 at 300 K and 1.0 at 77 K. For hydrogen, the ratio is 0.6 at 300 K and 3.0 at 77 K. Thus, at room temperature the population in the first excited rotational state is noticeably *higher* than that of the ground state, by approximately a factor of two for both molecules. However, by cooling the molecules to liquid nitrogen temperatures, we increase the ground state population and make it the most populated state. This means we have more molecules involved in the desired Raman process.

The affect of temperature can be further illustrated by examining the overall population distribution. The Boltzmann distribution discussed in Equation 6.32 also allows us to calculate the percentage of the overall molecular population that is in the nth rotational state given a temperature T.

$$\frac{P_n}{P_{total}} = \frac{(2n+1)\, e^{-\frac{h\nu_n}{kT}}}{\sum_{j=0}^{\infty} (2j+1)\, e^{-\frac{h\nu_j}{kT}}}, \tag{6.34}$$

where ν_j is the frequency separation between the ground state and the jth state. Figure 6.8 displays the percentages of the overall population that are in the lowest several rotational states at room temperature and at liquid nitrogen temperatures for both D_2 and H_2.

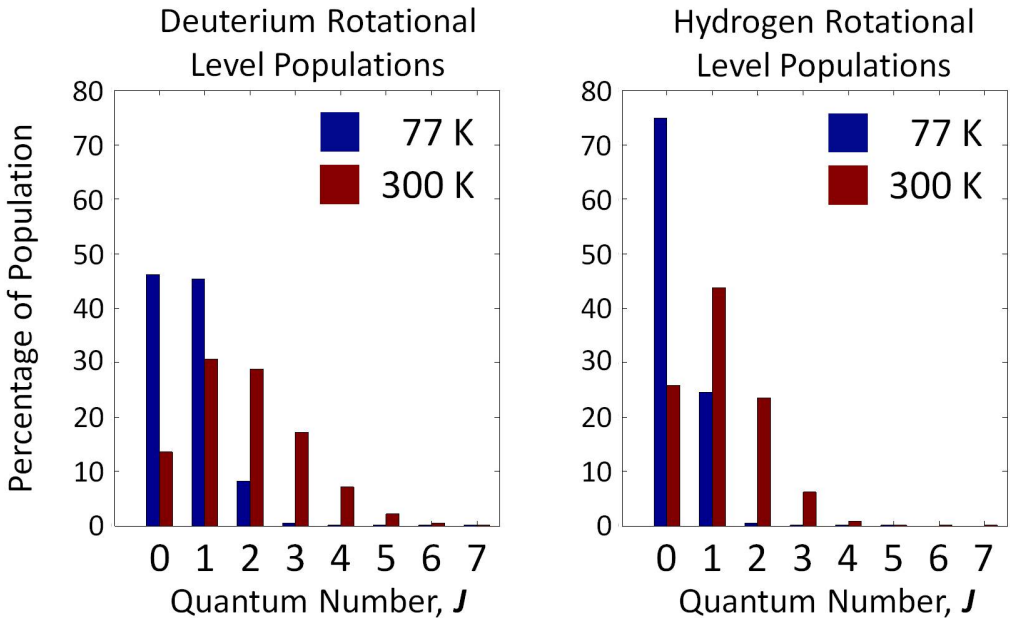

Figure 6.8 *Rotational Level Populations* This figure shows the percentages of the overall population that are found in the lowest several rotational states for the vibrational ground state. For both molecules at both temperatures the population percentages for excited vibrational states (not shown) are negligible. The larger energy spacing between states in hydrogen leads to lower populations in excited states. Note how cooling to liquid nitrogen temperatures significantly increases the populations in the lower states, which are the states used in our experiments.

In addition to the benefit of having more molecules in the proper quantum states, liquid nitrogen cooling narrows the linewidth of the Raman transition. Narrowing the linewidth of the transition means that more of the molecules are on resonance for any given frequency around the peak of

the resonance curve. Just as getting more molecules in the lower states increases the desired interaction of the laser and the molecules, a tighter grouping of resonances, that is, a narrower linewidth, increases the laser-molecule interactions. With more molecules on resonance, the gain of the Raman process is effectively increased, as the interaction is proportional to the number of participating molecules. Figure 6.9 illustrates this narrowing.

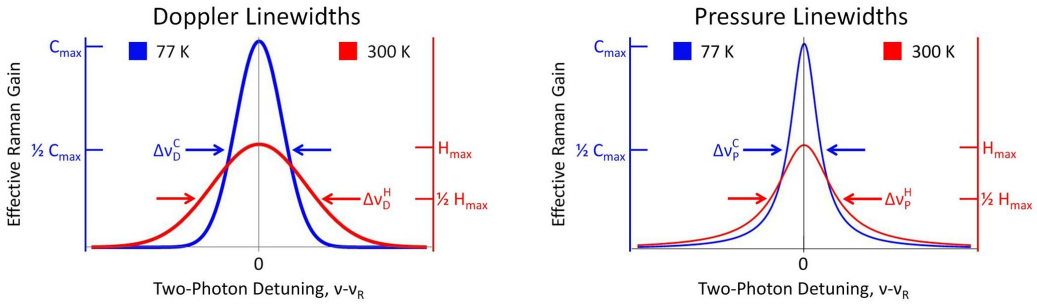

Figure 6.9 *Transition Linewidth and Temperature* This figure illustrates how cooling to liquid nitrogen temperatures narrows the linewidth of a Raman transition. Doppler and pressure broadening linewidths scale as the square root of temperature. Although the horizontal scale is arbitrary, it shows how the linewidths decrease by roughly a factor of two (by a factor of $\sqrt{\frac{300}{77}} \approx 1.97$) when the temperature is decreased from 300 K to 77 K. C_{max} and H_{max} are the maximum effective gains for cold and hot molecules, respectively. (These values are not necessarily the same for the two broadening mechanisms.) $\Delta\nu^C$ and $\Delta\nu^H$ are the full-width-half-maximum linewidths for cold and hot molecules, respectively. The subscript D refers the Doppler profile, which is inhomogeneous and therefore Gaussian. The subscript P refers to the pressure broadening profile, which is homogeneous and therefore Lorentzian. ν_R is the frequency of the Raman transition.

The temperature change affects the Raman linewidth by influencing both the Doppler linewidth and the pressure broadening linewidth. The total linewidth of the Raman transition (the Voigt profile) is given by the convolution of these two broadening mechanisms. (Single-photon transitions between the upper and lower Raman states are dipole forbidden, and the upper state is metastable. Thus, the lifetime is long, so lifetime broadening effects are small, and we will ignore them.)

Colder molecules move more slowly, which means the light they encounter has a smaller range of Doppler frequency shifts. This means they have a smaller spread of resonance frequencies, that

is, a narrower Doppler linewidth. Equation 6.35 shows the relationship between the full-width-half-maximum Doppler linewidth $\Delta\nu_D$ and temperature, T. (See Section 30.3 of Siegman [27].)

$$\Delta\nu_D = \nu_R \sqrt{8 \ln 2 \frac{kT}{mc^2}} \tag{6.35}$$

ν_R is the frequency of the Raman transition, and m is the mass of the molecule. k is the Boltzmann constant and c is the speed of light. Figure 6.9 illustrates the affect of temperature on Doppler linewidth.

Using the frequencies from Tables 6.1, F.2, and F.3, we can calculate the Doppler linewidths and see the narrowing benefit of liquid nitrogen cooling. Table 6.2 displays the full-width-half-maximum Doppler linewidths for a few relevant Raman transitions.

Molecule	Transition	$\Delta\nu_D$ at $T = 300$ K	$\Delta\nu_D$ at $T = 77$ K
	$\|v = 0, J = 0\rangle \rightarrow \|v = 1, J = 0\rangle$	556 MHz	282 MHz
$\mathbf{D}_2$	$\|v = 0, J = 0\rangle \rightarrow \|v = 0, J = 2\rangle$	32 MHz	17 MHz
$m = 4$ amu	$\|v = 0, J = 1\rangle \rightarrow \|v = 0, J = 3\rangle$	55 MHz	28 MHz
	$\|v = 0, J = 0\rangle \rightarrow \|v = 1, J = 0\rangle$	1094 MHz	554 MHz
$\mathbf{H}_2$	$\|v = 0, J = 0\rangle \rightarrow \|v = 0, J = 2\rangle$	93 MHz	47 MHz
$m = 2$ amu	$\|v = 0, J = 1\rangle \rightarrow \|v = 0, J = 3\rangle$	154 MHz	78 MHz

Table 6.2 *Temperature Dependence of Doppler Linewidths of Raman Transitions* This table gives the full-width-half-maximum Doppler linewidths $\Delta\nu_D$ of relevant vibrational and rotational transitions in molecular deuterium (D_2) and hydrogen (H_2). This highlights one of the advantages of working at liquid nitrogen temperatures: narrower Raman linewidths. The narrower linewidths are an effective increase in gain for our Raman processes, as they increase the number of molecules that see a given laser frequency as resonant.

The change in temperature also affects the Raman linewidth through changes in pressure broadening. Pressure, and thus pressure broadening, comes from molecular collisions. If we assume that the collisional cross-section of the molecules is constant with changing temperatures, which is a fairly reasonable assumption, the temperature dependence of molecular collisions comes from the

change in speed of the molecules. The collisional rate is approximately proportional to translational molecular speed. Molecular speed is proportional to the square root of kinetic energy, and energy is in turn proportional to the temperature. Thus, the collisional rate and pressure broadening is approximately proportional to the square root of temperature.

$$\begin{aligned} \Delta\nu_P &\sim R_{collisions} \sim \sigma_{collisions} \cdot v \\ \text{and} \qquad v &\sim \sqrt{E_{kinetic}} \sim \sqrt{kT} \\ &\implies \Delta\nu_P \sim \sqrt{T} \end{aligned} \tag{6.36}$$

In the above expressions, $\Delta\nu_P$ is the linewidth due to pressure broadening, and $R_{collisions}$ and $\sigma_{collisions}$ are the rate and cross-section of molecular collisions, respectively. v is the molecular speed; $E_{kinetic}$ is the kinetic energy; k is the Boltzmann constant; T is the temperature.

Therefore, just as with Doppler broadening, the linewidth is proportional to the square root of temperature, and cooling to liquid nitrogen temperatures decreases the pressure broadening linewidth by nearly a factor of two, as shown in Figure 6.9.

$$\sqrt{\frac{300\ K}{77\ K}} \approx 1.97 \tag{6.37}$$

We can also use the fact that $\Delta\nu_P \sim \sqrt{T}$ to extrapolate from room temperature data and see how the pressure broadening coefficient, σ_P, changes when the cavity is cooled to liquid nitrogen temperatures. σ_P is a measure of how $\Delta\nu_P$ changes as a function of pressure. Table 6.3 displays the pressure broadening coefficients at liquid nitrogen temperatures. $\Delta\nu_P$ can be estimated by multiplying these σ_P values by the molecular pressure used in the experiment. (σ_P is the slope of $\Delta\nu_P$ as a function of P. This functional relationship is close to linear at the pressures at which our experiments are typically performed. Note that this approximation ignores the offset from the nonzero y-intercept of this line, which is small.) The room temperature values come from the literature: rotational data - [66], vibrational data D_2 - [67], vibrational data H_2 - [68], general information, notation, and additional rotational data - [69]. (The units of some of the literature values have been changed for clarity of comparison.)

$\Delta\nu_P$ is proportional to $\sqrt{T}$, and from the ideal gas law, pressure P is proportional to T (assuming constant number density). Thus σ_P, which is the change in $\Delta\nu_P$ over the change in P, is proportional to $\frac{\sqrt{T}}{T} = \frac{1}{\sqrt{T}}$.

Molecule	Transition	σ_P at $T = 300$ K	σ_P at $T = 77$ K
D_2	$\|v = 0, J = 0\rangle \rightarrow \|v = 1, J = 0\rangle$	213 kHz / torr	415 kHz / torr
	$\|v = 0, J = 0\rangle \rightarrow \|v = 0, J = 2\rangle$	162 kHz / torr	316 kHz / torr
	$\|v = 0, J = 1\rangle \rightarrow \|v = 0, J = 3\rangle$	108 kHz / torr	210 kHz / torr
H_2	$\|v = 0, J = 0\rangle \rightarrow \|v = 1, J = 0\rangle$	86 kHz / torr	168 kHz / torr
	$\|v = 0, J = 0\rangle \rightarrow \|v = 0, J = 2\rangle$	48 kHz / torr	96 kHz / torr
	$\|v = 0, J = 1\rangle \rightarrow \|v = 0, J = 3\rangle$	59 kHz / torr	115 kHz / torr

Table 6.3 *Temperature Dependence of Pressure Broadening Coefficients* This table gives the pressure broadening coefficients σ_P of relevant vibrational and rotational transitions in molecular deuterium (D_2) and hydrogen (H_2). Although the pressure broadening linewidths are smaller at colder temperatures, the sensitivity of linewidth to pressure increases as temperature decreases.

Chapter 7

Progress in Yavuz Lab

The foundation for the molecular modulation experiment in the Yavuz Lab was in place when I joined the group. The hard work and progress of Deniz Yavuz, my advisor and the leader of the group, and older graduate students Daniel Sikes and Tyler Green made my work possible. Tyler especially was pivotal in designing and building much of the molecular modulation experiment, and he also trained me to take over the experiment. In this chapter we will review the progress made by Tyler, Deniz, Daniel, and myself that occurred before I became the principle student on the molecular modulation project. Much of the work described in this chapter is covered in more detail in Tyler's thesis [25].

We begin with a key milestone in the molecular modulation project that was accomplished by Tyler, Deniz, and Daniel just before my arrival in Yavuz Lab in January 2010 (Section 7.1). We will then review progress made by Tyler, Deniz, and myself while I was the junior graduate student on the project (Sections 7.2 and 7.3). In an attempt to avoid cumbersome phrases, all experiments will be described in the present tense.

7.1 CW Rotational Raman Generation

In this section, we describe an experiment demonstrating strong Stokes sideband generation with a rotational Raman transition in molecular deuterium [52]. Working at room temperature with an earlier version of the high-finesse cavity described in Chapter 6, we generate more than 320 mW of rotational Stokes output power in a continuous-wave Raman laser. Figure 7.1 shows the transmitted power in the pump and the Stokes beams as a function of the incident pump power.

This is among the largest output powers ever generated in gas-phase CW Raman lasing. Raman laser powers of a over 1 W have been achieved in photonic crystal fiber experiments [70], but as mentioned in Section 6.3, fiber experiments have the drawback of much larger linewidths, on the order of hundreds of MHz. The full-width-half-maximum linewidth of this high-power Raman laser was on the order of 10 kHz. The Raman lasing occurs with a deuterium gas pressure of 0.1 atm inside of the high-finesse cavity.

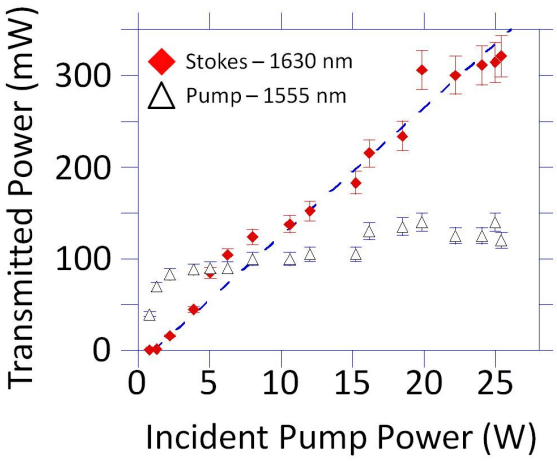

Figure 7.1 *Rotational Raman Laser* This figure shows the transmitted pump power (empty blue triangles) and the generated Stokes power (solid red diamonds) as a function of the incident pump power. The Raman medium is molecular deuterium gas at a pressure of 0.1 atm. The scattering transition is the $|\nu = 0, J = 1\rangle$ to $|\nu = 0, J = 3\rangle$ rotational transition, which has a transition frequency of 8.9 THz. The pump beam wavelength is 1555 nm, and the Stokes beam wavelength is 1630 nm. The Raman lasing threshold, the incident pump power at which Raman lasing begins to occur, is about 1 W. This is evidenced by the plateauing of the transmitted pump power. After this point, any additional incident pump power is being converted to Stokes power. The dotted line is a linear fit of the Stokes data.

The experimental arrangement is very similar to the one described in Chapter 4. There are two main differences: the seed laser and the cavity. The seed laser is at a wavelength of 1555 nm (instead of 1064 nm), and it is amplified with an erbium (rather than ytterbium) fiber amplifier. The cavity mirrors have the same high-power, high-reflectivity coating as the mirrors described in Section 6.3. They are highly reflective at both the pump (1555 nm) and the Stokes wavelengths (1630 nm), and they have a radius of curvature of 50 cm. The cavity is 27 cm long, about one third

of the length of the experimental cavity described in Section 6.3. This cavity is *not* liquid nitrogen cooled; this experiment is performed at room temperature.

The Raman scattering occurs on the $|\nu = 0, J = 1\rangle$ to $|\nu = 0, J = 3\rangle$ rotational transition in deuterium. In agreement with the calculation of Table 6.1, the transition frequency is 8.9 THz. Because the objective is to generate a single, strong Stokes beam rather than a broad, multi-ordered spectrum, the pump light is circularly polarized using a quarter-wave plate. This results in the preferential generation of the first-order Stokes beam, which has the opposite circular polarization as the pump [71]. This is due to the conservation of angular momentum. The molecule gains one quantum of angular momentum when the circularly polarized pump photon excites it to the virtual state, and then it gains another when the Stokes photon is emitted with the opposite circular polarization. The opposite circular polarization of the Stokes beam means that it will preferentially scatter to generate its frequency up-shifted sideband (the pump), rather than a second-order Stokes beam. (See Subsection 1.2.3 for a description of this two-photon Raman process, and the discussion of Figure 10.1 for more explanation of the connection between polarization and preferential sideband generation.)

This demonstration of strong CW Raman lasing in molecular deuterium is an important step towards demonstrating the feasibility of our CW molecular modulation scheme.

7.2 Coherent Raman Spectrum

Building upon the success of the high-power rotational Raman generation of Section 7.1, we expand our CW stimulated Raman scattering experiment to generate three CW spectral components covering about one octave of optical bandwidth [72]. Light modulation at a frequency of nearly 90 THz allows us to generate this broad spectrum. Furthermore, we demonstrate the mutual coherence of the three spectral components, and this indicates promise for using such a coherent spectrum to generate arbitrary optical waveforms.

The experimental arrangement is very similar to the experiment described in the previous section. The important differences are that the seed laser wavelength is 1064 nm and that the Raman lasing occurs on the $|v = 0, J = 0\rangle$ to $|v = 1, J = 0\rangle$ fundamental vibrational transition of

D_2. As shown in Table 6.1, this transition gives a modulation frequency of 89.6 THz, an order of magnitude higher than the rotational frequency, and almost $\frac{1}{3}$ of the frequency of the 1064 nm light. This large modulation frequency produces a spectrum spanning from 807 nm to 1560 nm, approximately 96% of an octave of bandwidth.

Inside the high-finesse cavity, the same cavity as in the rotational experiment, the locked 1064 nm laser intensity is strong enough to not only generate the vibrational Stokes sideband at 1560 nm, but also the anti-Stokes sideband at 807 nm. (See Subsection 1.2.3 for a discussion of Stokes and anti-Stokes scattering.) The Stokes beam is resonant with the high-finesse cavity. It builds up from noise from Raman scattering of the circulating pump beam, and the intracavity power builds up over many round trips. The intense pump and Stokes beam stimulate Raman scattering, and the resulting molecular coherence mixes with the pump beam to generate the anti-Stokes beam through four-wave mixing. In contrast to the Stokes beam, the anti-Stokes beam lies outside of the high-reflectivity range of the cavity mirrors, and therefore it is generated in a single pass through the cavity. The spectrum and the four-wave mixing process are illustrated in Figure 7.2.

After the cavity, the three beams are separated using an SF11 prism. We first measure the powers of the three beams for two different deuterium pressures, 0.1 atm and 0.5 atm. We generate 10s of mW of pump and Stokes light, and 10s of μW of anti-Stokes light. The anti-Stokes beam is much weaker because it is not resonant with the cavity. Figure 7.3 displays output pump, Stokes, and anti-Stokes powers as a function of the incident pump power for the two pressures. The threshold incident power for Raman lasing, the power at which Stokes and anti-Stokes generation occurs, is lower for the higher deuterium pressure, 0.5 atm. Note that even this higher pressure is more than an order of magnitude lower than those used in many CW Raman lasing experiments, and the effects of dispersion are still small [46, 50, 53].

In addition to measuring the powers of the three beams, we explore their mutual coherence. We look at two nonlinear $\chi^{(2)}$ processes in a 10-μm thick Beta-Barium-Borate (BBO) crystal. The quantum interference of the two processes is a function of their relative phases. This procedure is based on work by Hsieh *et al.* [40]. Figure 7.4 shows a schematic of this measurement process. The transmitted beams are separated using an SF11 prism, as with the power measurement. We

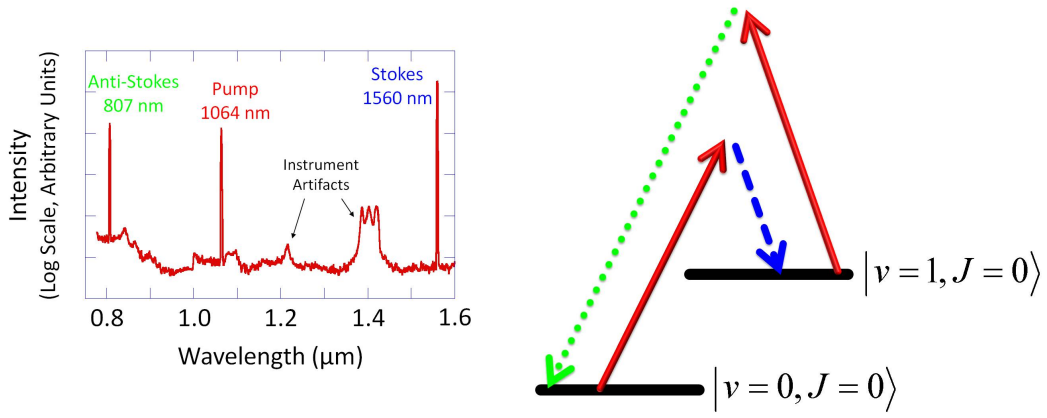

Figure 7.2 *Four-Wave Mixing* On the left is an optical spectrum analyzer scan displaying the anti-Stokes, pump, and Stokes beams. The anti-Stokes and Stokes beams are 89.6 THz, the modulation frequency, away from the pump beam. The figure on the right illustrates the four-wave mixing process that generates the anti-Stokes beam. The solid red arrows represent the pump beam at 1064 nm. As the pump beam resonates with the cavity, the Stokes beam builds up from noise from Raman scattering off of the $|v=0, J=0\rangle$ to $|v=1, J=0\rangle$ vibrational transition in molecular deuterium. The Stokes beam, at 1560 nm and represented by the dashed blue arrow, also resonates with the cavity. The intense pump and Stokes beams build up the molecular coherence between the states. This coherence mixes with the pump beam to generate an anti-Stokes beam through four-wave mixing, a $\chi^{(3)}$ nonlinear process. The anti-Stokes beam, at 807 nm and represented by the dotted green arrow, is not resonant with the cavity, and thus is generated in a single pass through the system.

place a 1-mm-thick BK7 glass slide in the beam path of the Stokes beam. The slide is mounted on an actuator so that the slide can be rotated. Small rotations modify the beam path, and thus the phase, of the Stokes beam. (The Stokes beam was chosen because of its convenient location and power, but modifying the phase of any of the three beams would have a similar effect.) Each of the three beams is then independently reflected back into the prism to recombine them. The recombined beams are then focused on the BBO crystal with an achromatic-doublet lens. (The BBO crystal must be thin in order to avoid dispersion of the three beams inside the medium. A thicker crystal would not maintain the relative phases of the beams.) In order to ensure that all three beams focus at the same location, we individually optimize the transmission of each beam through a pinhole aperture at the focal point.

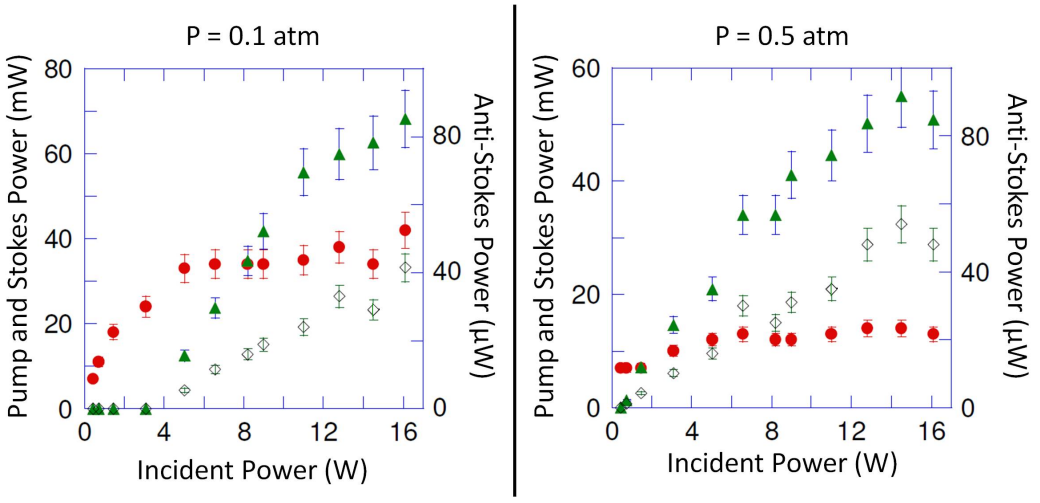

Figure 7.3 *Powers of the Generated Coherent Spectrum* These figures show the transmitted powers of the beams shown in the spectrum of Figure 7.2 as a function of the incident pump power for two different pressures. The solid red circles mark the transmitted pump power. Notice the characteristic plateauing of the transmitted pump power, as is characteristic of Raman lasing. (See also Figure 7.1.) The solid green triangles mark the transmitted Stokes power, and the empty black diamonds mark the transmitted anti-Stokes power. Note that the vertical scale is different for the anti-Stokes beam. The right vertical axis marks the anti-Stokes power in μW. Also notice that the vertical scale is different for the two plots.

Through the second-order $\chi^{(2)}$ nonlinearity of the BBO crystal, we generate a fourth beam at a wavelength of 532 nm. As shown in the inset of Figure 7.4, there are two different quantum mechanical processes in the crystal that can generate 532 nm light: two photons from the pump beam (second harmonic generation - SHG) or one photon each from the Stokes and anti-Stokes beams (sum-frequency generation - SFG). Depending on the relative phases of the three Raman beams, these two paths may interfere constructively or destructively, thus generating more or less 532 nm light. Controlling the phase of one of the three beams gives us enough relative phase control to manipulate this interference effect [32]. After the BBO crystal, all four beams are collimated, and then spatially separated by a prism. The generated 532 nm light is further isolated using a narrowband interference filter, and then its weak signal is detected using a single-photon-counting module.

Figure 7.5 shows the number of 532 nm photons detected per second as a function of the phase change of the Stokes beam due to the glass slide rotation. The figure includes experimental

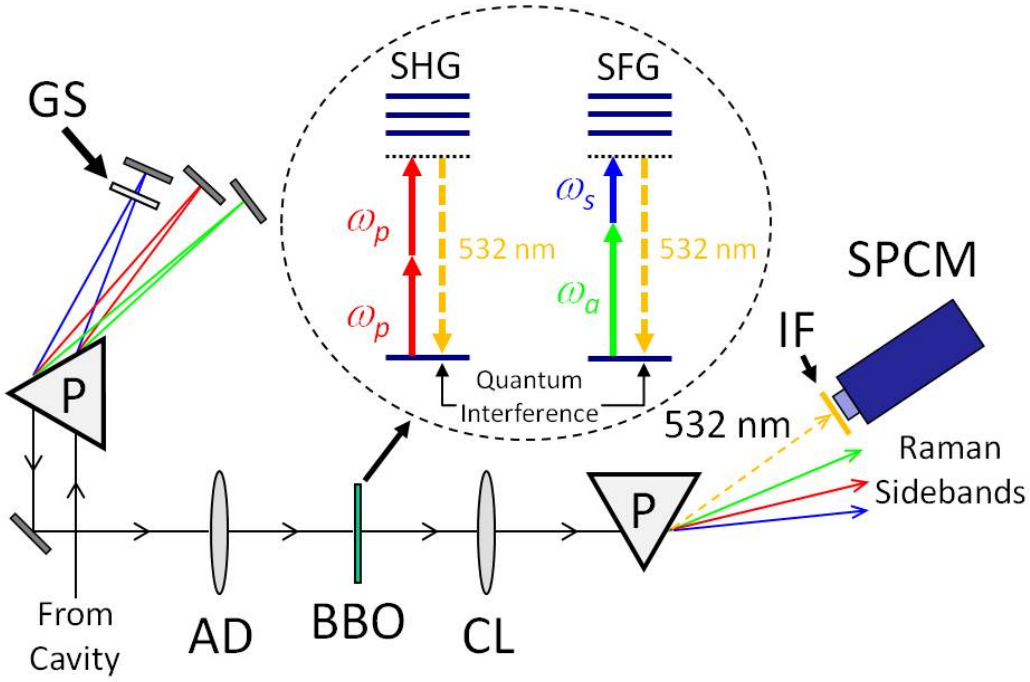

Figure 7.4 *Quantum Path Interference* The spectrum, consisting of the pump (ω_p), the Stokes (ω_S), and the anti-Stokes (ω_a) beams, is transmitted through the cavity and is spatially separated by a prism (P). The Stokes beam is manipulated by a glass slide (GS), which can rotate to change the path length and thus the phase of the beam. Individual mirrors then reflect the three beams back to the prism. The recombined beams are focused to a common focus by an achromatic doublet lens (AD). The beams are focused onto a 10-μm-thick Beta-Barium-Borate crystal (BBO). As shown in the inset, two second-order $\chi^{(2)}$ processes in the nonlinear crystal lead to the generation of 532 nm light. Two pump photons can create 532 nm light through second-harmonic generation (SHG), or one anti-Stokes photon and one Stokes photon can create 532 nm light through sum-frequency generation (SFG). Depending on the relative phases, the 532 nm light generated from these two processes can add constructively or destructively. After the BBO crystal, all four beams are sent through a collimating lens (CL) and then another prism (P) to spatially separate them again. The 532 nm light is then further isolated using a narrowband interference filter (IF) and detected using a single-photon-counting module (SPCM).

data points (red diamonds) as well as a numerical simulation (green line). The phase change is calculated from the refractive index and the rotation angle of the glass slide. In order to make the two interfering paths (SHG and SFG) more comparable, the pump beam was attenuated by 60% using a neutral density filter. (Recall that the anti-Stokes beam is orders of magnitude lower in power than the other beams because, unlike the other two beams, it is not resonant with the cavity.)

Before the BBO crystal, the powers and Gaussian waist sizes of the three beams are: Pump - 5.61 mW and 33 μm, Stokes - 39.4 mW and 36 μm, and anti-Stokes - 38 μW and 30μm. The solid line in Figure 7.5 is a numerical simulation of the interference based on these measured power values and beam sizes. The only two fitting parameters of the simulation are the unknown initial relative phase and an absolute vertical scaling; the contrast is calculated without any adjustable parameters. The fringe visibility (the amplitude over the average value) is around 75%. This large contrast of the experimental data, which is in good agreement with the theoretical calculation, suggests that there is significant quantum interference between the two 532 nm light generation paths. This implies that the three beams have almost perfect mutual phase coherence. The data takes about fifteen minutes to record and the relative phase drift between the three beams during this period is negligible.

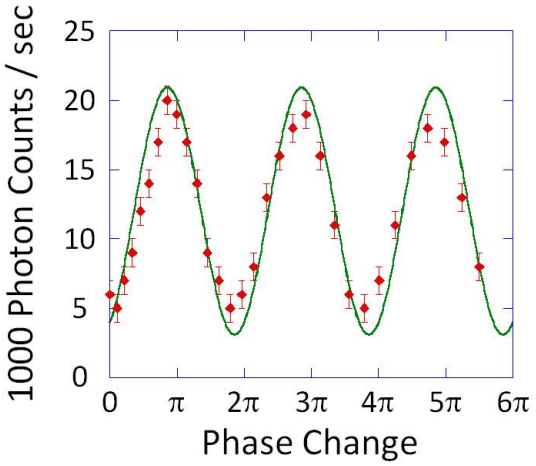

Figure 7.5 *Mutual Coherence Measurement* This figure shows the number of 532 nm photons detected per second by the photon counter as a function of introduced phase change of the Stokes beam. The sinusoidal pattern comes from the interference of the two quantum paths that generate 532 nm light. (See Figure 7.4.) The large visibility of the fringes suggest significant interference and thus excellent mutual phase coherence of the beams. The red diamonds mark experimental data points, and the green curve is a numerical simulation based on experimental parameters. The contrast of the simulated curve is calculated without any adjustable parameters.

At one of the maxima of the interference fringes, adding the fields of the three beams yields an AM-like waveform, with a relatively constant frequency and significant amplitude changes. This

is because the beat frequency envelope from the pump-Stokes beat note is in phase with the beat frequency envelope of the pump-anti-Stokes beat note. (The two beat frequencies are the same because both are spaced from the pump beam by the modulation frequency.) The superposition of these in-phase envelopes has maxima and minima (coincident with maxima and minima of the individual envelopes), and the waveform is thus AM-like.

At one of the minima of the interference fringes of Figure 7.5, the phases of the three beams are such that adding their fields yields an FM-like waveform, with relatively constant amplitude and changing frequency. This is because the pump-Stokes and pump-anti-Stokes beat frequency envelopes are now π out of phase with one another. The maxima of one envelope are coincident with the minima of the other, and therefore the superposition of the two envelopes has a relatively constant amplitude. The only significant modulation, then, is of the frequency, and the waveform is FM-like. (This frequency modulation was mostly negligible in the AM-like signal because near the maxima the frequency is mostly constant. The frequency modulation that occurs near the minima is negligible due to the low amplitude of the signal.)

In this way, the good phase coherence across the spectrum implied by Figure 7.5 demonstrates the ability for primitive waveform synthesis. Although we have not yet explored this option, the demonstrated phase control and near-perfect mutual coherence of the spectrum implies that with proper amplitude adjustment (through the use of neutral density filters) we can synthesize any waveform within the capabilities of this spectrum. Figure 7.6 shows what the synthesized temporal waveform would look like if the three Raman amplitudes were adjusted to be equal and if the phases were such to be at a maximum of the interference fringe. A near single-cycle optical waveform with a repetition period of 11 femtoseconds would be formed. A *single-cycle* optical waveform is a waveform whose pulse envelope has the same duration as the period of the electric field oscillation. The repetition period is equal to the inverse of the modulation frequency. (If this repetition period is too short for the desired application, pulses could be isolated using nonlinear gating processes [73].) Recall that because the three CW spectral components of this waveform are generated inside a high-finesse cavity, they have a full-width-half-maximum linewidth around 10

kHz. Therefore the temporal waveform of Figure 7.6 is predicted to maintain its structure without significant change for about $\frac{1}{10\ kHz}$ = 0.1 ms.

It is important to note that a key limitation of our experiment is the optical power of the generated spectrum, especially of the anti-Stokes beam. Due to the low generated anti-Stokes power, the synthesized waveform of Figure 7.6 has an average optical power of only a fraction of a mW.

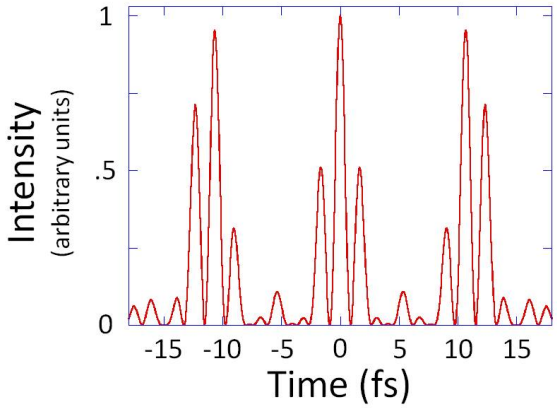

Figure 7.6 *Inferred Synthesized Temporal Waveform* This figure shows the intensity of an inferred synthesized waveform as a function of time. This assumes that the three spectral components of Figure 7.2 are combined while phase-locked and of equal amplitude. A near single-cycle optical waveform with a repetition period of 11 femtoseconds is formed. $t = 0$ fs is chosen to be one of the maxima of the pulse train. Note that because the absolute frequencies of the component beams are not integer multiples of their frequency difference (the modulation frequency), the carrier-envelope phase varies with time.

In this experiment, we demonstrate fully-coherent CW light modulation at a frequency of 89.6 THz. We generate significant anti-Stokes light at a wavelength that is not resonant with the cavity. Furthermore, we demonstrate phase control, and therefore a primitive form of waveform synthesis, using CW beams generated from stimulated Raman scattering. We view this experiment as the first step towards synthesizing arbitrary optical waveforms using CW spectral components. By increasing the efficiency of the scattering process and the number of generated Raman beams, we will be able to increase the number of degrees of freedom for temporal waveform synthesis.

7.3 Multiple-Order Rotational Raman Generation

An important limitation of the experiments described in the previous two sections is the low number of generated Raman sidebands. This is especially relevant in the quest for ultrashort pulse synthesis and arbitrary waveform generation. With a spectrum of only three Raman sidebands, well-defined pulse synthesis is not possible, and the range of waveforms that can be synthesized is severely limited. In this section, we discuss an experiment that significantly increases the number of Raman spectral components [74].

We demonstrate the generation of up to seven Raman sidebands (two anti-Stokes and five Stokes) with a combined average power exceeding 50 mW. The Raman scattering occurs on the $|v = 0, J = 0\rangle$ to $|v = 0, J = 2\rangle$ rotational transition in molecular deuterium. We achieve this generation at a pressure of around 0.01 atm. This is more than an order of magnitude lower than our previous experiments and thus more than two orders of magnitude lower than in typical CW stimulated Raman scattering experiments. This low pressure helps us to avoid detrimental phase mismatch between sidebands. Furthermore, when we increase the pressure to around 0.1 atm, we observe simultaneous $|v = 0, J = 0\rangle$ to $|v = 0, J = 2\rangle$ and $|v = 0, J = 1\rangle$ to $|v = 0, J = 3\rangle$ rotational stimulated Raman scattering. This increases the total number of Raman sidebands to more than ten.

The experiment arrangement is similar to that of those described in the previous two sections. The seed laser for this experiment has a wavelength of 1064 nm, and it is amplified by a ytterbium fiber amplifier. The key experimental change that leads to the high-order rotational generation is a new, liquid-nitrogen-cooled high-finesse cavity that cools the deuterium to 77 K. The cavity, except for a few minor modifications, is the one described in Section 6.3 and Appendix E, including the high-reflectivity mirror coating. In contrast to the cavity in the previous two sections, the mirrors have a radius of curvature of 100 cm, and the length of the cavity is 75 cm. Thus, the free spectral range is 200 MHz. (See Equation 5.1 for the definition of free spectral range.) This longer cavity increases the distance over which the lasers interact with the molecules, and it also decreases the maximum intensity inside of the cavity because the cavity waist is larger. However, the main

effects of the change in cavity are associated with the addition of liquid nitrogen, which increases rotational ground state populations and narrows transition linewidths as described in Section 6.3. Although we did not study this in-depth, we note that the Raman lasing threshold decreased to less than $\frac{1}{3}$ W, a decrease of over a factor of three compared to our room temperature experiments. (See Figure 7.1.)

When we lock the linearly-polarized pump laser to the liquid-nitrogen-cooled cavity, we observe multiple-order rotational stimulated Raman scattering. At low pressures, we find that scattering on the $|v = 0, J = 0\rangle$ to $|v = 0, J = 2\rangle$ transition is dominant. This transition frequency, and thus the spacing between successive Raman sidebands, is 5.4 THz. Figure 7.7 shows a typical spectrum that we observe on an optical spectrum analyzer at a deuterium pressure of around 0.01 atm and 20 W of incident pump power. In addition to the pump laser, we observe the generation of up to two anti-Stokes (AS1, AS2) and five Stokes (S1-S5) beams. The pump laser has a wavelength of 1064 nm, and the Raman spectral components range from 1025 nm to 1180 nm in wavelength.

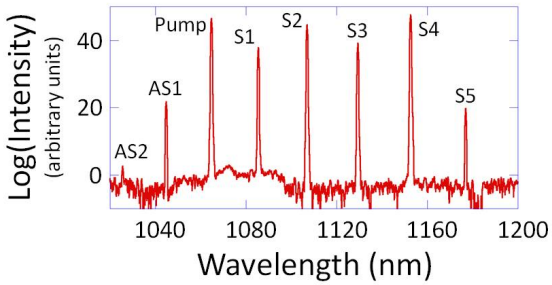

Figure 7.7 *Multiple-Order Rotational Raman Scattering - 0.01 atm D_2* This figure shows an optical spectrum analyzer scan of the spectral components generated by stimulated Raman scattering in our high-finesse cavity with 20 W incident pump power. The scattering occurs on the $|v = 0, J = 0\rangle$ to $|v = 0, J = 2\rangle$ rotational transition in molecular deuterium. The transition frequency, and thus the spacing between successive spectral components, is 5.4 THz. The spectrum contains the pump, two anti-Stokes (AS1, AS2) and five Stokes (S1-S5) beams. Note that the vertical scale is logarithmic.

We believe that the Stokes sidebands are generated through cascade stimulated Raman scattering. Each Stokes sideband behaves as an independent pump and produces the subsequent Stokes beam through Raman lasing at a cavity mode [75]. The anti-Stokes beams are generated through four-wave mixing as described in Figure 7.2. The pump and the Stokes beams drive the molecular

coherence of the transition, and this coherence mixes with the pump to produce the anti-Stokes beam. The anti-Stokes beam then mixes with the coherence to produce the second-order anti-Stokes beam.

We note that Luo *et al*. have observed CW cascade stimulated Raman scattering as well [76]. Their experiment was based on scattering in silicate fibers using multiple fiber Bragg gratings. As with the previously mentioned fiber-based experiments, the linewidths of the beams produced are significantly wider than the kHz-level linewidths of our high-finesse cavity experiments.

Figure 7.8 shows the powers transmitted through one of the mirrors as a function of the incident pump beam power at a deuterium pressure of around 0.01 atm. The powers of the pump, one anti-Stokes (AS1), and five orders of Stokes (S1-S5) beams from the spectrum of Figure 7.7 are displayed. The second-order anti-Stokes beam (AS2) had a power too low to accurately record. The maximum powers generated are 60 μW for AS1, 17.5 mW for the pump, 2.4 mW for S1, 9.2 mW for S2, 2.9 mW for S3, 24.5 mW for S4, and 43 μW for S5. The fifth-order Stokes sideband (S5) is weaker due to a significant drop in the mirror reflectivity at its wavelength.

As we increase the deuterium pressure, we observe more evenly distributed sideband powers with reduced total combined power. The reduction in combined power with increasing pressure is likely a result of changes in the cavity mode due to Raman thermal lensing effects as demonstrated by Brasseur and colleagues or due to nonlinear Raman self-focusing or defocusing [53]. Both of these effects are due to the intense fields inside of the cavity, where the higher intensities near the optical axis cause a gradient in the refractive index. The lower combined power is probably also due in part to a reduction in the performance of the cavity lock as a result of significant depletion of the pump beam and of disruptions caused by the temporal dynamics of the Raman lasing process.

At higher pressures, we also observe additional generation on the $|v = 0, J = 1\rangle$ to $|v = 0, J = 3\rangle$ rotational transition. This transition has a frequency of 8.9 THz, and thus this is the spacing between subsequent Raman sidebands. (Figure 6.8 shows that at liquid nitrogen temperatures, the $J = 0$ and $J = 1$ rotational states have roughly equal populations, so it is reasonable to expect simultaneous scattering off of both transitions.) We find the competition between $|v = 0, J = 0\rangle$ to $|v = 0, J = 2\rangle$ and $|v = 0, J = 1\rangle$ to $|v = 0, J = 3\rangle$ generation to be sensitive to the mirror

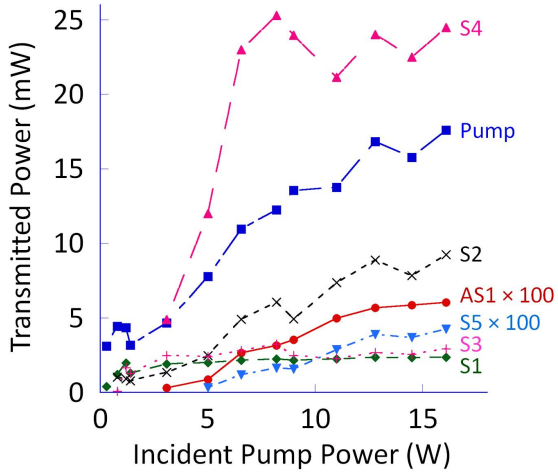

Figure 7.8 *Power Curves - Rotational Raman Scattering - 0.01 atm D_2* This figure shows power curves for the rotational spectral components shown in Figure 7.7. Powers are displayed for the pump beam, five orders of Stokes beams (S1-S5), and one anti-Stokes beam (AS1) as a function of incident pump power. The second-order anti-Stokes beam was too weak to record accurate power measurements. Note that due to their low powers, the fifth Stokes beam and first anti-Stokes powers are multiplied by 100 to improve their visibility. The 20% error bars on each measurement are not shown to increase clarity. At the maximum incident pump power, the combined power of the Raman spectral components is over 50 mW.

alignment, tuning of the cavity length, and the absolute frequency of the pump laser beam. The sensitivity is likely due to the changing frequency overlap between the longitudinal modes of the cavity and the Raman transition lineshapes. We have not yet investigated the competition between the two rotational transitions in detail.

Figure 7.9 shows a typical spectrum generated at a deuterium pressure of around 0.1 atm with an incident pump power of 9 W. In addition to the one anti-Stokes beam (AS1) and five Stokes beams (S1-S5) from the $|v = 0, J = 0\rangle$ to $|v = 0, J = 2\rangle$ transition, the pump beam generates the first Stokes sideband on the $|v = 0, J = 1\rangle$ to $|v = 0, J = 3\rangle$ transition. We label this beam $\mathbf{P}'$, as it acts as a new pump and generates a new set of sidebands on the $|v = 0, J = 0\rangle$ to $|v = 0, J = 2\rangle$ transition. We label this new spectrum with bold, blue, and primed labels. The total optical power in the generated spectrum of Figure 7.9 is approximately 25 mW.

One drawback of the approach used to produce the above Raman spectra is that the frequency difference between adjacent spectral components in not exactly constant. This is because the

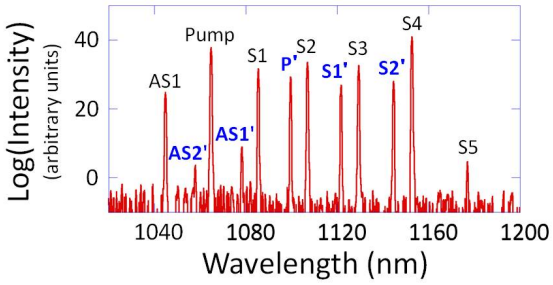

Figure 7.9 *Multiple-Order Rotational Raman Scattering - 0.1 atm D_2* This figure shows an optical spectrum analyzer scan of the spectral components generated by stimulated Raman scattering in our high-finesse cavity with 9 W of incident pump power. The scattering occurs on both the $|v = 0, J = 0\rangle$ to $|v = 0, J = 2\rangle$ and the $|v = 0, J = 1\rangle$ to $|v = 0, J = 3\rangle$ rotational transitions in molecular deuterium. The transition frequencies of these transitions are 5.4 THz and 8.9 THz, respectively. The spectrum contains the pump, one anti-Stokes (AS1) and five Stokes (S1-S5) beams from the $|v = 0, J = 0\rangle$ to $|v = 0, J = 2\rangle$ transition. It also contains the first-order Stokes beam from the $|v = 0, J = 1\rangle$ to $|v = 0, J = 3\rangle$ transition. This Stokes beam, labeled **P′**, becomes the pump beam for a new spectrum of $|v = 0, J = 0\rangle$ to $|v = 0, J = 2\rangle$ scattering. This second spectrum, whose components are labeled in bold, blue, and primed labels, contains two anti-Stokes beams (**AS1′**, **AS2′**) and two Stokes beams (**S1′**, **S2′**). Note that the vertical scale is logarithmic.

Stokes sidebands are produced through cascade stimulated Raman scattering, and not four-wave mixing. (Although both processes can occur, cascade scattering occurs more readily than four-wave mixing due to the high finesse of our cavity.) Each subsequent Stokes beam is generated from the previous sideband through Raman lasing in the cavity starting from noise. (Note that this is *not* the case for the anti-Stokes beams. Anti-Stokes processes are based on transitions from higher energy states to lower energy states. In general, the higher energy states have lower populations, and thus the population inversion necessary for lasing is absent. Furthermore, because the anti-Stokes beams are not lasing, yet the cavity mirrors are still highly reflective at their wavelengths, the presence of the cavity actually *decreases* the anti-Stokes transmitted power. There is no enhancement in power from being resonant with the cavity, and very little light is transmitted through the highly-reflective mirrors.) Because each beam is produced through a lasing process, the frequency of the generated beam necessarily corresponds to a cavity resonance, as shown in Figure 3.1. However, each generated beam is at a different frequency, and thus each sideband has a unique set of cavity resonances. These sets of resonances do not necessarily overlap with one

another. Therefore, the two-photon detuning and the frequency of the Raman transition can vary between different orders of sidebands. Figure 7.10 illustrates this variability.

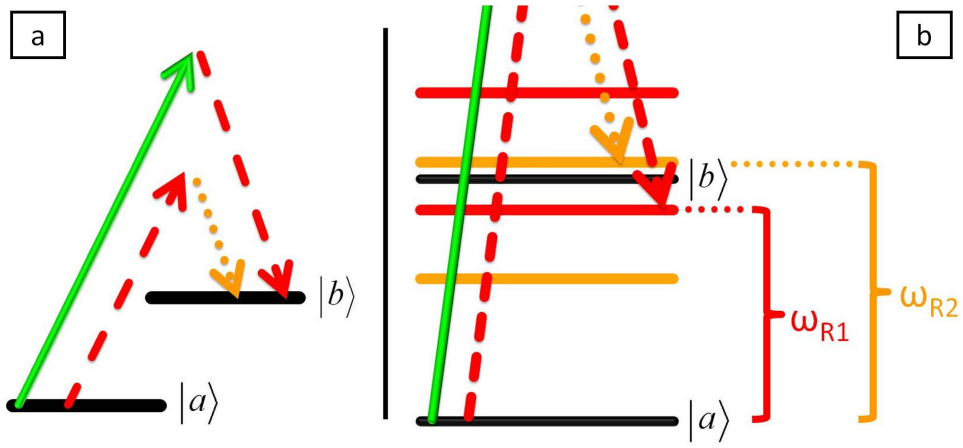

Figure 7.10 *Frequency Variation with Cascade Scattering* This figure illustrates the source of frequency variation with cascade Raman scattering. (a) This is a simplified view of first- and second-order Raman scattering from Figure 1.9. $|a\rangle$ and $|b\rangle$ are the molecular ro-vibrational states. The solid green arrow is the pump beam. The dashed red arrows are the first-order Stokes beam, and the dotted orange arrow is the second-order Stokes beam. (b) This is a more detailed view of the lower half of diagram (a). It includes the cavity resonances for the first- and second-order Stokes beams (red and orange lines, respectively). Because the different orders of Stokes beams have different frequencies, their cavity resonances are different. This means that the frequencies of the two-photon Raman transitions for the first-order (ω_{R1}) and second-order (ω_{R2}) beams are different. Thus, the frequency separation between adjacent Stokes beams is variable.

This frequency variability is a significant drawback to this method of Raman spectrum generation. However, the variability can, in principle, be measured and corrected. Nonlinear optical mixing methods can be used to measure the frequency of the sidebands, and frequency-tuning elements (acousto-optic modulators, for example) can be placed in the path of each sideband, as was done with the phase-modulating glass slide in Figure 7.4. In this way, one could precisely control the frequencies if an equidistant Raman spectrum were desired. Alternatively, as shown by Zaitsu and Imasaka, for a spectrum of just a few Raman beams, the frequencies of the sidebands can be controlled by tuning the resonances of the cavity using a dispersive gas [77].

We note that the spectral components of the spectra of Figures 7.7 and 7.9 have random phases, yet those phases are well-defined relative to one another. (The randomness comes from the fact

that the generation of each Stokes beam is initiated from noise by spontaneous Raman scattering.) Because they have a definite phase relationship, an external phase mask could be used to correct the phases to produce a phase-locked spectrum. If we assume the ideal case of phase-locked spectral components with comparable amplitudes, the spectrum of Figure 7.7 would synthesize approximately 20-fs-long optical pulses with 186 fs between pulses.

In the following chapters, we will explore further experiments that build upon these results. We will discuss how we expand our spectrum by simultaneously scattering off of both vibrational transitions as in Section 7.2 and rotational transitions as in this section. We will also discuss progress towards using such scattering as a molecular modulation. Before we move on, however, we note two interesting aspects of this rotational experiment that merit further attention. We have not yet explored either in depth. The first is the wide range of transverse Gaussian modes that we observe in the rotational beams. For certain cavity alignments, we observe (with an infrared viewer) all Stokes and anti-Stokes beams to be in the TEM_{00} spatial mode. However, a slight change in the alignment of one of the cavity mirrors, the cavity length, or the laser frequency can change the spatial modes. We observe intricate TEM_{nm} spatial modes with very high n and m. These beams have intricate spatial profiles much more complex than those displayed in Figure 6.5. We generally try to avoid such modes by making adjustments to the cavity end-clamp-tightening bolts to regain TEM_{00} modes. However, further study of these modes would perhaps teach us more about the subtleties of cavity alignment.

Another observation that merits further attention is our possible observation of scattering off of the forbidden $|v = 0, J = 0\rangle$ to $|v = 0, J = 1\rangle$ transition. Figure 7.11 shows a preliminary optical spectrum analyzer scan with a peak spaced 1.8 THz away from the pump. This is the transition frequency associated with the $|v = 0, J = 0\rangle$ to $|v = 0, J = 1\rangle$ Raman transition, which is dipole forbidden for symmetric homonuclear molecules like D_2. Observation of significant Raman scattering off of this transition would be a notable discovery.

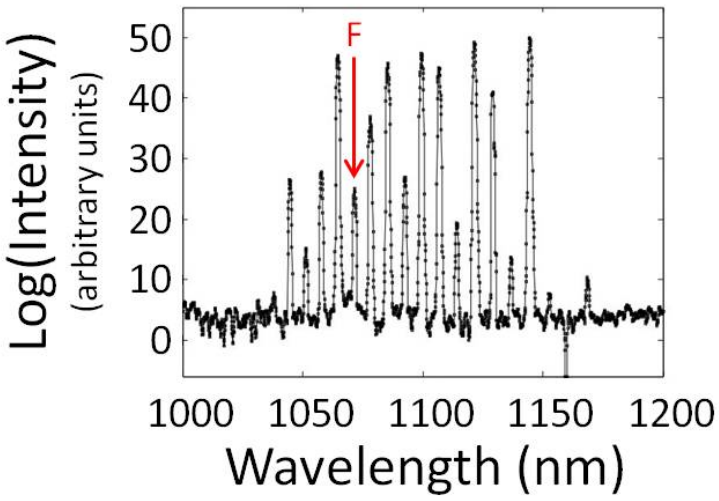

Figure 7.11 *Possible Observation of Forbidden Transition* This figure shows an optical spectrum analyzer scan of the spectral components generated by stimulated Raman scattering in our high-finesse cavity. Among the complex spectrum is a beam, marked with a red F, that is located around 1.8 THz from the pump beam. This corresponds with Raman scattering off of the $|v = 0, J = 0\rangle$ to $|v = 0, J = 1\rangle$ rotational transition in molecular deuterium. This transition is dipole forbidden for a symmetric homonuclear molecule like D_2. Note that the vertical scale is logarithmic.

Chapter 8

Broadband Spectrum Generation

In this chapter, we will discuss further progress in broadband spectrum generation using stimulated Raman scattering. We expand upon the work described in Chapter 7 and experimentally demonstrate a CW ro-vibrational Raman spectrum that is two octaves wide with spectral components ranging from 800 nm to 3100 nm in wavelength [78]. To our knowledge, the nearly two-octave-wide spectrum described in this chapter is the broadest spectrum ever produced in the CW domain. As in previous chapters, the spectrum is produced in low-pressure molecular deuterium inside a high-finesse cavity, and this yields spectral components with narrow frequency linewidths. We use an optical heterodyne detector to measure the absolute full-width-half-maximum linewidths, and we find them to be on the order of 10 kHz.

The experimental arrangement used to generate this broad spectrum is identical to the one described in Section 7.3. We use a seed laser with a wavelength of 1064 nm that is amplified to 20 W using a ytterbium-doped fiber amplifier. The linearly-polarized amplified beam is then coupled to the same 75-cm-long, liquid-nitrogen-cooled high-finesse cavity. The high-reflectivity cavity mirrors are also identical to those in Section 7.3.

At deuterium gas pressures of order 0.1 atm, we observe that when the pump laser at 1064 nm is locked to the cavity, the vibrational Stokes sideband at 1560 nm on the $|v = 0, J = 0\rangle$ to $|v = 1, J = 0\rangle$ transition is generated through Raman lasing. Just as described in 7.2, these pump and generated Stokes beams drive the molecular coherence and produce the vibrational anti-Stokes beam through four-wave mixing. In this experiment, in addition to this anti-Stokes beam at a wavelength of 807 nm, four-wave mixing also produces a second-order vibrational Stokes beam

at 2923 nm. Both the anti-Stokes beam and the second-order Stokes beam are outside of the high-reflectivity ranges of the cavity mirrors. They are not resonant, but are produced in a single pass through the cavity.

In addition to this vibrational Raman generation, we simultaneously observe rotational Raman lasing on the $|v = 0, J = 0\rangle$ to $|v = 0, J = 2\rangle$ transition, similar to that seen in the experiment of Section 7.3. The mirrors of the cavity have such high reflectivity in the wavelength ranges around 1010 - 1150 nm and around 1430 - 1620 nm that this rotational generation can build up from noise. Just as in Section 7.3, we produce multiple-order rotational Stokes sidebands through cascade Raman lasing. The generated rotational Stokes beam behaves as an independent pump and produces the subsequent higher-order rotational Stokes sideband through Raman lasing. The resulting rotational Stokes beams also mix with the vibrational molecular coherence to generate rotational spectra near each vibrational sideband.

Due to this simultaneous vibrational and rotational Raman generation, we observe a broad ro-vibrational spectrum. The frequencies ν_{nm} in the spectrum have the form

$$\nu_{nm} = \nu_{pump} + n\nu_{mod}^{vib} + m\nu_{mod}^{rot}, \tag{8.1}$$

where ν_{pump} is the frequency of the pump beam, and n and m are integers. ν_{mod}^{vib} and ν_{mod}^{rot} are the vibrational and the rotational Raman modulation frequencies, respectively. ν_{mod}^{vib} is the frequency of the $|v = 0, J = 0\rangle$ to $|v = 1, J = 0\rangle$ vibrational transition, which is 89.6 THz. ν_{mod}^{rot} is the frequency of the $|v = 0, J = 0\rangle$ to $|v = 0, J = 2\rangle$ rotational transition, which is 5.4 THz. (See Table 6.1 and Appendix F for more on transition frequencies.)

Figure 8.1 shows the generated ro-vibrational spectrum that is transmitted through one of the cavity mirrors. The 800 - 1650 nm region is recorded on an optical spectrum analyzer in a single scan. The combined power of the two mid-infrared sidebands (2923 nm and 3086 nm) is measured using a germanium (Ge) filter and a lead selenide (PbSe) photodiode. The relative power of these two beams is inferred using the properties of the filter and the photodiode. The optical powers for all rotational groups were measured, and the approximate relative powers of the rotational beams in each group can be inferred by the relative heights of the peaks in Figure 8.1. By slightly changing the cavity length or seed laser frequency, we have some control over the relative strength of

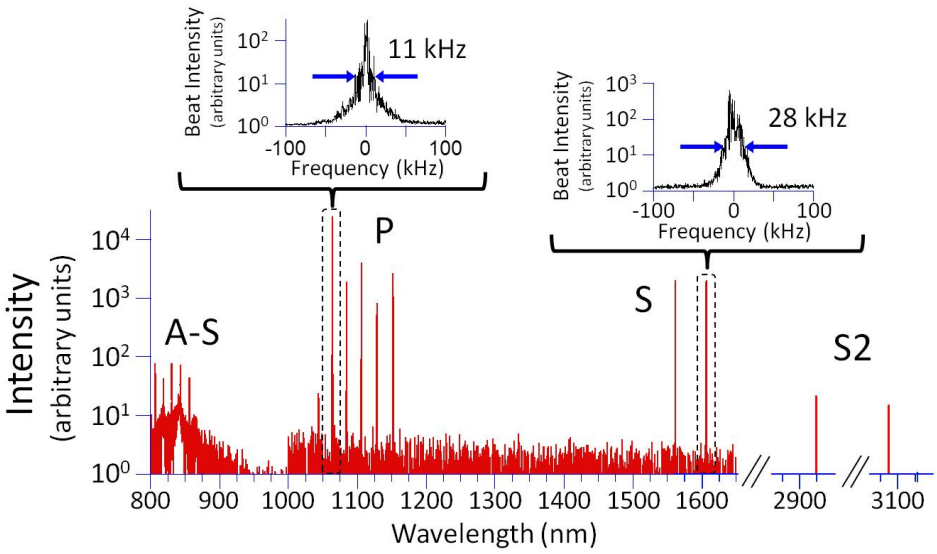

Figure 8.1 *Broadband Ro-Vibrational Spectrum* This figure shows the ro-vibrational spectrum generated through stimulated Raman scattering in a high-finesse cavity. The mirrors have high reflectivity at wavelengths around 1010 - 1150 nm and around 1430 - 1620 nm. The Raman medium is molecular deuterium gas at a pressure of 0.1 atm. The spectrum is obtained by locking a single 1064-nm-wavelength pump laser to the cavity. The scattering transitions are the $|v = 0, J = 0\rangle$ to $|v = 1, J = 0\rangle$ vibrational transition (89.6 THz) and the $|v = 0, J = 0\rangle$ to $|v = 0, J = 2\rangle$ rotational transition (5.4 THz). The 800 - 1650 nm region is recorded on an optical spectrum analyzer in a single scan, and the mid-infrared beams are measured using a PbSe photodiode. In the spectrum analyzer scan, the change in the background level between 800 - 900 nm and the jump in the background level at 1000 nm are instrument artifacts. The insets show optical heterodyne linewidth measurements of the full-width-half-maximum frequency linewidth for the 1064 nm and 1605 nm beams. See Table 8.1 for powers of each rotational group: **A-S** anti-Stokes, **P** pump, **S** Stokes, **S2** second-order Stokes.

the vibrational and rotational transitions. This is because the Raman lasing process depends critically on the overlap of the frequencies of the longitudinal cavity modes with the Raman transition linewidths. Changing the cavity length or seed frequency tunes the position of the cavity modes in or out of resonance with a particular Raman transition, thereby adjusting its strength. The powers of the rotational groups shown in Figure 8.1 are given in Table 8.1.

Recall that neither the anti-Stokes nor the second-order Stokes group beams are resonant with the cavity. As discussed below Figure 7.9, the cavity mirrors serve to diminish rather than to

Rotational Group	Approximate Wavelength Range	Power
Pump	1044 - 1152 nm	15 mW
First-Order Vibrational Stokes	1560 - 1605 nm	20 mW
First-Order Vibrational Anti-Stokes	807 - 857 nm	50 μW
Second-Order Vibrational Stokes	2923 - 3086 nm	1 μW

Table 8.1 *Optical Powers of Rotational Groups* This table gives the powers of the rotational spectra around each of the vibrational beams in Figure 8.1. The approximate relative powers of the individual rotational sidebands in each group can be determined by examining the relative heights of the peaks in the figure.

enhance the transmitted powers for these beams. The second-order Stokes beams are further attenuated by the cavity and chamber optics, which absorb light in the mid-infrared.

To further explore the generated spectrum, we measure the absolute frequency linewidths of the spectral components in the pump and in the first-order vibrational Stokes regions. Nick Brewer, a graduate student in our research group, has constructed an optical heterodyne detector for performing such linewidth measurements. The detector splits the sideband to be measured into two paths and delays one of them using a 10 km-long optical fiber. This delay, which is around 50 μs, allows us to compare the current laser frequency to the laser frequency from 50 μs ago. This comparison measures the temporal coherence of the beam. The measurement is made by recombining the delayed and undelayed beams on a fast photodiode. This allows us to observe the beat intensity as a function of frequency, giving us a measure of the laser linewidth.

We find the beat linewidth measurements to be fairly sensitive to our experimental conditions, especially to the quality of the Pound-Drever-Hall lock that keeps the seed laser resonant with the cavity. As a result, the linewidth measurements for all beams vary by as much as a factor of two from day to day, and even from measurement to measurement. However, for each of the seven spectral components we examine (five near the pump and two near the vibrational Stokes), we find the full-width-half-maximum beat linewidth to be consistently at the 10 kHz level. The insets in Figure 8.1 show sample beat measurements for the beams at 1064 nm and at 1605 nm. For this

particular measurement, the full-width-half-maximum linewidths at the two wavelengths are found to be 11 kHz and 28 kHz, respectively. There is nothing fundamental about the 10 kHz absolute linewidth. We believe that the linewidths of the sidebands are currently limited by imperfections in the locking feedback electronics that cannot fully account for perturbations to the system. Brasseur and colleagues have demonstrated Raman lasing linewidths on the order of 1 kHz [47], and with technical improvements, this should be attainable in our experiment.

Figure 8.2 shows the spatial profiles of many of the ro-vibrational sidebands in the broadband spectrum. In this measurement, the generated spectrum transmitted through one of the cavity mirrors is spatially dispersed with an SF11 prism. All of the beams are captured in one image taken with a digital camera (with the aid of fluorescent target materials). The beams are then allowed to propagate farther and further spatially disperse, allowing us to photograph the individual rotational beams using the same method. Finally, we use a charge-coupled-device-based (CCD-based) beam profiler to image those beams visible to the CCD. We see that all beams have clean TEM_{00} Gaussian profiles because they are produced in a high-finesse cavity. (As mentioned at the end of Section 7.3, we can change the cavity length and alignment to observe lasing in higher-order transverse spatial modes. We typically observe reduced sideband generation efficiency when the sidebands are lasing in higher-order spatial modes.)

As with the purely rotational scattering of Section 7.3, with this broadband ro-vibrational spectrum we can observe simultaneous rotational generation on multiple transitions. In the spectrum of Figure 8.1, the rotational scattering was exclusively from the ground state on the $|v = 0, J = 0\rangle$ to $|v = 0, J = 2\rangle$ transition. However, at liquid nitrogen temperatures, the thermal populations of the $J = 0$, $J = 1$, and $J = 2$ rotational levels are 46%, 45%, and 8%, respectively. (See Figure 6.8.) Thus, if the cavity is appropriately tuned, significant rotational scattering starting from each of these J levels is possible.

Figure 8.3 highlights the details of the pump and the vibrational anti-Stokes regions of a mixed rotational spectrum at a pressure of 0.2 atm. The pump produces five rotational sidebands (AS1, S1-S4) on the $|v = 0, J = 0\rangle$ to $|v = 0, J = 2\rangle$ transition. The modulation frequency of this transition is 5.4 THz. (See Table 6.1.) The pump also produces a rotational Stokes sideband on

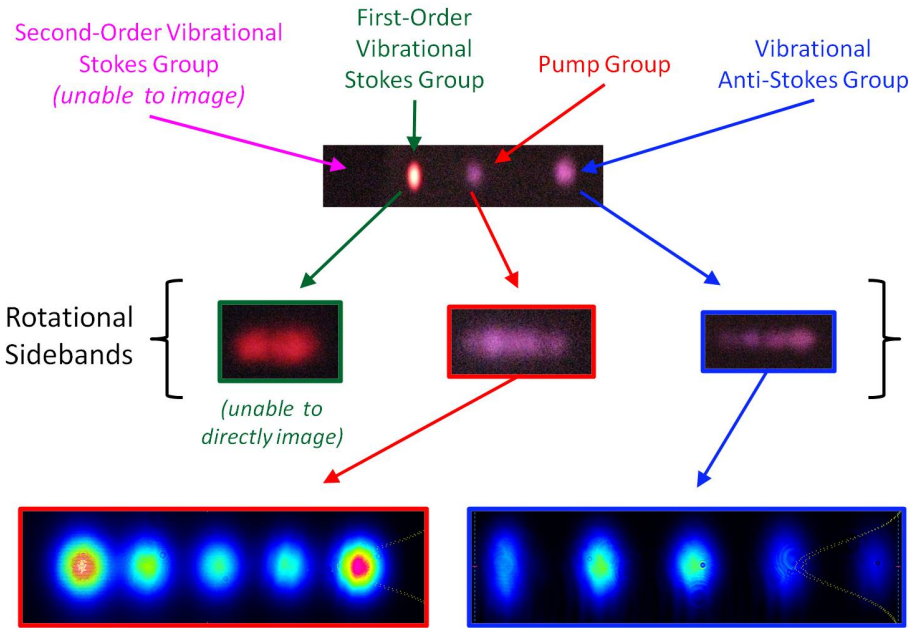

Figure 8.2 *Ro-Vibrational Spectrum Spatial Profiles* This figure displays images of the spatial profiles of many of the spectral components from the broadband Raman spectrum. The spectrum transmitted through one of our cavity mirrors is spatially dispersed by an SF11 prism. The top image captures all of the beams in the spectrum that we can image. For the second row of images, the beams are allowed to propagate farther to allow for further spatial separation. Thus, the individual rotational sidebands that make up the groups in the first image can be resolved. The bottom row displays beam profiles as captured by a CCD-based beam profiler. All beams have a nearly-perfectly Gaussian spatial profile from being generated in the TEM_{00} mode of the high-finesse cavity. Note that the Gaussian profiles in the images are somewhat distorted by the prism.

the $|v = 0, J = 1\rangle$ to $|v = 0, J = 3\rangle$ transition. This beam is labeled in blue as **P′**, and it is 8.9 THz away from the pump. (See Table 6.1.) This beam acts as an independent pump and generates the primed spectrum (**AS1′**, **S1′**, **S2′**) by scattering off of the $|v = 0, J = 0\rangle$ to $|v = 0, J = 2\rangle$ transition. A third, separate first-order Stokes sideband from the pump beam is generated on the $|v = 0, J = 2\rangle$ to $|\nu = 0, J = 4\rangle$ transition, which has a modulation frequency of 12.4 THz. (Table F.2 lists the frequencies of the rotational states. Calculating the difference between the frequencies of the states of a transition yields the transition frequency.) This third Stokes beam similarly produces the double-primed spectrum (**AS2″**, **AS1″**, **S1″**, **S2″**) on the $|v = 0, J = 0\rangle$ to $|v = 0, J = 2\rangle$ transition.

The spectrum is further enriched through four-wave mixing. Just as the pump mixes with the coherence to generate the vibrational anti-Stokes beam as described in Figure 7.2, all of the spectral components mentioned in the previous paragraph can mix with the coherence to generate new sidebands. Those new sidebands that fall in the anti-Stokes region of the spectrum are shown in Figure 8.3. They are labeled with the label of the beam that mixed with the coherence to create them along with a subscript v to denote that they were generated through vibrational coherence. Although it is not shown in the figure, four-wave mixing also produces sidebands near the first- and second-order vibrational Stokes beams near 1560 nm and near 2923 nm. In total, this Raman generation produces around 30 ro-vibrational sidebands.

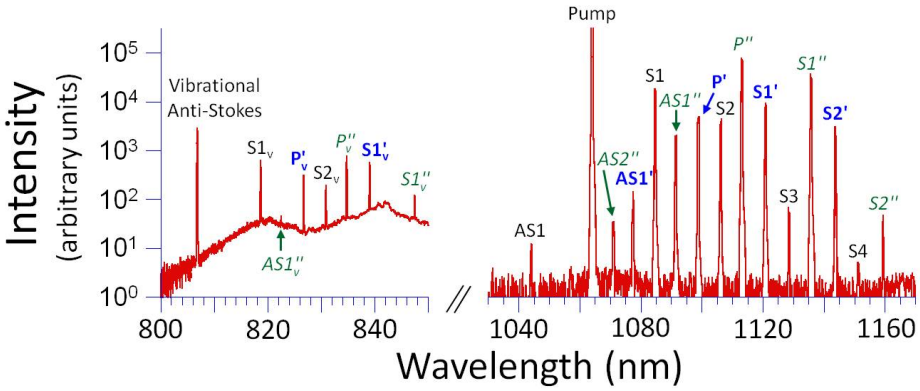

Figure 8.3 *Ro-Vibrational Spectrum - Multiple Rotational Transitions* This figure displays part of the rich ro-vibrational spectrum produced through stimulated Raman scattering in a high-finesse cavity. The spectrum is produced through simultaneous scattering off of three rotational transitions and one vibrational transition. The spectrum labeled in black was produced through rotational scattering exclusively on the $|v = 0, J = 0\rangle$ to $|v = 0, J = 2\rangle$ transition. The primed spectrum labeled in boldface blue was produced through rotational scattering on both the $|v = 0, J = 1\rangle$ to $|v = 0, J = 3\rangle$ and the $|v = 0, J = 0\rangle$ to $|v = 0, J = 2\rangle$ transitions. The double-primed spectrum labeled in green italics was produced through rotational scattering on both the $|v = 0, J = 2\rangle$ to $|v = 0, J = 4\rangle$ and the $|v = 0, J = 0\rangle$ to $|v = 0, J = 2\rangle$ transitions. The left section of the figure around the vibrational anti-Stokes beam was produced through four-wave mixing. The sidebands are labeled with the label of the beam that mixed with the coherence to generate them and a subscript v to indicate that they were generated through vibrational coherence. Not shown are sidebands near the first- and second-order vibrational Stokes beams produced through four-wave mixing. In total, this Raman spectrum contains around 30 ro-vibrational spectral components. Note that the top of the pump peak does not fit on the vertical scale. The rise in the background level between 800 and 850 nm is an instrument artifact.

The broadband spectrum described in this chapter is, to our knowledge, the broadest spectrum ever produced through CW molecular modulation. We close this chapter with a discussion of the applications of such a broadband spectrum to temporal waveform synthesis. We will concentrate on the spectrum of Figure 8.1. There is not a rational relationship between the pump frequency (281.8 THz) and the vibrational and rotational modulation frequencies (89.6 THz and 5.4 THz). Thus, the synthesized temporal waveform will be quasi-periodic. If we assume that all the spectral components are adjusted to have equal amplitudes and aligned phases (as we did in Figure 7.6), the spectrum of Figure 8.1 would synthesize a quasi-periodic train of pulses with significant carrier-envelope phase drift between pulses. (If desired, the carrier-envelope phase drift could be stabilized using a method similar to the *f-to-2f* self-referencing technique used with titanium-sapphire lasers [79].) The calculated pulse train is shown in Figure 8.4. Note that features with periods of both 11 fs ($\approx \frac{1}{89.6\ THz}$) and 185 fs ($\approx \frac{1}{5.4\ THz}$) are present. The inset details highlight the fact that some of the pulses in the pulse train would have a sub-optical-cycle duration of 0.9 fs. This short pulse duration is due to the broadness of the spectrum. Very roughly speaking, the duration of the pulse goes as the inverse of the bandwidth of the spectrum. (We note that, as with Figure 7.6, the optical power of the such pulses would be limited by power of the weakest spectral component.)

Synthesizing such a pulse train will require phase and amplitude control of the generated spectrum, which is one of our major goals for the near future. Such phase and amplitude control could be provided by a programmable liquid crystal array [35]. Once synthesized, the temporal waveforms can be measured and characterized using cross-correlation studies with nonlinear media or multiphoton ionization processes [10, 34, 35, 41].

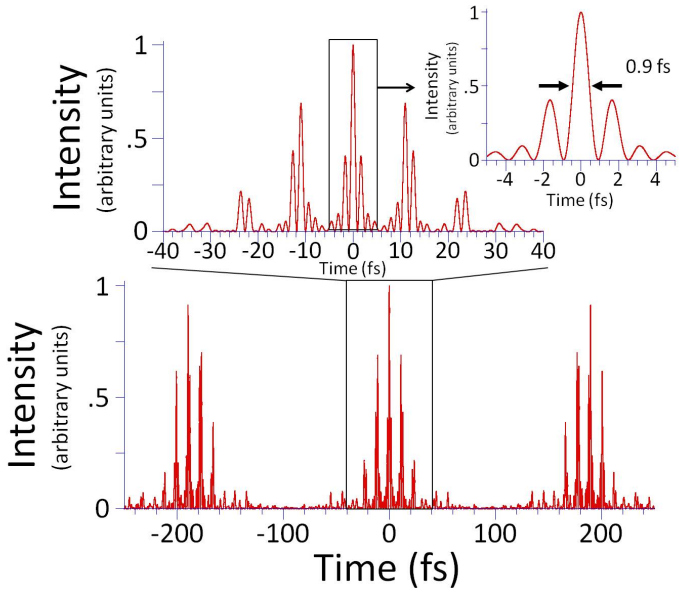

Figure 8.4 *Calculated Quasi-Periodic Pulse Train* This figure shows the pulse train that would be generated if the spectrum of Figure 8.1 were adjusted so that the spectral components all have equal amplitudes and aligned phases. Because there is not a rational relationship between the pump frequency and the vibrational and rotational modulation frequencies, the synthesized temporal waveform is quasi-periodic. The insets show details of this calculated pulse train, including the central sub-optical-cycle pulse that has a sub-femtosecond duration.

Chapter 9

Independent Mixing Beam Modulation

In Chapters 7 and 8, we focused on generating a coherent spectrum using stimulated Raman scattering. The pump beam generates a Stokes beam from noise through Raman lasing, and then the pump and this generated Stokes beam build up coherence between molecular energy levels. This coherence then mixes with the pump (and other beams resonant with the cavity) to generate additional Raman sidebands. (See Figure 7.2.) In this chapter we discuss an essential step in developing a practical molecular modulator. We demonstrate that the molecular coherence in our high-finesse cavity can be used to modulate a completely independent CW mixing beam [80]. This work is motivated by promising previous experiments performed with pulsed lasers [71, 81].

Our CW molecular modulator has a modulation frequency of 17.6 THz, and it can modulate any beam within the optical range of the spectrum, wavelengths from roughly 100 nm to 10 μm. In addition to these broadband capabilities, the modulation efficiency of our device is independent of the incident optical power, and therefore our modulator is capable of modulating arbitrarily weak signals. These characteristics of our modulator highlight our motivations for pursuing *molecular* modulation.

Molecular modulation is technically challenging, and the modulation efficiency is low. Initial results suggest our modulator has a single-pass efficiency (defined as the total sideband power divided by the incident pump power) varying between 10^{-4} and 10^{-8} over its operating range. Despite these drawbacks, molecular modulation offers two distinct advantages over readily available alternatives such as AOMs and EOMs: high modulation frequencies and broadband input capabilities. AOMs and EOMs typically have modulation frequencies in the 10s or 100s of MHz. The faster of the two methods is electro-optic modulation, and the fastest EOMs have modulation

frequencies of a few hundred GHz [82, 83, 84, 85, 86]. In contrast, molecular modulators can have modulation frequencies exceeding 100 THz, more than three orders of magnitude higher than the fastest EOMs [32]. In this experiment, the modulation frequency is 17.6 THz, a relatively modest frequency for a molecular modulation, yet still orders of magnitude higher than other modulation methods. The large modulation frequency means that the wavelengths of the sidebands are substantially different from the incident mixing wavelength. As described below, a mixing beam at a wavelength of 785 nm is modulated by our modulator to produce frequency up-shifted and down-shifted sidebands at wavelengths of 750 nm and 823 nm, respectively. Furthermore, while AOMs and EOMs typically can modulate light whose wavelength ranges over 10s or 100s of nanometers, molecular modulators can, as mentioned above, modulate light of any wavelength in the optical spectrum.

Just as high modulation frequencies and broadband input capabilities set molecular modulation apart from other modulation methods, the use of an independent mixing beam sets this experiment apart from other CW molecular modulation experiments. In other CW molecular modulation experiments, both from our lab (Chapters 7 and 8) and from other research groups (Chapter 3), Raman sidebands are generated from the coherence mixing with the pump or the Raman sideband beams. These beams are generally resonant with the cavity, and they typically have very high intracavity intensities. Thus, in these works, beam modulation only occurs at very specific wavelengths. This is a significant limitation. A device that can modulate any independent mixing beam, even at wavelengths that are not necessarily resonant with the cavity, has much more versatility. The experiment described in this chapter is the first to demonstrate such modulation: a separate, non-resonant laser beam makes a single pass through a cavity, and frequency sidebands shifted by 17.6 THz are produced.

As with our other experiments, we build up molecular coherence in a high-finesse cavity. We drive this coherence with two intense, resonant laser fields: the seed laser that is locked to the cavity that serves as the pump beam, and the Stokes beam that starts from Raman lasing in the cavity. In this case, the Raman scattering occurs on the $|v = 0, J = 1\rangle$ to $|v = 0, J = 3\rangle$ rotational transition in molecular hydrogen, H_2. This transition has a frequency of 17.6 THz, which gives us

our modulation frequency. (Note that if one uses the difference of the values in Table F.3, one gets 17.5 THz for this transition frequency. This discrepancy is due to rounding in the table values.) The pump laser is at a wavelength of 1064 nm, and the Stokes beam is at 1135 nm. With the molecules prepared in a coherent state by the strong, resonant pump and Stokes beams, a third, weaker and non-resonant laser beam at a wavelength of 785 nm is sent through the system. This mixing beam is modulated by the coherently rotating molecules through four-wave mixing, and this produces sidebands at wavelengths of 750 nm and 823 nm. The mirrors of the cavity are not highly reflective at 785 nm, and thus this modulation is produced in a single pass through the system. Figure 9.1 illustrates this process.

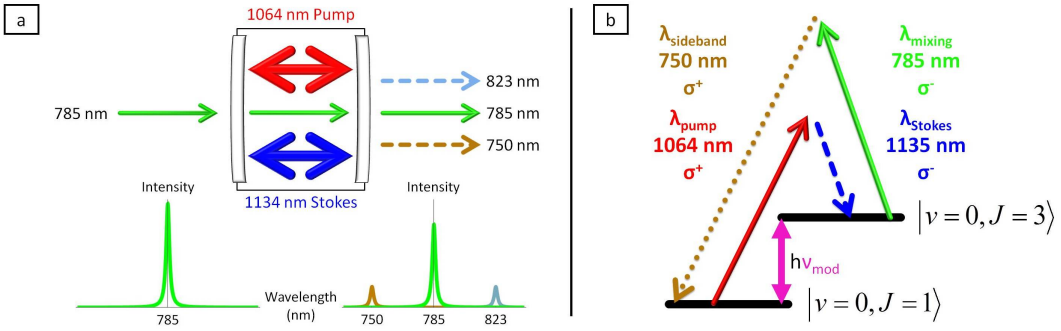

Figure 9.1 *Mixing Experiment Overview* (a) We drive hydrogen molecules to a coherent rotational state using intense pump and Stokes beams inside a high-finesse cavity. A third laser beam at a wavelength of 785 nm passes through the system and is modulated by the coherently rotating molecules through four-wave mixing. This generates sidebands at 823 nm and 750 nm, 17.6 THz from the mixing laser frequency. At the bottom of the figure, plots of intensity as a function of wavelength display the spectral components at the input and the output of the cavity, highlighting the effects of modulation. (b) This figure shows the relevant energy diagram for the process described in (a). It is very similar to the four-wave mixing process shown in Figure 7.2, but it is an independent mixing beam (λ_{mixing}), rather than the pump beam, that mixes with the coherence generated by the pump (λ_{pump}) and Stokes (λ_{Stokes}) beams to produce a sideband ($\lambda_{sideband}$). ν_{mod} is the modulation frequency, which is 17.6 THz. The σ^- polarization of the mixing beam preferentially produces the frequency up-shifted sideband at a wavelength of 750 nm. Not shown is the opposite case, in which a σ^+ polarization preferentially generates a frequency down-shifted 823 nm beam.

The experimental arrangement is very similar to those described in Chapters 7 and 8. As mentioned, the seed laser is at a wavelength of 1064 nm, and it is amplified by a ytterbium fiber

amplifier. The Pound-Drever-Hall locking electronics are the same as those described in Figure 5.7. The cavity used is, with some minor modifications, the 75-cm-long cavity described in Appendix E. The cavity is *not* cooled with liquid nitrogen for this experiment. The Raman transition used is the $|v = 0, J = 1\rangle$ to $|v = 0, J = 3\rangle$ rotational transition in molecular hydrogen. Note that we choose hydrogen over deuterium for this experiment. There are two main reasons for this, both of which are related to the fact that hydrogen has a larger energy spacing between rotational levels, as shown by the tables in Appendix F. This larger spacing results in molecules that are more concentrated in fewer lower rotational energy levels. Thus, we have a larger population in a single rotational state, the $|v = 0, J = 1\rangle$ state in hydrogen, than we would with any single state in deuterium. (See Figure 6.8.) This larger spacing also means that the modulation frequency of our modulator is larger.

To increase the efficiency of the desired rotational Raman scattering, we circularly polarize the incident pump beam. When the pump laser is locked to the cavity, we observe CW Raman lasing of the Stokes beam with opposite circular polarization, as depicted in Figure 9.1 (b). (See the discussion around Figure 10.1 for more explanation of the connection between polarization and sideband generation.) Figure 9.2 displays the transmitted pump and Stokes powers through the cavity as functions of the incident pump power. For these data, the hydrogen gas pressure in the cavity is 0.33 atm. At the highest incident power, we observe 2 mW of pump and 39 mW of Stokes power transmitted through the output mirror.

The solid lines in Figure 9.2 are fits to the data based on the Raman laser model developed by Carlsten and colleagues [47]. The lines are fit to the data using several adjustable parameters. The fit shown uses $R_p = 0.9998$ and $R_S = 0.9992$ for the reflectivities of the mirrors at the pump and at the Stokes wavelengths, and $T_p = 80$ parts per million (ppm) and $T_S = 65$ ppm for the mirror transmittance at the two wavelengths. The plane-wave gain coefficient, which helps to determine the Raman gain for the Stokes beam, is $\alpha = 4.4 \times 10^{-9}$ cm/W. (The plane-wave gain coefficient is related to the cross-sections of the stimulated Raman scattering and the dephasing of the Raman medium. See the appendix of the article by Tsunemi and colleagues for more details on the gain

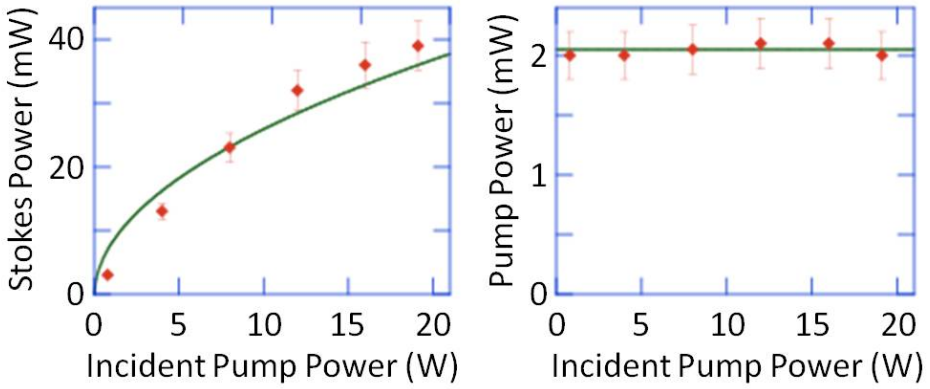

Figure 9.2 *Pump and Stokes Output* These plots display the pump and the Stokes output powers as functions of incident pump power. The Raman lasing medium is molecular hydrogen with a gas pressure of around $\frac{1}{3}$ atm at room temperature. The Raman scattering occurs on the $|v = 0, J = 1\rangle$ to $|v = 0, J = 3\rangle$ rotational transition. The roughly constant pump output and the increasing Stokes output are characteristic of the Raman lasing process used to generate the Stokes beam. (See Figures 7.1 and 7.3 for other examples.) The points are experimental data and the solid lines are theoretical best fit curves based on the Raman lasing model developed by the Carlsten group. (See main text.) Note that the vertical scales in the two plots are different.

coefficient [87].) These parameters do not yield an exact fit to the data; more precise data and further calculations are needed to gain more confidence in the accuracy of the parameter values.

The data above are taken with a gas pressure of 0.33 atm, but we investigate Raman lasing at pressures ranging from 0.05 to 1.5 atm. We observe that an increase in pressure is accompanied by a reduction in the transmitted pump and Stokes powers. For example, at a pressure of 0.08 atm, the highest transmitted pump and Stokes powers are 11 mW and 69 mW, respectively, whereas at 1.5 atm, these quantities are 1.2 mW and 18 mW. This drop in Stokes power is qualitatively consistent with the model, as the output Stokes power is inversely proportional to the square root of the Raman gain constant, which increases with increasing pressure [47, 87]. The decreasing pump power may be due to a decrease in the effectiveness of the locking circuit, which is disrupted more at higher gas pressures by the temporal dynamics of the Raman lasing process.

We next discuss modulating the mixing beam with the molecular coherence that is established by the intense intracavity pump and Stokes fields. As shown in Figure 9.3, the source of the mixing beam is a 785 nm ECDL whose output is amplified by a semiconductor tapered amplifier.

Around 100 mW of this mixing beam is incident on the cavity. (The mixing beam intensity is significantly lower than the 10s of kW/cm^2 circulating intensities of the driving lasers. Thus, the mixing beam does not noticeably interfere with the established molecular coherence. Although it is not currently an issue, in principle the affect of the mixing beam on the coherence does limit the maximum mixing beam intensity.) Although the modulator can modulate an arbitrarily weak beam, the mixing beam is amplified to increase the optical power of the generated sidebands to more easily detectable levels. The mixing beam is focused to a Gaussian waist of 420 μm at the center of the cavity. The cavity mode waists of the pump and the Stokes beams are 810 μm and 836 μm, respectively. The overlap and relative size of these beam waists is important. As discussed in Section 2.1, the Raman coherence is proportional to the product of the pump and the Stokes electric fields. The strongest fields, and thus the highest coherence, is located near the optical axis at the center of the Gaussian beams. To achieve maximum efficiency, we want the mixing beam to travel through this region of maximum coherence.

We detect the modulation by coupling the transmitted 785 nm mixing beam to an optical spectrum analyzer. (Optical notch (band-stop) filters are used to decrease the amount of 785 nm light, which makes the much weaker sidebands easier to see.) As shown in Figure 9.1, if the mixing beam has the same (opposite) circular polarization as the pump, the frequency down-shifted (up-shifted) sideband is produced. This is due to angular momentum selection rules, as discussed in Section 7.1 and near Figure 10.1. In our experiment, because the mixing beam is combined with the pump beam using polarization-selective optics, we do not have independent control of the mixing beam polarization. The mixing beam is elliptically polarized due to the imperfect affect that a quarter-wave plate meant for 1064 nm light has on the 785 nm beam. This elliptically polarized mixing beam produces both up-shifted and down-shifted sidebands at wavelengths of 750 nm and 823 nm. The power ratio of these sidebands is $P_{750}/P_{823} \approx 3$.

Figure 9.4 shows the fraction of the mixing power that is converted into the frequency up-shifted sideband as a function of the incident pump power. The hydrogen pressure for this experiment is 0.33 atm. The highest conversion efficiency that we achieve is 2.3×10^{-6}. We define conversion efficiency as the ratio of the transmitted sideband power (P_{out}^{750}) to the incident mixing

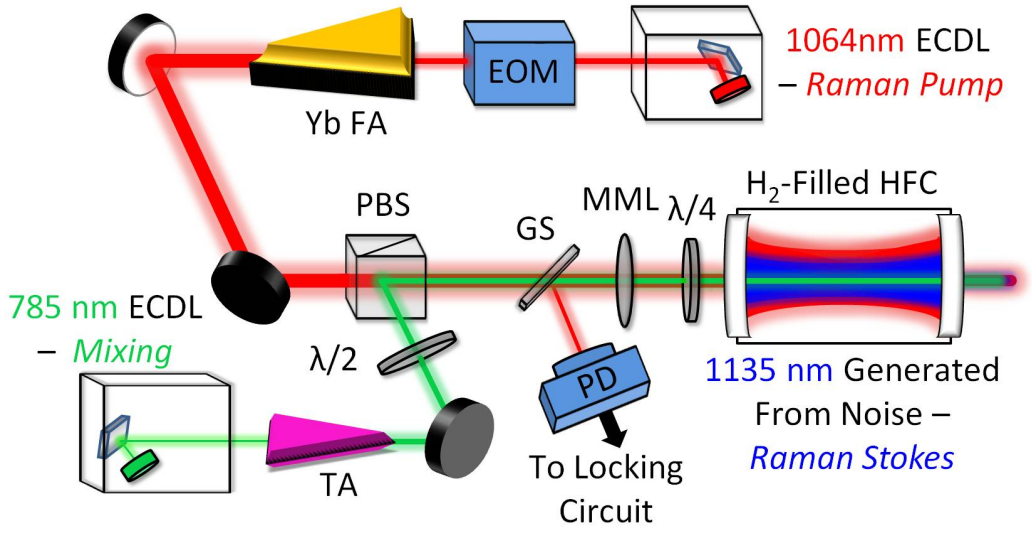

Figure 9.3 *Mixing Experiment Schematic* This figure shows the experimental schematic for the mixing experiment. Much of it is the same as the basic schematic of Figure 4.1. We seed our experiment with a custom-built external cavity diode laser (**ECDL**). The continuous-wave (CW) beam is modulated by an electro-optic modulator (**EOM**) so that it can be used in a Pound-Drever-Hall locking scheme. The ECDL output is on the order of 10 mW, and this seeds a ytterbium fiber amplifier (**Yb FA**). The output of the Yb FA is up to 30 W of CW power in a single spatial mode and a single frequency mode. The Yb FA output is circularly polarized by a quarter-wave plate (λ**/4**) and coupled to a high-finesse cavity (**HFC**) using a mode-matching lens (**MML**). Raman scattering in the HFC generates a Raman Stokes beam, which also resonates in the HFC. A glass slide (**GS**) picks off part of the reflection from the cavity and sends the signal to the locking circuit through a photodiode (**PD**). An independent mixing beam with a wavelength of 785 nm is generated by a separate ECDL and amplified by a semiconductor tapered amplifier (**TA**). The amplified beam is overlapped with the pump beam using a half-wave plate (λ**/2**) and a polarizing beam splitter (**PBS**). The mixing beam travels through the cavity and mixes with the coherence from the pump and Stokes beams to generate frequency sidebands through four-wave mixing. The mixing beam is not resonant with the cavity so the modulation occurs in a single pass through the system.

beam power (P_{in}^{785}). As mentioned above, due to the ellipticity of the polarization of the mixing beam, roughly three times as much power is converted to the frequency up-shifted 750 nm sideband as is to the frequency down-shifted 823 nm sideband. The fraction of total power converted into both 750 nm and 823 nm light is about 3×10^{-6}. We observe efficiencies within a factor of two of those in Figure 9.4 for gas pressures between 0.05 and 1.5 atm. At a pressure of 0.08 atm, the modulation efficiency is only 30% lower than shown in the figure. Although the conversion

efficiency is low, this is the first experiment in which molecules have been driven to a sufficiently coherent state by CW lasers that they could be used for CW modulation of an independent laser. Furthermore, as discussed in Section 7.2, the modulation process is coherent, and as a result, the mixing beam and the two sidebands have a well-defined, though initially unknown, relative phase. This phase can be detected and manipulated using a phase mask, and these three beams can be used to synthesize simple optical waveforms.

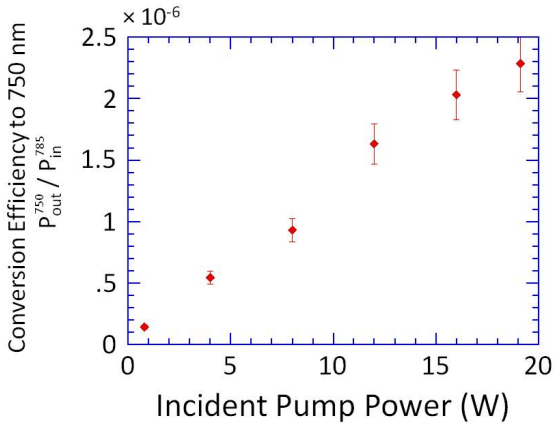

Figure 9.4 *Mixing Experiment Conversion Efficiency* This figure shows the conversion efficiency of the 785 nm mixing beam to the 750 nm sideband as a function of the input pump beam power. We define conversion efficiency to 750 nm light as the ratio of the transmitted sideband power (P_{out}^{750}) to the incident mixing beam power (P_{in}^{785}). The conversion to the frequency down-shifted 823 nm sideband, which occurs simultaneously, is about $\frac{1}{3}$ as efficient. This is due to the elliptical polarization of the mixing beam. The hydrogen pressure in the cavity is 0.33 atm for this experiment.

One of the key features of our molecular modulator is that it can be used to modulate any frequency within the optical region of the spectrum. The large transparency window of the hydrogen molecules (which is related to the large single-photon detuning discussed in Subsection 1.2.3) and the low operating gas pressure (which leads to low dispersion) make this possible. H_2 molecules are not infrared-active, and the first electronic resonance occurs in the Lyman band at a wavelength of 111 nm, and thus they are transparent to much of the optical spectrum. Figure 9.5 shows the predicted conversion efficiency of our modulator to the frequency up-shifted sideband. The plot shows the calculated efficiency over a wavelength range of 120 nm to 10 μm at gas pressures of

0.33 atm (solid red line) and 0.08 atm (dashed green line). We assume optimal polarization of the mixing beam for these calculations.

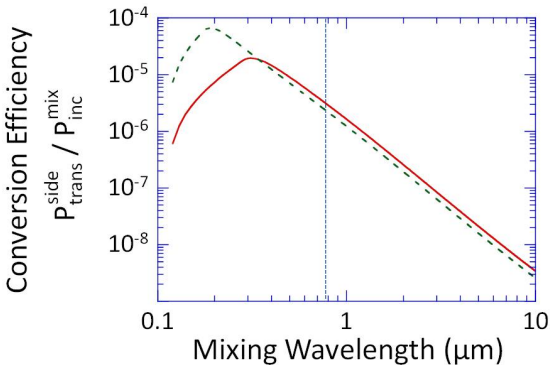

Figure 9.5 *Mixing Conversion Efficiency as a Function of Wavelength* This figure shows the predicted conversion efficiency of our molecular modulator as a function of the wavelength of the mixing beam. The conversion efficiency is defined as the ratio of the transmitted power of the frequency up-shifted sideband (P^{side}_{trans}) over the incident power of the mixing beam (P^{mix}_{inc}). The solid red line is the efficiency with a hydrogen pressure of 0.33 atm, and the dotted green line is the efficiency with a hydrogen pressure of 0.08 atm. The conversion efficiency increases with decreasing mixing wavelength for most of the optical region of the spectrum. At short wavelengths, however, phase-mismatch between the sideband and the mixing beam starts to play a role, and that creates a sharp drop-off in the efficiency. The vertical line marks the mixing beam wavelength used in our experiment.

To calculate the efficiency, we use the matrix elements and energy levels of the ro-vibrational levels in the Lyman and Werner bands [88] and calculate the dispersion and Raman coupling of H_2 at different wavelengths. We then use these results to numerically solve propagation equations that describe the generation of the sideband from the mixing beam. (See Equation 2.33 for the propagation equation and Appendix C for more details.) Diffractive effects and consideration of the mode overlap of the mixing beam with the pump and the Stokes beams are also taken into account in the calculations.

Generally, as the wavelength of the carrier beam becomes shorter, one expects an increase in modulation efficiency. There are several reasons for this. With a decrease in wavelength, the frequencies get closer to electronic resonances (that is, the single-photon detuning decreases), and thus the Raman interaction is stronger. A decrease in wavelength also means less divergence of the

mixing beam, and hence better overlap with the pump and the Stokes cavity modes in the cavity. As mentioned above, better overlap means stronger interaction. Finally, as seen in Equation 2.33, the propagation equation scales linearly with frequency, so shorter wavelength means higher frequency and thus stronger Raman interaction. The general trend of increasing efficiency with decreasing wavelength is evident in Figure 9.5.

The figure also illustrates that this trend abruptly ends a certain wavelength, after which the efficiency drops sharply. The drop is due to the sideband-mixing beam phase-mismatch becoming a significant factor. Dispersion, and thus phase-mismatch, is less of an issue at lower pressures, and so the phase-mismatch drop-off with 0.08 atm of H_2 happens at a shorter wavelength than with 0.33 atm of H_2 .

It is important to note that Figure 9.5 represents the maximum usable bandwidth of our modulator. It does *not* take into account the transmittance of the cavity mirrors nor that of the vacuum chamber windows. In our experiment, the mirrors and windows are made of a fused silica substrate that transmits well in the region 170 nm - 3 μm. Other wavelengths experience significant absorption traveling through the mirrors and the windows. If our modulator were to be used for wavelengths outside of this spectral region, we would need a different substrate for the optics or different geometries for overlapping the mixing beam with the cavity modes.

In these calculations, we also calculate the coherence, ρ_{ab}. (To calculate the coherence, we numerically solve the Schrödinger Equation of the Raman system (Equation A.123) to find c_a and c_b. The product $c_a c_b^*$ is the coherence.) As discussed around Equation 2.45, our modulator would be maximally efficient with a coherence value of $|\rho_{ab}^{max}| = 0.5$. Our current experimental coherence value is $|\rho_{ab}| \approx 6.7 \times 10^{-5}$. Modulation efficiency is proportional to $|\rho_{ab}|^2$. Thus, this low coherence explains the low modulation efficiency in this initial mixing experiment. Although the efficiency is low, this experiment has demonstrated the feasibility of CW molecular modulation of an independent mixing beam. See Section 11.1 for further discussion of coherence and steps we are currently taking to increase the efficiency of our modulator.

Chapter 10

A Tunable, Coherent Terahertz Source - Simulations

In this chapter we use computer simulations to explore one possible application of the molecular modulator described in Chapter 9: a tunable source of coherent terahertz (THz) radiation [42]. The proposed THz source is based on the frequency down-shifting of an infrared laser using highly-coherent molecular vibrations. The source could operate in either the pulsed or the CW regime, and it would be tunable over much of the THz region of the spectrum (1 - 10 THz). In the pulsed regime, we predict average output powers of order 10 mW and peak powers approaching 1 MW. In the CW regime, we predict powers exceeding 100 μW with spectral linewidths on the hertz level.

The THz region of the electromagnetic spectrum is sometimes referred to as the *terahertz gap*, as it has proven difficult to develop light sources at these frequencies. Despite the difficulties, interest in THz radiation sources has continued to grow over the last two decades. There is an extensive list of potential applications of THz sources in a variety of fields including communications, bio-technology, quality control, and remote sensing and imaging [89]. Although significant advances have been made in recent years [90], including CW THz generation [91, 92], obtaining a high-power and widely-tunable coherent source of THz radiation remains a challenging task.

In this chapter, we propose a novel method of producing widely tunable THz radiation: molecular modulation. Four-wave mixing in a coherently prepared molecular gas can be used to frequency down-shift an infrared beam to the THz range. As shown in Figure 10.1, the THz generation process is very similar to the four-wave mixing process of Figure 7.2. Intense pump (E_p) and Stokes (E_S) beams drive a Raman transition and build up coherence between molecular ro-vibrational states $|a\rangle$ and $|b\rangle$. Then an independent mixing beam (E_m) mixes with the coherence to generate

a frequency down-shifted sideband (E_{THz}). The key is that the mixing beam is chosen to be at a frequency very close to the Raman transition frequency. (Recall that single photon excitations between the ro-vibrational levels are dipole forbidden.) This means that the generated sideband, E_{THz}, has a very low frequency and a long wavelength. With an appropriately chosen mixing beam frequency, this frequency can be in the THz range. Furthermore, the frequency of the mixing beam can be tuned to tune the frequency of the sideband. Thus, as discussed in more detail below, we can generate a wide range of THz frequencies. The predicted combination of peak output power and tuning range of this proposed THz source exceeds the capabilities of existing devices [89, 90].

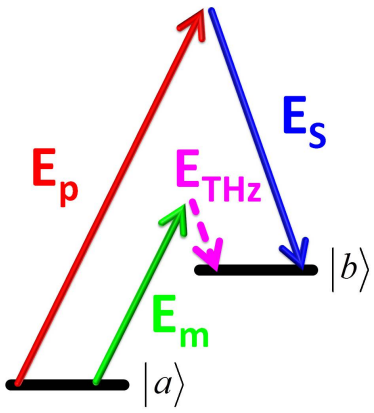

Figure 10.1 *Terahertz Generation through Four-Wave Mixing* This figure illustrates a four-wave mixing process that could be used to produce tunable THz radiation using molecular modulation. Intense pump (E_p) and Stokes (E_S) beams drive a Raman transition and build up coherence between molecular ro-vibrational states $|a\rangle$ and $|b\rangle$. Then an independent mixing beam (E_m) mixes with the coherence to generate a frequency down-shifted sideband (E_{THz}). The key is that E_m is chosen to be at a frequency very close to the Raman transition frequency. With an appropriate choice of mixing frequency, the generated sideband, E_{THz}, can have a frequency in the THz range. This THz frequency is tuned across the THz region by tuning the mixing beam frequency.

As mentioned at the end of Section 7.1 and in the discussion of Figure 9.1, polarization can be used to preferentially generate certain sidebands [71]. When the driving beams are oppositely circularly polarized, the generation of higher-order Stokes and anti-Stokes beams is suppressed due to angular momentum selection rules. In this case, by using a mixing beam with the same (or

opposite) circular polarization as the pump beam, one can preferentially generate the frequency down-shifted (or up-shifted) sideband. Thus, by using an infrared mixing beam with the same polarization as the pump, we can preferentially generate the frequency down-shifted sideband in the THz regime. In this way the molecular medium is utilized as an efficient frequency converter [71]. As mentioned in Chapter 9, the mixing process is a linear function of the mixing beam intensity, and thus the frequency converter works with an arbitrarily weak mixing beam.

We will examine two different schemes for generating THz radiation through molecular modulation, both of which use realistic experimental parameters. The two schemes are shown in Figure 10.2. In the first scheme, shown in Figure 10.2 (a), we propose using Q-switched pulsed pump and Stokes lasers to drive molecular coherence in a deuterium-gas-filled cell. An independent pulsed mixing beam then passes through the cell and is frequency down-shifted by this coherence, and pulsed THz radiation is produced. Figure 10.2 (b) shows the second scheme, which is similar to our experiment described in Chapter 9. CW pump and Stokes beams first establish a CW molecular coherence inside a high-finesse cavity. Then a CW mixing beam that is not necessarily resonant with the cavity (that is, the mirrors do not have a high reflectivity at the mixing laser wavelength) is frequency down-shifted in a single pass to produce CW THz radiation.

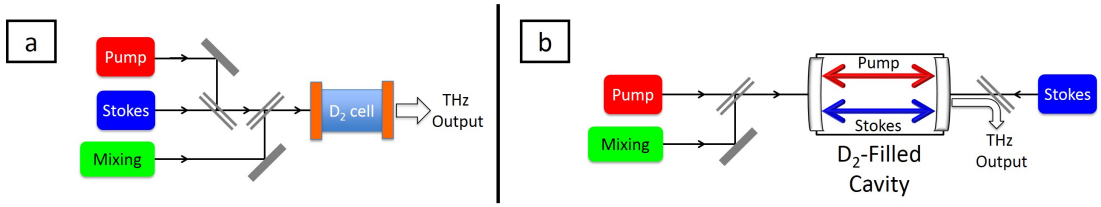

Figure 10.2 *Terahertz Generation Schematics* This figure displays the two schemes we propose for generating coherent THz radiation. In both schematics, the solid gray rectangles are mirrors, and the pairs of gray lines are partially transmissive mirrors used to combine beams. (a) The first scheme is a pulsed THz source. Q-switched pump and Stokes lasers are loosely focused on a Raman cell to drive molecular coherence in the deuterium inside. An independent Q-switched mixing laser then passes through the cell and is modulated by the coherence, producing coherent THz pulses. (b) This second scheme is a CW THz source. CW pump and Stokes beams are coupled to a deuterium-filled high-finesse cavity. The intense intracavity fields of these resonant beams drive the molecules to a coherent state. A non-resonant CW mixing beam then passes through the cavity and is modulated in a single pass, generating coherent CW THz radiation.

We proceed with a more detailed description of our proposed scheme. Our calculations are based on the work of Harris and colleagues [21], as described in Chapter 2 and Appendices A - D.

Due to the long wavelength of THz radiation, diffractive effects are important, so we consider the modulation process in all three spatial dimensions. (Note that this differs from Appendix C, in which we ignored the diffractive effects. In Appendix C, we dropped terms in the transverse directions x and y.) We assume near-monochromatic excitation and work with the slowly-varying envelope $E_{THz}\left(x,y,z\right)$ such that the total THz field $\hat{E}_{THz}$ is

$$\hat{E}_{THz}\left(x,y,z,t\right)=\mathcal{R}e\left\{E_{THz}\left(x,y,z\right)e^{j\left(\omega_{THz}t-k_{THz}z\right)}\right\}, \tag{10.1}$$

where ω_{THz} is the angular frequency and $k_{THz}=\frac{\omega_{THz}}{c}$ is the wave number. x, y, and z are the spatial dimensions, and t is time. j is the imaginary unit, and $\mathcal{R}e\{...\}$ is the real part of the quantity in the brackets.

The molecular coherence is established with the intense pump and Stokes laser beams, E_p and E_S. We take the mixing beam, E_m, to be sufficiently weak so that it does not interfere with the coherence preparation. (This is true as long as the mixing beam intensity is much lower than the driving beam intensities.) Furthermore, due to low conversion efficiency, the mixing beam intensity is nearly constant. Thus, we ignore any depletion of the mixing laser as a result of the generation of the THz sideband. For this THz sideband generated through four-wave mixing of the coherence and the mixing beam, the slowly-varying-envelope propagation equation is

$$\frac{\partial E_{THz}}{\partial z}+\frac{j}{2k_{THz}}\left(\frac{\partial^2 E_{THz}}{\partial x^2}+\frac{\partial^2 E_{THz}}{\partial y^2}\right)=-j\eta\hbar\omega_{THz}N\left(a\rho_{aa}E_{THz}+d\rho_{bb}E_{THz}+b\rho_{ab}E_m\right), \tag{10.2}$$

where $\eta=\sqrt{\frac{\mu_0}{\epsilon_0}}$, N is the molecular number density, and $\hbar$ is the reduced Planck's constant [93]. The populations of the ro-vibrational Raman states $|a\rangle$ and $|b\rangle$ are given by ρ_{aa} and ρ_{bb}, the diagonal density matrix elements. ρ_{ab} is the molecular coherence, the off-diagonal matrix element of the density matrix. (See Appendix D for more details on the matrix elements.) The coupling and dispersion constants, a, d, and b, determine the refractive index of the gas and the Raman polarizability. As shown in Chapter 2, these constants are calculated by summing over the

many ro-vibrational levels in the excited electronic configuration using the corresponding matrix elements and detunings. (See Equations 2.16 - 2.18.)

As discussed in Section 2.2, we assume that the molecular system is prepared adiabatically to a state that is smoothly connected to the unperturbed ground state. Adiabatic preparation can be achieved with a small two-photon detuning from the Raman resonance. (See Equation 2.3 for a definition of the two-photon detuning.) The driving two-photon Rabi frequency for the Raman excitation is $B = b_p E_p E_S^*$, where b_p is the Raman coupling constant at the pump wavelength. (See Equations 2.13 and 2.18.) The quantities $A/2$ and $D/2$ are the Stark shifts of the Raman levels $|a\rangle$ and $|b\rangle$ due to the intense pump and Stokes beams. (See Equations 2.12 and 2.15.) Recall that θ and ϕ are defined by the following relationships (Equations 2.28 and 2.29):

$$\theta = \tan^{-1}\left(\frac{2\,|B|}{A - D + 2\Delta\omega}\right), \tag{10.3}$$

and

$$B = |B|^{j\phi}\,. \tag{10.4}$$

With these definitions, the adiabatic solution for the density matrix elements of the Raman transition are given as in Equations 2.38 - 2.40:

$$\rho_{aa} = \cos^2\left(\frac{\theta}{2}\right), \tag{10.5}$$

$$\rho_{bb} = \sin^2\left(\frac{\theta}{2}\right), \tag{10.6}$$

and

$$\rho_{ab} = \frac{1}{2}\sin\left(\theta\right)e^{j\phi}. \tag{10.7}$$

We perform our numerical simulations using MathWorks Matlab. We calculate the conversion efficiency from the mixing beam to the generated THz wave by numerically integrating Equation 10.2 together with the adiabatic solution of Equations 10.5 - 10.7 on a three dimensional x-y-z grid. We consider scattering off of the $|v = 0, J = 0\rangle$ to $|v = 1, J = 2\rangle$ ro-vibrational transition in molecular deuterium at a transition frequency of 94.8 THz. (See Table F.2. Also note that this transition is different than those previously discussed. We now consider a change in vibrational

state *and* rotational state. The change in rotational state is due to the circular polarization of the driving lasers.) We assume the molecules are cooled to the rotational ground state. This could be achieved using a liquid nitrogen bath, as in our experiments. We take the pump and the Stokes laser beams to be at wavelengths of 1042 nm and 1554 nm. If the mixing beam wavelength is tuned over the range of 3128 nm to 2860 nm, the 94.8 THz modulation frequency means that the generated THz radiation is tuned over the frequency range of 1 - 10 THz, covering the terahertz gap.

We analyze THz generation with realistic experimental conditions for the two schemes described in Figure 10.2. In both the pulsed and the CW schemes, we take the pump, the Stokes, and the mixing beams to have Gaussian spatial profiles with beam waists of 1 mm. We take into account the refractive index and the dispersion of the molecular gas for all the beams. In doing so, we include the effects of phase-mismatch as the THz wave is generated along the cell. In both cases we take the molecular interaction region (the cell for the pulsed case, and the cavity for the CW case) to be 50 cm long, and we assume a deuterium number density of $N = 2.69 \times 10^{19}$/cm^3 (equivalent to 1 amagat). The conversion efficiency is maximized when the molecules are in a maximally coherent state, $|\rho_{ab}^{max}| = 0.5$.

Figure 10.3 (a) shows the conversion efficiency from the mixing beam to the THz beam for the pulsed source. For this calculation, we take both the pump and the Stokes beams to have a pulse energy of 1 J with a 10 ns pulse duration. The peak power is 100 MW and the peak intensity at the focus is 6.36 GW/cm^2 for both laser beams. We take the two-photon detuning to be $\Delta\omega = 2\pi \times 0.5$ GHz. For these parameters, the molecular coherence achieved at the focus is $|\rho_{ab}| = 0.3$. The conversion efficiency from the mixing beam to the generated beam varies from 3×10^{-5} to 2×10^{-2} as the generated frequency is tuned over the terahertz gap from 1 THz to 10 THz. As discussed with Figure 9.5, we observe a trend of increasing efficiency for increasing frequency (decreasing wavelength). If we assume a mixing beam with the modest parameters of 100 mJ per pulse at a 10 Hz repetition rate, these efficiencies would produce an average power of 30 μW with a peak power of 0.3 kW at 1 THz. At 10 THz, this would yield 20 mW of average power with a peak power of 0.2 MW.

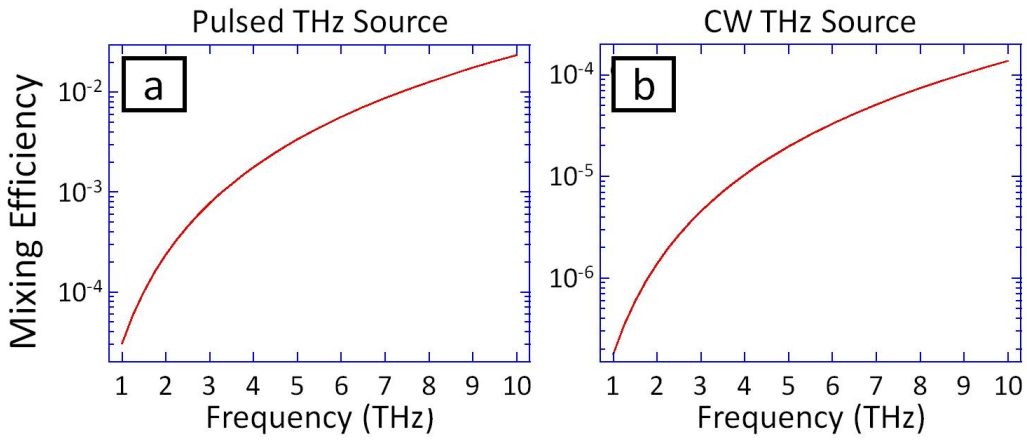

Figure 10.3 *Terahertz Source: Calculated Mixing Efficiency* This figure shows the simulated conversion efficiency from the mixing beam to the generated THz beam for a pulsed (a) and a CW (b) THz source based on molecular modulation. The calculations are based on state-of-the-art, yet experimentally achievable, parameters. Details about the parameters can be found in the main text. Note that the vertical scales on the two plots are different.

Figure 10.3 (b) shows the conversion efficiency from the mixing beam to the THz beam for the CW source. For this calculation, we take our pump and Stokes beams to both have powers of 200 W. (Such single-mode CW lasers are commercially available. They are based on ytterbium- and erbium-doped fiber amplifiers similar to the ones in our experiments.) We assume the cavity mirrors have reflectivities of 99.995% at both of these wavelengths. (This is similar to the reflectivities of our mirrors.) With these parameters, when the lasers are locked to the cavity, the intracavity circulating power for each laser is 4 MW and the circulating intensity at the focus is 255 MW/cm^2. (Meng and coworkers have shown that high-quality dielectric coatings can handle over 100 MW/cm^2 of optical power without sustaining damage [94].) For this CW case, we take the two-photon detuning to be $\Delta\omega = 2\pi \times 0.25$ GHz. The intracavity intensities drive a molecular coherence that reaches $|\rho_{ab}| = 0.024$ at the beam waist. This yields a conversion efficiency that varies from 1.8×10^{-7} to 1.4×10^{-4} as the output is tuned from 1 THz to 10 THz. This efficiency means that a 1 W mixing beam would produce a CW output power of 0.2 μW to 0.1 mW of THz radiation as the output frequency is tuned over this frequency range.

In this CW case, it is important to note that the frequency linewidth of the generated THz wave is determined by the linewidth of the interacting lasers, and not by the linewidth of the Raman transition. Because the pump and Stokes beams are locked to the longitudinal modes of a high-finesse cavity, their linewidths can be made very narrow. This means that the linewidth of the molecular oscillations can also be made very narrow. As a result, if a frequency stabilized mixing laser beam were used, it would be possible in principle to generate THz radiation with 1-Hz-level linewidths.

We conclude this chapter with Figure 10.4, which depicts the THz beam generated by one of the molecular modulation schemes described above. Figure 10.4 (a) is a two-dimensional false-color intensity plot for a generated 1 THz beam from the THz source. Figure 10.4 (b) is a cross-section of the profile taken at the output of the modulator.

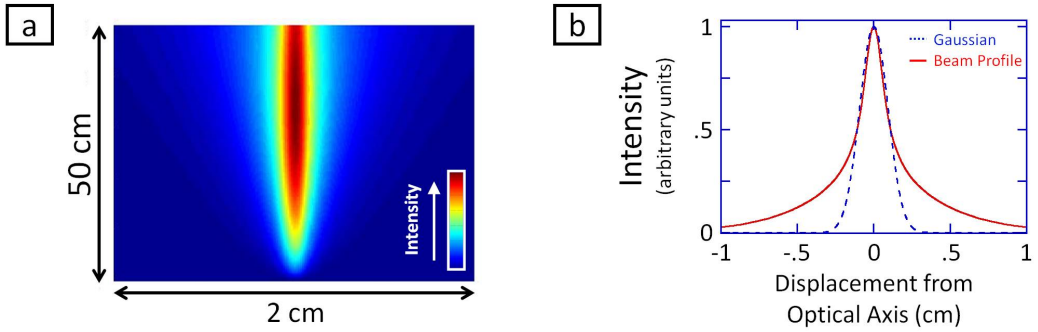

Figure 10.4 *Terahertz Beam Profile* This figure displays a simulated 1 THz beam generated by one of the molecular modulation schemes described above. (a) This is a two-dimensional, false-color intensity plot for the generated THz beam inside of the modulator. Note that the relative horizontal scale has been greatly expanded to show details. The propagation direction is upwards, and the output of the modulator is at the top of the image. (b) This is an intensity profile (solid red line) of one of the transverse directions of the THz beam at the output of the modulator. Due to the significant divergence of the THz wave, the output beam is not exactly Gaussian. For comparison, a Gaussian intensity profile with the same width is also plotted (dashed blue line).

Chapter 11

Current Work and Future Directions

In this thesis, we have described the development of a CW molecular modulator based on stimulated Raman scattering in a high-finesse cavity. We have demonstrated that the modulator can be used to generate a broad, coherent spectrum that spans nearly two octaves of optical bandwidth. We have shown that the spectral components have Gaussian spatial profiles and narrow frequency linewidths. Furthermore, we have verified that our modulator is capable of modulating an independent mixing beam in a single pass through the system. We have demonstrated modulation frequencies up to 10s of THz. We have also discussed possible applications of this molecular modulation technology, including the potential for generating coherent THz radiation.

In this final chapter, we examine two on-going research projects and then discuss one plan for the near future. We first discuss our efforts to improve the efficiency of our modulator by using an independent Stokes beam to drive the molecular coherence. We present motivations for this change and the experimental schematic, and we discuss some preliminary results and current challenges. Next we briefly discuss recent efforts to expand the independent mixing beam experiment of Chapter 9 to vibrational transitions. Initial results indicate that we can modulate a mixing beam by 89.6 THz in a single pass through our optical system. We close this chapter with a discussion of an exciting upcoming stage of our experiment: using our modulator to broaden the already broad spectrum of a titanium-sapphire laser.

11.1 Independent Stokes Beam

All of our experiments described in this thesis are based on building up a strong molecular coherence. We generate this coherence by driving two-photon transitions using intense intracavity pump and Stokes beams. The coherence is approximately proportional to the product of the pump and the Stokes fields (See Equations 2.13 and 2.41.), so in order to maximize coherence, it is desirable to have high intensities for both the pump and the Stokes beams. The limitations on our intracavity pump and Stokes intensities are one of the main obstacles to improving our coherence and thus our modulation capabilities.

Our cavity has a high finesse for both the pump and the Stokes wavelengths, and both lasers are simultaneously resonant with the cavity. However, our intracavity intensities are limited by the process by which we are generating the Stokes beam. As discussed in Section 7.1 and elsewhere, we are producing the Stokes beam through Raman lasing in the cavity. Because the energy for the Stokes beam is coming from the pump beam, this severely limits our pump intensities. This is evident in how the transmitted pump power plateaus once the Stokes generation begins. After that point, any additional incident pump power goes into generating more Stokes power, rather than increasing the transmitted pump power. See Figure 7.1 for an example of this behavior. (Recall that the transmitted power is directly related to the circulating power through the transmittance of the cavity mirrors.) We have shown that Raman lasing is an effective method of producing a Stokes beam. However, in order to maximize coherence, we would like to be able to have strong circulating Stokes intensities without sacrificing any pump intensity. Our solution to this issue is to work with an independent Stokes beam, as shown in Figure 11.1. The mixing beam in the figure is shown at a wavelength of 785 nm, but as discussed in Chapter 9, this arrangement can be used to modulate a wide range of mixing beams.

Because coherence is proportional to the product of the pump and the Stokes fields, a scheme that does not rely on Raman lasing can significantly improve coherence and thus modulation efficiency. By tuning the pump frequency and adjusting the cavity length, we can find modes in which the pump resonates with the cavity, but little to no Raman lasing occurs. In this case, the

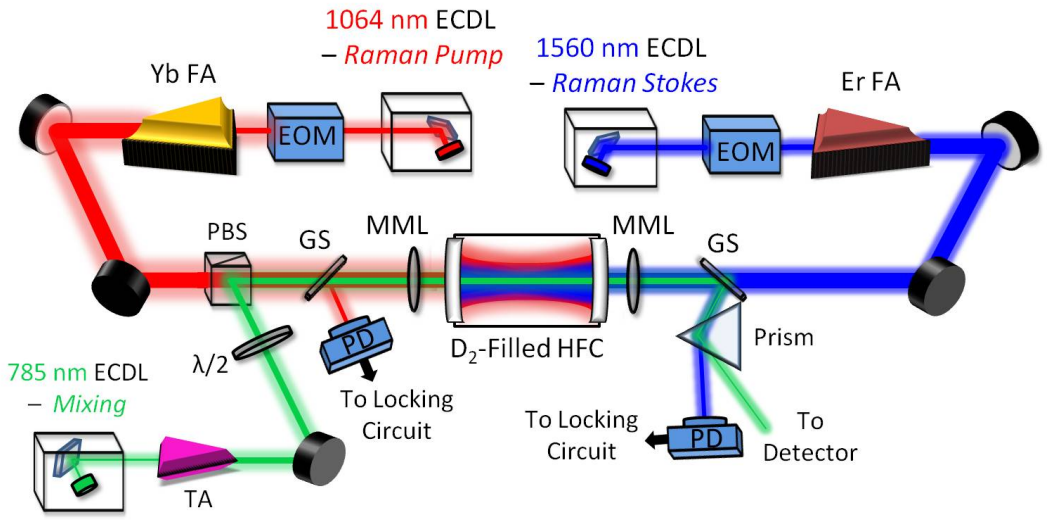

Figure 11.1 *Independent Stokes Beam: Experimental Schematic* This figure illustrates the experimental arrangement for our molecular modulation experiments with independent pump and Stokes beams. It is very similar to the mixing beam schematic seen in Figure 9.3, but now along with the pump laser, amplifier, and optics, there is an analogous arrangement for the independent Stokes laser. Both lasers come from extended cavity diode lasers (**ECDL**s), and they are modulated for frequency locking purposes by electro-optic modulators (**EOM**s). They are then amplified by fiber amplifiers (**FA**s), ytterbium-doped for the 1064 nm pump laser, and erbium-doped for the 1560 nm Stokes laser. The two amplified beams are simultaneously coupled to the high-finesse cavity (**HFC**) by mode-matching lenses (**MML**s). The glass slides (**GS**s) pick off part of the beams, and the photodiodes (**PD**s) monitor the reflected signals from the cavity for locking purposes. In this case, the slow feedback of each locking circuit feeds back to the piezoelectric transducer (PZT) in the associated ECDL, rather than that in the HFC. We found that the two locks interfered with one another more when one was feeding back to the HFC mirror PZT and one was feeding back to the ECDL PZT. (See Section 5.2 for more details on the locking circuit.) Once the independent pump and Stokes beams establish coherence by driving molecular transitions in the deuterium in the cavity, the mixing ECDL produces a beam that is amplified by a tapered amplifier (**TA**) and then overlapped with the other beams using a half-wave plate (**λ/2**) and a polarizing beam splitter (**PBS**). The beam is modulated in a single pass through the HFC. The modulated mixing beam is picked off by the GS, spatially dispersed using a prism, and sent to an optical detector.

intracavity pump intensity continues to increase with increasing incident pump power. The Stokes beam is then produced independently as shown in Figure 11.1. The Stokes beam is produced in a similar manner to the pump beam, and it has similarly high intracavity intensities.

If we extrapolate the behavior of the pump power before the Raman threshold is reached, this gives us a rough approximation of how the pump would behave in the absence of Raman lasing. Figure 11.2 illustrates this point for the data from one of the plots of Figure 7.3. This rough estimate suggests that the intracavity pump intensities would be around 140 mW at 16 W of incident pump power. This is about 3.5 times higher than with Raman lasing depleting the pump. If we assume that our independent Stokes laser would have similar performance, this also increases our Stokes circulating intensity by a factor of around 1.75. (This is a conservative estimate, as we have found the 1560 nm light to have higher intracavity intensities than 1064 nm light for similar incident powers.) Intensity is the magnitude of the electric field squared, and coherence is proportional to the product of the electric fields. Thus, to find the improvement in coherence, we take the product of the square roots of these intensity improvement factors. This yields a coherence that is improved by a factor of $\sqrt{3.5} \times \sqrt{1.75} \approx 2.5$. The form of the propagation equation (Equation 2.33) suggests that the generated field is proportional to coherence. The generated intensity is then proportional to the coherence squared. This means that a factor of 2.5 factor of improvement in coherence yields a factor of $2.5^2 = 6.25$ factor of improvement in mixing efficiency. We note that the intracavity pump intensity continues to increase linearly with increasing incident pump power for the non-Raman-lasing case, and the pump intensity stays relatively constant for the Raman-lasing case. This means that the improvement in coherence would be even larger for higher incident pump values.

We have experimentally implemented the scheme illustrated in Figure 11.1, and we have some preliminary data, though we have not yet incorporated the mixing beam. Although it is challenging, we can simultaneously lock the 20 W pump and Stokes beams to the HFC. The quality of the lock, as is the case with all of our experiments, depends on the amount of gas in the cavity. The best simultaneous locks last on the order of 10 s before one of the lasers falls out of resonance. While this is definitely long enough to perform our current experiments, we would like to improve the performance of our simultaneous lock. We have begun some initial investigations of the time dynamics of the dual locks, but this has so far not yielded any conclusive information.

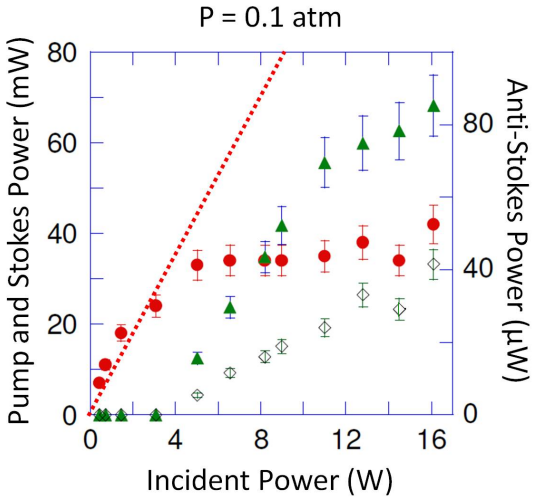

Figure 11.2 *Independent Stokes Beam Extrapolation Estimate* This figure displays the Raman lasing data of one of the plots of Figure 7.3. The red dotted line has been added as a rough extrapolation of the pump power data at incident powers lower than the Raman lasing threshold. This extrapolation provides a rough estimate of the behavior of the pump laser in the absence of Raman lasing. It suggests that there would be about 140 mW of pump light transmitted for 16 W of incident pump light. Assuming similar behavior for an independent Stokes beam, this would lead to an improvement of about a factor of 6.25 in the mixing efficiency. See text for details.

However, we have seen evidence of coherence generated from the independent pump and Stokes beams. We monitor the anti-Stokes generation, which comes from the mixing of the pump beam with the coherence, as a proxy for the coherence itself. Although we attempt to work at modes that have no Raman lasing, it is challenging to distinguish between anti-Stokes generation that comes from the pump and the Stokes from Raman lasing and that which comes from the pump and the independent Stokes. In order to distinguish between the two generation methods, we use a wavemeter to closely monitor the frequency of the pump and the Stokes seed lasers. With Raman lasing, it is guaranteed that the frequency of the Stokes beam is separated from the pump frequency by the modulation frequency (with some variation as discussed in Figure 7.10). With an independent Stokes beam, this frequency separation is no longer assured. We have the freedom to tune the frequency of the Stokes beam, which we do by changing the angle of the feedback grating in the ECDL. Only when the frequency of the Stokes beam is tuned so that the frequency difference of the pump and the Stokes beam matches that of the Raman transition can the two lasers build

up coherence between the Raman states. Thus, only with the correct frequency difference can the anti-Stokes beam be generated.

The Raman linewidth of the transition is large enough to contain several cavity resonances, and we can see anti-Stokes generation when lasing in any of the cavity modes within the Raman linewidth. (The full-width-half-maximum Raman linewidth is a few hundred MHz, and the free spectral range of the cavity is 200 MHz. The cavity linewidth is on the order of 10 kHz.) The closer a particular mode is to the Raman resonance, the more anti-Stokes generation we observe, as illustrated in Figure 11.3.

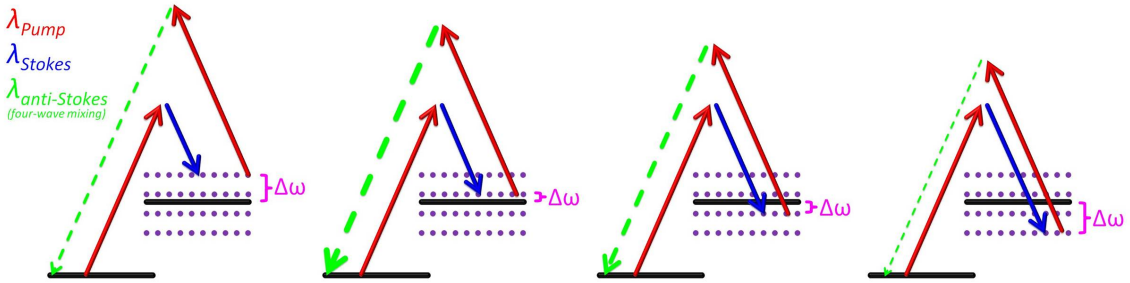

Figure 11.3 *Two-Photon Detuning and Anti-Stokes Generation* This figure illustrates how changing the two-photon detuning, $\Delta\omega$, affects the amount of anti-Stokes generation. In each of the four images, the Stokes laser is tuned to a different cavity resonance (dotted purple line). The frequency difference between the cavity resonance and the Raman resonance determines $\Delta\omega$. The Raman resonance is the frequency difference between the two ro-vibrational levels (solid black lines). When the detuning is small, the two-photon transition is close to the Raman resonance, and thus there is more anti-Stokes generation. The thickness of the anti-Stokes (green and dashed) arrow represents its relative power, with thicker arrows being higher power. In order to change $\Delta\omega$, the frequency of the Stokes beam (blue arrow) is changed to match cavity resonances while the frequency of the pump beam (red arrow) remains constant.

We tune to different cavity resonances (with different two-photon-detunings) by tuning the frequency of the Stokes laser while keeping the pump laser frequency constant. By recording the generated anti-Stokes power at each cavity resonance (that is, at each resonant Stokes laser frequency), we measure a resonance curve for the Raman transition. Figure 11.4 shows one such resonance curve. We infer the frequency of the Raman resonance to be the frequency difference between the pump and the Stokes lasers that leads to the maximum anti-Stokes generation. As an

aside, we note that this resonance curve method could provide a novel, precise measurement of the frequency of the Raman transition. If frequency-stabilized pump and Stokes lasers are used, the frequency of the two-photon transition, and thus the energy splitting of the ro-vibrational levels, could be determined with high precision.

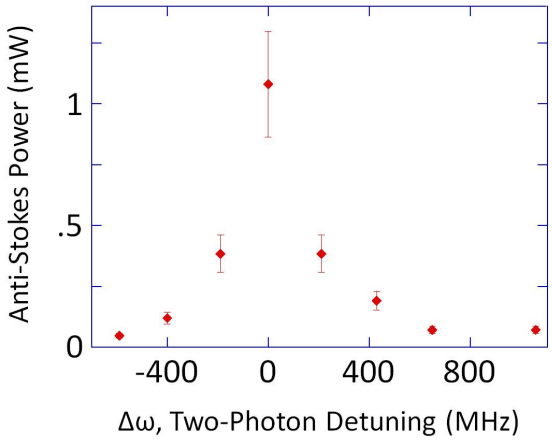

Figure 11.4 *Two-Photon Resonance* This figure shows the connection between the two-photon Raman resonance and the generation of anti-Stokes light. The independent pump and Stokes beams drive a molecular coherence that mixes with the pump beam to generate an anti-Stokes beam through four-wave mixing. By changing the frequency of the Stokes beam, we change the two-photon detuning from the Raman resonance, $\Delta\omega$. When the two-photon detuning is small, the coherence is high, and there is more anti-Stokes generation. By tuning across the Raman resonance, we generate a resonance curve. A detuning of zero corresponds to the frequency separation of the pump and the Stokes beams being exactly equal to the frequency of the Raman transition. Each data point in this experimental plot corresponds to a tuning configuration similar to those illustrated in Figure 11.3. The full-width-half-maximum linewidth of a few hundred MHz is roughly what we expect from the Doppler and pressure broadening linewidth contributions discussed in Section 6.3.

Although the early results have been promising, there are still outstanding issues with this independent Stokes beam experiment. The first, mentioned above, is the competition between the Raman lasing Stokes beam and the independent Stokes beam. We have explored the dependence of both processes on gas pressure, but it appears that both are optimized at pressures of around 0.1 - 0.3 atm. At any given pressure, it is difficult to distinguish how much of the anti-Stokes light is generated from each process. However, the resonance curve of Figure 11.4 gives us confidence

that the independent pump and Stokes beam are in fact interacting. Anti-Stokes light generated from Raman lasing would not show such dependence on the independent Stokes laser frequency. The fact that we can generate this resonance curve indicates that, although they come from separate sources, the pump and the Stokes beams are coherent enough to drive this coherent Raman process. Both lasers have full-width-half-maximum linewidths around 10 kHz due to the high-finesse cavity, and this ensures that they are at least coherent of timescales of roughly $\frac{1}{10\text{ kHz}} = .1$ ms.

Another outstanding issue is our inability to observe the dependence of anti-Stokes generation on the independent Stokes beam power. As mentioned in the beginning of this section, the coherence scales as the electric field of the Stokes beam. Thus, we should see a clear increase in anti-Stokes generation when the Stokes power increases. However, this has not been the case. We are able to observe anti-Stokes generation with an incident Stokes power anywhere from 100s of mW to 20 W. There is not a discernible difference in the amount of anti-Stokes generation. We hypothesize this may be because the independent laser is currently serving only to seed a Raman lasing process. After the small amount of Stokes light seeds the Raman process, the Raman lasing takes over and drives the coherence. More work is needed to determine if this is the cause of the lack of observed power dependence and, if so, what can be done to suppress this Raman lasing.

Despite these challenges, as mentioned above, the independent Stokes beam arrangement holds great promise for improving the efficiency of our modulator, and this experiment merits further investigation.

Far below the optimal $|\rho_{ab}^{max}| = 0.5$, the modulation efficiency roughly scales as $I_p I_S N^2 L^2$, where I_p and I_S are the intensities of the two driving lasers, N is the number density, and L is the length of the interaction region. (This comes from Equation 2.44.) We are currently focusing on improving I_p and I_S. As mentioned in Section 7.3, the quality of the cavity lock decreases with higher densities, and this decreases the intracavity intensities of the beams. Phase matching also becomes more of a problem at higher densities. There is also a trade-off with increasing the interaction length. A longer interaction length requires a longer cavity, and a longer cavity requires more loosely focused beams. Thus, increasing the interaction length also decreases the intensities.

A longer interaction length also increases phase matching issues. Because of these complications, we have decided to focus on improving the intensities.

The pulsed laser modulation experiments discussed in Chapter 3 were performed with near maximal coherence, $|\rho_{ab}| \approx 0.5$. The experiment of Chapter 9 had a coherence of $|\rho_{ab}| \approx 6.7 \times 10^{-5}$. With the independent Stokes beam experiment, we hope to increase our pump and Stokes intensities. Because we are no longer relying on Raman lasing, our aim is to achieve intensities near those that we achieve in an evacuated cavity. This would increase our coherence to $|\rho_{ab}| \approx 1.4 \times 10^{-3}$. Working with an independent Stokes beam, along with technical improvements such as narrowing the linewidths of our ECDLs, improving the spatial coupling of our lasers to the cavity, and further developing our feedback circuitry could make this goal achievable.

A longer term goal for the project is to achieve a coherence of $|\rho_{ab}| \approx 1.4 \times 10^{-2}$. By using a cavity with a smaller mode size ($w_0 \approx 200$ μm) and higher power ($>$ 100 W) fiber amplifiers, we aim to achieve intracavity circulating intensities approaching 100 MW/cm^2 for both laser beams. (In the mixing experiment of Chapter 9, the mode size is around 800 μm, and the circulating intensities are around 0.5 MW/cm^2.) While not maximally coherent, such a modulator would yield a 1% conversion efficiency, which would be sufficient for most applications.

11.2 Independent Mixing Beam Modulation at 89.6 THz

Our current research efforts are focused on recreating the molecular modulation experiments of Chapter 9 at a higher modulation frequency. We modulate an independent, non-resonant laser using stimulated Raman scattering in our high-finesse cavity. In a single pass through our modulator, frequency sidebands located 89.6 THz from the mixing laser are produced through four-wave mixing.

As with the experiment of Chapter 9, the molecules are prepared to a coherent state using an intense intracavity pump field. The pump field generates the Stokes field through Raman lasing. Whereas our previous experiment used the $|v = 0, J = 1\rangle$ to $|v = 0, J = 3\rangle$ rotational transition in molecular hydrogen, which has a modulation frequency of 17.6 THz, our current experiment relies on scattering off of the $|v = 0, J = 0\rangle$ to $|v = 1, J = 0\rangle$ vibrational transition in molecular

deuterium, which has a modulation frequency of 89.6 THz. The pump laser is at a wavelength of 1064 nm, and the vibrational Stokes beam is at a wavelength of 1560 nm. As in Chapter 9, the mixing laser is at a wavelength of 785 nm. A modulation frequency of 89.6 THz yields frequency up- and down-shifted sidebands at wavelengths of 636 nm and 1026 nm, respectively. In this experiment the light is linearly polarized. This polarization does not preferentially generate one sideband over the other. However, we have thus far focused on the frequency up-shifted beam. The higher frequency 636 nm light is generated more efficiently. (See the discussion around Figure 9.5.) It is also further away in wavelength from the powerful pump beam at 1064 nm, and thus is easier to detect. Figure 11.5 displays an overview of the experiment.

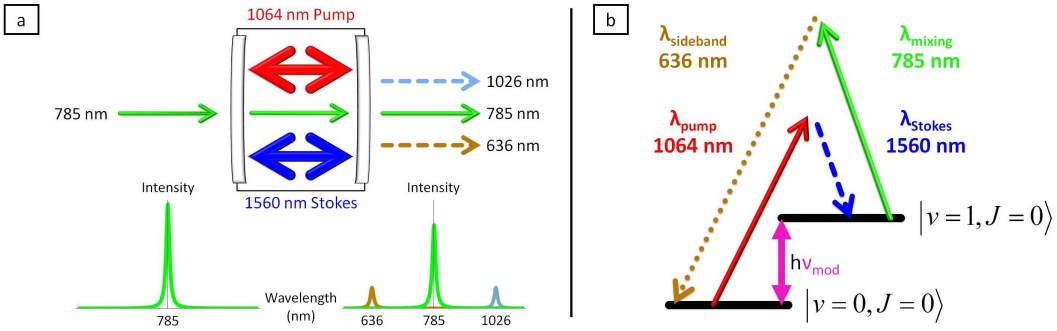

Figure 11.5 *Vibrational Mixing Experiment Overview* This independent mixing beam modulation experiment is similar to the one described in Figure 9.1. (a) Inside a high-finesse cavity, we drive deuterium molecules to a coherent vibrational state using intense pump and Stokes beams. A third laser beam at a wavelength of 785 nm passes through the system and is modulated by the coherently vibrating molecules through four-wave mixing. This generates sidebands at 1026 nm and 636 nm, 89.6 THz from the mixing laser frequency. At the bottom of the figure, plots of intensity as a function of wavelength display the spectral components at the input and the output of the cavity, highlighting the effects of modulation. (b) This figure shows the relevant energy diagram for the process described in (a). It is very similar to the four-wave mixing process shown in Figure 7.2, but it is an independent mixing beam (λ_{mixing}), rather than the pump beam, that mixes with the coherence generated by the pump (λ_{pump}) and Stokes (λ_{Stokes}) beams to produce a sideband ($\lambda_{sideband}$). ν_{mod} is the modulation frequency, which is 89.6 THz. We show only the generation of the frequency up-shifted sideband here, but the light is linearly polarized, so there is no preferential generation of one sideband over another.

Figure 11.6 shows the experimental arrangement for the vibrational mixing experiment. It is similar to our rotational mixing experiment shown in Figure 9.3, including the gas pressure, which

is approximately $\frac{1}{3}$ atm, and the mixing beam power, which is on the order of 100 mW. In addition to the change of Raman medium and transition mentioned above, there are two main changes. First, we use an optical chopper and lock-in amplifier to aid in the detection of the weak sideband in the presence of scatter from the significantly stronger pump, Stokes, and mixing beams. Also, as mentioned above, we use linearly polarized light. See Figure 11.6 for more details.

We are still in the early stages of this experiment, and we do not yet have any definitive data on the conversion efficiency. However, we have definitively observed the 636 nm sideband. The optical chopper and lock-in amplifier have proven vital in allowing us to distinguish the sideband signal from background scattered light. We are still optimizing the experiment, but we are currently measuring conversion efficiencies from the mixing beam to the frequency up-shifted sideband to be around 5.5×10^{-7}. We expect there is a similar amount of power in the frequency down-shifted sideband. For the same mixing wavelength (785 nm), this is approaching the efficiency of the rotational mixing experiment of Chapter 9. (See Figure 9.5.) We are confident that this efficiency can be improved by optimizing the mixing beam alignment and its overlap with the intracavity pump and Stokes beams. We have begun to optimize this by coupling the tapered amplifier output through a single-mode optical fiber in order to improve the Gaussian beam shape and to eliminate some of the amplified spontaneous emission. (This emission has a broad frequency linewidth. It is essentially wasted power, as it is not converted to the main frequency sidebands at 636 nm and 1026 nm.)

Although there remains much work to be done, this independent mixing beam experiment shows promise. As with the rotational mixing beam experiment of Chapter 9, this 89.6 THz modulator can modulate light in a large portion of the optical spectrum. With improved efficiency, such a high-frequency broadband optical modulator would be a unique and powerful tool.

11.3 Future Directions

We conclude with a discussion of one exciting prospect for expanding the utility of our molecular modulator. Throughout this thesis, we have focused on modulating a monochromatic laser beam. However, as discussed in Chapter 9, the modulator is capable of modulating light over a

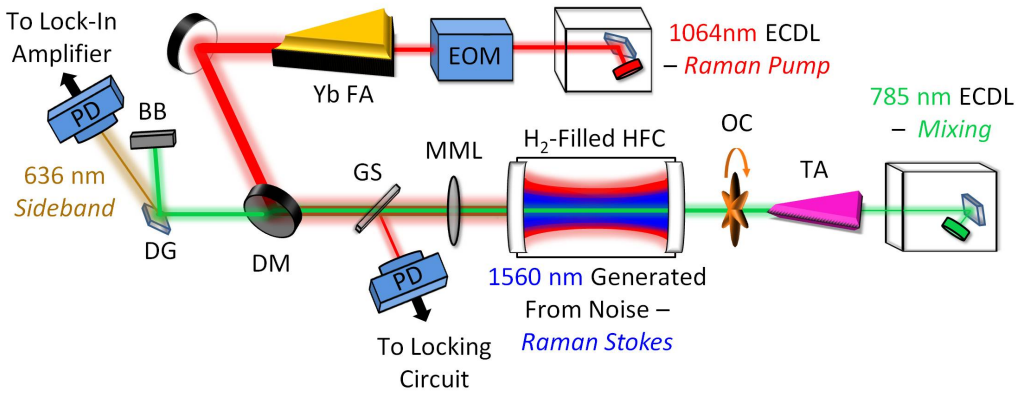

Figure 11.6 *Vibrational Mixing Experiment Schematic* This figure shows a schematic for our vibrational mixing experiment. It is very similar to the rotational mixing experiment illustrated in Figure 9.3. As with our other experiments, the pump laser comes from a custom-built external cavity diode laser (**ECDL**) at a wavelength of 1064 nm. The continuous-wave (CW) beam is modulated by an electro-optic modulator (**EOM**) so that it can be used in a Pound-Drever-Hall locking scheme. The ECDL output is on the order of 10 mW, and this seeds a ytterbium fiber amplifier (**Yb FA**). The output of the Yb FA is up to 30 W of CW power in a single spatial mode and a single frequency mode. The Yb FA output is coupled to a high-finesse cavity (**HFC**) using a mode-matching lens (**MML**). Raman scattering in the HFC generates a Raman Stokes beam at a wavelength of 1560 nm, which also resonates in the HFC. The HFC and locking electronics are the same as those in Chapter 9. A glass slide (**GS**) picks off part of the reflection from the cavity and sends the signal to the locking circuit through a photodiode (**PD**). An independent mixing beam with a wavelength of 785 nm is generated by a separate ECDL, and amplified by a semiconductor tapered amplifier (**TA**). The amplified beam is modulated at a frequency of 500 Hz using and optical chopper (**OC**). This chopper, in conjunction with a lock-in amplifier, aids in the detection of the weak sideband in the presence of scatter from the much more powerful pump, Stokes, and mixing beams. The mixing beam travels through the cavity and mixes with the coherence from the pump and Stokes beams to generate frequency sidebands through four-wave mixing. The mixing beam is not resonant with the cavity so the modulation occurs in a single pass through the system. The chopper-modulated mixing beam and frequency up-shifted sideband are separated from the transmitted pump and Stokes light (and the frequency down-shifted sideband) using a low-pass dichroic mirror (**DM**). The mixing beam and the frequency up-shifted sideband are then spatially separated using a dispersive grating (**DG**), and the mixing beam is blocked using a beam block (**BB**). The chopper-modulated frequency up-shifted sideband is detected using a PD and a lock-in amplifier.

large range of wavelengths, and thus it can also be used to modulate broadband signals. We plan to use our modulator to modulate a frequency comb titanium-sapphire laser in the CW regime. (Titanium-sapphire lasers have shown promise in pulsed modulation experiments [95, 96, 97, 81].)

A titanium-sapphire frequency comb is a broadband coherent light source, typically with several hundred thousand individual spectral components covering a wavelength range of 700 nm to 900 nm. (See the Nobel lectures by Hall [98] and by Hänsch [99], and the article by Hall and colleagues [100] for more information on titanium-sapphire lasers.)

With its broad, coherent spectrum of narrow linewidth lasers, a titanium-sapphire frequency comb is similar to the broadband spectra we describe in Chapter 8. However, rather than viewing titanium-sapphire frequency combs as a competing technology, we believe that molecular modulation could serve to enhance the capabilities of frequency combs. Currently, the bandwidths (and tuning ranges) of titanium-sapphire frequency combs are limited to roughly 650 nm to 1100 nm due to the gain bandwidth of the titanium ions. We propose increasing this bandwidth using our molecular modulator. If the broadband output of a frequency comb passes through a molecular modulator, each spectral component produces frequency up-shifted and down-shifted sidebands. This greatly extends the spectral coverage of the comb as illustrated in Figure 11.7.

A broadened titanium-sapphire spectrum would be useful for all of the applications mentioned in the introduction of this thesis. Broadening the already broad spectrum could yield millions of CW spectral components, each with a narrow frequency linewidth. This increases the utility of the spectrum as a spectroscopy tool, as it makes accessible atomic and molecular transitions spanning a wide range of energies. Because pulse duration and spectral bandwidth are inversely related, a broader spectrum allows for the generation of shorter ultrashort pulses. Furthermore, as illustrated in Figure 11.8, with appropriate phase and amplitude control, the spectrum could be used to synthesize arbitrary optical waveforms with unprecedented resolution [19]. With more spectral components, there are more degrees of freedom. Thus, a wider range of waveforms can be generated with a higher resolution. The potential for creating such a powerful tool motivates us to continue our work with CW molecular modulation.

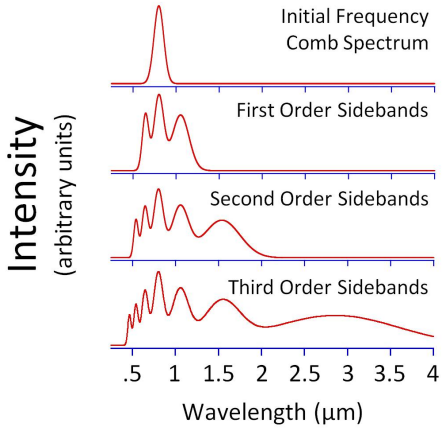

Figure 11.7 *Frequency Comb Modulation* This figure illustrates the effect of our molecular modulator on a titanium-sapphire frequency comb. The top plot shows a typical output spectrum from a frequency comb. This would be the *input* to our modulator. (There are too many closely-spaced spectral components to show them individually here. We instead use a single curve to represent the envelope that contains the hundreds of thousands of individual spectral components.) In the second highest plot, we show the *output* of our modulator, assuming that our modulator adds a single Stokes and anti-Stokes sideband to each spectral component with 60% conversion efficiency. The modulation frequency is taken to be 89.6 THz, which is from scattering off of the $|v = 0, J = 0\rangle$ to $|v = 1, J = 0\rangle$ vibrational transition in molecular deuterium. The third and fourth highest plots include second- and third-order sidebands, again assuming a conversion efficiency of 60%.

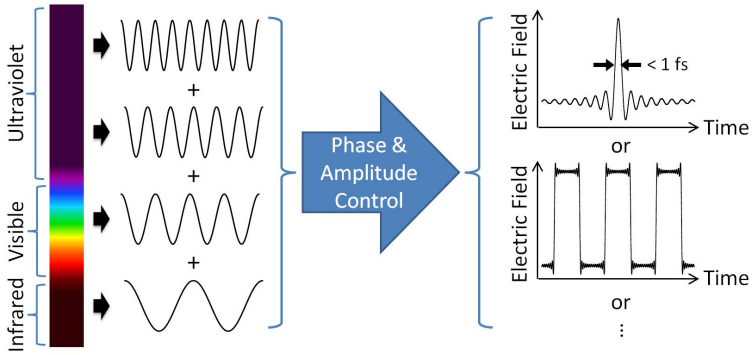

Figure 11.8 *Arbitrary Optical Waveform Generation* This figure illustrates the potential of a broadband spectrum for arbitrary optical waveform generation. With its broadband capabilities, a molecular modulator would be able to modulate the already broad output of a titanium-sapphire laser. The resulting spectrum could contain a few million CW Fourier components that span the entire optical region of the spectrum. With appropriate phase and amplitude control, such a broad, coherent spectrum could be used to Fourier synthesize arbitrary optical waveforms with sub-femtosecond resolution.

REFERENCES

[1] M. F. Kling and M. J. J. Vrakking, Annual Review of Physical Chemistry **59**, 463 (2008).

[2] H. A. Haus, IEEE Journal of Selected Topics in Quantum Electronics **6**, 1173 (2000).

[3] T. Brabec and F. Krausz, Reviews of Modern Physics **72**, 545 (2000).

[4] B. W. J. McNeil and N. R. Thompson, Nature Photonics **4**, 814 (2010).

[5] G. Cerullo and S. De Silvestri, Review of Scientific Instruments **74**, 1 (2003).

[6] S.-W. Huang *et al.*, Nature Photonics **5**, 475 (2011).

[7] S. Lohss *et al.*, Nature Photonics **4**, 33 (2010).

[8] G. Ycas, S. Osterman, and S. A. Diddams, Optics Letters **37**, 2199 (2012).

[9] A. Wirth *et al.*, Science (New York, N.Y.) **334**, 195 (2011).

[10] A. Sokolov and S. E. Harris, Journal of Optics B: Quantum and Semiclassical Optics **5**, R1 (2003).

[11] S. Baker, I. A. Walmsley, J. W. G. Tisch, and J. P. Marangos, Nature Photonics **5**, 664 (2011).

[12] H. Walther and T. W. Hänsch, Reviews of Modern Physics **71**, 242 (1999).

[13] R. S. Judson and H. Rabitz, Physical Review Letters **68**, 1500 (1992).

[14] M. Shapiro and P. Brumer, Reports on Progress in Physics **66**, 859 (2003).

[15] A. Gandman, L. Rybak, and Z. Amitay, Physical Review Letters **113**, 043003 (2014).

[16] T. Udem, R. Holzwarth, and T. W. Hänsch, Nature **416**, 233 (2002).

[17] M. M. Boyd *et al.*, Science (New York, N.Y.) **314**, 1430 (2006).

[18] A. M. Weiner, Optics Communications **284**, 3669 (2011).

[19] D. D. Yavuz, Science (New York, N.Y.) **331**, 1142 (2011).

[20] D. Grischkowsky, M. M. T. Loy, and P. F. Liao, Physical Review A **12**, 2514 (1975).

[21] S. E. Harris and A. V. Sokolov, Physical Review A **55**, R4019 (1997).

[22] A. V. Sokolov, D. D. Yavuz, and S. E. Harris, Optics Letters **24**, 557 (1999).

[23] D. D. Yavuz, A. V. Sokolov, and S. E. Harris, Physical Review Letters **84**, 75 (2000).

[24] D. D. Yavuz, *A Raman approach for generating ultrashort pulses*, Ph.d. thesis, Stanford University, 2003.

[25] J. T. Green, *Optical cavity-based continuous-wave Raman generation*, Ph.d. thesis, University of Wisconsin - Madison, 2010.

[26] J. J. Sakurai, *Modern Quantum Mechanics*, 4th ed. (Pearson Education, Inc., 1994).

[27] A. E. Siegman, *Lasers* (University Science Books, Mill Valley, CA, 1986).

[28] S. Yoshikawa and T. Imasaka, Optics Communications **96**, 94 (1993).

[29] A. E. Kaplan, Physical Review Letters **73**, 1243 (1994).

[30] H. Kawano, T. Mori, Y. Hirakawa, and T. Imasaka, Optics Communications **160**, 277 (1999).

[31] A. V. Sokolov, D. R. Walker, D. D. Yavuz, G. Y. Yin, and S. E. Harris, Physical Review Letters **85**, 562 (2000).

[32] A. Sokolov, D. Yavuz, D. Walker, G. Yin, and S. Harris, Physical Review A **63**, 051801 (2001).

[33] L. L. Losev, Y. Yoshimura, H. Otsuka, Y. Hirakawa, and T. Imasaka, Review of Scientific Instruments **73**, 2200 (2002).

[34] D. Yavuz, D. Walker, M. Shverdin, G. Yin, and S. Harris, Physical Review Letters **91**, 233602 (2003).

[35] M. Shverdin, D. Walker, D. Yavuz, G. Yin, and S. Harris, Physical Review Letters **94**, 033904 (2005).

[36] N. Zhavoronkov and G. Korn, Physical Review Letters **88**, 203901 (2002).

[37] W.-J. Chen *et al.*, Physical Review Letters **100**, 163906 (2008).

[38] O. Shitamichi and T. Imasaka, Optics Express **20**, 27959 (2012).

[39] T. Suzuki, N. Sawayama, and M. Katsuragawa, Optics Letters **33**, 2809 (2008).

[40] Z.-M. Hsieh *et al.*, Physical Review Letters **102**, 213902 (2009).

[41] H.-S. Chan *et al.*, Science (New York, N.Y.) **331**, 1165 (2011).

[42] D. D. Yavuz and J. J. Weber, Optics Letters **37**, 4191 (2012).

[43] H. S. Margolis *et al.*, Science (New York, N.Y.) **306**, 1355 (2004).

[44] D. Yavuz, Physical Review A **76**, 011805 (2007).

[45] K. Shinzen, Y. Hirakawa, and T. Imasaka, Physical Review Letters **87**, 223901 (2001).

[46] J. K. Brasseur, K. S. Repasky, and J. L. Carlsten, Optics Letters **23**, 367 (1998).

[47] J. K. Brasseur, P. A. Roos, K. S. Repasky, and J. L. Carlsten, Journal of the Optical Society of America B **16**, 1305 (1999).

[48] L. S. Meng, K. S. Repasky, P. A. Roos, and J. L. Carlsten, Optics Letters **25**, 472 (2000).

[49] J. K. Brasseur, P. A. Roos, L. S. Meng, and J. L. Carlsten, Co-linear anti-Stokes generation from a CW Raman laser, in *Quantum Electronics and Laser Science Conference, 2000. (QELS 2000). Technical Digest*, pp. 244–245, 2000.

[50] L. S. Meng, P. A. Roos, and J. L. Carlsten, Optics Letters **27**, 1226 (2002).

[51] K. Ihara *et al.*, Applied Physics Letters **88**, 074101 (2006).

[52] J. T. Green, D. E. Sikes, and D. D. Yavuz, Optics Letters **34**, 2563 (2009).

[53] J. K. Brasseur *et al.*, Applied Optics **43**, 1162 (2004).

[54] S.-I. Zaitsu, H. Izaki, and T. Imasaka, Physical Review Letters **100**, 073901 (2008).

[55] S.-I. Zaitsu and T. Imasaka, Optics Communications **285**, 347 (2012).

[56] J. Q. Liang, M. Katsuragawa, F. Le Kien, and K. Hakuta, Physical Review Letters **85**, 2474 (2000).

[57] F. Couny and F. Benabid, Journal of Optics A: Pure and Applied Optics **11**, 103002 (2009).

[58] M. Zhi and A. V. Sokolov, Optics Letters **32**, 2251 (2007).

[59] M. Zhi and A. V. Sokolov, IEEE Journal of Selected Topics in Quantum Electronics **18**, 460 (2012).

[60] M. Hase, M. Katsuragawa, A. M. Constantinescu, and H. Petek, New Journal of Physics **15**, 055018 (2013).

[61] R. W. P. Drever *et al.*, Applied Physics B Photophysics and Laser Chemistry **31**, 97 (1983).

[62] E. D. Black, American Journal of Physics **69**, 79 (2001).

[63] R. W. Fox, C. W. Oates, and L. W. Hollberg, Stabilizing Diode Lasers to High-Finesse Cavities, in *Experimental Methods in the Physical Sciences*, edited by R. D. van Zee and J. P. Looney, volume 40, chap. 1, pp. 1–46, Elsevier Science, San Diego, CA, 1st ed., 2003.

[64] G. A. Massey and A. E. Siegman, Applied Optics **8**, 975 (1969).

[65] G. Herzberg, *Molecular Spectra and Molecular Structure: I. Spectra of Diatomic Molecules*, 2nd ed. (D. Van Nostrand Company, New York, 1950).

[66] H. G. M. Edwards, D. A. Long, and G. Sherwood, Journal of Raman Spectroscopy **22**, 607 (1991).

[67] D. A. Russell and W. B. Roh, Journal of Molecular Spectroscopy **124**, 240 (1987).

[68] A. M. Toich, D. W. Melton, and W. B. Roh, Optics Communications **55**, 406 (1985).

[69] R. A. J. Keijser, J. R. Lombardi, K. D. Van Den Hout, B. C. Sanctuary, and H. F. P. Knaap, Physica **76**, 585 (1974).

[70] F. Couny, F. Benabid, and P. Light, Physical Review Letters **99**, 143903 (2007).

[71] A. V. Sokolov *et al.*, Optics Letters **26**, 728 (2001).

[72] J. T. Green, J. J. Weber, and D. D. Yavuz, Physical Review A **82**, 011805 (2010).

[73] Y. Miyoshi *et al.*, Optics Express **16**, 2570 (2008).

[74] J. T. Green, J. J. Weber, and D. D. Yavuz, Optics Letters **36**, 897 (2011).

[75] S.-I. Zaitsu, C. Eshima, and K. Ihara, Journal of the Optical Society of America B **24**, 1037 (2007).

[76] Z. Luo *et al.*, Optics Communications **265**, 616 (2006).

[77] S.-I. Zaitsu and T. Imasaka, Applied Optics **49**, 1586 (2010).

[78] J. J. Weber and D. D. Yavuz, Optics Letters **38**, 2449 (2013).

[79] A. Vernaleken *et al.*, Optics Express **20**, 18387 (2012).

[80] J. J. Weber, J. T. Green, and D. D. Yavuz, Physical Review A **85**, 013805 (2012).

[81] P. J. Bustard, B. J. Sussman, and I. A. Walmsley, Physical Review Letters **104**, 193902 (2010).

[82] M. Liu *et al.*, Nature **474**, 64 (2011).

[83] Y.-Q. Lu, M. Xiao, and G. J. Salamo, Applied Physics Letters **78**, 1035 (2001).

[84] S. Shi and D. W. Prather, Advances in OptoElectronics **2011** (2011).

[85] M. Chaciski *et al.*, Journal of Lightwave Technology **27**, 3410 (2009).

[86] M. Hochberg *et al.*, Nature Materials **5**, 703 (2006).

[87] A. Tsunemi, K. Nagasaka, and H. Tashiro, Applied Optics **31**, 4165 (1992).

[88] H. Abgrall and E. Roueff, Astronomy & Astrophysics Supplement Series **79**, 313 (1989).

[89] M. Tonouchi, Nature Photonics **1**, 97 (2007).

[90] S. Preu, G. H. Dohler, S. Malzer, L. J. Wang, and A. C. Gossard, Journal of Applied Physics **109**, 061301 (2011).

[91] M. Scheller *et al.*, Optics Express **18**, 27112 (2010).

[92] H. Tanoto *et al.*, Nature Photonics **6**, 2 (2012).

[93] M. Shverdin, D. Yavuz, and D. Walker, Physical Review A **69**, 031801 (2004).

[94] L. S. Meng, J. K. Brasseur, and D. K. Neumann, Optics Express **13**, 10085 (2005).

[95] F. Kien, N. Shon, and K. Hakuta, Physical Review A **64**, 051803 (2001).

[96] N. Shon, F. Le Kien, K. Hakuta, and A. Sokolov, Physical Review A **65**, 033809 (2002).

[97] S. Gundry *et al.*, Optics Letters **30**, 180 (2005).

[98] J. Hall, Reviews of Modern Physics **78**, 1279 (2006).

[99] T. Hänsch, Reviews of Modern Physics **78**, 1297 (2006).

[100] J. L. Hall, S. A. Diddams, S. T. Cundiff, and D. J. Jones, IEEE Journal of Quantum Electronics **37**, 1482 (2001).

Appendix A: Effective Hamiltonian of the Raman System

Consider the interaction of a molecular system (a dilute gas of molecules) and Raman sidebands of complex amplitudes E_q and angular frequencies ω_q. Let $|a\rangle$ and $|b\rangle$ be the ground and excited Raman states, respectively, and let $|i\rangle$ be the upper electronic electronic-ro-vibrational states. For simplicity, we will assume that the transitions have arbitrarily small linewidths. The Raman sideband frequencies are harmonically spaced, so

$$\omega_q = \omega_0 + q\omega_m \tag{A.1}$$

with

$$\omega_m \equiv \omega_b - \omega_a - \Delta\omega, \tag{A.2}$$

where $\Delta\omega$ is the two-photon detuning, which is assumed to be small compared to the Raman frequency: $\omega_{Raman} \equiv \omega_b - \omega_a \gg \Delta\omega$.

The Schrödinger equation for the molecular wavefunction $|\psi\rangle$ is

$$j\hbar\frac{d\,|\psi\rangle}{dt} \quad = \quad \hat{H}\,|\psi\rangle\,. \tag{A.3}$$

Write the Hamiltonian for the molecule-sideband interaction as the sum of an unperturbed Hamiltonian and an interaction Hamiltonian as follows:

$$\hat{H} \quad \equiv \quad \hat{H}_0 + \hat{H}_I. \tag{A.4}$$

Assume that the only relevant interaction between the electric field and the molecule is the dipole interaction. Ignoring insignificant interactions between upper ro-vibrational states, this dipole approximation yields unperturbed and interaction Hamiltonians defined as follows:

$$\hat{H}_0 \equiv \hbar\omega_a\,|a\rangle\,\langle a| + \hbar\omega_b\,|b\rangle\,\langle b| + \sum_i \hbar\omega_i\,|i\rangle\,\langle i| \tag{A.5}$$

and

$$\begin{aligned}
\hat{H}_I \quad &\equiv \quad -E\,(t)\,\hat{P} \\
&= \quad -E\,(t)\sum_i \mu_{ai}\,|a\rangle\,\langle i| - E\,(t)\sum_i \mu_{bi}\,|b\rangle\,\langle i| \\
&\qquad - E^*\,(t)\sum_i \mu^*_{ai}\,|i\rangle\,\langle a| - E^*\,(t)\sum_i \mu^*_{bi}\,|i\rangle\,\langle b|\,,
\end{aligned} \tag{A.6}$$

where $E(t)$ is the electric field, $\hat{P}$ is the dipole moment operator, and μ_{nm} is the matrix element between states $|n\rangle$ and $|m\rangle$. *denotes a complex conjugate.

Expand the wavefunction in the interaction picture, expressing the time dependence as the product of the Schrödinger-picture time dependence and a time-dependent constant. Using the fact that, for eigenkets $|n\rangle$ of a Hamiltonian $\hat{H}$ with eigenvalues $E_n = \hbar\omega_n$,

$$\begin{aligned} e^{-j\frac{\hat{H}}{\hbar}t}|n\rangle &= e^{-j\frac{E_n}{\hbar}t}|n\rangle \\ &= e^{-j\frac{\hbar\omega_n}{\hbar}t}|n\rangle \\ &= e^{-j\omega_n t}|n\rangle, \end{aligned} \tag{A.7}$$

the wavefunction in the interaction picture is given by

$$|\psi(t)\rangle = c_a(t)\,e^{-j\omega_a t}|a\rangle + c_b(t)\,e^{-j\omega_b t}|b\rangle + \sum_i c_i(t)\,e^{-j\omega_i t}|i\rangle, \tag{A.8}$$

where $c_n(t)$ is the time-dependent probability amplitude of state $|n\rangle$.

Assume that the probability amplitudes vary slowly in comparison to the inverse of the single-photon detuning $\delta\omega$ from $|i\rangle$, the upper electronic ro-vibrational states.

Now plug $|\psi(t)\rangle$ (Equation A.8) into the above Schrödinger equation (Equation A.3). The left-hand side yields

$$j\hbar\frac{d|\psi\rangle}{dt} = j\hbar\frac{d}{dt}\left[c_a(t)\,e^{-j\omega_a t}|a\rangle + c_b(t)\,e^{-j\omega_b t}|b\rangle + \sum_i c_i(t)\,e^{-j\omega_i t}|i\rangle\right]. \tag{A.9}$$

Differentiation using the product rule yields

$$\begin{aligned} j\hbar\frac{d|\psi\rangle}{dt} &= j\hbar\Bigg\{\left[\frac{dc_a}{dt}e^{-j\omega_a t} + c_a(t)\left(-j\omega_a e^{-j\omega_a t}\right)\right]|a\rangle + \left[\frac{dc_b}{dt}e^{-j\omega_b t} + c_b(t)\left(-j\omega_b e^{-j\omega_b t}\right)\right]|b\rangle \\ &\quad + \sum_i\left[\frac{dc_i}{dt}e^{-j\omega_i t} + c_i(t)\left(-j\omega_i e^{-j\omega_i t}\right)\right]|i\rangle\Bigg\}. \end{aligned} \tag{A.10}$$

Now examine the right-hand side of the above Schrödinger equation (Equation A.3), using the composite Hamiltonian (Equation A.4).

$$\hat{H}|\psi\rangle = \left(\hat{H}_0 + \hat{H}_I\right)|\psi\rangle = \hat{H}_0|\psi\rangle + \hat{H}_I|\psi\rangle \tag{A.11}$$

Plug in $\hat{H}_0$, $\hat{H}_I$, and $|\psi\rangle$ (Equations A.5, A.6, and A.8); the terms of the above (Equation A.11) become

$$\begin{aligned}\hat{H}_0 |\psi\rangle &= \left[\hbar\omega_a |a\rangle \langle a| + \hbar\omega_b |b\rangle \langle b| + \sum_i \hbar\omega_i |i\rangle \langle i|\right] \\ &\quad \times \left[c_a(t) e^{-j\omega_a t} |a\rangle + c_b(t) e^{-j\omega_b t} |b\rangle + \sum_i c_i(t) e^{-j\omega_i t} |i\rangle\right]\end{aligned} \tag{A.12}$$

and

$$\begin{aligned}\hat{H}_I |\psi\rangle &= \left[- E(t) \sum_i \mu_{ai} |a\rangle \langle i| - E(t) \sum_i \mu_{bi} |b\rangle \langle i| \right. \\ &\quad \left. - E^*(t) \sum_i \mu^*_{ai} |i\rangle \langle a| - E^*(t) \sum_i \mu^*_{bi} |i\rangle \langle b| \right] \\ &\quad \times \left[c_a(t) e^{-j\omega_a t} |a\rangle + c_b(t) e^{-j\omega_b t} |b\rangle + \sum_i c_i(t) e^{-j\omega_i t} |i\rangle\right].\end{aligned} \tag{A.13}$$

Using the orthonormality of states, $\langle n | m\rangle = \delta_{nm}$, these reduce to

$$\hat{H}_0 |\psi\rangle = \left[\hbar\omega_a c_a(t) e^{-j\omega_a t} |a\rangle + \hbar\omega_b c_b(t) e^{-j\omega_b t} |b\rangle + \sum_i \hbar\omega_i c_i(t) e^{-j\omega_i t} |i\rangle\right] \tag{A.14}$$

and

$$\begin{aligned}\hat{H}_I |\psi\rangle &= \left[-E(t) \sum_i \mu_{ai} c_i(t) e^{-j\omega_i t} |a\rangle - E(t) \sum_i \mu_{bi} c_i(t) e^{-j\omega_i t} |b\rangle \right. \\ &\quad \left. \times -E^*(t) \sum_i \mu^*_{ai} c_a(t) e^{-j\omega_a t} |i\rangle - E^*(t) \sum_i \mu^*_{bi} c_b(t) e^{-j\omega_b t} |i\rangle\right].\end{aligned} \tag{A.15}$$

Summing these expressions and gathering like kets, the right-hand side of Schrödinger equation (Equation A.3) becomes

$$\begin{aligned}\hat{H}\left|\psi\right\rangle &= \hat{H}_0\left|\psi\right\rangle + \hat{H}_I\left|\psi\right\rangle \\ &= \left[\hbar\omega_a c_a\left(t\right)e^{-j\omega_a t} - E\left(t\right)\sum_i \mu_{ai}c_i\left(t\right)e^{-j\omega_i t}\right]\left|a\right\rangle \\ &\quad + \left[\hbar\omega_b c_b\left(t\right)e^{-j\omega_b t} - E\left(t\right)\sum_i \mu_{bi}c_i\left(t\right)e^{-j\omega_i t}\right]\left|b\right\rangle \\ &\quad + \Bigg[\sum_i \hbar\omega_i c_i\left(t\right)e^{-j\omega_i t} - E^*\left(t\right)\sum_i \mu_{ai}^* c_a\left(t\right)e^{-j\omega_a t} \\ &\qquad - E^*\left(t\right)\sum_i \mu_{bi}^* c_b\left(t\right)e^{-j\omega_b t}\Bigg]\left|i\right\rangle . \end{aligned} \tag{A.16}$$

By orthogonality of the state kets, the coefficients of each ket on the left side of the Schrödinger equation must equal the corresponding coefficients on the right side. Equate the coefficients of $\left|a\right\rangle$, $\left|b\right\rangle$, and $\left|i\right\rangle$ from the left-hand side (Equation A.10) with those from the right-hand side (Equation A.16) in order to find three coupled equations.

$\left|a\right\rangle$ ***coefficient:***

$$j\hbar\left[\frac{dc_a}{dt}e^{-j\omega_a t} + c_a\left(t\right)\left(-j\omega_a e^{-j\omega_a t}\right)\right] = \hbar\omega_a c_a\left(t\right)e^{-j\omega_a t} - E\left(t\right)\sum_i \mu_{ai}c_i\left(t\right)e^{-j\omega_i t} \tag{A.17}$$

Cancel the common $c_a\left(t\right)$ term.

$$j\hbar\frac{dc_a}{dt}e^{-j\omega_a t} = -E\left(t\right)\sum_i \mu_{ai}c_i\left(t\right)e^{-j\omega_i t} \tag{A.18}$$

Solve for $\frac{dc_a}{dt}$ using $\frac{1}{j} = -j$.

$$\frac{dc_a}{dt} = \frac{j}{\hbar}E\left(t\right)\sum_i \mu_{ai}c_i\left(t\right)e^{j(\omega_a-\omega_i)t} \tag{A.19}$$

$\left|b\right\rangle$ ***coefficient:***

$$j\hbar\left[\frac{dc_b}{dt}e^{-j\omega_b t} + c_b\left(t\right)\left(-j\omega_b e^{-j\omega_b t}\right)\right] = \hbar\omega_b c_b\left(t\right)e^{-j\omega_b t} - E\left(t\right)\sum_i \mu_{bi}c_i\left(t\right)e^{-j\omega_i t} \tag{A.20}$$

Cancel the common $c_b(t)$ term.

$$j\hbar\frac{dc_b}{dt}e^{-j\omega_b t} = -E(t)\sum_i \mu_{bi}c_i(t)\,e^{-j\omega_i t} \tag{A.21}$$

Solve for $\frac{dc_b}{dt}$ using $\frac{1}{j} = -j$.

$$\frac{dc_b}{dt} = \frac{j}{\hbar}E(t)\sum_i \mu_{bi}c_i(t)\,e^{j(\omega_b-\omega_i)t} \tag{A.22}$$

(Any one) $|i\rangle$ ***coefficient:***

$$\begin{aligned} j\hbar&\left[\frac{dc_i}{dt}e^{-j\omega_i t} + c_i(t)\left(-j\omega_i e^{-j\omega_i t}\right)\right] \\ &= \hbar\omega_i c_i(t)\,e^{-j\omega_i t} - E^*(t)\,\mu_{ai}^* c_a(t)\,e^{-j\omega_a t} - E^*(t)\,\mu_{bi}^* c_b(t)\,e^{-j\omega_b t} \end{aligned} \tag{A.23}$$

Cancellation of the common $c_i(t)$ term yields

$$j\hbar\frac{dc_i}{dt}e^{-j\omega_i t} = -E^*(t)\,\mu_{ai}^* c_a(t)\,e^{-j\omega_a t} - E^*(t)\,\mu_{bi}^* c_b(t)\,e^{-j\omega_b t}. \tag{A.24}$$

Solve for $\frac{dc_i}{dt}$ using $\frac{1}{j} = -j$.

$$\frac{dc_i}{dt} = \frac{j}{\hbar}E^*(t)\left[\mu_{ai}^* c_a(t)\,e^{j(\omega_i-\omega_a)t} + \mu_{bi}^* c_b(t)\,e^{j(\omega_i-\omega_b)t}\right] \tag{A.25}$$

Now use the fact that the total (physical and therefore real) electric field, $E(t)$, is the sum of the Raman sidebands:

$$E(t) = \frac{1}{2}\sum_q E_q e^{j(\omega_q t - k_q z)} + \frac{1}{2}\sum_q E_q^* e^{-j(\omega_q t - k_q z)}, \tag{A.26}$$

where $k_q \equiv \frac{\omega_q}{c}$ from the free space dispersion relation, which is valid because we assume a dilute gas of molecules.

Substitute the expression for $E(t)$ (Equation A.26) into the equation for $\frac{dc_a}{dt}$ (Equation A.19).

$$\begin{aligned} \frac{dc_a}{dt} &= \frac{j}{\hbar}\left[\frac{1}{2}\sum_q E_q e^{j(\omega_q t-k_q z)} + \frac{1}{2}\sum_q E_q^* e^{-j(\omega_q t-k_q z)}\right]\sum_i \mu_{ai}c_i(t)\,e^{j(\omega_a-\omega_i)t} \\ &= \frac{j}{2\hbar}\sum_q\sum_i\left[E_q\mu_{ai}e^{j(\omega_q+\omega_a-\omega_i)t-jk_q z} + E_q^*\mu_{ai}e^{j(-\omega_q+\omega_a-\omega_i)t+jk_q z}\right]c_i(t) \end{aligned} \tag{A.27}$$

An analogous substitution of the same expression for $E(t)$ (Equation A.26) into the equation for $\frac{dc_b}{dt}$ (Equation A.22) yields

$$\begin{aligned}\frac{dc_b}{dt} &= \frac{j}{\hbar}\left[\frac{1}{2}\sum_q E_q e^{j(\omega_q t - k_q z)} + \frac{1}{2}\sum_q E_q^* e^{-j(\omega_q t - k_q z)}\right]\sum_i \mu_{bi} c_i(t)\, e^{j(\omega_b-\omega_i)t} \\ &= \frac{j}{2\hbar}\sum_q\sum_i \left[E_q \mu_{bi} e^{j(\omega_q+\omega_b-\omega_i)t - jk_q z} + E_q^* \mu_{bi} e^{j(-\omega_q+\omega_b-\omega_i)t + jk_q z}\right] c_i(t)\end{aligned}$$

. (A.28)

Substitute the equation for $E(t)$ (Equation A.26) in the equation for $\frac{dc_i}{dt}$ (Equation A.25).

$$\begin{aligned}\frac{dc_i}{dt} &= \frac{j}{\hbar}\left[\frac{1}{2}\sum_q E_q e^{j(\omega_q t - k_q z)} + \frac{1}{2}\sum_q E_q^* e^{-j(\omega_q t - k_q z)}\right]^* \\ &\quad \times\left[\mu_{ai}^* c_a(t)\, e^{j(\omega_i-\omega_a)t} + \mu_{bi}^* c_b(t)\, e^{j(\omega_i-\omega_b)t}\right] \\ &= \frac{j}{2\hbar}\sum_q\Big[E_q \mu_{ai}^* c_a(t)\, e^{j(\omega_q+\omega_i-\omega_a)t - jk_q z} + E_q^* \mu_{ai}^* c_a(t)\, e^{j(-\omega_q+\omega_i-\omega_a)t + jk_q z} \\ &\quad + E_q \mu_{bi}^* c_b(t)\, e^{j(\omega_q+\omega_i-\omega_b)t - jk_q z} + E_q^* \mu_{bi}^* c_b(t)\, e^{j(-\omega_q+\omega_i-\omega_b)t + jk_q z}\Big]\end{aligned}$$

(A.29)

Now assume that the upper electronic ro-vibrational states are outside of the range of single-photon resonances. This implies that the variation in the exponentials in the previous equation is significantly faster than the variation of the E_q envelopes. Thus, $c_i(t)$ can be found by integrating the derivative with respect to time, treating the slowly-varying $c_a(t) \equiv c_a$, $c_b(t) \equiv c_b$, and E_q as constants.

Perform a formal integration on $\frac{dc_i}{dt}$ (Equation A.29), and use $\int e^{\alpha t+\beta z} dt = \frac{e^{\alpha t+\beta z}}{\alpha}$, to find

$$\begin{aligned}c_i(t) &= \frac{j}{2\hbar}\sum_q\left[\frac{E_q \mu_{ai}^* c_a}{j(\omega_q+\omega_i-\omega_a)} e^{j(\omega_q+\omega_i-\omega_a)t - jk_q z} + \frac{E_q^* \mu_{ai}^* c_a}{j(-\omega_q+\omega_i-\omega_a)} e^{j(-\omega_q+\omega_i-\omega_a)t + jk_q z}\right. \\ &\quad \left. + \frac{E_q \mu_{bi}^* c_b}{j(\omega_q+\omega_i-\omega_b)} e^{j(\omega_q+\omega_i-\omega_b)t - jk_q z} + \frac{E_q^* \mu_{bi}^* c_b}{j(-\omega_q+\omega_i-\omega_b)} e^{j(-\omega_q+\omega_i-\omega_b)t + jk_q z}\right].\end{aligned}$$

(A.30)

Cancel the factor of j.

$$= \frac{1}{2\hbar}\sum_q \left[\frac{E_q \mu_{ai}^* c_a}{(\omega_q + \omega_i - \omega_a)} e^{j(\omega_q+\omega_i-\omega_a)t - jk_q z} + \frac{E_q^* \mu_{ai}^* c_a}{(-\omega_q + \omega_i - \omega_a)} e^{j(-\omega_q+\omega_i-\omega_a)t + jk_q z} \right.$$
$$\left. + \frac{E_q \mu_{bi}^* c_b}{(\omega_q + \omega_i - \omega_b)} e^{j(\omega_q+\omega_i-\omega_b)t - jk_q z} + \frac{E_q^* \mu_{bi}^* c_b}{(-\omega_q + \omega_i - \omega_b)} e^{j(-\omega_q+\omega_i-\omega_b)t + jk_q z} \right] \tag{A.31}$$

Substitute this expression for $c_i\,(t)$ (Equation A.31) into the expression for $\frac{dc_a}{dt}$ (Equation A.27).

$$\frac{dc_a}{dt} = \frac{j}{2\hbar}\sum_q \sum_i \left[E_q \mu_{ai} e^{j(\omega_q+\omega_a-\omega_i)t - jk_q z} + E_q^* \mu_{ai} e^{j(-\omega_q+\omega_a-\omega_i)t + jk_q z} \right]$$
$$\times \frac{1}{2\hbar}\sum_q \left[\frac{E_q \mu_{ai}^* c_a}{\omega_q + \omega_i - \omega_a} e^{j(\omega_q+\omega_i-\omega_a)t - jk_q z} + \frac{E_q^* \mu_{ai}^* c_a}{-\omega_q + \omega_i - \omega_a} e^{j(-\omega_q+\omega_i-\omega_a)t + jk_q z} \right.$$
$$\left. + \frac{E_q \mu_{bi}^* c_b}{\omega_q + \omega_i - \omega_b} e^{j(\omega_q+\omega_i-\omega_b)t - jk_q z} + \frac{E_q^* \mu_{bi}^* c_b}{-\omega_q + \omega_i - \omega_b} e^{j(-\omega_q+\omega_i-\omega_b)t + jk_q z} \right] \tag{A.32}$$

Distribute. (In the third sum of the equation above, replace the dummy index of q with y to avoid confusion.)

$$
\begin{aligned}
&\frac{dc_a}{dt} \\
&= \sum_i \left(\frac{j}{2\hbar} \sum_q \left[E_q \mu_{ai} e^{j(\omega_q+\omega_a-\omega_i)t-jk_qz} \right] \right) \left(\frac{1}{2\hbar} \sum_y \left[\frac{E_y \mu_{ai}^* c_a}{\omega_y+\omega_i-\omega_a} e^{j(\omega_y+\omega_i-\omega_a)t-jk_yz} \right] \right) \\
&+ \sum_i \left(\frac{j}{2\hbar} \sum_q \left[E_q \mu_{ai} e^{j(\omega_q+\omega_a-\omega_i)t-jk_qz} \right] \right) \left(\frac{1}{2\hbar} \sum_y \left[\frac{E_y^* \mu_{ai}^* c_a}{-\omega_y+\omega_i-\omega_a} e^{j(-\omega_y+\omega_i-\omega_a)t+jk_yz} \right] \right) \\
&+ \sum_i \left(\frac{j}{2\hbar} \sum_q \left[E_q \mu_{ai} e^{j(\omega_q+\omega_a-\omega_i)t-jk_qz} \right] \right) \left(\frac{1}{2\hbar} \sum_y \left[\frac{E_y \mu_{bi}^* c_b}{\omega_y+\omega_i-\omega_b} e^{j(\omega_y+\omega_i-\omega_b)t-jk_yz} \right] \right) \\
&+ \sum_i \left(\frac{j}{2\hbar} \sum_q \left[E_q \mu_{ai} e^{j(\omega_q+\omega_a-\omega_i)t-jk_qz} \right] \right) \left(\frac{1}{2\hbar} \sum_y \left[\frac{E_y^* \mu_{bi}^* c_b}{-\omega_y+\omega_i-\omega_b} e^{j(-\omega_y+\omega_i-\omega_b)t+jk_yz} \right] \right) \\
&+ \sum_i \left(\frac{j}{2\hbar} \sum_q \left[E_q^* \mu_{ai} e^{j(-\omega_q+\omega_a-\omega_i)t+jk_qz} \right] \right) \left(\frac{1}{2\hbar} \sum_y \left[\frac{E_y \mu_{ai}^* c_a}{\omega_y+\omega_i-\omega_a} e^{j(\omega_y+\omega_i-\omega_a)t-jk_yz} \right] \right) \\
&+ \sum_i \left(\frac{j}{2\hbar} \sum_q \left[E_q^* \mu_{ai} e^{j(-\omega_q+\omega_a-\omega_i)t+jk_qz} \right] \right) \left(\frac{1}{2\hbar} \sum_y \left[\frac{E_y^* \mu_{ai}^* c_a}{-\omega_y+\omega_i-\omega_a} e^{j(-\omega_y+\omega_i-\omega_a)t+jk_yz} \right] \right) \\
&+ \sum_i \left(\frac{j}{2\hbar} \sum_q \left[E_q^* \mu_{ai} e^{j(-\omega_q+\omega_a-\omega_i)t+jk_qz} \right] \right) \left(\frac{1}{2\hbar} \sum_y \left[\frac{E_y \mu_{bi}^* c_b}{\omega_y+\omega_i-\omega_b} e^{j(\omega_y+\omega_i-\omega_b)t-jk_yz} \right] \right) \\
&+ \sum_i \left(\frac{j}{2\hbar} \sum_q \left[E_q^* \mu_{ai} e^{j(-\omega_q+\omega_a-\omega_i)t+jk_qz} \right] \right) \left(\frac{1}{2\hbar} \sum_y \left[\frac{E_y^* \mu_{bi}^* c_b}{-\omega_y+\omega_i-\omega_b} e^{j(-\omega_y+\omega_i-\omega_b)t+jk_yz} \right] \right)
\end{aligned}
\tag{A.33}
$$

Distribute in each term, pulling constant terms out of the sums.

$$
\begin{aligned}
&\frac{dc_a}{dt} \\
= \;& \frac{j}{4\hbar^2}\sum_i |\mu_{ai}|^2 \left(\sum_q \left[E_q e^{j\omega_q t - jk_q z}\right]\right)\left(\sum_y \left[\frac{E_y}{\omega_y+\omega_i-\omega_a} e^{j\omega_y t - jk_y z}\right]\right) c_a \\
+ \;& \frac{j}{4\hbar^2}\sum_i |\mu_{ai}|^2 \left(\sum_q \left[E_q e^{j\omega_q t - jk_q z}\right]\right)\left(\sum_y \left[\frac{E_y^*}{-\omega_y+\omega_i-\omega_a} e^{-j\omega_y t + jk_y z}\right]\right) c_a \\
+ \;& \frac{j}{4\hbar^2}\sum_i \mu_{ai}\mu_{bi}^* \left(\sum_q \left[E_q e^{j\omega_q t - jk_q z}\right]\right)\left(\sum_y \left[\frac{E_y}{\omega_y+\omega_i-\omega_b} e^{j\omega_y t - jk_y z}\right]\right) c_b e^{j(\omega_a-\omega_b)t} \\
+ \;& \frac{j}{4\hbar^2}\sum_i \mu_{ai}\mu_{bi}^* \left(\sum_q \left[E_q e^{j\omega_q t - jk_q z}\right]\right)\left(\sum_y \left[\frac{E_y^*}{-\omega_y+\omega_i-\omega_b} e^{-j\omega_y t + jk_y z}\right]\right) c_b e^{j(\omega_a-\omega_b)t} \\
+ \;& \frac{j}{4\hbar^2}\sum_i |\mu_{ai}|^2 \left(\sum_q \left[E_q^* e^{-j\omega_q t + jk_q z}\right]\right)\left(\sum_y \left[\frac{E_y}{\omega_y+\omega_i-\omega_a} e^{j\omega_y t - jk_y z}\right]\right) c_a \\
+ \;& \frac{j}{4\hbar^2}\sum_i |\mu_{ai}|^2 \left(\sum_q \left[E_q^* e^{-j\omega_q t + jk_q z}\right]\right)\left(\sum_y \left[\frac{E_y^*}{-\omega_y+\omega_i-\omega_a} e^{-j\omega_y t + jk_y z}\right]\right) c_a \\
+ \;& \frac{j}{4\hbar^2}\sum_i \mu_{ai}\mu_{bi}^* \left(\sum_q \left[E_q^* e^{-j\omega_q t + jk_q z}\right]\right)\left(\sum_y \left[\frac{E_y}{\omega_y+\omega_i-\omega_b} e^{j\omega_y t - jk_y z}\right]\right) c_b e^{j(\omega_a-\omega_b)t} \\
+ \;& \frac{j}{4\hbar^2}\sum_i \mu_{ai}\mu_{bi}^* \left(\sum_q \left[E_q^* e^{-j\omega_q t + jk_q z}\right]\right)\left(\sum_y \left[\frac{E_y^*}{-\omega_y+\omega_i-\omega_b} e^{-j\omega_y t + jk_y z}\right]\right) c_b e^{j(\omega_a-\omega_b)t}
\end{aligned}
\tag{A.34}
$$

Now assume that the two-photon transition is near resonance, and use the rotating wave approximation: neglect all terms that rapidly oscillate. Examine each individual line of the above expression for $\frac{dc_a}{dt}$ (Equation A.34).

In the first line, the time dependence goes as

$$
\sum_q \left[e^{j\omega_q t}\right]\left(\sum_y \left[e^{j\omega_y t}\right]\right). \tag{A.35}
$$

Note that the terms in this product of sums have the form

$$
e^{j\omega_q t}\left(e^{j\omega_y t}\right) = e^{j(\omega_q+\omega_y)t}. \tag{A.36}
$$

Use the definition of ω_q (Equation A.1).

$$\begin{aligned} &= e^{j\{[\omega_0+q\omega_m]+[\omega_0+y\omega_m]\}t} \\ &= e^{j[2\omega_0+(q+y)\omega_m]t}. \end{aligned} \tag{A.37}$$

$\omega_0 \gg \omega_m$, so for any values of q and y, the first term dominates. Thus, each term oscillates at least as fast as $e^{j2\omega_0 t}$ and can be neglected under the rotating wave approximation. Since all terms in the product of sums are negligible, the first line of the expression for $\frac{dc_a}{dt}$ (Equation A.34) contributes nothing.

In the second line of the expression for $\frac{dc_a}{dt}$ (Equation A.34), the time dependence of each term goes as

$$e^{j\omega_q t}\left(e^{-j\omega_y t}\right) = e^{j(\omega_q-\omega_y)t}. \tag{A.38}$$

The definition of ω_q (Equation A.1) yields

$$\begin{aligned} &= e^{j\{[\omega_0+q\omega_m]-[\omega_0+y\omega_m]\}t} \\ &= e^{j[(q-y)\omega_m]t}. \end{aligned} \tag{A.39}$$

For $q \neq y$, these terms oscillate at least as fast as $e^{j\omega_m t}$ and can be neglected. Only the $q = y$ terms survive.

Thus, under the rotating wave approximation, setting the dummy variable $y = q$, the second line of the expression for $\frac{dc_a}{dt}$ (Equation A.34) is reduced to the following:

$$\begin{aligned} &\frac{j}{4\hbar^2}\sum_i \left|\mu_{ai}\right|^2 \left(\sum_q \left[E_q e^{j\omega_q t - jk_q z}\right]\right)\left(\sum_q \left[\frac{E_q^*}{-\omega_q+\omega_i-\omega_a} e^{-j\omega_q t+jk_q z}\right]\right) c_a \\ = &\frac{j}{4\hbar^2}\sum_i \left|\mu_{ai}\right|^2 \sum_q \frac{\left|E_q\right|^2}{-\omega_q+\omega_i-\omega_a}\left[e^{j\omega_q t-jk_q z}\right]\left[e^{-j\omega_q t+jk_q z}\right] c_a \\ = &\frac{j}{4\hbar^2}\sum_i \left|\mu_{ai}\right|^2 \sum_q \frac{\left|E_q\right|^2}{-\omega_q+\omega_i-\omega_a} c_a. \end{aligned} \tag{A.40}$$

In the third line of the expression for $\frac{dc_a}{dt}$ (Equation A.34), the time dependence of each term goes as

$$e^{j\omega_q t}\left(e^{j\omega_y t}\right) e^{j(\omega_a-\omega_b)t} = e^{j(\omega_q+\omega_y+\omega_a-\omega_b)t}. \tag{A.41}$$

Insert the definition of ω_q (Equation A.1) and then that of ω_m (Equation A.2).

$$\begin{aligned} &= e^{j([\omega_0+q\omega_m]+[\omega_0+y\omega_m]+\omega_a-\omega_b)t} \\ &= e^{j\{[\omega_0+q(\omega_b-\omega_a-\Delta\omega)]+[\omega_0+y(\omega_b-\omega_a-\Delta\omega)]+\omega_a-\omega_b\}t} \\ &= e^{j\{2\omega_0+(q+y-1)(\omega_b-\omega_a)-(q+y)\Delta\omega\}t} \end{aligned} \tag{A.42}$$

Since $\omega_0 \gg (\omega_b - \omega_a) \gg \Delta\omega$, this oscillates approximately as $e^{j2\omega_0 t}$ and can be neglected. Thus, the contributions of the third line of the expression for $\frac{dc_a}{dt}$ (Equation A.34) vanish.

In the fourth line of the expression for $\frac{dc_a}{dt}$ (Equation A.34), the time dependence of each term goes as

$$e^{j\omega_q t}\left(e^{-j\omega_y t}\right)e^{j(\omega_a-\omega_b)t} = e^{j(\omega_q-\omega_y+\omega_a-\omega_b)t}. \tag{A.43}$$

Substitute for ω_q (Equation A.1) and ω_m (Equation A.2) as above.

$$\begin{aligned} &= e^{j([\omega_0+q\omega_m]-[\omega_0+y\omega_m]+\omega_a-\omega_b)t} \\ &= e^{j\{[\omega_0+q(\omega_b-\omega_a-\Delta\omega)]-[\omega_0+y(\omega_b-\omega_a-\Delta\omega)]+\omega_a-\omega_b\}t} \\ &= e^{j\{(q-y-1)(\omega_b-\omega_a)-(q-y)\Delta\omega\}t} \end{aligned} \tag{A.44}$$

Since $(\omega_b - \omega_a) \gg \Delta\omega$, the first term dominates. Thus, the time dependence is approximately

$$e^{j(q-y-1)(\omega_b-\omega_a)t} \tag{A.45}$$

Unless $q - y - 1 = 0 \Rightarrow y = q - 1$, this oscillates at least as fast as $e^{j(\omega_b-\omega_a)t}$ and thus vanishes with the rotating wave approximation.

The fourth line of the expression for $\frac{dc_a}{dt}$ (Equation A.34) is then reduced to the following by setting $y = q - 1$.

$$\begin{aligned} &\frac{j}{4\hbar^2}\sum_i \mu_{ai}\mu_{bi}^*\left(\sum_q \left[E_q e^{j\omega_q t - jk_q z}\right]\right)\left(\sum_{q-1}\left[\frac{E_{q-1}^*}{-\omega_{q-1}+\omega_i-\omega_b}e^{-j\omega_{q-1}t+jk_{q-1}z}\right]\right)c_b e^{j(\omega_a-\omega_b)t} \\ = \;& \frac{j}{4\hbar^2}\sum_i \mu_{ai}\mu_{bi}^*\sum_q \frac{E_q E_{q-1}^*}{-\omega_{q-1}+\omega_i-\omega_b}\left[e^{j(\omega_q-\omega_{q-1}+\omega_a-\omega_b)t+j(-k_q+k_{q-1})z}\right]c_b \end{aligned} \tag{A.46}$$

Now rewrite this expression. Examine the denominator.

$$-\omega_{q-1}+\omega_i-\omega_b \tag{A.47}$$

First rewrite ω_{q-1} using the definition of ω_q (Equation A.1).

$$\begin{aligned} \omega_{q-1} &= \omega_0 + (q-1)\,\omega_m \\ &= (\omega_0 + q\omega_m) - \omega_m \\ &= \omega_q - \omega_m \end{aligned} \tag{A.48}$$

Plug this into the denominator (Equation A.47).

$$\begin{aligned} -\omega_{q-1} + \omega_i - \omega_b &= -(\omega_q - \omega_m) + \omega_i - \omega_b \\ &= -\omega_q + \omega_m + \omega_i - \omega_b \end{aligned} \tag{A.49}$$

Use the definition of ω_m (Equation A.2).

$$\begin{aligned} &= -\omega_q + (\omega_b - \omega_a - \Delta\omega) + \omega_i - \omega_b \\ &= -\omega_q - \omega_a - \Delta\omega + \omega_i \end{aligned} \tag{A.50}$$

Now use the fact that $(\omega_b - \omega_a) \gg \Delta\omega$ and $\omega_i \gg \Delta\omega$, and the denominator (Equation A.47) becomes approximately

$$\approx -\omega_q - \omega_a + \omega_i. \tag{A.51}$$

Now examine $\omega_q - \omega_{q-1} + \omega_a - \omega_b$ from the exponent of the expression for the fourth line (Equation A.46).

Using the results from above (Equation A.48),

$$\begin{aligned} \omega_q - \omega_{q-1} + \omega_a - \omega_b &= \omega_q - (\omega_q - \omega_m) + \omega_a - \omega_b \\ &= \omega_m + \omega_a - \omega_b. \end{aligned} \tag{A.52}$$

Use the definition of ω_m (Equation A.2).

$$\begin{aligned} &= (\omega_b - \omega_a - \Delta\omega) + \omega_a - \omega_b \\ &= -\Delta\omega \end{aligned} \tag{A.53}$$

Another term in the exponent of the fourth line (Equation A.46), $-k_q + k_{q-1}$, can be rewritten in a similar manner.

Using the definition

$$k_q \equiv k_0 + qk_m, \tag{A.54}$$

rewrite the term as follows:

$$-k_q + k_{q-1} = -\left(k_0 + qk_m\right) + \left(k_0 + \left[q-1\right]k_m\right) = -k_m. \tag{A.55}$$

Now plug the above (Equations A.51, A.53, and A.55) into the fourth line of the equation (Equation A.46).

$$\begin{aligned} & \frac{j}{4\hbar^2}\sum_i \mu_{ai}\mu_{bi}^* \sum_q \frac{E_q E_{q-1}^*}{-\omega_{q-1}+\omega_i-\omega_b}\left[e^{j(\omega_q-\omega_{q-1}+\omega_a-\omega_b)t+j(-k_q+k_{q-1})z}\right] c_b \\ = \; & \frac{j}{4\hbar^2}\sum_i \mu_{ai}\mu_{bi}^* \sum_q \frac{E_q E_{q-1}^*}{-\omega_q-\omega_a+\omega_i}\left(e^{-j\Delta\omega t - jk_m z}\right) c_b \end{aligned} \tag{A.56}$$

Now examine the fifth line of the expression for $\frac{dc_a}{dt}$ (Equation A.34). The time dependence of each term goes as

$$e^{-j\omega_q t}\left(e^{j\omega_y t}\right) = e^{j(-\omega_q+\omega_y)t}. \tag{A.57}$$

The argument is analogous to that of the second line with the only difference being a sign switch between ω_q and ω_y.

The definition of ω_q (Equation A.1) yields

$$e^{j\{-[\omega_0+q\omega_m]+[\omega_0+y\omega_m]\}t} = e^{j[(-q+y)\omega_m]t}. \tag{A.58}$$

For $q \neq y$, these terms oscillate at least as fast as $e^{j\omega_m t}$ and can be neglected. Only $q = y$ terms survive.

Thus, under the rotating wave approximation, the fifth line of the expression for $\frac{dc_a}{dt}$ (Equation A.34) is reduced to the following by setting $y = q$.

$$\begin{aligned} & \frac{j}{4\hbar^2}\sum_i \left|\mu_{ai}\right|^2 \left(\sum_q \left[E_q e^{-j\omega_q t + jk_q z}\right]\right)\left(\sum_q \left[\frac{E_q^*}{\omega_q+\omega_i-\omega_a}e^{j\omega_q t - jk_q z}\right]\right) c_a \\ = \; & \frac{j}{4\hbar^2}\sum_i \left|\mu_{ai}\right|^2 \sum_q \frac{\left|E_q\right|^2}{\omega_q+\omega_i-\omega_a}\left[e^{-j\omega_q t+jk_q z}\right]\left[e^{j\omega_q t - jk_q z}\right] c_a \\ = \; & \frac{j}{4\hbar^2}\sum_i \left|\mu_{ai}\right|^2 \sum_q \frac{\left|E_q\right|^2}{\omega_q+\omega_i-\omega_a} c_a \end{aligned} \tag{A.59}$$

Examine the sixth line of the expression for $\frac{dc_a}{dt}$ (Equation A.34). This, up to a negative sign, is the same as the first line. The time dependence of each term goes as

$$e^{-j\omega_q t}\left(e^{-j\omega_y t}\right) = e^{-j(\omega_q+\omega_y)t}. \tag{A.60}$$

Use the definition ω_q (Equation A.1).

$$\begin{aligned} &= e^{-j\{[\omega_0+q\omega_m]+[\omega_0+y\omega_m]\}t} \\ &= e^{-j[2\omega_0+(q+y)\omega_m]t} \end{aligned} \tag{A.61}$$

$\omega_0 \gg \omega_m$, so for any values of q and y, the first term dominates. Thus, each term oscillates at least as fast as $e^{j2\omega_0 t}$ and can be neglected under the rotating wave approximation. Since all terms in the product of sums are negligible, the sixth line of the expression for $\frac{dc_a}{dt}$ (Equation A.34) contributes nothing.

Examine the seventh line of the expression for $\frac{dc_a}{dt}$ (Equation A.34). This is similar to the fourth line with a change of signs. The time dependence of each term goes as

$$e^{-j\omega_q t}\left(e^{j\omega_y t}\right)e^{j(\omega_a-\omega_b)t} = e^{j(-\omega_q+\omega_y+\omega_a-\omega_b)t}. \tag{A.62}$$

Substituting for ω_q and ω_m (Equations A.1 and A.2) as above, this yields

$$\begin{aligned} &= e^{j(-[\omega_0+q\omega_m]+[\omega_0+y\omega_m]+\omega_a-\omega_b)t} \\ &= e^{j\{-[\omega_0+q(\omega_b-\omega_a-\Delta\omega)]+[\omega_0+y(\omega_b-\omega_a-\Delta\omega)]+\omega_a-\omega_b\}t} \\ &= e^{j\{(-q+y-1)(\omega_b-\omega_a)+(q-y)\Delta\omega\}t}. \end{aligned} \tag{A.63}$$

Since $(\omega_b-\omega_a) \gg \Delta\omega$, the first term dominates, so the time dependence is approximately $e^{j(-q+y-1)(\omega_b-\omega_a)t}$. Unless $-q+y-1=0 \Rightarrow q=y-1$, this oscillates at least as fast as $e^{j(\omega_b-\omega_a)t}$ and thus vanishes.

The seventh line of the expression for $\frac{dc_a}{dt}$ (Equation A.34) is then reduced to the following by setting $q=y-1$.

$$\begin{aligned} &\frac{j}{4\hbar^2}\sum_i \mu_{ai}\mu_{bi}^*\left(\sum_{y-1}\left[E_{y-1}^* e^{-j\omega_{y-1}t+jk_{y-1}z}\right]\right)\left(\sum_y\left[\frac{E_y}{\omega_y+\omega_i-\omega_b}e^{j\omega_y t-jk_y z}\right]\right)c_b e^{j(\omega_a-\omega_b)t} \\ = &\frac{j}{4\hbar^2}\sum_i \mu_{ai}\mu_{bi}^*\sum_y \frac{E_{y-1}^* E_y}{\omega_y+\omega_i-\omega_b}\left[e^{j(-\omega_{y-1}+\omega_y+\omega_a-\omega_b)t+j(k_{y-1}-k_y)z}\right]c_b \end{aligned} \tag{A.64}$$

Rewrite the exponent of this expression.

Use the definition of ω_q (Equation A.1).

$$\begin{aligned} -\omega_{y-1} + \omega_y + \omega_a - \omega_b &= -\left(\omega_0 + [y-1]\,\omega_m\right) + \omega_y + \omega_a - \omega_b \\ &= -\left[(\omega_0 + y\omega_m) - \omega_m\right] + \omega_y + \omega_a - \omega_b \\ &= -\left[\omega_y - \omega_m\right] + \omega_y + \omega_a - \omega_b \\ &= \omega_m + \omega_a - \omega_b \end{aligned} \tag{A.65}$$

Use the definition of ω_m (Equation A.2).

$$\begin{aligned} &= (\omega_b - \omega_a - \Delta\omega) + \omega_a - \omega_b \\ &= -\Delta\omega \end{aligned} \tag{A.66}$$

Another term in the exponent, $k_{y-1} - k_y$, can be rewritten in a similar manner.

Use the definition of k_q (Equation A.54).

$$\begin{aligned} k_{y-1} - k_y &= (k_0 + [y-1]\,k_m) - (k_0 + yk_m) \\ &= -k_m \end{aligned} \tag{A.67}$$

Now plug in the above equations (Equations A.66 and A.67) in the expression for the seventh line above (A.64). The seventh line of the expression for $\frac{dc_a}{dt}$ (Equation A.34) becomes

$$\begin{aligned} &\frac{j}{4\hbar^2} \sum_i \mu_{ai}\mu_{bi}^* \sum_y \frac{E_{y-1}^* E_y}{\omega_y + \omega_i - \omega_b} \left[e^{j(-\omega_{y-1} + \omega_y + \omega_a - \omega_b)t + j(k_{y-1} - k_y)z}\right] c_b \\ = \;& \frac{j}{4\hbar^2} \sum_i \mu_{ai}\mu_{bi}^* \sum_y \frac{E_{y-1}^* E_y}{\omega_y + \omega_i - \omega_b} \left(e^{-j\Delta\omega t - jk_m z}\right) c_b. \end{aligned} \tag{A.68}$$

Now examine the eighth line of the expression for $\frac{dc_a}{dt}$ (Equation A.34). It is similar to the third line. The time dependence goes as

$$e^{-j\omega_q t}\left(e^{-j\omega_y t}\right) e^{j(\omega_a - \omega_b)t} = e^{j(-\omega_q - \omega_y + \omega_a - \omega_b)t}. \tag{A.69}$$

Insert the definitions of ω_q and ω_m (Equations A.1 and A.2).

$$\begin{aligned} &= e^{j(-[\omega_0+q\omega_m]-[\omega_0+y\omega_m]+\omega_a-\omega_b)t} \\ &= e^{j\{-[\omega_0+q(\omega_b-\omega_a-\Delta\omega)]-[\omega_0+y(\omega_b-\omega_a-\Delta\omega)]+\omega_a-\omega_b\}t} \\ &= e^{j\{-2\omega_0-(q+y+1)(\omega_b-\omega_a)+(q+y)\Delta\omega\}t} \end{aligned} \tag{A.70}$$

Since $\omega_0 \gg (\omega_b - \omega_a) \gg \Delta\omega$, this oscillates approximately as $e^{-j2\omega_0 t}$ and can be neglected. Thus, the contributions of the eighth line of the expression for $\frac{dc_a}{dt}$ (Equation A.34) vanish.

Therefore, under the rotating wave approximation, the only nonvanishing contributions to the expression for $\frac{dc_a}{dt}$ (Equation A.34) are from the second, fourth, fifth, and seventh lines (Equations A.40, A.56, A.59, and A.68). Summing the contributions from these lines yields the following approximation of the expression for $\frac{dc_a}{dt}$ (Equation A.34). (Change the dummy variable y to q in Equation A.68 to match the other equations).

$$\begin{aligned} \frac{dc_a}{dt} &= \frac{j}{4\hbar^2}\sum_i |\mu_{ai}|^2 \sum_q \frac{|E_q|^2}{-\omega_q+\omega_i-\omega_a} c_a \\ &+ \frac{j}{4\hbar^2}\sum_i \mu_{ai}\mu_{bi}^* \sum_q \frac{E_q E_{q-1}^*}{-\omega_q-\omega_a+\omega_i} \left(e^{-j\Delta\omega t - jk_m z}\right) c_b \\ &+ \frac{j}{4\hbar^2}\sum_i |\mu_{ai}|^2 \sum_q \frac{|E_q|^2}{\omega_q+\omega_i-\omega_a} c_a \\ &+ \frac{j}{4\hbar^2}\sum_i \mu_{ai}\mu_{bi}^* \sum_q \frac{E_{q-1}^* E_q}{\omega_q+\omega_i-\omega_b} \left(e^{-j\Delta\omega t - jk_m z}\right) c_b \end{aligned} \tag{A.71}$$

Now for the equation for $\frac{dc_b}{dt}$. This is very similar to the process for $\frac{dc_a}{dt}$.

Plug the expression for $c_i\,(t)$ (Equation A.31) into the expression for $\frac{dc_b}{dt}$ (Equation A.28).

$$\begin{aligned}\frac{dc_b}{dt} &= \frac{j}{2\hbar}\sum_q\sum_i\left[E_q\mu_{bi}e^{j(\omega_q+\omega_b-\omega_i)t-jk_qz}+E_q^*\mu_{bi}e^{j(-\omega_q+\omega_b-\omega_i)t+jk_qz}\right]\\ &\times\frac{1}{2\hbar}\sum_q\left[\frac{E_q\mu_{ai}^*c_a}{(\omega_q+\omega_i-\omega_a)}e^{j(\omega_q+\omega_i-\omega_a)t-jk_qz}\right.\\ &+\frac{E_q^*\mu_{ai}^*c_a}{(-\omega_q+\omega_i-\omega_a)}e^{j(-\omega_q+\omega_i-\omega_a)t+jk_qz}\\ &+\frac{E_q\mu_{bi}^*c_b}{(\omega_q+\omega_i-\omega_b)}e^{j(\omega_q+\omega_i-\omega_b)t-jk_qz}\\ &\left.+\frac{E_q^*\mu_{bi}^*c_b}{(-\omega_q+\omega_i-\omega_b)}e^{j(-\omega_q+\omega_i-\omega_b)t+jk_qz}\right]\end{aligned}\tag{A.72}$$

Note that this is very similar to the expression for $\frac{dc_a}{dt}$ (Equation A.32). The only difference between the equations (Equations A.32 and A.72) is that a is replaced by b in the first term. Thus, since the second term is symmetric under the interchange of a and b, we can use the results for $\frac{dc_a}{dt}$ (Equation A.34) interchanging a and b.

$$
\begin{aligned}
&\frac{dc_b}{dt} \\
= \;& \frac{j}{4\hbar^2}\sum_i |\mu_{bi}|^2 \left(\sum_q \left[E_q e^{j\omega_q t - jk_q z}\right]\right)\left(\sum_y \left[\frac{E_y}{\omega_y+\omega_i-\omega_b} e^{j\omega_y t - jk_y z}\right]\right) c_b \\
+ \;& \frac{j}{4\hbar^2}\sum_i |\mu_{bi}|^2 \left(\sum_q \left[E_q e^{j\omega_q t - jk_q z}\right]\right)\left(\sum_y \left[\frac{E_y^*}{-\omega_y+\omega_i-\omega_b} e^{-j\omega_y t + jk_y z}\right]\right) c_b \\
+ \;& \frac{j}{4\hbar^2}\sum_i \mu_{bi}\mu_{ai}^* \left(\sum_q \left[E_q e^{j\omega_q t - jk_q z}\right]\right)\left(\sum_y \left[\frac{E_y}{\omega_y+\omega_i-\omega_a} e^{j\omega_y t - jk_y z}\right]\right) c_a e^{j(\omega_b-\omega_a)t} \\
+ \;& \frac{j}{4\hbar^2}\sum_i \mu_{bi}\mu_{ai}^* \left(\sum_q \left[E_q e^{j\omega_q t - jk_q z}\right]\right)\left(\sum_y \left[\frac{E_y^*}{-\omega_y+\omega_i-\omega_a} e^{-j\omega_y t + jk_y z}\right]\right) c_a e^{j(\omega_b-\omega_a)t} \\
+ \;& \frac{j}{4\hbar^2}\sum_i |\mu_{bi}|^2 \left(\sum_q \left[E_q^* e^{-j\omega_q t + jk_q z}\right]\right)\left(\sum_y \left[\frac{E_y}{\omega_y+\omega_i-\omega_b} e^{j\omega_y t - jk_y z}\right]\right) c_b \\
+ \;& \frac{j}{4\hbar^2}\sum_i |\mu_{bi}|^2 \left(\sum_q \left[E_q^* e^{-j\omega_q t + jk_q z}\right]\right)\left(\sum_y \left[\frac{E_y^*}{-\omega_y+\omega_i-\omega_b} e^{-j\omega_y t + jk_y z}\right]\right) c_b \\
+ \;& \frac{j}{4\hbar^2}\sum_i \mu_{bi}\mu_{ai}^* \left(\sum_q \left[E_q^* e^{-j\omega_q t + jk_q z}\right]\right)\left(\sum_y \left[\frac{E_y}{\omega_y+\omega_i-\omega_a} e^{j\omega_y t - jk_y z}\right]\right) c_a e^{j(\omega_b-\omega_a)t} \\
+ \;& \frac{j}{4\hbar^2}\sum_i \mu_{bi}\mu_{ai}^* \left(\sum_q \left[E_q^* e^{-j\omega_q t + jk_q z}\right]\right)\left(\sum_y \left[\frac{E_y^*}{-\omega_y+\omega_i-\omega_a} e^{-j\omega_y t + jk_y z}\right]\right) c_a e^{j(\omega_b-\omega_a)t}
\end{aligned}
\tag{A.73}
$$

As above, use the rotating wave approximation, and neglect all terms that rapidly oscillate. Examine each line of the expression for $\frac{dc_b}{dt}$ (Equation A.73).

In the first line, the time dependence of each term goes as

$$
e^{j\omega_q t}\left(e^{j\omega_y t}\right) = e^{j(\omega_q+\omega_y)t}. \tag{A.74}
$$

Use the definition of ω_q (Equation A.1).

$$
\begin{aligned}
&= e^{j\{[\omega_0+q\omega_m]+[\omega_0+y\omega_m]\}t} \\
&= e^{j[2\omega_0+(q+y)\omega_m]t}
\end{aligned}
\tag{A.75}
$$

$\omega_0 \gg \omega_m$, so for any values of q and y, the first term dominates. Thus, each term oscillates at least as fast as $e^{j2\omega_0 t}$ and can be neglected under the rotating wave approximation. Since all terms in the product of sums are negligible, the first line of the expression for $\frac{dc_b}{dt}$ (Equation A.73) contributes nothing.

In the second line of the expression for $\frac{dc_b}{dt}$ (Equation A.73), the time dependence of each term goes as

$$e^{j\omega_q t}\left(e^{-j\omega_y t}\right) = e^{j(\omega_q - \omega_y)t}. \tag{A.76}$$

The definition of ω_q (Equation A.1) yields

$$\begin{aligned} &= e^{j\{[\omega_0 + q\omega_m] - [\omega_0 + y\omega_m]\}t} \\ &= e^{j[(q-y)\omega_m]t}. \end{aligned} \tag{A.77}$$

For $q \neq y$, these terms oscillate at least as fast as $e^{j\omega_m t}$ and can be neglected. Only $q = y$ terms survive.

Thus, under the rotating wave approximation, by setting $q = y$, the second line of the expression for $\frac{dc_b}{dt}$ (Equation A.73) is reduced to the following:

$$\begin{aligned} &\frac{j}{4\hbar^2}\sum_i |\mu_{bi}|^2 \left(\sum_q \left[E_q e^{j\omega_q t - jk_q z}\right]\right)\left(\sum_q \left[\frac{E_q^*}{-\omega_q + \omega_i - \omega_b} e^{-j\omega_q t + jk_q z}\right]\right) c_b \\ = &\frac{j}{4\hbar^2}\sum_i |\mu_{bi}|^2 \sum_q \frac{|E_q|^2}{-\omega_q + \omega_i - \omega_b}\left[e^{j\omega_q t - jk_q z}\right]\left[e^{-j\omega_q t + jk_q z}\right] c_b \\ = &\frac{j}{4\hbar^2}\sum_i |\mu_{bi}|^2 \sum_q \frac{|E_q|^2}{-\omega_q + \omega_i - \omega_b} c_b. \end{aligned} \tag{A.78}$$

In the third line of the expression for $\frac{dc_b}{dt}$ (Equation A.73), the time dependence of each term goes as

$$e^{j\omega_q t}\left(e^{j\omega_y t}\right) e^{j(\omega_b - \omega_a)t} = e^{j(\omega_q + \omega_y + \omega_b - \omega_a)t}. \tag{A.79}$$

Insert the definitions of ω_q and ω_m (Equations A.1 and A.2).

$$\begin{aligned} &= e^{j([\omega_0 + q\omega_m] + [\omega_0 + y\omega_m] + \omega_b - \omega_a)t} \\ &= e^{j\{[\omega_0 + q(\omega_b - \omega_a - \Delta\omega)] + [\omega_0 + y(\omega_b - \omega_a - \Delta\omega)] + \omega_b - \omega_a\}t} \\ &= e^{j\{2\omega_0 + (q+y+1)(\omega_b - \omega_a) - (q+y)\Delta\omega\}t} \end{aligned} \tag{A.80}$$

Since $\omega_0 \gg (\omega_b - \omega_a) \gg \Delta\omega$, this oscillates approximately as $e^{j2\omega_0 t}$ and can be neglected. Thus, the contributions of the third line of the expression for $\frac{dc_b}{dt}$ (Equation A.73) vanish.

In the fourth line of the expression for $\frac{dc_b}{dt}$ (Equation A.73), the time dependence of each term goes as

$$e^{j\omega_q t}\left(e^{-j\omega_y t}\right)e^{j(\omega_b-\omega_a)t} = e^{j(\omega_q-\omega_y+\omega_b-\omega_a)t}. \tag{A.81}$$

Substituting for ω_q and ω_m as above (using Equations A.1 and A.2),

$$\begin{aligned} &= e^{j([\omega_0+q\omega_m]-[\omega_0+y\omega_m]+\omega_b-\omega_a)t} \\ &= e^{j\{[\omega_0+q(\omega_b-\omega_a-\Delta\omega)]-[\omega_0+y(\omega_b-\omega_a-\Delta\omega)]+\omega_b-\omega_a\}t} \\ &= e^{j\{(q-y+1)(\omega_b-\omega_a)-(q-y)\Delta\omega\}t}. \end{aligned} \tag{A.82}$$

Since $(\omega_b - \omega_a) \gg \Delta\omega$, the first term dominates. Thus, the time dependence is approximately $e^{j(q-y+1)(\omega_b-\omega_a)t}$.

Unless $q-y+1=0 \Rightarrow q = y-1$, this oscillates at least as fast as $e^{j(\omega_b-\omega_a)t}$ and thus vanishes.

The fourth line of the expression for $\frac{dc_b}{dt}$ (Equation A.73) is then reduced to the following by setting $q = y-1$:

$$\begin{aligned} &\frac{j}{4\hbar^2}\sum_i \left[\mu_{bi}\mu_{ai}^* \left(\sum_{y-1}\left[E_{y-1}e^{j\omega_{y-1}t-jk_{y-1}z}\right]\right)\right. \\ &\qquad \left.\times\left(\sum_y\left[\frac{E_y^*}{-\omega_y+\omega_i-\omega_a}e^{-j\omega_y t+jk_y z}\right]\right)\right]c_a e^{j(\omega_b-\omega_a)t} \\ = \;& \frac{j}{4\hbar^2}\sum_i \mu_{bi}\mu_{ai}^* \sum_q \frac{E_{y-1}E_y^*}{-\omega_y+\omega_i-\omega_a}\left[e^{j(\omega_{y-1}-\omega_y+\omega_b-\omega_a)t+j(-k_{y-1}+k_y)z}\right]c_a. \end{aligned} \tag{A.83}$$

Rewrite the exponent of this expression. Use the definition of ω_q (Equation A.1).

$$\begin{aligned} \omega_{y-1}-\omega_y+\omega_a-\omega_b &= (\omega_0+[y-1]\,\omega_m)-\omega_y+\omega_b-\omega_a \\ &= [(\omega_0+y\omega_m)-\omega_m]-\omega_y+\omega_b-\omega_a \\ &= [\omega_y-\omega_m]-\omega_y+\omega_b-\omega_a \\ &= -\omega_m+\omega_b-\omega_a \end{aligned} \tag{A.84}$$

Use the definition of ω_m (Equation A.2).

$$\begin{aligned} &= -(\omega_b - \omega_a - \Delta\omega) + \omega_b - \omega_a \\ &= \Delta\omega \end{aligned} \tag{A.85}$$

Another term in the exponent,$-k_{y-1} + k_y$, can be rewritten in a similar manner.

Use the definition of k_q (Equation A.54).

$$\begin{aligned} -k_{y-1} + k_y &= -(k_0 + [y-1]\,k_m) + (k_0 + yk_m) \\ &= k_m \end{aligned} \tag{A.86}$$

Now plug the above (Equations A.85 and A.86) into the expression for the fourth line (Equation A.83). The fourth line of the expression for $\frac{dc_b}{dt}$ (Equation A.73) becomes

$$\begin{aligned} &\frac{j}{4\hbar^2}\sum_i \mu_{bi}\mu_{ai}^* \left(\sum_q \left[E_q e^{j\omega_q t - jk_q z}\right]\right)\left(\sum_y \left[\frac{E_y^*}{-\omega_y + \omega_i - \omega_a} e^{-j\omega_y t + jk_y z}\right]\right) c_a e^{j(\omega_b - \omega_a)t} \\ = \;& \frac{j}{4\hbar^2}\sum_i \mu_{bi}\mu_{ai}^* \sum_y \frac{E_{y-1}E_y^*}{-\omega_y + \omega_i - \omega_a}\left[e^{j\Delta\omega t + jk_m z}\right] c_a. \end{aligned} \tag{A.87}$$

Now examine the fifth line of the expression for $\frac{dc_b}{dt}$ (Equation A.73). The argument is analogous to that of the second line with the only difference being a sign switch between ω_q and ω_y. The time dependence of each term goes as

$$e^{-j\omega_q t}\left(e^{j\omega_y t}\right) = e^{j(-\omega_q + \omega_y)t}. \tag{A.88}$$

The definition of ω_q (Equation A.1) yields

$$\begin{aligned} &= e^{j\{-[\omega_0 + q\omega_m] + [\omega_0 + y\omega_m]\}t} \\ &= e^{j[(-q+y)\omega_m]t}. \end{aligned} \tag{A.89}$$

For $q \neq y$, these terms oscillate at least as fast as $e^{j\omega_m t}$ and can be neglected. Only $q = y$ terms survive.

Thus, under the rotating wave approximation, the second line of the expression for $\frac{dc_b}{dt}$ (Equation A.73) is reduced to the following by setting $y = q$:

$$\begin{aligned} & \frac{j}{4\hbar^2}\sum_i |\mu_{bi}|^2 \left(\sum_q \left[E_q e^{-j\omega_q t + jk_q z}\right]\right)\left(\sum_q \left[\frac{E_q^*}{\omega_q+\omega_i-\omega_b} e^{j\omega_q t - jk_q z}\right]\right) c_b \\ = & \frac{j}{4\hbar^2}\sum_i |\mu_{bi}|^2 \sum_q \frac{|E_q|^2}{\omega_q+\omega_i-\omega_b}\left[e^{-j\omega_q t + jk_q z}\right]\left[e^{j\omega_q t - jk_q z}\right] c_b \\ = & \frac{j}{4\hbar^2}\sum_i |\mu_{bi}|^2 \sum_q \frac{|E_q|^2}{\omega_q+\omega_i-\omega_b} c_b. \end{aligned} \tag{A.90}$$

Examine the sixth line of the expression for $\frac{dc_b}{dt}$ (Equation A.73). This, up to a negative sign, is the same as the first line. The time dependence of each term goes as

$$e^{-j\omega_q t}\left(e^{-j\omega_y t}\right) = e^{-j(\omega_q+\omega_y)t}. \tag{A.91}$$

Use the definition of ω_q (Equation A.1).

$$\begin{aligned} = & \; e^{-j\{[\omega_0+q\omega_m]+[\omega_0+y\omega_m]\}t} \\ = & \; e^{-j[2\omega_0+(q+y)\omega_m]t} \end{aligned} \tag{A.92}$$

$\omega_0 \gg \omega_m$, so for any value of q and y, the first term dominates. Thus, each term oscillates at least as fast as $e^{j2\omega_0 t}$ and can be neglected under the rotating wave approximation. Since all terms in the product of sums are negligible, the sixth line of the expression for $\frac{dc_b}{dt}$ (Equation A.73) contributes nothing.

Examine the seventh line of the expression for $\frac{dc_b}{dt}$ (Equation A.73). This is similar to the fourth line with a change of signs. The time dependence of each term goes as

$$e^{-j\omega_q t}\left(e^{j\omega_y t}\right) e^{j(\omega_b-\omega_a)t} = e^{j(-\omega_q+\omega_y+\omega_b-\omega_a)t}. \tag{A.93}$$

Substitute for ω_q and ω_m as above (using Equations A.1 and A.2).

$$\begin{aligned} = & \; e^{j(-[\omega_0+q\omega_m]+[\omega_0+y\omega_m]+\omega_b-\omega_a)t} \\ = & \; e^{j\{-[\omega_0+q(\omega_b-\omega_a-\Delta\omega)]+[\omega_0+y(\omega_b-\omega_a-\Delta\omega)]+\omega_b-\omega_a\}t} \\ = & \; e^{j\{(-q+y+1)(\omega_b-\omega_a)+(q-y)\Delta\omega\}t} \end{aligned} \tag{A.94}$$

Since $(\omega_b - \omega_a) \gg \Delta\omega$, the first term dominates. Thus, the time dependence is approximately $e^{j(-q+y+1)(\omega_b-\omega_a)t}$.

Unless $-q + y + 1 = 0 \Rightarrow y = q - 1$, this oscillates at least as fast as $e^{j(\omega_b-\omega_a)t}$ and thus vanishes.

The seventh line of the expression for $\frac{dc_b}{dt}$ (Equation A.73) is then reduced to the following by setting $y = q - 1$:

$$\begin{aligned} & \frac{j}{4\hbar^2} \sum_i \mu_{bi}\mu_{ai}^* \left(\sum_q \left[E_q^* e^{-j\omega_q t + jk_q z} \right] \right) \left(\sum_{q-1} \left[\frac{E_{q-1}}{\omega_{q-1} + \omega_i - \omega_a} e^{j\omega_{q-1}t - jk_{q-1}z} \right] \right) c_a e^{j(\omega_b-\omega_a)t} \\ = \; & \frac{j}{4\hbar^2} \sum_i \mu_{bi}\mu_{ai}^* \sum_q \frac{E_q^* E_{q-1}}{\omega_{q-1} + \omega_i - \omega_a} \left[e^{j(-\omega_q+\omega_{q-1}+\omega_b-\omega_a)t + j(k_q-k_{q-1})z} \right] c_a. \end{aligned} \tag{A.95}$$

Rewrite this expression. Use the expression above for ω_{q-1} (Equation A.48) to rewrite the denominator.

$$\omega_{q-1} + \omega_i - \omega_a = (\omega_q - \omega_m) + \omega_i - \omega_a \tag{A.96}$$

Use the definition of ω_m (Equation A.2).

$$\begin{aligned} &= \omega_q - (\omega_b - \omega_a - \Delta\omega) + \omega_i - \omega_a \\ &= \omega_q - \omega_b + \Delta\omega + \omega_i \end{aligned} \tag{A.97}$$

Now use the fact that $(\omega_b - \omega_a) \gg \Delta\omega$ and $\omega_i \gg \Delta\omega$, and the denominator of the above (Equation A.95) becomes approximately

$$\approx \omega_q - \omega_b + \omega_i. \tag{A.98}$$

Now examine $-\omega_q + \omega_{q-1} + \omega_b - \omega_a$ from the exponent of the seventh line (Equation A.95).

Use the expression above for ω_{q-1} (Equation A.48).

$$\begin{aligned} -\omega_q + \omega_{q-1} + \omega_b - \omega_a &= -\omega_q + (\omega_q - \omega_m) + \omega_b - \omega_a \\ &= -\omega_m + \omega_b - \omega_a \end{aligned} \tag{A.99}$$

Use the definition of ω_m (Equation A.2).

$$\begin{aligned} &= -(\omega_b - \omega_a - \Delta\omega) + \omega_b - \omega_a \\ &= \Delta\omega \end{aligned} \tag{A.100}$$

Another term in the exponent, $k_q - k_{q-1}$, can be rewritten in a similar manner. Use the definition of k_q (Equation A.54).

$$\begin{aligned} k_q - k_{q-1} &= (k_0 + qk_m) - (k_0 + [q-1]\, k_m) \\ &= k_m \end{aligned} \tag{A.101}$$

Now plug the above (Equations A.98, A.100, and A.101) into the seventh line (Equation A.95). The seventh line of the expression for $\frac{dc_b}{dt}$ (Equation A.73) becomes

$$\begin{aligned} & \frac{j}{4\hbar^2} \sum_i \mu_{bi}\mu_{ai}^* \sum_q \frac{E_q^* E_{q-1}}{\omega_{q-1} + \omega_i - \omega_a} \left[e^{j(-\omega_q + \omega_{q-1} + \omega_b - \omega_a)t + j(k_q - k_{q-1})z}\right] c_a \\ = & \frac{j}{4\hbar^2} \sum_i \mu_{bi}\mu_{ai}^* \sum_q \frac{E_q^* E_{q-1}}{\omega_q - \omega_b + \omega_i} \left[e^{j\Delta\omega t + jk_m z}\right] c_a. \end{aligned} \tag{A.102}$$

Now examine the eighth line of the expression for $\frac{dc_b}{dt}$ (Equation A.73). This is similar to the third line. The time dependence goes as

$$e^{-j\omega_q t}\left(e^{-j\omega_y t}\right) e^{j(\omega_b - \omega_a)t} = e^{j(-\omega_q - \omega_y + \omega_b - \omega_a)t}. \tag{A.103}$$

Insert the definitions of ω_q and ω_m (Equations A.1 and A.2).

$$\begin{aligned} &= e^{j(-[\omega_0 + q\omega_m] - [\omega_0 + y\omega_m] + \omega_b - \omega_a)t} \\ &= e^{j\{-[\omega_0 + q(\omega_b - \omega_a - \Delta\omega)] - [\omega_0 + y(\omega_b - \omega_a - \Delta\omega)] + \omega_b - \omega_a\}t} \\ &= e^{j\{-2\omega_0 - (q+y-1)(\omega_b - \omega_a) + (q+y)\Delta\omega\}t} \end{aligned} \tag{A.104}$$

Since $\omega_0 \gg (\omega_b - \omega_a) \gg \Delta\omega$, this oscillates approximately as $e^{-j2\omega_0 t}$ and can be neglected. Thus, the contributions of the eighth line of the expression for $\frac{dc_b}{dt}$ (Equation A.73) vanish.

Therefore, under the rotating wave approximation, the only nonvanishing contributions to the expression for $\frac{dc_b}{dt}$ (Equation A.73) are from the second, fourth, fifth, and seventh lines (Equations A.78, A.87, A.90, and A.102). Summing the contributions from these lines yields the following approximation of the expression for $\frac{dc_b}{dt}$ (Equation A.73). (Change the dummy variable y to q in

Equation A.87 to match other equations.)

$$\begin{aligned}\frac{dc_b}{dt} &= \frac{j}{4\hbar^2}\sum_i |\mu_{bi}|^2 \sum_q \frac{|E_q|^2}{-\omega_q+\omega_i-\omega_b} c_b \\ &+\frac{j}{4\hbar^2}\sum_i \mu_{bi}\mu_{ai}^* \sum_q \frac{E_{q-1}E_q^*}{-\omega_q+\omega_i-\omega_a}\left(e^{j\Delta\omega t+jk_m z}\right) c_a \\ &+\frac{j}{4\hbar^2}\sum_i |\mu_{bi}|^2 \sum_q \frac{|E_q|^2}{\omega_q+\omega_i-\omega_b} c_b \\ &+\frac{j}{4\hbar^2}\sum_i \mu_{bi}\mu_{ai}^* \sum_q \frac{E_q^*E_{q-1}}{\omega_q-\omega_b+\omega_i}\left(e^{j\Delta\omega t+jk_m z}\right) c_a \end{aligned} \tag{A.105}$$

The equations for $\frac{dc_a}{dt}$ and $\frac{dc_b}{dt}$ can be simplified by defining coupling and dispersion constants. First rewrite the equation for $\frac{dc_a}{dt}$ (Equation A.71).

$$\begin{aligned}\frac{dc_a}{dt} &= \frac{j}{4\hbar^2}\sum_i |\mu_{ai}|^2 \sum_q \frac{|E_q|^2}{-\omega_q+\omega_i-\omega_a} c_a \\ &+\frac{j}{4\hbar^2}\sum_i \mu_{ai}\mu_{bi}^* \sum_q \frac{E_q E_{q-1}^*}{-\omega_q-\omega_a+\omega_i}\left(e^{-j\Delta\omega t-jk_m z}\right) c_b \\ &+\frac{j}{4\hbar^2}\sum_i |\mu_{ai}|^2 \sum_q \frac{|E_q|^2}{\omega_q+\omega_i-\omega_a} c_a \\ &+\frac{j}{4\hbar^2}\sum_i \mu_{ai}\mu_{bi}^* \sum_q \frac{E_{q-1}^*E_q}{\omega_q+\omega_i-\omega_b}\left(e^{-j\Delta\omega t-jk_m z}\right) c_b \end{aligned} \tag{A.106}$$

Group like terms and rearrange.

$$\begin{aligned}\frac{dc_a}{dt} &= \frac{j}{2}\sum_q \Bigg\{ \frac{1}{2\hbar^2}\sum_i |\mu_{ai}|^2 \left[\frac{1}{(\omega_i-\omega_a)-\omega_q}+\frac{1}{(\omega_i-\omega_a)+\omega_q}\right]|E_q|^2 c_a \\ &+\frac{1}{2\hbar^2}\sum_i \mu_{ai}\mu_{bi}^* \left[\frac{1}{(\omega_i-\omega_a)-\omega_q}+\frac{1}{(\omega_i-\omega_b)+\omega_q}\right] E_q E_{q-1}^* \left(e^{-j\Delta\omega t-jk_m z}\right) c_b \Bigg\} \end{aligned} \tag{A.107}$$

Now rewrite the equation for $\frac{dc_b}{dt}$ (Equation A.105).

$$\begin{aligned}\frac{dc_b}{dt} &= \frac{j}{4\hbar^2}\sum_i |\mu_{bi}|^2 \sum_q \frac{|E_q|^2}{-\omega_q+\omega_i-\omega_b} c_b \\ &+\frac{j}{4\hbar^2}\sum_i \mu_{bi}\mu_{ai}^* \sum_q \frac{E_{q-1}E_q^*}{-\omega_q+\omega_i-\omega_a}\left(e^{j\Delta\omega t+jk_m z}\right) c_a \\ &+\frac{j}{4\hbar^2}\sum_i |\mu_{bi}|^2 \sum_q \frac{|E_q|^2}{\omega_q+\omega_i-\omega_b} c_b \\ &+\frac{j}{4\hbar^2}\sum_i \mu_{bi}\mu_{ai}^* \sum_q \frac{E_q^* E_{q-1}}{\omega_q-\omega_b+\omega_i}\left(e^{j\Delta\omega t+jk_m z}\right) c_a \end{aligned} \tag{A.108}$$

Group like terms and rearrange.

$$\begin{aligned}\frac{dc_b}{dt} &= \frac{j}{2}\sum_q \Bigg\{ \frac{1}{2\hbar^2}\sum_i |\mu_{bi}|^2 \left[\frac{1}{(\omega_i-\omega_b)-\omega_q}+\frac{1}{(\omega_i-\omega_b)+\omega_q}\right] |E_q|^2 c_b \\ &+\frac{1}{2\hbar^2}\sum_i \mu_{ai}^*\mu_{bi}\left[\frac{1}{(\omega_i-\omega_a)-\omega_q}+\frac{1}{(\omega_i-\omega_b)+\omega_q}\right] E_q^* E_{q-1}\left(e^{j\Delta\omega t+jk_m z}\right) c_a \Bigg\}\end{aligned} \tag{A.109}$$

Now define coupling and dispersion constants as in the main text.

$$\frac{1}{2\hbar^2}\sum_i |\mu_{ai}|^2 \left[\frac{1}{(\omega_i-\omega_a)-\omega_q}+\frac{1}{(\omega_i-\omega_a)+\omega_q}\right] \equiv a_q \tag{A.110}$$

$$\frac{1}{2\hbar^2}\sum_i \mu_{ai}\mu_{bi}^* \left[\frac{1}{(\omega_i-\omega_a)-\omega_q}+\frac{1}{(\omega_i-\omega_b)+\omega_q}\right] \equiv b_q \tag{A.111}$$

$$\frac{1}{2\hbar^2}\sum_i |\mu_{bi}|^2 \left[\frac{1}{(\omega_i-\omega_b)-\omega_q}+\frac{1}{(\omega_i-\omega_b)+\omega_q}\right] \equiv d_q \tag{A.112}$$

With these definitions, simplify the expressions above (Equations A.107 and A.109).

$$\frac{dc_a}{dt} = \frac{j}{2}\sum_q \left[a_q |E_q|^2 c_a + b_q E_q E_{q-1}^* \left(e^{-j\Delta\omega t-jk_m z}\right) c_b\right] \tag{A.113}$$

$$\frac{dc_b}{dt} = \frac{j}{2}\sum_q \left[d_q |E_q|^2 c_b + b_q^* E_q^* E_{q-1}\left(e^{j\Delta\omega t+jk_m z}\right) c_a\right] \tag{A.114}$$

Now make the following phase transformation to the constants to simplify the equations.

$$c_a \equiv \tilde{c}_a \tag{A.115}$$

$$c_b \equiv \tilde{c}_b e^{j\Delta\omega t+jk_m z} \tag{A.116}$$

Plug these phase transformed constants into the equation for $\frac{dc_a}{dt}$ (Equation A.113).

$$\frac{d\tilde{c}_a}{dt} = \frac{j}{2}\sum_q \left\{a_q \left|E_q\right|^2 \left[\tilde{c}_a\right] + b_q E_q E_{q-1}^* \left(e^{-j\Delta\omega t - jk_m z}\right)\left[\tilde{c}_b e^{j\Delta\omega t + jk_m z}\right]\right\} \quad \text{(A.117)}$$

$$\frac{d\tilde{c}_a}{dt} = \frac{j}{2}\sum_q \left[a_q \left|E_q\right|^2 \tilde{c}_a + b_q E_q E_{q-1}^* \tilde{c}_b\right] \quad \text{(A.118)}$$

The phase transformed version of the equation for $\frac{dc_b}{dt}$ (Equation A.114) is then

$$\frac{d\left[\tilde{c}_b e^{j\Delta\omega t + jk_m z}\right]}{dt} = \frac{j}{2}\sum_q \left\{d_q \left|E_q\right|^2 \left[\tilde{c}_b e^{j\Delta\omega t + jk_m z}\right] + b_q^* E_q^* E_{q-1}\left(e^{j\Delta\omega t + jk_m z}\right)\left[\tilde{c}_a\right]\right\}. \quad \text{(A.119)}$$

Differentiate the left-hand side of this equation using the product rule.

$$\begin{aligned}
\frac{d\tilde{c}_b}{dt}e^{j\Delta\omega t + jk_m z} &+ \frac{d}{dt}\left[e^{j\Delta\omega t + jk_m z}\right]\tilde{c}_b \\
&= \frac{j}{2}\sum_q \left[d_q \left|E_q\right|^2 \tilde{c}_b e^{j\Delta\omega t + jk_m z} + b_q^* E_q^* E_{q-1}\left(e^{j\Delta\omega t + jk_m z}\right)\tilde{c}_a\right] \\
\frac{d\tilde{c}_b}{dt}e^{j\Delta\omega t + jk_m z} &+ j\Delta\omega\left[e^{j\Delta\omega t + jk_m z}\right]\tilde{c}_b \\
&= \frac{j}{2}\sum_q \left[d_q \left|E_q\right|^2 \tilde{c}_b e^{j\Delta\omega t + jk_m z} + b_q^* E_q^* E_{q-1}\left(e^{j\Delta\omega t + jk_m z}\right)\tilde{c}_a\right]
\end{aligned} \quad \text{(A.120)}$$

Now multiply both sides by $e^{-j\Delta\omega t - jk_m z}$.

$$\frac{d\tilde{c}_b}{dt} + j\Delta\omega\tilde{c}_b = \frac{j}{2}\sum_q \left[d_q \left|E_q\right|^2 \tilde{c}_b + b_q^* E_q^* E_{q-1}\tilde{c}_a\right]$$

Solve for $\frac{d\tilde{c}_b}{dt}$ and rearrange.

$$\begin{aligned}
\frac{d\tilde{c}_b}{dt} &= \frac{j}{2}\sum_q \left[d_q \left|E_q\right|^2 \tilde{c}_b + b_q^* E_q^* E_{q-1}\tilde{c}_a\right] - j\Delta\omega\tilde{c}_b \\
&= \frac{j}{2}\sum_q \left[\left(d_q \left|E_q\right|^2 - 2\Delta\omega\right)\tilde{c}_b + b_q^* E_q^* E_{q-1}\tilde{c}_a\right]
\end{aligned} \quad \text{(A.121)}$$

Combine these two phase-transformed equations (Equations A.118 and A.121) into a vector equation.

$$\frac{d}{dt}\begin{bmatrix}\tilde{c}_a \\ \tilde{c}_b\end{bmatrix} = \frac{j}{2}\begin{bmatrix}\sum_q a_q \left|E_q\right|^2 & \sum_q b_q E_q E_{q-1}^* \\ \sum_q b_q^* E_q^* E_{q-1} & \sum_q d_q \left|E_q\right|^2 - 2\Delta\omega\end{bmatrix}\begin{bmatrix}\tilde{c}_a \\ \tilde{c}_b\end{bmatrix} \quad \text{(A.122)}$$

Multiply both sides by $j\hbar$, noting $j^2 = -1$.

$$j\hbar\frac{d}{dt}\begin{bmatrix}\tilde{c}_a\\ \tilde{c}_b\end{bmatrix} = -\frac{\hbar}{2}\begin{bmatrix}\sum_q a_q |E_q|^2 & \sum_q b_q E_q E_{q-1}^* \\ \sum_q b_q^* E_q^* E_{q-1} & \sum_q d_q |E_q|^2 - 2\Delta\omega\end{bmatrix}\begin{bmatrix}\tilde{c}_a\\ \tilde{c}_b\end{bmatrix} \tag{A.123}$$

Note that this now has the form of the Schrödinger equation (Equation A.3),

$$j\hbar\frac{d|\psi\rangle}{dt} = \hat{H}|\psi\rangle$$

with the wavefunction

$$|\psi\rangle = \begin{bmatrix}\tilde{c}_a\\ \tilde{c}_b\end{bmatrix} \tag{A.124}$$

and an effective Hamiltonian

$$\hat{H} = -\frac{\hbar}{2}\begin{bmatrix}\sum_q a_q |E_q|^2 & \sum_q b_q E_q E_{q-1}^* \\ \sum_q b_q^* E_q^* E_{q-1} & \sum_q d_q |E_q|^2 - 2\Delta\omega\end{bmatrix}. \tag{A.125}$$

This can be simplified by defining the following variables:

$$\sum_q a_q |E_q|^2 \equiv A \tag{A.126}$$

$$\sum_q b_q E_q E_{q-1}^* \equiv B \tag{A.127}$$

$$\sum_q b_q^* E_q^* E_{q-1} = B^* \equiv C \tag{A.128}$$

$$\sum_q d_q |E_q|^2 \equiv D. \tag{A.129}$$

With these variables, the effective Hamiltonian (Equation A.125) then becomes

$$\hat{H} = -\frac{\hbar}{2}\begin{bmatrix}A & B\\ C & D - 2\Delta\omega\end{bmatrix}. \tag{A.130}$$

Appendix B: Eigenstates and Eigenvalues of the Hamiltonian

As derived in Appendix A, the effective Hamiltonian of our Raman system is

$$\hat{H} = -\frac{\hbar}{2}\begin{bmatrix} A & B \\ B^* & D - 2\Delta\omega \end{bmatrix}. \tag{B.1}$$

All variables are defined as in Appendix A (Equations A.126 - A.129), and we have used the fact that $C = B^*$.

To find the eigenvalues E_i of this 2×2 matrix, we first calculate the determinant of the following matrix.

$$\begin{aligned} \hat{H} - E_i I_{2\times2} &= -\frac{\hbar}{2}\begin{bmatrix} A & B \\ B^* & D - 2\Delta\omega \end{bmatrix} - E_i \begin{bmatrix} 1 & 0 \\ 0 & 1 \end{bmatrix} \\ &= \begin{bmatrix} -\frac{\hbar}{2}A - E_i & -\frac{\hbar}{2}B \\ -\frac{\hbar}{2}B^* & -\frac{\hbar}{2}(D - 2\Delta\omega) - E_i \end{bmatrix} \\ &= \begin{bmatrix} -\frac{\hbar}{2}A - E_i & -\frac{\hbar}{2}B \\ -\frac{\hbar}{2}B^* & -\frac{\hbar}{2}D + \frac{\hbar}{2}2\Delta\omega - E_i \end{bmatrix}, \end{aligned} \tag{B.2}$$

where $I_{2\times2}$ is the 2×2 identity matrix.

Calculate the determinant of the matrix and set it equal to zero to get a characteristic equation.

$$\begin{aligned} \left|\hat{H} - E_i I_{2\times2}\right| &= \begin{vmatrix} -\frac{\hbar}{2}A - E_i & -\frac{\hbar}{2}B \\ -\frac{\hbar}{2}B^* & -\frac{\hbar}{2}D + \frac{\hbar}{2}2\Delta\omega - E_i \end{vmatrix} \\ &= \left(-\frac{\hbar}{2}A - E_i\right)\left(-\frac{\hbar}{2}D + \frac{\hbar}{2}2\Delta\omega - E_i\right) - \frac{\hbar^2}{4}|B|^2 \end{aligned} \tag{B.3}$$

Expand, group like powers of E_i, and set equal to zero.

$$\begin{aligned} &= \frac{\hbar^2}{4}AD - \frac{\hbar^2}{4}2A\Delta\omega + \frac{\hbar}{2}AE_i + \frac{\hbar}{2}E_iD - \frac{\hbar}{2}2\Delta\omega E_i + E_i^2 - \frac{\hbar^2}{4}|B|^2 \\ &= E_i^2 + \frac{\hbar}{2}(A + D - 2\Delta\omega)E_i + \frac{\hbar^2}{4}\left(AD - 2A\Delta\omega - |B|^2\right) = 0 \end{aligned} \tag{B.4}$$

Use the quadratic equation to solve for E_i.

$$E_i = \frac{-\frac{\hbar}{2}(A + D - 2\Delta\omega) \pm \sqrt{\frac{\hbar^2}{4}(A + D - 2\Delta\omega)^2 - 4(1)\frac{\hbar^2}{4}\left(AD - 2A\Delta\omega - |B|^2\right)}}{2(1)} \tag{B.5}$$

Now pull out the common $\sqrt{\frac{\hbar^2}{4}} = \frac{\hbar}{2}$ from the radical, expand the quadratic term, and simplify to rewrite the eigenvalues.

$$\begin{aligned} E_i &= \frac{1}{2}\Bigg[\frac{\hbar}{2}\left(-A - D + 2\Delta\omega\right) \\ &\qquad \pm\frac{\hbar}{2}\sqrt{A^2 + D^2 + 4\left(\Delta\omega\right)^2 + 2AD - 4A\Delta\omega - 4D\Delta\omega - 4AD + 8A\Delta\omega + 4\left|B\right|^2}\Bigg] \\ &= \frac{1}{2}\Bigg[\frac{\hbar}{2}\left(-A - D + 2\Delta\omega\right) \\ &\qquad \pm\frac{\hbar}{2}\sqrt{A^2 + D^2 + 4\left(\Delta\omega\right)^2 - 4D\Delta\omega - 2AD + 4A\Delta\omega + 4\left|B\right|^2}\Bigg] \end{aligned} \tag{B.6}$$

We can write this in a more compact way by writing the first six terms under the radical as a quadratic term. Doing so and pulling a factor of $-\frac{\hbar}{2}$ out front gives us eigenvalues of

$$E_\pm = -\frac{\hbar}{4}\left[\left(A + D - 2\Delta\omega\right) \mp \sqrt{\left(A - D + 2\Delta\omega\right)^2 + 4\left|B\right|^2}\right]. \tag{B.7}$$

Note that $E_+ > E_-$. The $\pm$ in $E_\pm$ refers to the higher $(+)$ and lower $(-)$ eigenvalues (and not to the sign to use in $\mp$).

Now that we have the eigenvalues of our effective Hamiltonian, the energies $E_\pm$, we can calculate our eigenstates $|\pm\rangle$ that satisfy

$$\hat{H}\left|\pm\right\rangle = E_\pm\left|\pm\right\rangle. \tag{B.8}$$

We can rewrite this requirement as

$$\left(\hat{H} - E_\pm I_{2\times 2}\right)\left|\pm\right\rangle = \left|0\right\rangle, \tag{B.9}$$

where $|0\rangle$ is the zero vector.

Defining

$$\left|\pm\right\rangle \equiv \begin{bmatrix} c_{a\pm} \\ c_{b\pm} \end{bmatrix}, \tag{B.10}$$

we can rewrite this as a matrix equation using the previously derived Hamiltonian. (See Equation B.1 and Appendix A.)

$$\begin{aligned}
\left(\hat{H} - E_{\pm} I_{2\times 2}\right)|\pm\rangle &= |0\rangle \\
\left(-\frac{\hbar}{2}\begin{bmatrix} A & B \\ B^* & D-2\Delta\omega \end{bmatrix} - E_{\pm}\begin{bmatrix} 1 & 0 \\ 0 & 1 \end{bmatrix}\right)\begin{bmatrix} c_{a\pm} \\ c_{b\pm} \end{bmatrix} &= \begin{bmatrix} 0 \\ 0 \end{bmatrix} \\
\left(-\frac{\hbar}{2}\begin{bmatrix} A & B \\ B^* & D-2\Delta\omega \end{bmatrix} - \begin{bmatrix} E_{\pm} & 0 \\ 0 & E_{\pm} \end{bmatrix}\right)\begin{bmatrix} c_{a\pm} \\ c_{b\pm} \end{bmatrix} &= \begin{bmatrix} 0 \\ 0 \end{bmatrix} \\
\begin{bmatrix} -\frac{\hbar}{2}A - E_{\pm} & -\frac{\hbar}{2}B \\ -\frac{\hbar}{2}B^* & -\frac{\hbar}{2}D + \frac{\hbar}{2}2\Delta\omega - E_{\pm} \end{bmatrix}\begin{bmatrix} c_{a\pm} \\ c_{b\pm} \end{bmatrix} &= \begin{bmatrix} 0 \\ 0 \end{bmatrix}
\end{aligned} \tag{B.11}$$

This gives us two linear equations:

$$\left(-\frac{\hbar}{2}A - E_{\pm}\right)c_{a\pm} + \left(-\frac{\hbar}{2}B\right)c_{b\pm} = 0, \tag{B.12}$$

and

$$\left(-\frac{\hbar}{2}B^*\right)c_{a\pm} + \left(-\frac{\hbar}{2}D + \frac{\hbar}{2}2\Delta\omega - E_{\pm}\right)c_{b\pm} = 0. \tag{B.13}$$

Solve the Equation B.12 for $c_{a\pm}$ in terms of $c_{b\pm}$. (It is equivalent to solve Equation B.13 for $c_{a\pm}$ in terms of $c_{b\pm}$. See *Aside 1* below.)

Begin by adding the $c_{b\pm}$ term to both sides.

$$\left(-\frac{\hbar}{2}A - E_{\pm}\right)c_{a\pm} = \left(\frac{\hbar}{2}B\right)c_{b\pm} \tag{B.14}$$

Divide both sides by the factor preceding $c_{a\pm}$.

$$\begin{aligned}
\left(-\frac{\hbar}{2}A - E_{\pm}\right)c_{a\pm} &= \left(\frac{\hbar}{2}B\right)c_{b\pm} \\
c_{a\pm} &= \frac{\frac{\hbar}{2}B}{-\frac{\hbar}{2}A - E_{\pm}}c_{b\pm}
\end{aligned} \tag{B.15}$$

Now let us examine the following relationship in more detail. If we ignore normalization for the moment, we have the freedom to choose one of the coefficients. For convenience, choose

$$c_{b\pm} \equiv -\frac{\hbar}{2}A - E_{\pm}. \tag{B.16}$$

Inserting this into Equation B.15, we find

$$\begin{aligned} c_{a\pm} &= \frac{\frac{\hbar}{2}B}{-\frac{\hbar}{2}A - E_\pm} c_{b\pm} \\ c_{a\pm} &= \frac{\frac{\hbar}{2}B}{-\frac{\hbar}{2}A - E_\pm}\left(-\frac{\hbar}{2}A - E_\pm\right) \\ c_{a\pm} &= \frac{\hbar}{2}B. \end{aligned} \tag{B.17}$$

Thus,

$$\begin{bmatrix} c_{a\pm} \\ c_{b\pm} \end{bmatrix} = \begin{bmatrix} \frac{\hbar}{2}B \\ -\frac{\hbar}{2}A - E_\pm \end{bmatrix}, \tag{B.18}$$

or

$$|\pm\rangle = \left(\frac{\hbar}{2}B\right)|a\rangle + \left(-\frac{\hbar}{2}A - E_\pm\right)|b\rangle. \tag{B.19}$$

Now we insert $E_\pm$ from above (Equation B.7), and rearrange to obtain

$$\begin{aligned} &|\pm\rangle \\ &= \left(\frac{\hbar}{2}B\right)|a\rangle + \left(-\frac{\hbar}{2}A - \left(-\frac{\hbar}{4}\left[(A+D-2\Delta\omega) \mp \sqrt{(A-D+2\Delta\omega)^2 + 4|B|^2}\right]\right)\right)|b\rangle \\ &= \left(\frac{\hbar}{2}B\right)|a\rangle + \left(-\frac{\hbar}{2}A + \frac{\hbar}{2}\frac{1}{2}\left[(A+D-2\Delta\omega) \mp \sqrt{(A-D+2\Delta\omega)^2 + 4|B|^2}\right]\right)|b\rangle \\ &= \left(\frac{\hbar}{2}B\right)|a\rangle + \left(\frac{\hbar}{2}\frac{1}{2}\left[(-A+D-2\Delta\omega) \mp \sqrt{(A-D+2\Delta\omega)^2 + 4|B|^2}\right]\right)|b\rangle. \end{aligned} \tag{B.20}$$

Finally we pull out a negative sign in the first term of the $|b\rangle$ coefficient so that the first term in the parentheses matches the quadratic term in the parentheses under the radical.

$$|\pm\rangle = \left(\frac{\hbar}{2}B\right)|a\rangle + \left(\frac{\hbar}{2}\frac{1}{2}\left[-(A-D+2\Delta\omega) \mp \sqrt{(A-D+2\Delta\omega)^2 + 4|B|^2}\right]\right)|b\rangle. \tag{B.21}$$

Any scalar multiple of an eigenstate is also an eigenstate, and we have not yet normalized these states. Thus, for mostly aesthetic reasons, we choose to multiply by $\frac{4}{\hbar}$ and work with the following new eigenstates:

$$|\pm\rangle' = 2B|a\rangle + \left[-(A-D+2\Delta\omega) \mp \sqrt{(A-D+2\Delta\omega)^2 + 4|B|^2}\right]|b\rangle. \tag{B.22}$$

(Again, we could have reached an alternate, equivalent eigenstate had we followed the argument of *Aside 1*. See *Aside 2*.)

We will concentrate on the lower energy of these eigenstates,

$$|-\rangle' = 2B\,|a\rangle + \left[-\left(A - D + 2\Delta\omega\right) + \sqrt{(A - D + 2\Delta\omega)^2 + 4\,|B|^2}\right]|b\rangle\,, \tag{B.23}$$

which has energy

$$E_- = -\frac{\hbar}{4}\left[(A + D - 2\Delta\omega) + \sqrt{(A - D + 2\Delta\omega)^2 + 4\,|B|^2}\right]. \tag{B.24}$$

(In *Aside 3* below, we show how one arrives at the same result if one follows the arguments of the other *Asides*.)

We focus on this lower energy state because it is smoothly connected to the unperturbed ground state, $|a\rangle$. We know this because of the adiabatic theorem of quantum mechanics as described in the main text.

Now let us rewrite $|-\rangle'$ in a more standard form. To make the calculation easier to follow, we will define

$$x \equiv A - D + 2\Delta\omega \tag{B.25}$$

and

$$y \equiv 2B. \tag{B.26}$$

This yields

$$|-\rangle' = y\,|a\rangle + \left(-x + \sqrt{x^2 + y^2}\right)|b\rangle\,. \tag{B.27}$$

As before, any scalar multiple of an eigenstate is also an eigenstate, so we choose to divide by $\frac{1}{\sqrt{x^2+y^2}}$ to get the new eigenstate

$$|-\rangle'' = \frac{y}{\sqrt{x^2 + y^2}}\,|a\rangle + \left(\frac{-x}{\sqrt{x^2 + y^2}} + 1\right)|b\rangle\,. \tag{B.28}$$

To rewrite this, we now define an angle θ using the triangle as shown below.

With this definition, we can rewrite our eigenstate using trigonometric functions as follows:

$$|-\rangle'' = \sin\theta\,|a\rangle + (-\cos\theta + 1)\,|b\rangle\,. \tag{B.29}$$

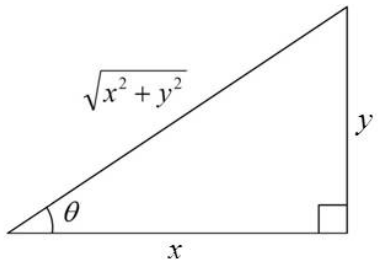

Now we use half-angle identities to rewrite $\sin\theta$ and $\cos\theta$ in terms of $\frac{\theta}{2}$.

$$\begin{aligned} |-\rangle'' &= 2\sin\left(\frac{\theta}{2}\right)\cos\left(\frac{\theta}{2}\right)|a\rangle + \left[-\left(1-2\sin^2\left(\frac{\theta}{2}\right)\right)+1\right]|b\rangle \\ &= 2\sin\left(\frac{\theta}{2}\right)\cos\left(\frac{\theta}{2}\right)|a\rangle + 2\sin^2\left(\frac{\theta}{2}\right)|b\rangle \end{aligned} \tag{B.30}$$

Again we divide by a scalar, $2\sin\left(\frac{\theta}{2}\right)$ this time, to get a simplified rescaled eigenvector.

$$|-\rangle''' = \cos\left(\frac{\theta}{2}\right)|a\rangle + \sin\left(\frac{\theta}{2}\right)|b\rangle \tag{B.31}$$

Finally, we will define a phase for these components. Until now, we have ignored the phase of the components. However, in the original state, Equation B.23, the coefficient of $|a\rangle$ carries the phase of B; each term in the sum is proportional to $E_q E_{q-1}^*$, which gives B its complex phase. Define a phase angle ϕ such that $B = |B|^{j\phi}$. The coefficient of $|b\rangle$ is purely real; it depends only on A and D, which are proportional to $|E_q|^2$, and on the magnitude of B. Thus, $|b\rangle$ has no phase term. With proper phases, then, Equation B.31 becomes

$$|-\rangle'''' = \cos\left(\frac{\theta}{2}\right)|a\rangle\, e^{j\phi} + \sin\left(\frac{\theta}{2}\right)|b\rangle\,. \tag{B.32}$$

The overall phase of the eigenstate is arbitrary. Thus, for aesthetic reasons of symmetry, shift the overall phase of the eigenstate by $-\frac{\phi}{2}$. This yields the final eigenstate of

$$|\psi\rangle = \cos\left(\frac{\theta}{2}\right)e^{j\frac{\phi}{2}}|a\rangle + \sin\left(\frac{\theta}{2}\right)e^{-j\frac{\phi}{2}}|b\rangle\,. \tag{B.33}$$

The angles are as defined above, with

$$\theta = \tan^{-1}\left(\frac{y}{x}\right) = \tan^{-1}\left(\frac{2|B|}{A-D+2\Delta\omega}\right) \tag{B.34}$$

and

$$B = |B|^{j\phi}. \tag{B.35}$$

Note that because $|e^{j\alpha}| = 1$ and $\sin^2\beta + \cos^2\beta = 1$ for all α and β, $|\psi\rangle$ is a normalized eigenstate.

$$\begin{aligned} |c_a|^2 + |c_b|^2 &= \left(\cos\left(\frac{\theta}{2}\right)\left|e^{j\frac{\phi}{2}}\right|\right)^2 + \left(\sin\left(\frac{\theta}{2}\right)\left|e^{-j\frac{\phi}{2}}\right|\right)^2 \\ &= \sin^2\left(\frac{\theta}{2}\right) + \cos^2\left(\frac{\theta}{2}\right) \\ &= 1 \end{aligned} \tag{B.36}$$

Aside 1:

We can also solve the second equation (Equation B.13) for $c_{a\pm}$ in terms of $c_{b\pm}$. Again begin by adding the $c_{b\pm}$ term to both sides.

$$\left(-\frac{\hbar}{2}B^*\right)c_{a\pm} = \left(\frac{\hbar}{2}D - \frac{\hbar}{2}2\Delta\omega + E_\pm\right)c_{b\pm} \tag{B.37}$$

Divide both sides by the factor preceding $c_{a\pm}$.

$$c_{a\pm} = \frac{\frac{\hbar}{2}D - \frac{\hbar}{2}2\Delta\omega + E_\pm}{-\frac{\hbar}{2}B^*}c_{b\pm} \tag{B.38}$$

Although Equation B.15 and Equation B.38 are not obviously equivalent, we can show that they are based on the requirement that the determinant of the matrix $\hat{H} - E_i I_{2\times 2}$ equals zero.

From Equation B.3, we have

$$\begin{vmatrix} -\frac{\hbar}{2}A - E_\pm & -\frac{\hbar}{2}B \\ -\frac{\hbar}{2}B^* & -\frac{\hbar}{2}D + \frac{\hbar}{2}2\Delta\omega - E_\pm \end{vmatrix} = 0. \tag{B.39}$$

Calculating the determinant, we have

$$\left(-\frac{\hbar}{2}A - E_\pm\right)\left(-\frac{\hbar}{2}D + \frac{\hbar}{2}2\Delta\omega - E_\pm\right) - \left(-\frac{\hbar}{2}B\right)\left(-\frac{\hbar}{2}B^*\right) = 0. \tag{B.40}$$

We can rearrange to get equivalent ratios. Begin by adding the second term to both sides.

$$\left(-\frac{\hbar}{2}A - E_\pm\right)\left(-\frac{\hbar}{2}D + \frac{\hbar}{2}2\Delta\omega - E_\pm\right) = \left(-\frac{\hbar}{2}B\right)\left(-\frac{\hbar}{2}B^*\right) \tag{B.41}$$

Next divide both sides by $\left(-\frac{\hbar}{2}A - E_{\pm}\right)\left(-\frac{\hbar}{2}B^{*}\right)$.

$$\frac{-\frac{\hbar}{2}D + \frac{\hbar}{2}2\Delta\omega - E_{\pm}}{-\frac{\hbar}{2}B^{*}} = \frac{-\frac{\hbar}{2}B}{-\frac{\hbar}{2}A - E_{\pm}} \tag{B.42}$$

Finally, multiply both sides by -1 to get

$$\frac{\frac{\hbar}{2}D - \frac{\hbar}{2}2\Delta\omega + E_{\pm}}{-\frac{\hbar}{2}B^{*}} = \frac{\frac{\hbar}{2}B}{-\frac{\hbar}{2}A - E_{\pm}}. \tag{B.43}$$

Note that these two equivalent ratios are the same as the ratios in Equation B.15 and Equation B.38, so the two relationships between $c_{a\pm}$ and $c_{b\pm}$ are equivalent.

Aside 2:

We could have also chosen to use the relationship from Equation B.38,

$$c_{a\pm} = \frac{\frac{\hbar}{2}D - \frac{\hbar}{2}2\Delta\omega + E_{\pm}}{-\frac{\hbar}{2}B^{*}}c_{b\pm}. \tag{B.44}$$

Following identical logic, we are free to choose

$$c_{b\pm} = -\frac{\hbar}{2}B^{*}. \tag{B.45}$$

This leads to

$$\begin{aligned} c_{a\pm} &= \frac{\frac{\hbar}{2}D - \frac{\hbar}{2}2\Delta\omega + E_{\pm}}{-\frac{\hbar}{2}B^{*}}c_{b\pm} \\ &= \frac{\frac{\hbar}{2}D - \frac{\hbar}{2}2\Delta\omega + E_{\pm}}{-\frac{\hbar}{2}B^{*}}\left(-\frac{\hbar}{2}B^{*}\right) \\ &= \frac{\hbar}{2}D - \frac{\hbar}{2}2\Delta\omega + E_{\pm}. \end{aligned} \tag{B.46}$$

Thus,

$$\begin{bmatrix} c_{a\pm} \\ c_{b\pm} \end{bmatrix} = \begin{bmatrix} \frac{\hbar}{2}D - \frac{\hbar}{2}2\Delta\omega + E_{\pm} \\ -\frac{\hbar}{2}B^{*} \end{bmatrix}, \tag{B.47}$$

or

$$|\pm\rangle = \left(\frac{\hbar}{2}D - \frac{\hbar}{2}2\Delta\omega + E_{\pm}\right)|a\rangle + \left(-\frac{\hbar}{2}B^{*}\right)|b\rangle. \tag{B.48}$$

Now we insert $E_\pm$ from above (Equation B.7), and rearrange to obtain

$$\begin{aligned}
|\pm\rangle &= \left(\frac{\hbar}{2}D - \frac{\hbar}{2}2\Delta\omega + \left(-\frac{\hbar}{4}\left[(A+D-2\Delta\omega) \mp \sqrt{(A-D+2\Delta\omega)^2 + 4\left|B\right|^2}\right]\right)\right)|a\rangle \\
&\quad + \left(-\frac{\hbar}{2}B^*\right)|b\rangle \\
&= \left(\frac{\hbar}{2}D - \frac{\hbar}{2}2\Delta\omega + \left(-\frac{\hbar}{2}\frac{1}{2}\left[(A+D-2\Delta\omega) \mp \sqrt{(A-D+2\Delta\omega)^2 + 4\left|B\right|^2}\right]\right)\right)|a\rangle \\
&\quad + \left(-\frac{\hbar}{2}B^*\right)|b\rangle \\
&= \left(\frac{\hbar}{2}\frac{1}{2}\left[(-A+D-2\Delta\omega) \pm \sqrt{(A-D+2\Delta\omega)^2 + 4\left|B\right|^2}\right]\right)|a\rangle \\
&\quad + \left(-\frac{\hbar}{2}B^*\right)|b\rangle\,. \qquad \text{(B.49)}
\end{aligned}$$

Finally we pull out a negative sign in the first term of the $|b\rangle$ coefficient so that the first term in the parentheses matches the quadratic term in the parentheses under the radical.

$$|\pm\rangle = \left(\frac{\hbar}{2}\frac{1}{2}\left[-(A-D+2\Delta\omega) \pm \sqrt{(A-D+2\Delta\omega)^2 + 4\left|B\right|^2}\right]\right)|a\rangle + \left(-\frac{\hbar}{2}B^*\right)|b\rangle \quad \text{(B.50)}$$

Any scalar multiple of an eigenstate is also an eigenstate, and we have not yet normalized these states. Thus, for mostly aesthetic reasons, we choose to multiply by $-\frac{4}{\hbar}$ and work with the following new eigenstates:

$$|\pm\rangle' = \left[(A-D+2\Delta\omega) \mp \sqrt{(A-D+2\Delta\omega)^2 + 4\left|B\right|^2}\right]|a\rangle + 2B^*|b\rangle\,, \qquad \text{(B.51)}$$

which is equivalent to Equation B.22.

Aside 3:

A similar argument can be made using the lower energy alternative eigenstate from Equation B.51,

$$|-\rangle' = \left[(A-D+2\Delta\omega) + \sqrt{(A-D+2\Delta\omega)^2 + 4\left|B\right|^2}\right]|a\rangle + 2B^*|b\rangle\,. \qquad \text{(B.52)}$$

Again rewrite $|-\rangle'$ in a more standard form. To make the calculation easier to follow, we will define

$$x \equiv A - D + 2\Delta\omega \qquad \text{(B.53)}$$

and

$$y \equiv 2B^*. \tag{B.54}$$

This now yields

$$|-\rangle' = \left(x + \sqrt{x^2 + y^2}\right)|a\rangle + y\,|b\rangle\,. \tag{B.55}$$

As before, any scalar multiple of an eigenstate is also an eigenstate, so we choose to divide by $\frac{1}{\sqrt{x^2+y^2}}$ to get the new eigenstate

$$|-\rangle'' = \left(\frac{x}{\sqrt{x^2+y^2}} + 1\right)|a\rangle + \frac{y}{\sqrt{x^2+y^2}}\,|b\rangle\,. \tag{B.56}$$

To rewrite this, we now define an angle θ using the triangle as shown below:

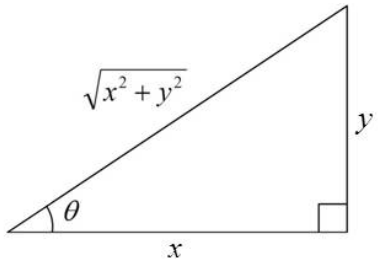

With this definition, we can rewrite our eigenstate using trigonometric functions

$$|-\rangle'' = (\cos\theta + 1)\,|a\rangle + \sin\theta\,|b\rangle\,. \tag{B.57}$$

Now we use half-angle identities to rewrite $\sin\theta$ and $\cos\theta$ in terms of $\frac{\theta}{2}$.

$$|-\rangle'' = 2\cos^2\left(\frac{\theta}{2}\right)|a\rangle + 2\cos\left(\frac{\theta}{2}\right)\sin\left(\frac{\theta}{2}\right)|b\rangle \tag{B.58}$$

Again we divide by a scalar, $2\cos\left(\frac{\theta}{2}\right)$ this time, to get the following simplified rescaled eigenvector:

$$|-\rangle''' = \cos\left(\frac{\theta}{2}\right)|a\rangle + \sin\left(\frac{\theta}{2}\right)|b\rangle\,. \tag{B.59}$$

Finally, we will define a phase for these components. Until now, we have ignored the phase of the components. However, in the original state, Equation B.51, the coefficient of $|a\rangle$ is purely real; it depends only on A and D, which are proportional to $|E_q|^2$, and on the magnitude of B.

Thus, $|a\rangle$ has no phase term. The coefficient of $|b\rangle$ carries the phase of B^*; each term in the sum is proportional to $E_q^* E_{q-1}$, which gives B^* its complex phase. The phase angle ϕ is defined such that

$$B = |B|^{j\phi} . \tag{B.60}$$

Thus, the phase of B^* is $-\phi$. With proper phases, then, Equation B.59 becomes

$$|-\rangle'''' = \cos\left(\frac{\theta}{2}\right)|a\rangle + \sin\left(\frac{\theta}{2}\right)|b\rangle\, e^{-j\phi}. \tag{B.61}$$

The overall phase of the eigenstate is arbitrary. Thus, for aesthetic reasons of symmetry, shift the overall phase of the eigenstate by $\frac{\phi}{2}$. This yields the final eigenstate of

$$|\psi\rangle = \cos\left(\frac{\theta}{2}\right) e^{j\frac{\phi}{2}}|a\rangle + \sin\left(\frac{\theta}{2}\right) e^{-j\frac{\phi}{2}}|b\rangle . \tag{B.62}$$

The angles are as defined above, with

$$\theta = \tan^{-1}\left(\frac{y}{x}\right) = \tan^{-1}\left(\frac{2\,|B|}{A - D + 2\Delta\omega}\right) \tag{B.63}$$

and

$$B = |B|^{j\phi} . \tag{B.64}$$

This is the same result we obtained when we chose to use the other eigenstates.

Appendix C: Propagation in the Raman Medium

The expectation value of the dipole moment operator is given (as discussed in the main text in Section 2.3) by

$$P(t) = \langle \psi(t) | \hat{P} | \psi(t) \rangle. \tag{C.1}$$

The wavefunction and dipole moment operator are given by

$$|\psi(t)\rangle \equiv c_a(t) e^{-j\omega_a t} |a\rangle + c_b(t) e^{-j\omega_b t} |b\rangle + \sum_i c_i(t) e^{-j\omega_i t} |i\rangle \tag{C.2}$$

and

$$\hat{P} \equiv \sum_i \mu_{ai} |a\rangle\langle i| + \sum_i \mu_{bi} |b\rangle\langle i| + \sum_i \mu_{ai}^* |i\rangle\langle a| + \sum_i \mu_{bi}^* |i\rangle\langle b|. \tag{C.3}$$

Calculate the expectation value. Begin by acting $\hat{P}$ on $|\psi(t)\rangle$ (Equation C.3 on Equation C.2).

$$\begin{aligned} \hat{P}|\psi(t)\rangle &= \left(\sum_i \mu_{ai} |a\rangle\langle i| + \sum_i \mu_{bi} |b\rangle\langle i| + \sum_i \mu_{ai}^* |i\rangle\langle a| + \sum_i \mu_{bi}^* |i\rangle\langle b| \right) \\ &\quad \times \left(c_a(t) e^{-j\omega_a t} |a\rangle + c_b(t) e^{-j\omega_b t} |b\rangle + \sum_i c_i(t) e^{-j\omega_i t} |i\rangle \right) \end{aligned} \tag{C.4}$$

Using the orthonormality of states, $\langle n | m \rangle = \delta_{nm}$, this reduces to

$$\hat{P}|\psi(t)\rangle = \sum_i \mu_{ai} |a\rangle c_i(t) e^{-j\omega_i t} + \mu_{bi} |b\rangle c_i(t) e^{-j\omega_i t} + \mu_{ai}^* |i\rangle c_a(t) e^{-j\omega_a t} + \mu_{bi}^* |i\rangle c_b(t) e^{-j\omega_b t}. \tag{C.5}$$

Now act $\langle \psi(t) |$ on $\hat{P}|\psi(t)\rangle$ (Equation C.5) to get $P(t)$ (Equation C.1).

$$\begin{aligned} P(t) &= \langle \psi | \hat{P} | \psi \rangle \\ &= \left(c_a^*(t) e^{j\omega_a t} \langle a| + c_b^*(t) e^{j\omega_b t} \langle b| + \sum_i c_i^*(t) e^{j\omega_i t} \langle i| \right) \\ &\quad \times \left(\sum_i \mu_{ai} |a\rangle c_i(t) e^{-j\omega_i t} + \mu_{bi} |b\rangle c_i(t) e^{-j\omega_i t} \right. \\ &\quad \left. + \mu_{ai}^* |i\rangle c_a(t) e^{-j\omega_a t} + \mu_{bi}^* |i\rangle c_b(t) e^{-j\omega_b t} \right) \end{aligned} \tag{C.6}$$

Again use the orthonormality of states, $\langle n|m\rangle = \delta_{nm}$. Leaving out the explicit time dependence for clarity, this yields

$$\begin{aligned} & P(t) \\ &= \sum_i c_a^* c_i \mu_{ai} e^{j(\omega_a-\omega_i)t} + \sum_i c_b^* c_i \mu_{bi} e^{j(\omega_b-\omega_i)t} + \sum_i c_a c_i^* \mu_{ai}^* e^{j(\omega_i-\omega_a)t} + \sum_i c_b c_i^* \mu_{bi}^* e^{j(\omega_i-\omega_b)t}. \end{aligned} \tag{C.7}$$

Now use the expression for c_i from the derivation of the effective Hamiltonian. (See Equation A.31 and Appendix A.)

$$\begin{aligned} c_i \;=\; & \frac{1}{2\hbar}\sum_q \left[\frac{E_q \mu_{ai}^* c_a}{(\omega_q+\omega_i-\omega_a)} e^{j(\omega_q+\omega_i-\omega_a)t-jk_qz} + \frac{E_q^* \mu_{ai}^* c_a}{(-\omega_q+\omega_i-\omega_a)} e^{j(-\omega_q+\omega_i-\omega_a)t+jk_qz} \right. \\ & \left. + \frac{E_q \mu_{bi}^* c_b}{(\omega_q+\omega_i-\omega_b)} e^{j(\omega_q+\omega_i-\omega_b)t-jk_qz} + \frac{E_q^* \mu_{bi}^* c_b}{(-\omega_q+\omega_i-\omega_b)} e^{j(-\omega_q+\omega_i-\omega_b)t+jk_qz} \right] \end{aligned} \tag{C.8}$$

Plug this expression (Equation C.8) in to the above expression for $P(t)$ (Equation C.7). For clarity, examine one term at a time.

The first term of the equation above becomes

$$\begin{aligned} \sum_i c_a^* c_i \mu_{ai} e^{j(\omega_a-\omega_i)t} \;=\; & \sum_i c_a^* \mu_{ai} e^{j(\omega_a-\omega_i)t} \\ & \times \left\{ \frac{1}{2\hbar}\sum_q \left[\frac{E_q \mu_{ai}^* c_a}{(\omega_q+\omega_i-\omega_a)} e^{j(\omega_q+\omega_i-\omega_a)t-jk_qz} \right. \right. \\ & + \frac{E_q^* \mu_{ai}^* c_a}{(-\omega_q+\omega_i-\omega_a)} e^{j(-\omega_q+\omega_i-\omega_a)t+jk_qz} \\ & + \frac{E_q \mu_{bi}^* c_b}{(\omega_q+\omega_i-\omega_b)} e^{j(\omega_q+\omega_i-\omega_b)t-jk_qz} \\ & \left. \left. + \frac{E_q^* \mu_{bi}^* c_b}{(-\omega_q+\omega_i-\omega_b)} e^{j(-\omega_q+\omega_i-\omega_b)t+jk_qz} \right] \right\}. \end{aligned} \tag{C.9}$$

Distribute, and rewrite this as

$$= \frac{1}{2\hbar}\sum_i\sum_q \left|c_a\right|^2\left|\mu_{ai}\right|^2 E_q \frac{1}{\omega_q+\omega_i-\omega_a}e^{j\omega_q t-jk_q z} \tag{C.10}$$

$$+\frac{1}{2\hbar}\sum_i\sum_q \left|c_a\right|^2\left|\mu_{ai}\right|^2 E_q^* \frac{1}{-\omega_q+\omega_i-\omega_a}e^{-j\omega_q t+jk_q z} \tag{C.11}$$

$$+\frac{1}{2\hbar}\sum_i\sum_q c_a^* c_b \mu_{ai}\mu_{bi}^* E_q \frac{1}{\omega_q+\omega_i-\omega_b}e^{j\left(\omega_q+\omega_a-\omega_b\right)t-jk_q z} \tag{C.12}$$

$$+\frac{1}{2\hbar}\sum_i\sum_q c_a^* c_b \mu_{ai}\mu_{bi}^* E_q^* \frac{1}{-\omega_q+\omega_i-\omega_b}e^{j\left(-\omega_q+\omega_a-\omega_b\right)t+jk_q z}. \tag{C.13}$$

Now examine the second term of the equation for $P\left(t\right)$ (Equation C.7).

$$\begin{aligned}\sum_i c_b^* c_i \mu_{bi} e^{j(\omega_b-\omega_i)t} &= \sum_i c_b^*\mu_{bi}e^{j(\omega_b-\omega_i)t} \\ &\times\Bigg\{\frac{1}{2\hbar}\sum_q\Bigg[\frac{E_q\mu_{ai}^* c_a}{\left(\omega_q+\omega_i-\omega_a\right)}e^{j(\omega_q+\omega_i-\omega_a)t-jk_q z} \\ &+\frac{E_q^*\mu_{ai}^* c_a}{\left(-\omega_q+\omega_i-\omega_a\right)}e^{j(-\omega_q+\omega_i-\omega_a)t+jk_q z} \\ &+\frac{E_q\mu_{bi}^* c_b}{\left(\omega_q+\omega_i-\omega_b\right)}e^{j(\omega_q+\omega_i-\omega_b)t-jk_q z} \\ &+\frac{E_q^*\mu_{bi}^* c_b}{\left(-\omega_q+\omega_i-\omega_b\right)}e^{j(-\omega_q+\omega_i-\omega_b)t+jk_q z}\Bigg]\Bigg\}\end{aligned} \tag{C.14}$$

Distribute, and rewrite this as

$$= \frac{1}{2\hbar}\sum_i\sum_q c_a c_b^* \mu_{ai}^*\mu_{bi} E_q \frac{1}{\omega_q+\omega_i-\omega_a}e^{j\left(\omega_q-\omega_a+\omega_b\right)t-jk_q z} \tag{C.15}$$

$$+\frac{1}{2\hbar}\sum_i\sum_q c_a c_b^* \mu_{ai}^*\mu_{bi} E_q^* \frac{1}{-\omega_q+\omega_i-\omega_a}e^{j\left(-\omega_q-\omega_a+\omega_b\right)t+jk_q z} \tag{C.16}$$

$$+\frac{1}{2\hbar}\sum_i\sum_q \left|c_b\right|^2\left|\mu_{bi}\right|^2 E_q \frac{1}{\omega_q+\omega_i-\omega_b}e^{j\omega_q t-jk_q z} \tag{C.17}$$

$$+\frac{1}{2\hbar}\sum_i\sum_q \left|c_b\right|^2\left|\mu_{bi}\right|^2 E_q^* \frac{1}{-\omega_q+\omega_i-\omega_b}e^{-j\omega_q t+jk_q z}. \tag{C.18}$$

The third term of the equation for $P(t)$ (Equation C.7) is

$$\begin{aligned}\sum_i c_a c_i^* \mu_{ai}^* e^{j\left(\omega_i-\omega_a\right)t} &= \sum_i c_a \mu_{ai}^* e^{j\left(\omega_i-\omega_a\right)t} \\ &\times\left\{\frac{1}{2\hbar}\sum_q\left[\frac{E_q\mu_{ai}^* c_a}{\left(\omega_q+\omega_i-\omega_a\right)}e^{j\left(\omega_q+\omega_i-\omega_a\right)t-jk_qz}\right.\right. \\ &+\frac{E_q^*\mu_{ai}^* c_a}{\left(-\omega_q+\omega_i-\omega_a\right)}e^{j\left(-\omega_q+\omega_i-\omega_a\right)t+jk_qz} \\ &+\frac{E_q\mu_{bi}^* c_b}{\left(\omega_q+\omega_i-\omega_b\right)}e^{j\left(\omega_q+\omega_i-\omega_b\right)t-jk_qz} \\ &\left.\left.+\frac{E_q^*\mu_{bi}^* c_b}{\left(-\omega_q+\omega_i-\omega_b\right)}e^{j\left(-\omega_q+\omega_i-\omega_b\right)t+jk_qz}\right]\right\}^*. \end{aligned} \tag{C.19}$$

Take the complex conjugate and distribute.

$$= \frac{1}{2\hbar}\sum_i\sum_q\left|c_a\right|^2\left|\mu_{ai}\right|^2 E_q^*\frac{1}{\omega_q+\omega_i-\omega_a}e^{-j\omega_q t+jk_qz} \tag{C.20}$$

$$+\frac{1}{2\hbar}\sum_i\sum_q\left|c_a\right|^2\left|\mu_{ai}\right|^2 E_q\frac{1}{-\omega_q+\omega_i-\omega_a}e^{j\omega_q t-jk_qz} \tag{C.21}$$

$$+\frac{1}{2\hbar}\sum_i\sum_q c_a c_b^*\mu_{ai}^*\mu_{bi}E_q^*\frac{1}{\omega_q+\omega_i-\omega_b}e^{j\left(-\omega_q-\omega_a+\omega_b\right)t+jk_qz} \tag{C.22}$$

$$+\frac{1}{2\hbar}\sum_i\sum_q c_a c_b^*\mu_{ai}^*\mu_{bi}E_q\frac{1}{-\omega_q+\omega_i-\omega_b}e^{j\left(\omega_q-\omega_a+\omega_b\right)t-jk_qz} \tag{C.23}$$

Note that this is the complex conjugate of the first term (lines C.10, C.11, C.12, and C.13).

Now for the fourth term of the equation for $P(t)$ (Equation C.7).

$$\begin{aligned}\sum_i c_b c_i^* \mu_{bi}^* e^{j(\omega_i-\omega_b)t} &= \sum_i c_b \mu_{bi}^* e^{j(\omega_i-\omega_b)t} \\ &\times\left\{\frac{1}{2\hbar}\sum_q\left[\frac{E_q\mu_{ai}^* c_a}{\left(\omega_q+\omega_i-\omega_a\right)}e^{j\left(\omega_q+\omega_i-\omega_a\right)t-jk_qz}\right.\right. \\ &+\frac{E_q^*\mu_{ai}^* c_a}{\left(-\omega_q+\omega_i-\omega_a\right)}e^{j(-\omega_q+\omega_i-\omega_a)t+jk_qz} \\ &+\frac{E_q\mu_{bi}^* c_b}{(\omega_q+\omega_i-\omega_b)}e^{j(\omega_q+\omega_i-\omega_b)t-jk_qz} \\ &\left.\left.+\frac{E_q^*\mu_{bi}^* c_b}{(-\omega_q+\omega_i-\omega_b)}e^{j(-\omega_q+\omega_i-\omega_b)t+jk_qz}\right]\right\}^* \end{aligned} \tag{C.24}$$

Take the complex conjugate and distribute.

$$= \frac{1}{2\hbar}\sum_i\sum_q c_a^* c_b \mu_{ai}\mu_{bi}^* E_q^* \frac{1}{\omega_q+\omega_i-\omega_a} e^{j(-\omega_q+\omega_a-\omega_b)t+jk_qz} \tag{C.25}$$

$$+\frac{1}{2\hbar}\sum_i\sum_q c_a^* c_b \mu_{ai}\mu_{bi}^* E_q \frac{1}{-\omega_q+\omega_i-\omega_a} e^{j(\omega_q+\omega_a-\omega_b)t-jk_qz} \tag{C.26}$$

$$+\frac{1}{2\hbar}\sum_i\sum_q |c_b|^2 |\mu_{bi}|^2 E_q^* \frac{1}{\omega_q+\omega_i-\omega_b} e^{-j\omega_q t+jk_qz} \tag{C.27}$$

$$+\frac{1}{2\hbar}\sum_i\sum_q |c_b|^2 |\mu_{bi}|^2 E_q \frac{1}{-\omega_q+\omega_i-\omega_b} e^{j\omega_q t-jk_qz} \tag{C.28}$$

Note that this is the complex conjugate of the second term (lines C.15, C.16, C.17, and C.18).

Now rewrite these terms in terms of the coupling and dispersion constants used in the previous derivation in order to get a more concise expression for $P(t)$.

$$a_q \equiv \frac{1}{2\hbar^2}\sum_i |\mu_{ai}|^2 \left[\frac{1}{(\omega_i-\omega_a)-\omega_q}+\frac{1}{(\omega_i-\omega_a)+\omega_q}\right] \tag{C.29}$$

$$b_q \equiv \frac{1}{2\hbar^2}\sum_i \mu_{ai}\mu_{bi}^* \left[\frac{1}{(\omega_i-\omega_a)-\omega_q}+\frac{1}{(\omega_i-\omega_b)+\omega_q}\right] \tag{C.30}$$

$$d_q \equiv \frac{1}{2\hbar^2}\sum_i |\mu_{bi}|^2 \left[\frac{1}{(\omega_i-\omega_b)-\omega_q}+\frac{1}{(\omega_i-\omega_b)+\omega_q}\right] \tag{C.31}$$

In order to simplify the expression, first sum pairs of lines.

First sum lines C.10 and C.21.

$$\begin{aligned} & \frac{1}{2\hbar}\sum_i\sum_q |c_a|^2 |\mu_{ai}|^2 E_q \frac{1}{\omega_q+\omega_i-\omega_a} e^{j\omega_q t-jk_qz} \\ + \quad & \frac{1}{2\hbar}\sum_i\sum_q |c_a|^2 |\mu_{ai}|^2 E_q \frac{1}{-\omega_q+\omega_i-\omega_a} e^{j\omega_q t-jk_qz} \\ = \quad & \frac{1}{2\hbar}\sum_i\sum_q |c_a|^2 |\mu_{ai}|^2 E_q e^{j\omega_q t-jk_qz}\left(\frac{1}{\omega_q+\omega_i-\omega_a}+\frac{1}{-\omega_q+\omega_i-\omega_a}\right) \end{aligned} \tag{C.32}$$

Pull the terms independent of i out in front of the sum over i, and rewrite using $\frac{1}{2\hbar} = \hbar\frac{1}{2\hbar^2}$.

$$= \hbar\sum_q |c_a|^2 E_q e^{j\omega_q t-jk_qz}\left[\frac{1}{2\hbar^2}\sum_i |\mu_{ai}|^2\left(\frac{1}{\omega_q+\omega_i-\omega_a}+\frac{1}{-\omega_q+\omega_i-\omega_a}\right)\right] \tag{C.33}$$

Use the above definition of a_q (Equation C.29).

$$= \hbar \sum_q |c_a|^2 E_q e^{j\omega_q t - jk_q z} a_q \tag{C.34}$$

Now sum lines C.11 and C.20.

$$\begin{aligned} & \frac{1}{2\hbar} \sum_i \sum_q |c_a|^2 |\mu_{ai}|^2 E_q^* \frac{1}{-\omega_q + \omega_i - \omega_a} e^{-j\omega_q t + jk_q z} \\ + \quad & \frac{1}{2\hbar} \sum_i \sum_q |c_a|^2 |\mu_{ai}|^2 E_q^* \frac{1}{\omega_q + \omega_i - \omega_a} e^{-j\omega_q t + jk_q z} \\ = \quad & \frac{1}{2\hbar} \sum_i \sum_q |c_a|^2 |\mu_{ai}|^2 E_q^* e^{-j\omega_q t + jk_q z} \left(\frac{1}{-\omega_q + \omega_i - \omega_a} + \frac{1}{\omega_q + \omega_i - \omega_a} \right) \end{aligned} \tag{C.35}$$

As above, pull the terms independent of i out in front of the sum over i, and rewrite using $\frac{1}{2\hbar} = \hbar \frac{1}{2\hbar^2}$.

$$= \hbar \sum_q |c_a|^2 E_q^* e^{-j\omega_q t + jk_q z} \left[\frac{1}{2\hbar^2} \sum_i |\mu_{ai}|^2 \left(\frac{1}{-\omega_q + \omega_i - \omega_a} + \frac{1}{\omega_q + \omega_i - \omega_a} \right) \right] \tag{C.36}$$

Use the above definition of a_q (Equation C.29).

$$= \hbar \sum_q |c_a|^2 E_q^* e^{-j\omega_q t + jk_q z} a_q \tag{C.37}$$

Now sum lines C.17 and C.28.

$$\begin{aligned} & \frac{1}{2\hbar} \sum_i \sum_q |c_b|^2 |\mu_{bi}|^2 E_q \frac{1}{\omega_q + \omega_i - \omega_b} e^{j\omega_q t - jk_q z} \\ + \quad & \frac{1}{2\hbar} \sum_i \sum_q |c_b|^2 |\mu_{bi}|^2 E_q \frac{1}{-\omega_q + \omega_i - \omega_b} e^{j\omega_q t - jk_q z} \\ = \quad & \frac{1}{2\hbar} \sum_i \sum_q |c_b|^2 |\mu_{bi}|^2 E_q e^{j\omega_q t - jk_q z} \left(\frac{1}{\omega_q + \omega_i - \omega_b} + \frac{1}{-\omega_q + \omega_i - \omega_b} \right) \end{aligned} \tag{C.38}$$

As above, pull the terms independent of i out in front of the sum over i, and rewrite using $\frac{1}{2\hbar} = \hbar\frac{1}{2\hbar^2}$.

$$= \hbar \sum_q |c_b|^2 E_q e^{j\omega_q t - jk_q z} \left[\frac{1}{2\hbar^2} \sum_i |\mu_{bi}|^2 \left(\frac{1}{\omega_q + \omega_i - \omega_b} + \frac{1}{-\omega_q + \omega_i - \omega_b} \right) \right] \tag{C.39}$$

Use the above definition of d_q (Equation C.31).

$$= \hbar \sum_q |c_b|^2 E_q e^{j\omega_q t - jk_q z} d_q \tag{C.40}$$

Now sum lines C.18 and C.27.

$$\begin{aligned} & \frac{1}{2\hbar} \sum_i \sum_q |c_b|^2 |\mu_{bi}|^2 E_q^* \frac{1}{-\omega_q + \omega_i - \omega_b} e^{-j\omega_q t + jk_q z} \\ + \quad & \frac{1}{2\hbar} \sum_i \sum_q |c_b|^2 |\mu_{bi}|^2 E_q^* \frac{1}{\omega_q + \omega_i - \omega_b} e^{-j\omega_q t + jk_q z} \\ = \quad & \frac{1}{2\hbar} \sum_i \sum_q |c_b|^2 |\mu_{bi}|^2 E_q^* e^{-j\omega_q t + jk_q z} \left(\frac{1}{-\omega_q + \omega_i - \omega_b} + \frac{1}{\omega_q + \omega_i - \omega_b} \right) \end{aligned} \tag{C.41}$$

As above, pull the terms independent of i out in front of the sum over i, and rewrite using $\frac{1}{2\hbar} = \hbar\frac{1}{2\hbar^2}$.

$$= \hbar \sum_q |c_b|^2 E_q^* e^{-j\omega_q t + jk_q z} \left[\frac{1}{2\hbar^2} \sum_i |\mu_{bi}|^2 \left(\frac{1}{-\omega_q + \omega_i - \omega_b} + \frac{1}{\omega_q + \omega_i - \omega_b} \right) \right] \tag{C.42}$$

Use the definition of d_q (Equation C.31).

$$= \hbar \sum_q |c_b|^2 E_q^* e^{-j\omega_q t + jk_q z} d_q \tag{C.43}$$

Next sum lines C.16 and C.22.

$$\begin{aligned} & \frac{1}{2\hbar}\sum_i\sum_q c_a c_b^* \mu_{ai}^* \mu_{bi} E_q^* \frac{1}{-\omega_q+\omega_i-\omega_a} e^{j(-\omega_q-\omega_a+\omega_b)t+jk_qz} \\ + & \frac{1}{2\hbar}\sum_i\sum_q c_a c_b^* \mu_{ai}^* \mu_{bi} E_q^* \frac{1}{\omega_q+\omega_i-\omega_b} e^{j(-\omega_q-\omega_a+\omega_b)t+jk_qz} \\ = & \frac{1}{2\hbar}\sum_i\sum_q c_a c_b^* \mu_{ai}^* \mu_{bi} E_q^* e^{j(-\omega_q-\omega_a+\omega_b)t+jk_qz}\left(\frac{1}{-\omega_q+\omega_i-\omega_a}+\frac{1}{\omega_q+\omega_i-\omega_b}\right) \end{aligned} \tag{C.44}$$

As above, pull the terms independent of i out in front of the sum over i, and rewrite using $\frac{1}{2\hbar} = \hbar\frac{1}{2\hbar^2}$.

$$= \hbar\sum_q c_a c_b^* E_q^* e^{j(-\omega_q-\omega_a+\omega_b)t+jk_qz}\left[\frac{1}{2\hbar^2}\sum_i \mu_{ai}^*\mu_{bi}\left(\frac{1}{-\omega_q+\omega_i-\omega_a}+\frac{1}{\omega_q+\omega_i-\omega_b}\right)\right] \tag{C.45}$$

The expression in the brackets is the complex conjugate of the definition of b_q (Equation C.30).

$$= \hbar\sum_q c_a c_b^* E_q^* e^{j(-\omega_q-\omega_a+\omega_b)t+jk_qz} b_q^* \tag{C.46}$$

Rewrite the exponent of this term. Begin by recalling the definitions of ω_q and ω_m from Appendix A.

$$\omega_q = \omega_0 + q\omega_m \tag{C.47}$$

with

$$\omega_m \equiv \omega_b - \omega_a - \Delta\omega \tag{C.48}$$

Rewrite the first term in the exponent using the definition of ω_q (Equation C.47).

$$-\omega_q - \omega_a + \omega_b = -\left(\omega_0 + q\omega_m\right) - \omega_a + \omega_b \tag{C.49}$$

Now use the definition of ω_m (Equation C.48).

$$= -\omega_0 - q\left(\omega_b - \omega_a - \Delta\omega\right) - \omega_a + \omega_b \tag{C.50}$$

Subtract and add $\Delta\omega$.

$$\begin{aligned} &= -\omega_0 - q\left(\omega_b - \omega_a - \Delta\omega\right) + \left(-\omega_a + \omega_b - \Delta\omega\right) + \Delta\omega \\ &= -\omega_0 - (q-1)\left(\omega_b - \omega_a - \Delta\omega\right) + \Delta\omega \end{aligned} \tag{C.51}$$

Use the definition of ω_m (Equation C.48).

$$= -\omega_0 - (q-1)\,\omega_m + \Delta\omega \tag{C.52}$$

Use the definition of ω_q (Equation C.47).

$$= -\omega_{q-1} + \Delta\omega \tag{C.53}$$

Substitute this back into the exponent above (Equation C.46).

$$\begin{aligned} &\hbar \sum_q c_a c_b^* E_q^* e^{j(-\omega_q - \omega_a + \omega_b)t + jk_q z} b_q^* \\ = \quad &\hbar \sum_q c_a c_b^* E_q^* e^{j(-\omega_{q-1} + \Delta\omega)t + jk_q z} b_q^* \end{aligned} \tag{C.54}$$

Now change the index variable from $q \to q+1$.

$$= \hbar \sum_{q+1} c_a c_b^* E_{q+1}^* e^{j(-\omega_q + \Delta\omega)t + jk_{q+1} z} b_{q+1}^* \tag{C.55}$$

Define k_q as in Appendix A.

$$k_q \equiv k_0 + qk_m \tag{C.56}$$

Use this definition to rewrite k_{q+1}.

$$\begin{aligned} k_{q+1} &= k_0 + (q+1)k_m \\ &= (k_0 + qk_m) + k_m \\ &= k_q + k_m \end{aligned} \tag{C.57}$$

Substitute this back into the above exponent (Equation C.55). Also factor out a -1 from the first term.

$$\begin{aligned} &\hbar \sum_{q+1} c_a c_b^* E_{q+1}^* e^{j(-\omega_q + \Delta\omega)t + jk_{q+1} z} b_{q+1}^* \\ = \quad &\hbar \sum_{q+1} c_a c_b^* E_{q+1}^* e^{-j(\omega_q - \Delta\omega)t + j(k_q + k_m) z} b_{q+1}^* \end{aligned} \tag{C.58}$$

Since the sum covers all Fourier components (q spans all integers), summing over q is the same as summing over $q+1$.

$$= \hbar \sum_q c_a c_b^* E_{q+1}^* e^{-j(\omega_q - \Delta\omega)t + j(k_q + k_m)z} b_{q+1}^* \tag{C.59}$$

Now sum lines C.12 and C.26.

$$\begin{aligned} & \frac{1}{2\hbar} \sum_i \sum_q c_a^* c_b \mu_{ai} \mu_{bi}^* E_q \frac{1}{\omega_q + \omega_i - \omega_b} e^{j(\omega_q + \omega_a - \omega_b)t - jk_q z} \\ + \quad & \frac{1}{2\hbar} \sum_i \sum_q c_a^* c_b \mu_{ai} \mu_{bi}^* E_q \frac{1}{-\omega_q + \omega_i - \omega_a} e^{j(\omega_q + \omega_a - \omega_b)t - jk_q z} \\ = \quad & \frac{1}{2\hbar} \sum_i \sum_q c_a^* c_b \mu_{ai} \mu_{bi}^* E_q e^{j(\omega_q + \omega_a - \omega_b)t - jk_q z} \left(\frac{1}{\omega_q + \omega_i - \omega_b} + \frac{1}{-\omega_q + \omega_i - \omega_a} \right) \end{aligned} \tag{C.60}$$

As above, pull the terms independent of i out in front of the sum over i, and rewrite using $\frac{1}{2\hbar} = \hbar \frac{1}{2\hbar^2}$.

$$= \hbar \sum_q c_a^* c_b E_q e^{j(\omega_q + \omega_a - \omega_b)t - jk_q z} \left[\frac{1}{2\hbar^2} \sum_i \mu_{ai} \mu_{bi}^* \left(\frac{1}{\omega_q + \omega_i - \omega_b} + \frac{1}{-\omega_q + \omega_i - \omega_a} \right) \right] \tag{C.61}$$

Use the definition of b_q (Equation C.30).

$$= \hbar \sum_q c_a^* c_b E_q e^{j(\omega_q + \omega_a - \omega_b)t - jk_q z} b_q \tag{C.62}$$

Rewrite the first term in the exponent. First use the definition of ω_q (Equation C.47).

$$\omega_q + \omega_a - \omega_b = (\omega_0 + q\omega_m) + \omega_a - \omega_b \tag{C.63}$$

Use the definition of ω_m (Equation C.48).

$$= \omega_0 + q\left(\omega_b - \omega_a - \Delta\omega\right) + \omega_a - \omega_b \tag{C.64}$$

Add and subtract $\Delta\omega$.

$$\begin{aligned} = \quad & \omega_0 + q\left(\omega_b - \omega_a - \Delta\omega\right) + \left(\omega_a - \omega_b + \Delta\omega\right) - \Delta\omega \\ = \quad & \omega_0 + q\left(\omega_b - \omega_a - \Delta\omega\right) - \left(-\omega_a + \omega_b - \Delta\omega\right) - \Delta\omega \\ = \quad & \omega_0 + (q-1)\left(\omega_b - \omega_a - \Delta\omega\right) - \Delta\omega \end{aligned} \tag{C.65}$$

Use the definition of ω_m (Equation C.48).

$$= \omega_0 + (q-1)\,\omega_m - \Delta\omega \tag{C.66}$$

Use the definition of ω_q (Equation C.47).

$$= \omega_{q-1} - \Delta\omega \tag{C.67}$$

Plug this into the exponent of the above equation (Equation C.62).

$$\begin{aligned} &\hbar \sum_q c_a^* c_b E_q e^{j(\omega_q+\omega_a-\omega_b)t-jk_q z} b_q \\ &= \hbar \sum_q c_a^* c_b E_q e^{j(\omega_{q-1}-\Delta\omega)t-jk_q z} b_q \end{aligned} \tag{C.68}$$

Now make a change of index variable from $q \to q+1$.

$$= \hbar \sum_{q+1} c_a^* c_b E_{q+1} e^{j(\omega_q-\Delta\omega)t-jk_{q+1} z} b_{q+1} \tag{C.69}$$

As above, since q spans all integers, the sum can be taken to be over q instead of $q+1$.

$$= \hbar \sum_{q} c_a^* c_b E_{q+1} e^{j(\omega_q-\Delta\omega)t-jk_{q+1} z} b_{q+1} \tag{C.70}$$

Now replace k_{q+1} as above (Equation C.57).

$$= \hbar \sum_{q} c_a^* c_b E_{q+1} e^{j(\omega_q-\Delta\omega)t-j(k_q+k_m) z} b_{q+1} \tag{C.71}$$

Next sum lines C.15 and C.23.

$$\begin{aligned} & \frac{1}{2\hbar} \sum_i \sum_q c_a c_b^* \mu_{ai}^* \mu_{bi} E_q \frac{1}{\omega_q + \omega_i - \omega_a} e^{j(\omega_q-\omega_a+\omega_b)t-jk_q z} \\ + \quad & \frac{1}{2\hbar} \sum_i \sum_q c_a c_b^* \mu_{ai}^* \mu_{bi} E_q \frac{1}{-\omega_q + \omega_i - \omega_b} e^{j(\omega_q-\omega_a+\omega_b)t-jk_q z} \\ = \quad & \frac{1}{2\hbar} \sum_i \sum_q c_a c_b^* \mu_{ai}^* \mu_{bi} E_q e^{j(\omega_q-\omega_a+\omega_b)t-jk_q z} \left(\frac{1}{\omega_q + \omega_i - \omega_a} + \frac{1}{-\omega_q + \omega_i - \omega_b} \right) \end{aligned} \tag{C.72}$$

Once again pull the terms independent of i out in front of the sum over i and rewrite using $\frac{1}{2\hbar} = \hbar\frac{1}{2\hbar^2}$.

$$= \hbar \sum_q c_a c_b^* E_q e^{j(\omega_q - \omega_a + \omega_b)t - jk_q z} \left[\frac{1}{2\hbar^2} \sum_i \mu_{ai}^* \mu_{bi} \left(\frac{1}{\omega_q + \omega_i - \omega_a} + \frac{1}{-\omega_q + \omega_i - \omega_b} \right) \right] \tag{C.73}$$

Now rewrite the denominators in the parentheses using the definitions of ω_q and ω_m.

For the first denominator, begin with the definition of ω_q (Equation C.47).

$$\omega_q + \omega_i - \omega_a = (\omega_0 + q\omega_m) + \omega_i - \omega_a \tag{C.74}$$

Add and subtract ω_m.

$$\begin{aligned} &= (\omega_0 + q\omega_m + \omega_m) - \omega_m + \omega_i - \omega_a \\ &= [\omega_0 + (q+1)\,\omega_m] - \omega_m + \omega_i - \omega_a \end{aligned} \tag{C.75}$$

Use the definition of ω_q (Equation C.47).

$$= \omega_{q+1} - \omega_m + \omega_i - \omega_a \tag{C.76}$$

Use the definition of ω_m (Equation C.48).

$$\begin{aligned} &= \omega_{q+1} - (\omega_b - \omega_a - \Delta\omega) + \omega_i - \omega_a \\ &= \omega_{q+1} - \omega_b + \Delta\omega + \omega_i \end{aligned} \tag{C.77}$$

As in the previous derivation, we are assuming that the detuning, $\Delta\omega$, is small compared to ω_b, ω_{q+1}, and ω_i. Thus the first denominator can be approximated as

$$\approx \omega_{q+1} - \omega_b + \omega_i. \tag{C.78}$$

Similarly, the second denominator in the above (Equation C.73) can be rewritten, beginning by using the definition of ω_q (Equation C.47).

$$-\omega_q + \omega_i - \omega_b = -(\omega_0 + q\omega_m) + \omega_i - \omega_b \tag{C.79}$$

Subtract and add ω_m.

$$\begin{aligned} &= -\left(\omega_0 + q\omega_m + \omega_m\right) + \omega_m + \omega_i - \omega_b \\ &= -\left(\omega_0 + \left(q+1\right)\omega_m\right) + \omega_m + \omega_i - \omega_b \end{aligned} \tag{C.80}$$

Use the definition of ω_q (Equation C.47).

$$= -\omega_{q+1} + \omega_m + \omega_i - \omega_b \tag{C.81}$$

Use the definition of ω_m (Equation C.48).

$$\begin{aligned} &= -\omega_{q+1} + \left(\omega_b - \omega_a - \Delta\omega\right) + \omega_i - \omega_b \\ &= -\omega_{q+1} - \omega_a - \Delta\omega + \omega_i \end{aligned} \tag{C.82}$$

Assuming a small detuning as above, the second denominator is approximately

$$\approx -\omega_{q+1} - \omega_a + \omega_i. \tag{C.83}$$

Substituting these rewritten denominators (Equations C.78 and C.83) into the expression for the sum of lines C.15 and C.23 (Equation C.73), it becomes

$$\begin{aligned} &\hbar \sum_q c_a c_b^* E_q e^{j(\omega_q - \omega_a + \omega_b)t - jk_q z} \left[\frac{1}{2\hbar^2} \sum_i \mu_{ai}^* \mu_{bi} \left(\frac{1}{\omega_q + \omega_i - \omega_a} + \frac{1}{-\omega_q + \omega_i - \omega_b}\right)\right] \\ \approx\ &\hbar \sum_q c_a c_b^* E_q e^{j(\omega_q - \omega_a + \omega_b)t - jk_q z} \left[\frac{1}{2\hbar^2} \sum_i \mu_{ai}^* \mu_{bi} \left(\frac{1}{\omega_{q+1} - \omega_b + \omega_i} + \frac{1}{-\omega_{q+1} - \omega_a + \omega_i}\right)\right]. \end{aligned} \tag{C.84}$$

Note the expression in the bracket is complex conjugate of the definition of b_q with $q = q + 1$ (Equation C.30), so

$$= \hbar \sum_q c_a c_b^* E_q e^{j(\omega_q - \omega_a + \omega_b)t - jk_q z} b_{q+1}^*. \tag{C.85}$$

Rewrite the first part of the exponent using the definition of ω_q (Equation C.47).

$$\omega_q - \omega_a + \omega_b = \left(\omega_0 + q\omega_m\right) - \omega_a + \omega_b \tag{C.86}$$

Now use the definition of ω_m (Equation C.48).

$$= \omega_0 + q\left(\omega_b - \omega_a - \Delta\omega\right) - \omega_a + \omega_b \tag{C.87}$$

Subtract and add $\Delta\omega$.

$$\begin{aligned} &= \omega_0 + q\left(\omega_b - \omega_a - \Delta\omega\right) + \left(-\omega_a + \omega_b - \Delta\omega\right) + \Delta\omega \\ &= \omega_0 + (q+1)\left(\omega_b - \omega_a - \Delta\omega\right) + \Delta\omega \end{aligned} \tag{C.88}$$

Now use the definition of ω_m again.

$$= \left[\omega_0 + (q+1)\,\omega_m\right] + \Delta\omega \tag{C.89}$$

Again, use the definition of ω_q (Equation C.47) with $q = q + 1$.

$$= \omega_{q+1} + \Delta\omega \tag{C.90}$$

Plug this back in the exponent above (Equation C.85).

$$\begin{aligned} &\hbar \sum_q c_a c_b^* E_q e^{j(\omega_q - \omega_a + \omega_b)t - jk_q z} b_{q+1}^* \\ &= \hbar \sum_q c_a c_b^* E_q e^{j(\omega_{q+1} + \Delta\omega)t - jk_q z} b_{q+1}^* \end{aligned} \tag{C.91}$$

Now change the index variable from $q \to q - 1$.

$$= \hbar \sum_{q-1} c_a c_b^* E_{q-1} e^{j(\omega_q + \Delta\omega)t - jk_{q-1} z} b_q^* \tag{C.92}$$

Use the definition of k_q (Equation C.56) to rewrite k_{q-1}.

$$\begin{aligned} k_{q-1} &= k_0 + (q-1)\,k_m \\ &= (k_0 + qk_m) - k_m \end{aligned} \tag{C.93}$$

Again use the definition of k_q (Equation C.56).

$$= k_q - k_m \tag{C.94}$$

Use this to replace k_{q-1} above (Equation C.92).

$$\begin{aligned} & \hbar \sum_{q-1} c_a c_b^* E_{q-1} e^{j(\omega_q + \Delta\omega)t - jk_{q-1}z} b_q^* \\ = \quad & \hbar \sum_{q-1} c_a c_b^* E_{q-1} e^{j(\omega_q + \Delta\omega)t - j(k_q - k_m)z} b_q^* \end{aligned} \tag{C.95}$$

As above, since q spans all integers, the sum can be taken to be over q instead of $q-1$.

$$= \hbar \sum_{q} c_a c_b^* E_{q-1} e^{j(\omega_q + \Delta\omega)t - j(k_q - k_m)z} b_q^* \tag{C.96}$$

Next sum lines C.13 and C.25.

$$\begin{aligned} & \frac{1}{2\hbar} \sum_i \sum_q c_a^* c_b \mu_{ai} \mu_{bi}^* E_q^* \frac{1}{-\omega_q + \omega_i - \omega_b} e^{j(-\omega_q + \omega_a - \omega_b)t + jk_q z} \\ + \quad & \frac{1}{2\hbar} \sum_i \sum_q c_a^* c_b \mu_{ai} \mu_{bi}^* E_q^* \frac{1}{\omega_q + \omega_i - \omega_a} e^{j(-\omega_q + \omega_a - \omega_b)t + jk_q z} \\ = \quad & \frac{1}{2\hbar} \sum_i \sum_q c_a^* c_b \mu_{ai} \mu_{bi}^* E_q^* e^{j(-\omega_q + \omega_a - \omega_b)t + jk_q z} \left(\frac{1}{-\omega_q + \omega_i - \omega_b} + \frac{1}{\omega_q + \omega_i - \omega_a} \right) \end{aligned} \tag{C.97}$$

As above, pull the terms independent of i out in front of the sum over i, and rewrite using $\frac{1}{2\hbar} = \hbar \frac{1}{2\hbar^2}$.

$$= \hbar \sum_q c_a^* c_b E_q^* e^{j(-\omega_q + \omega_a - \omega_b)t + jk_q z} \left[\frac{1}{2\hbar^2} \sum_i \mu_{ai} \mu_{bi}^* \left(\frac{1}{-\omega_q + \omega_i - \omega_b} + \frac{1}{\omega_q + \omega_i - \omega_a} \right) \right] \tag{C.98}$$

Rewrite the denominators in the parentheses using the above approximations (Equations C.78 and C.83).

$$= \hbar \sum_q c_a^* c_b E_q^* e^{j(-\omega_q + \omega_a - \omega_b)t + jk_q z} \left[\frac{1}{2\hbar^2} \sum_i \mu_{ai} \mu_{bi}^* \left(\frac{1}{-\omega_{q+1} + \omega_i - \omega_a} + \frac{1}{\omega_{q+1} + \omega_i - \omega_b} \right) \right] \tag{C.99}$$

Note that quantity in the bracket is the definition of b_q (Equation C.30) with $q = q+1$.

$$= \hbar \sum_q c_a^* c_b E_q^* e^{j(-\omega_q + \omega_a - \omega_b)t + jk_q z} b_{q+1} \tag{C.100}$$

Rewrite the first part of the exponent using the definition of ω_q (Equation C.47).

$$-\omega_q + \omega_a - \omega_b = -\left(\omega_0 + q\omega_m\right) + \omega_a - \omega_b \tag{C.101}$$

Now use the definition of ω_m (Equation C.48).

$$= -\omega_0 - q\left(\omega_b - \omega_a - \Delta\omega\right) + \omega_a - \omega_b \tag{C.102}$$

Add and subtract $\Delta\omega$.

$$\begin{aligned} &= -\omega_0 - q\left(\omega_b - \omega_a - \Delta\omega\right) + \left(\omega_a - \omega_b + \Delta\omega\right) - \Delta\omega \\ &= -\omega_0 - q\left(\omega_b - \omega_a - \Delta\omega\right) - \left(-\omega_a + \omega_b - \Delta\omega\right) - \Delta\omega \\ &= -\omega_0 - (q+1)\left(\omega_b - \omega_a - \Delta\omega\right) - \Delta\omega \end{aligned} \tag{C.103}$$

Now use the definition of ω_m (Equation C.48) again.

$$\begin{aligned} &= -\omega_0 - (q+1)\,\omega_m - \Delta\omega \\ &= -\left[\omega_0 + (q+1)\,\omega_m\right] - \Delta\omega \end{aligned} \tag{C.104}$$

The definition of ω_q (Equation C.47) yields

$$= -\omega_{q+1} - \Delta\omega. \tag{C.105}$$

Plug this back into the exponent above (Equation C.100).

$$\begin{aligned} &\hbar \sum_q c_a^* c_b E_q^* e^{j(-\omega_q + \omega_a - \omega_b)t + jk_q z} b_{q+1} \\ = \;& \hbar \sum_q c_a^* c_b E_q^* e^{j(-\omega_{q+1} - \Delta\omega)t + jk_q z} b_{q+1} \end{aligned} \tag{C.106}$$

Now change the index variable from $q \to q-1$.

$$= \hbar \sum_{q-1} c_a^* c_b E_{q-1}^* e^{j(-\omega_q - \Delta\omega)t + jk_{q-1} z} b_q \tag{C.107}$$

Use the expression above to replace k_{q-1} (Equation C.94).

$$= \hbar \sum_{q-1} c_a^* c_b E_{q-1}^* e^{j(-\omega_q - \Delta\omega)t + j(k_q - k_m) z} b_q \tag{C.108}$$

As above, since q spans all integers, the sum can be taken to be over q instead of $q-1$.

$$= \hbar \sum_q c_a^* c_b E_{q-1}^* e^{j(-\omega_q - \Delta\omega)t + j(k_q - k_m)z} b_q \tag{C.109}$$

Now combine all of these contributions (Equations C.34, C.37, C.40, C.43, C.59, C.71, C.96, and C.109) to get an expression for $P(t)$.

$$\begin{aligned} P(t) &= \hbar \sum_q |c_a|^2 E_q e^{j\omega_q t - jk_q z} a_q \\ &+ \hbar \sum_q |c_a|^2 E_q^* e^{-j\omega_q t + jk_q z} a_q \\ &+ \hbar \sum_q |c_b|^2 E_q e^{j\omega_q t - jk_q z} d_q \\ &+ \hbar \sum_q |c_b|^2 E_q^* e^{-j\omega_q t + jk_q z} d_q \\ &+ \hbar \sum_q c_a c_b^* E_{q+1}^* e^{-j(\omega_q - \Delta\omega)t + j(k_q + k_m)z} b_{q+1}^* \\ &+ \hbar \sum_q c_a^* c_b E_{q+1} e^{j(\omega_q - \Delta\omega)t - j(k_q + k_m)z} b_{q+1} \\ &+ \hbar \sum_q c_a c_b^* E_{q-1} e^{j(\omega_q + \Delta\omega)t - j(k_q - k_m)z} b_q^* \\ &+ \hbar \sum_q c_a^* c_b E_{q-1}^* e^{j(-\omega_q - \Delta\omega)t + j(k_q - k_m)z} b_q \end{aligned} \tag{C.110}$$

Next write the total dipole moment as a sum of its Fourier coefficients, in the form of the following:

$$P(t) = \frac{1}{2} \sum_q P_q e^{j\omega_q t - jk_q z} + \frac{1}{2} \sum_q P_q^* e^{-j\omega_q t + jk_q z}. \tag{C.111}$$

Begin by rearranging the above expression for $P(t)$ (Equation C.110) to match the Fourier form, dividing and multiplying all terms by 2.

$$\begin{aligned}
P(t) &= \frac{1}{2}\sum_q \left[2\hbar |c_a|^2 E_q a_q\right] e^{j\omega_q t - jk_q z} \\
&+\frac{1}{2}\sum_q \left[2\hbar |c_a|^2 E_q^* a_q\right] e^{-j\omega_q t + jk_q z} \\
&+\frac{1}{2}\sum_q \left[2\hbar |c_b|^2 E_q d_q\right] e^{j\omega_q t - jk_q z} \\
&+\frac{1}{2}\sum_q \left[2\hbar |c_b|^2 E_q^* d_q\right] e^{-j\omega_q t + jk_q z} \\
&+\frac{1}{2}\sum_q \left[2\hbar c_a c_b^* E_{q+1}^* b_{q+1}^* e^{j\Delta\omega t + jk_m z}\right] e^{-j\omega_q t + jk_q z} \\
&+\frac{1}{2}\sum_q \left[2\hbar c_a^* c_b E_{q+1} b_{q+1} e^{-j\Delta\omega t - jk_m z}\right] e^{j\omega_q t - jk_q z} \\
&+\frac{1}{2}\sum_q \left[2\hbar c_a c_b^* E_{q-1} b_q^* e^{j\Delta\omega t + jk_m z}\right] e^{j\omega_q t - jk_q z} \\
&+\frac{1}{2}\sum_q \left[2\hbar c_a^* c_b E_{q-1}^* b_q e^{-j\Delta\omega t - jk_m z}\right] e^{-j\omega_q t + jk_q z}
\end{aligned} \tag{C.112}$$

Group terms with like exponentials.

$$\begin{aligned}
P(t) &= \\
&\frac{1}{2}\sum_q \Big[2\hbar|c_a|^2 E_q a_q + 2\hbar|c_b|^2 E_q d_q + 2\hbar c_a^* c_b E_{q+1} b_{q+1} e^{-j\Delta\omega t - jk_m z} \\
&\qquad +2\hbar c_a c_b^* E_{q-1} b_q^* e^{j\Delta\omega t + jk_m z}\Big] e^{j\omega_q t - jk_q z} \\
&+\frac{1}{2}\sum_q \Big[2\hbar|c_a|^2 E_q^* a_q + 2\hbar|c_b|^2 E_q^* d_q + 2\hbar c_a c_b^* E_{q+1}^* b_{q+1}^* e^{j\Delta\omega t + jk_m z} \\
&\qquad +2\hbar c_a^* c_b E_{q-1}^* b_q e^{-j\Delta\omega t - jk_m z}\Big] e^{-j\omega_q t + jk_q z}
\end{aligned} \tag{C.113}$$

Note that $a_q = a_q^*$ and $d_q = d_q^*$ because both are real, so we can use the complex conjugate forms in the second bracket.

$$\begin{aligned} P(t) \;=\; & \\ & \frac{1}{2}\sum_q \Big[2\hbar\big|c_a\big|^2 E_q a_q + 2\hbar\big|c_b\big|^2 E_q d_q + 2\hbar c_a^* c_b E_{q+1} b_{q+1} e^{-j\Delta\omega t - jk_m z} \\ & \qquad +2\hbar c_a c_b^* E_{q-1} b_q^* e^{j\Delta\omega t + jk_m z}\Big] e^{j\omega_q t - jk_q z} \\ & +\frac{1}{2}\sum_q \Big[2\hbar\big|c_a\big|^2 E_q^* a_q^* + 2\hbar\big|c_b\big|^2 E_q^* d_q^* + 2\hbar c_a c_b^* E_{q+1}^* b_{q+1}^* e^{j\Delta\omega t + jk_m z} \\ & \qquad +2\hbar c_a^* c_b E_{q-1}^* b_q e^{-j\Delta\omega t - jk_m z}\Big] e^{-j\omega_q t + jk_q z} \end{aligned} \tag{C.114}$$

This allows us to simplify to

$$P(t) = \frac{1}{2}\sum_q P_q e^{j\omega_q t - jk_q z} + \frac{1}{2}\sum_q P_q^* e^{-j\omega_q t + jk_q z}, \tag{C.115}$$

with P_q defined as

$$P_q \equiv 2\hbar\left|c_a\right|^2 E_q a_q + 2\hbar\left|c_b\right|^2 E_q d_q + 2\hbar c_a^* c_b E_{q+1} b_{q+1} e^{-j\Delta\omega t - jk_m z} + 2\hbar c_a c_b^* E_{q-1} b_q^* e^{j\Delta\omega t + jk_m z}. \tag{C.116}$$

We can pull out the common $2\hbar$ to rewrite this term.

$$P_q = 2\hbar\big[\left|c_a\right|^2 E_q a_q + \left|c_b\right|^2 E_q d_q + c_a^* c_b E_{q+1} b_{q+1} e^{-j\Delta\omega t - jk_m z} + c_a c_b^* E_{q-1} b_q^* e^{j\Delta\omega t + jk_m z}\big] \tag{C.117}$$

The slowly-varying envelope equation for propagation in the z direction for each Fourier component of the electric field, E_q, is

$$\frac{\partial E_q}{\partial z} = -j\frac{1}{2}\eta\omega_q P_q, \tag{C.118}$$

where

$$\eta \equiv \sqrt{\frac{\mu}{\varepsilon_0}}. \tag{C.119}$$

Note that we have also assumed that diffraction effects are negligible, so we have dropped a second-order term in the transverse directions; $\nabla_\perp^2 E_q \approx 0$, where $\nabla_\perp \equiv \frac{\partial}{\partial x}\hat{x} + \frac{\partial}{\partial y}\hat{y}$.

Plug in the above expression for P_q (Equation C.117), and the envelope equation becomes

$$\begin{aligned}
&\frac{\partial E_q}{\partial z} \\
= \;& -j\frac{1}{2}\eta\omega_q \\
&\times\left[2\hbar\big[\,|c_a|^2 E_q a_q + |c_b|^2 E_q d_q + c_a^* c_b E_{q+1} b_{q+1} e^{-j\Delta\omega t - jk_m z} + c_a c_b^* E_{q-1} b_q^* e^{j\Delta\omega t + jk_m z}\big]\right] \\
= \;& -j\eta\hbar\omega_q \\
&\times\big[\,|c_a|^2 E_q a_q + |c_b|^2 E_q d_q + c_a^* c_b E_{q+1} b_{q+1} e^{-j\Delta\omega t - jk_m z} + c_a c_b^* E_{q-1} b_q^* e^{j\Delta\omega t + jk_m z}\big].
\end{aligned} \tag{C.120}$$

This expression can be simplified by making the following phase transformations:

$$c_a \equiv \tilde{c}_a \tag{C.121}$$

and

$$c_b \equiv \tilde{c}_b e^{j\Delta\omega t + jk_m z}. \tag{C.122}$$

Phase transforming the above (Equation C.120) yields

$$\begin{aligned}
\frac{\partial E_q}{\partial z} \;=\; & -j\eta\hbar\omega_q\Big[\big|\big(\tilde{c}_a\big)\big|^2 E_q a_q \\
&+\big|\big(\tilde{c}_b e^{j\Delta\omega t + jk_m z}\big)\big|^2 E_q d_q \\
&+\big(\tilde{c}_a^*\big)\big(\tilde{c}_b e^{j\Delta\omega t + jk_m z}\big) E_{q+1} b_{q+1} e^{-j\Delta\omega t - jk_m z} \\
&+\big(\tilde{c}_a\big)\big(\tilde{c}_b^* e^{-j\Delta\omega t - jk_m z}\big) E_{q-1} b_q^* e^{j\Delta\omega t + jk_m z}\Big].
\end{aligned} \tag{C.123}$$

Noting that $\left|e^{i\theta}\right| = 1$ for all θ and that $e^x + e^{-x} = e^0 = 1$ for all x, this reduces to

$$\frac{\partial E_q}{\partial z} = -j\eta\hbar\omega_q\left[|\tilde{c}_a|^2 E_q a_q + |\tilde{c}_b|^2 E_q d_q + \tilde{c}_a^*\tilde{c}_b E_{q+1} b_{q+1} + \tilde{c}_a\tilde{c}_b^* E_{q-1} b_q^*\right]. \tag{C.124}$$

Multiplication by the number of molecules per unit volume, N, yields the slowly-varying envelope equation for a macroscopic system.

$$\frac{\partial E_q}{\partial z} = -j\eta\hbar\omega_q N\left[|\tilde{c}_a|^2 E_q a_q + |\tilde{c}_b|^2 E_q d_q + \tilde{c}_a^*\tilde{c}_b E_{q+1} b_{q+1} + \tilde{c}_a\tilde{c}_b^* E_{q-1} b_q^*\right] \tag{C.125}$$

Appendix D: Density Matrix Elements

We will calculate the density matrix elements for our density matrix ρ for the previously calculated eigenstate: (See Equation B.33 and Appendix B.)

$$|\psi\rangle = \cos\left(\frac{\theta}{2}\right) e^{j\frac{\phi}{2}} |a\rangle + \sin\left(\frac{\theta}{2}\right) e^{-j\frac{\phi}{2}} |b\rangle . \tag{D.1}$$

Each element ρ_{mn} can be calculated with the inner products

$$\rho_{mn} \equiv \langle m|\psi\rangle \langle\psi|n\rangle . \tag{D.2}$$

First calculate ρ_{aa}.

$$\rho_{aa} = \langle a|\psi\rangle \langle\psi|a\rangle \tag{D.3}$$

Now plug in $|\psi\rangle$ from above, conjugating all terms for the bra term.

$$\rho_{aa} = \langle a| \left(\cos\left(\frac{\theta}{2}\right) e^{j\frac{\phi}{2}} |a\rangle + \sin\left(\frac{\theta}{2}\right) e^{-j\frac{\phi}{2}} |b\rangle\right) \left(\cos\left(\frac{\theta}{2}\right) e^{-j\frac{\phi}{2}} \langle a| + \sin\left(\frac{\theta}{2}\right) e^{j\frac{\phi}{2}} \langle b|\right) |a\rangle \tag{D.4}$$

Pull the θ terms out of the inner products. Then distribute and use orthonormality of states, $\langle n|m\rangle = \delta_{nm}$, to simplify the expression.

$$\begin{aligned}
\rho_{aa} &= \left(\cos\left(\frac{\theta}{2}\right) e^{j\frac{\phi}{2}} \langle a|a\rangle + \sin\left(\frac{\theta}{2}\right) e^{-j\frac{\phi}{2}} \langle a|b\rangle\right) \\
&\qquad \times \left(\cos\left(\frac{\theta}{2}\right) e^{-j\frac{\phi}{2}} \langle a|a\rangle + \sin\left(\frac{\theta}{2}\right) e^{j\frac{\phi}{2}} \langle b|a\rangle\right) \\
&= \left(\cos\left(\frac{\theta}{2}\right) e^{j\frac{\phi}{2}} (1) + \sin\left(\frac{\theta}{2}\right) e^{-j\frac{\phi}{2}} (0)\right) \left(\cos\left(\frac{\theta}{2}\right) e^{-j\frac{\phi}{2}} (1) + \sin\left(\frac{\theta}{2}\right) e^{j\frac{\phi}{2}} (0)\right) \\
&= \left(\cos\left(\frac{\theta}{2}\right) e^{j\frac{\phi}{2}}\right) \left(\cos\left(\frac{\theta}{2}\right) e^{-j\frac{\phi}{2}}\right) \\
\rho_{aa} &= \cos^2\left(\frac{\theta}{2}\right)
\end{aligned} \tag{D.5}$$

The calculations for ρ_{bb} are similar.

$$\rho_{bb} = \langle b|\psi\rangle \langle\psi|b\rangle \tag{D.6}$$

Now plug in $|\psi\rangle$ from above, conjugating all terms for the bra term.

$$\begin{aligned}\rho_{bb} &= \langle b| \left(\cos\left(\frac{\theta}{2}\right) e^{j\frac{\phi}{2}} |a\rangle + \sin\left(\frac{\theta}{2}\right) e^{-j\frac{\phi}{2}} |b\rangle\right) \\ &\quad \times \left(\cos\left(\frac{\theta}{2}\right) e^{-j\frac{\phi}{2}} \langle a| + \sin\left(\frac{\theta}{2}\right) e^{j\frac{\phi}{2}} \langle b|\right) |b\rangle \end{aligned} \tag{D.7}$$

Pull the θ terms out of the inner products. Then distribute and use orthonormality of states, $\langle n|m\rangle = \delta_{nm}$, to simplify the expression.

$$\begin{aligned}\rho_{bb} &= \left(\cos\left(\frac{\theta}{2}\right) e^{j\frac{\phi}{2}} \langle b|a\rangle + \sin\left(\frac{\theta}{2}\right) e^{-j\frac{\phi}{2}} \langle b|b\rangle\right) \\ &\quad \times \left(\cos\left(\frac{\theta}{2}\right) e^{-j\frac{\phi}{2}} \langle a|b\rangle + \sin\left(\frac{\theta}{2}\right) e^{j\frac{\phi}{2}} \langle b|b\rangle\right) \\ &= \left(\cos\left(\frac{\theta}{2}\right) e^{j\frac{\phi}{2}} (0) + \sin\left(\frac{\theta}{2}\right) e^{-j\frac{\phi}{2}} (1)\right) \left(\cos\left(\frac{\theta}{2}\right) e^{-j\frac{\phi}{2}} (0) + \sin\left(\frac{\theta}{2}\right) e^{j\frac{\phi}{2}} (1)\right) \\ &= \left(\sin\left(\frac{\theta}{2}\right) e^{-j\frac{\phi}{2}}\right) \left(\sin\left(\frac{\theta}{2}\right) e^{j\frac{\phi}{2}}\right) \\ \rho_{bb} &= \sin^2\left(\frac{\theta}{2}\right) \end{aligned} \tag{D.8}$$

Now consider the coherence, ρ_{ab}.

$$\rho_{ab} = \langle a|\psi\rangle \langle \psi|b\rangle \tag{D.9}$$

Now plug in $|\psi\rangle$ from above, conjugating all terms for the bra term.

$$\rho_{ab} = \langle a| \left(\cos\left(\frac{\theta}{2}\right) e^{j\frac{\phi}{2}} |a\rangle + \sin\left(\frac{\theta}{2}\right) e^{-j\frac{\phi}{2}} |b\rangle\right) \left(\cos\left(\frac{\theta}{2}\right) e^{-j\frac{\phi}{2}} \langle a| + \sin\left(\frac{\theta}{2}\right) e^{j\frac{\phi}{2}} \langle b|\right) |b\rangle \tag{D.10}$$

Pull the θ terms out of the inner products. Then distribute and use orthonormality of states, $\langle n|m\rangle = \delta_{nm}$, to simplify the expression.

$$\begin{aligned}
\rho_{ab} &= \left(\cos\left(\frac{\theta}{2}\right) e^{j\frac{\phi}{2}} \langle a|a\rangle + \sin\left(\frac{\theta}{2}\right) e^{-j\frac{\phi}{2}} \langle a|b\rangle\right) \\
&\qquad \times \left(\cos\left(\frac{\theta}{2}\right) e^{-j\frac{\phi}{2}} \langle a|b\rangle + \sin\left(\frac{\theta}{2}\right) e^{j\frac{\phi}{2}} \langle b|b\rangle\right) \\
&= \left(\cos\left(\frac{\theta}{2}\right) e^{j\frac{\phi}{2}} (1) + \sin\left(\frac{\theta}{2}\right) e^{-j\frac{\phi}{2}} (0)\right)\left(\cos\left(\frac{\theta}{2}\right) e^{-j\frac{\phi}{2}} (0) + \sin\left(\frac{\theta}{2}\right) e^{j\frac{\phi}{2}} (1)\right) \\
&= \left(\cos\left(\frac{\theta}{2}\right) e^{j\frac{\phi}{2}}\right)\left(\sin\left(\frac{\theta}{2}\right) e^{j\frac{\phi}{2}}\right) \\
&= \cos\left(\frac{\theta}{2}\right)\sin\left(\frac{\theta}{2}\right) e^{j\phi} \qquad \text{(D.11)}
\end{aligned}$$

Finally, we can rewrite this using a half-angle trigonometric formula:

$$\rho_{ab} = \frac{1}{2}\sin(\theta)\, e^{j\phi}. \qquad \text{(D.12)}$$

Recall that

$$\theta \equiv \tan^{-1}\left(\frac{2|B|}{A - D + 2\Delta\omega}\right), \qquad \text{(D.13)}$$

where B is related to the coupling of the two molecular states. If the coupling is weak, as is the case for many of our experiments, then the argument of the arctangent is small, and we can use the small angle approximation, $\arctan(x) \approx x$. This eliminates the arctangent in our expression.

$$\theta \approx \frac{2|B|}{A - D + 2\Delta\omega} \qquad \text{(D.14)}$$

The small angle approximation can then be used to rewrite ρ_{ab}.

$$\rho_{ab} = \frac{1}{2}\sin(\theta)\, e^{j\phi} \qquad \text{(D.15)}$$

For small x, we have $\sin(x) \approx x$.

$$\rho_{ab} \approx \frac{\theta}{2} e^{j\phi} \qquad \text{(D.16)}$$

The small angle approximation can also be used to rewrite ρ_{aa}.

From Equation D.5, we have

$$\rho_{aa} = \cos^2\left(\frac{\theta}{2}\right). \qquad \text{(D.17)}$$

For small x, we have $\cos(x) \approx 1 - \frac{x^2}{2}$.

Thus,

$$\begin{aligned} \rho_{aa} &= \cos\left(\frac{\theta}{2}\right)\cos\left(\frac{\theta}{2}\right) \\ &= \left(1 - \frac{\theta^2}{8}\right)\left(1 - \frac{\theta^2}{8}\right) \\ \rho_{aa} &\approx 1 - \frac{\theta^2}{4}, \end{aligned} \tag{D.18}$$

where we have ignored the very small higher-order θ terms.

Similarly, the small angle approximation can also be used to rewrite ρ_{bb} (Equation D.8).

$$\rho_{bb} = \sin^2\left(\frac{\theta}{2}\right) \tag{D.19}$$

For small x, we have $\sin(x) \approx x$.

Thus,

$$\begin{aligned} \rho_{bb} &= \sin\left(\frac{\theta}{2}\right)\sin\left(\frac{\theta}{2}\right) \\ &\approx \left(\frac{\theta}{2}\right)\left(\frac{\theta}{2}\right) \\ \rho_{bb} &\approx \frac{\theta^2}{4}. \end{aligned} \tag{D.20}$$

Thus, we can rewrite our matrix elements as

$$\begin{aligned} \rho_{ab} &= \frac{1}{2}\sin(\theta)\, e^{j\phi} \\ &\approx \frac{\theta}{2} e^{j\phi}, \end{aligned} \tag{D.21}$$

$$\begin{aligned} \rho_{aa} &= \cos^2\left(\frac{\theta}{2}\right) \\ &\approx 1 - \frac{\theta^2}{4}, \end{aligned} \tag{D.22}$$

and

$$\begin{aligned} \rho_{bb} &= \sin^2\left(\frac{\theta}{2}\right) \\ &\approx \frac{\theta^2}{4}, \end{aligned} \tag{D.23}$$

with the approximate equality holding for systems with weak coupling between states.

We can use the similarities between the matrix elements to rewrite the diagonal matrix elements in terms of the coherence.

Noting that for weak coupling,

$$\begin{aligned} |\rho_{ab}|^2 &\approx \left|\frac{\theta}{2}e^{j\phi}\right|^2 \\ &= \frac{\theta^2}{4}, \end{aligned} \tag{D.24}$$

we can rewrite

$$\rho_{aa} \approx 1 - |\rho_{ab}|^2 \tag{D.25}$$

and

$$\rho_{bb} \approx |\rho_{ab}|^2 . \tag{D.26}$$

Finally, we note that plugging in the approximate value of θ (Equation D.14) and recalling that $B = |B|^{j\phi}$, we can rewrite the coherence for a weakly coupled system.

$$\begin{aligned} \rho_{ab} &\approx \frac{\theta}{2}e^{j\phi} \\ &= \frac{1}{2}\frac{2\,|B|}{A - D + 2\Delta\omega}e^{j\phi} \\ &= \frac{B}{A - D + 2\Delta\omega} \end{aligned} \tag{D.27}$$

Appendix E: Cavity and Chamber Diagrams

This appendix has more detailed images of our high-finesse cavity and the surrounding vacuum chamber. The first image below is exactly Figure 6.7, which is reproduced here for reference. The second image is the same view of the cavity and chamber with additional parts labeled.

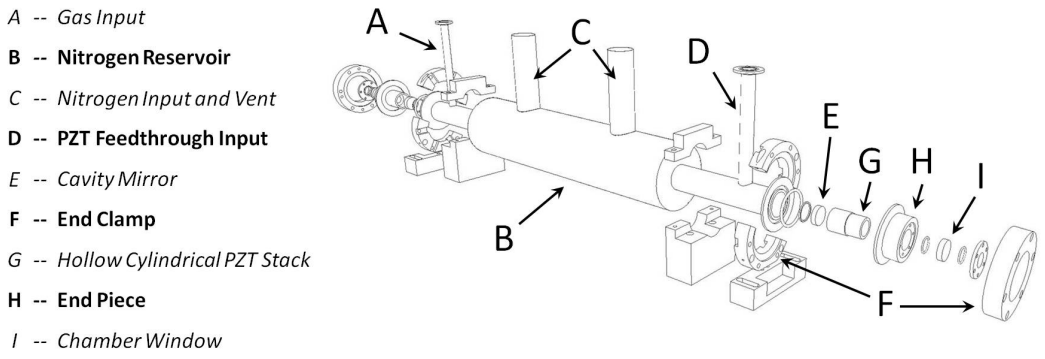

Figure E.1 *Cavity Diagram* This custom-designed 75-cm-long stainless-steel vacuum chamber houses the high-finesse cavity used in our experiment. (The drawing is to scale). The central cavity contains the cavity mirrors and the molecular gas. Surrounding the cavity there is an insulated 45-cm-long liquid nitrogen reservoir. (The insulation is not shown.) The end clamps hold the end pieces in place, maintaining the vacuum, while the end pieces themselves hold the cavity mirrors and anti-reflection-coated chamber windows. One of the end pieces also houses the piezoelectric transducer (PZT) that allows for slight adjustments of the cavity length. We align the cavity mirrors by making slight adjustments to the six end-clamp-tightening bolts. This allows us to change the pitch of the mirrors while maintaining a vacuum seal. Not shown are the three dial indicators per end piece that record its pitch.

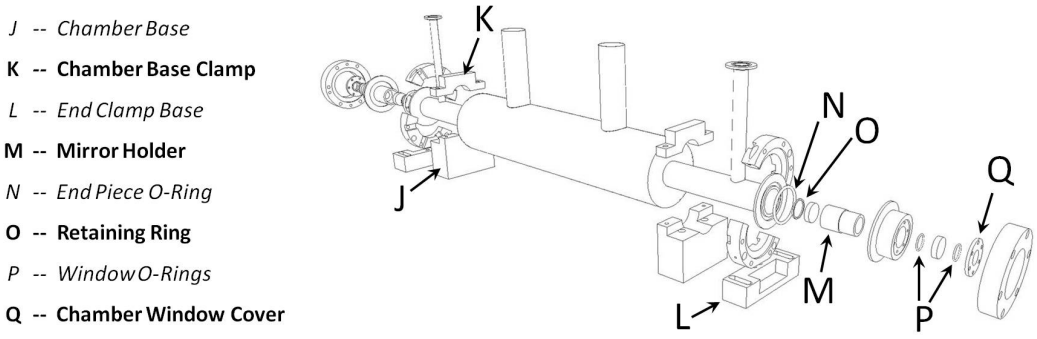

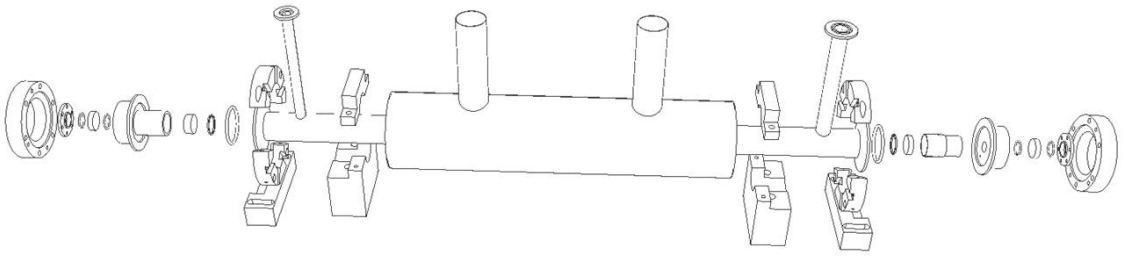

Figure E.2 *Full View* This view shows all of the pieces to the cavity and chamber. The table below lists all parts seen in the figure at the bottom of the page.

1	Outer End Clamp	12	PZT Feedthrough Input	23	Chamber Base
2	Chamber Window O-Rings	13	Inner End Clamp Top	24	Liquid Nitrogen Reservoir
3	End Piece with Mirror Holder	14	End Piece O-Ring	25	Chamber Base
4	Retaining Ring	15	Cavity Mirror	26	Main Cavity Tube
5	End Piece O-Ring	16	Piezoelectric Transducer Stack	27	Inner End Clamp Bottom
6	Inner End Clamp Top	17	Chamber Window	28	Retaining Ring
7	Gas Input	18	Chamber Window Cover	29	Mirror Holder
8	Chamber Base Clamp	19	Chamber Window Cover	30	End Piece
9	Nitrogen Input	20	Chamber Window	31	Chamber Window O-Rings
10	Nitrogen Vent	21	Cavity Mirror	32	Outer End Clamp
11	Chamber Base Clamp	22	Inner End Clamp Bottom		

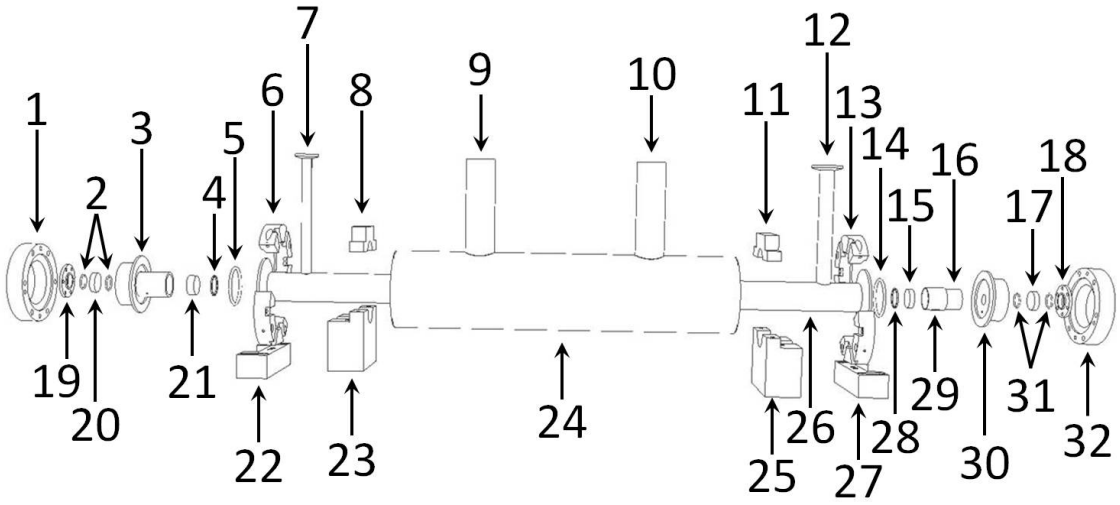

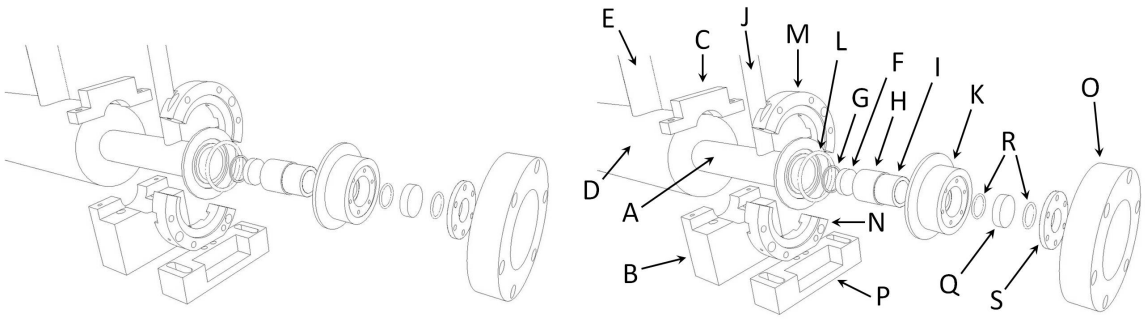

Figure E.3 *PZT Side Detail* This figure illustrates the PZT side of the cavity and chamber, both without and with labels. The text below explains the labels.

This figure shows a closer view of the PZT side of the cavity chamber. The main cavity chamber (A) is supported by the chamber base (B), which is attaches to the optical table, and the chamber base clamp (C). The chamber is held so the optics are 3 inches above the optical table. The central 45 cm of the 75-cm-long cavity is surrounded by a liquid nitrogen reservoir (D) that includes a nitrogen input / vent (E) for adding liquid nitrogen and allowing the boiled nitrogen gas to escape. The reservoir holds roughly 5 L of liquid nitrogen. To keep the chamber at a relatively steady temperature, and thus a relatively steady molecular density, we refill the nitrogen approximately every thirty minutes while running the experiment. The cavity mirror (F) is held by the retaining ring (G) and the mirror holder (H), which is attached to the PZT stack (I). The PZT stack expands and contracts depending on the voltage applied to it through a conductor (not shown) that comes through the PZT feedthrough input (J) through a Kwik-Flange (KF25) vacuum flange. This allows for slight adjustments in the cavity length. The PZT stack is epoxied to the end piece (K). The end piece Viton o-ring (L) holds the vacuum seal of the chamber between the end piece and the main chamber. Although it is a standard Kwik-Flange vacuum flange (KF50), the end piece is attached using a custom end clamp (M, N, and O). The inner end clamps (M, N) mate with the outer flange of the cavity, then are attached to one another. The outer end clamp (O) mates with the end piece and holds it in place when it is attached to the inner clamp. The custom end clamps are necessary because they provide pitch control of the cavity mirrors. The six bolts that hold the inner and outer parts of the end clamp together can be adjusted to slightly change the pitch of the

end piece (and therefore of the mirror) while still maintaining a vacuum seal. The inner end clamp is attached to the table through a base (P), which gives a stable reference point and makes the end clamp adjustments more repeatable. Not shown are the three dial indicators that are attached to the inner end clamp. The indicators reach from the inner end clamp to rest on the outer end clamp. The tips of these three indicators define a plane that indicates the pitch of the mirror. This can be used as a reference to make pitch adjustments more systematic and repeatable. The end piece houses the chamber window (Q), which, together with the chamber window Viton o-rings (R) and the chamber window cover (S), seals the vacuum. The cavity window has anti-reflective coating for near the pump and the Stokes wavelengths. It is also mounted at an angle of 3° relative to the optical axis in order to avoid back-reflection and etalon effects.

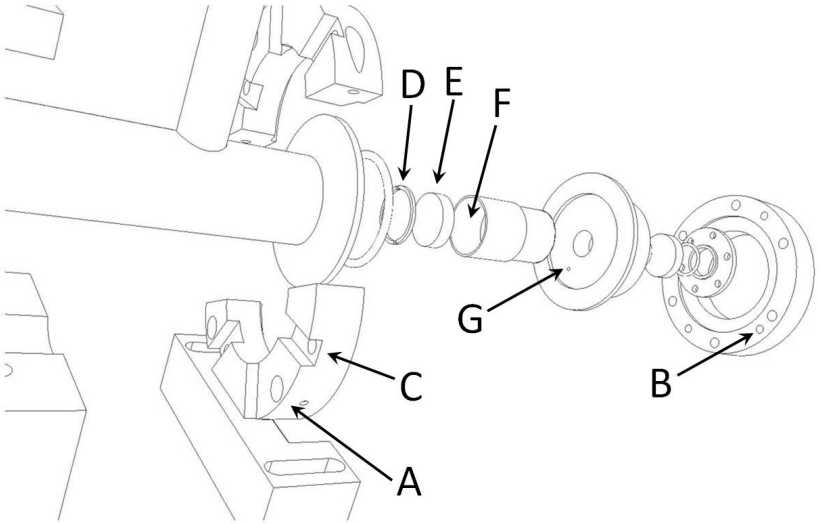

Figure E.4 *PZT Back Side Detail* This figure illustrates the reverse of the PZT side of the cavity and chamber. This view shows where some of dial indicators are held in the inner clamp by set screws (A) and also some of the indentations in the outer clamp on which the dial indicators rest (B). Also visible are the slots in the back of the inner end clamp (C). These slots hold the nuts so that the end-clamp-tightening bolts can be easily tightened from the front of the outer end clamp. This diagram angle also gives a better view of the retaining ring (D) that holds the cavity mirror (E) in place by screwing into the threaded inner surface of the mirror holder (F). Barely visible is a small hole (G) that connects the main chamber with the small volume of empty space between the mirror and the chamber window. This is to help ensure that this part of the chamber is properly evacuated by the vacuum pump.

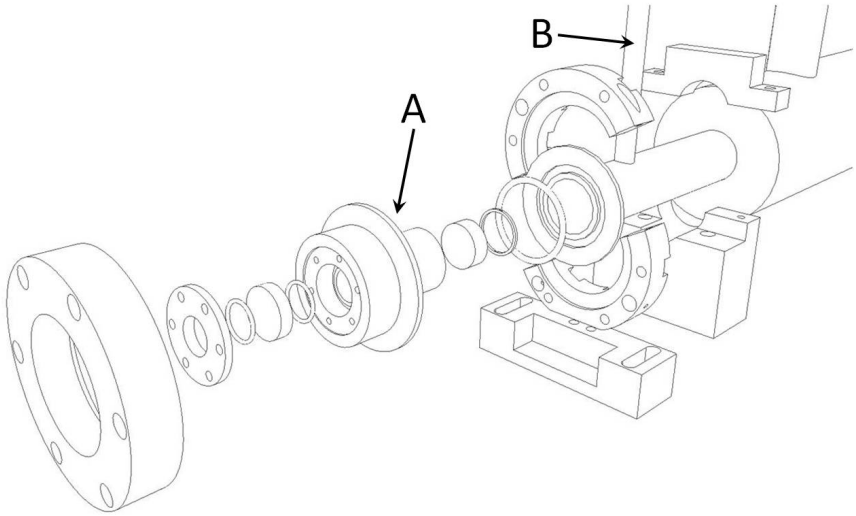

Figure E.5 *Non-PZT Side Detail* This figure illustrates the side of the cavity and chamber opposite the one shown in Figure E.3. Almost all features are identical. The main difference is that there is no PZT stack to adjust this mirror. The mirror holder is included as a part of the end piece (A). Also, instead of a PZT feedthrough, this side has the gas input (B). This is the connection (a KF16 vacuum flange) where the vacuum pump is connected to evacuate the chamber. Through this same connection, the molecular gas is added. Not shown is the manometer used to gauge the gas pressure in the cavity. The figure below shows the reverse view of this side of the cavity. Again visible is the end piece that includes the mirror holder (C), including the small hole (D) for evacuating the area between the window and the mirror, as mentioned in Figure E.4.

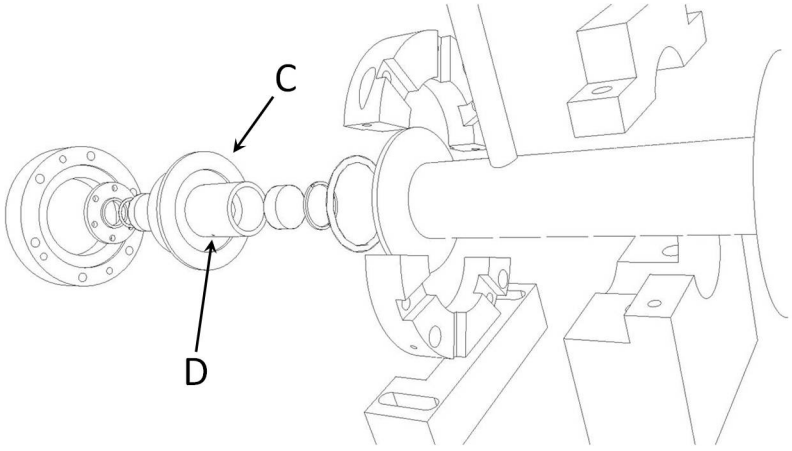

Figure E.6 *Non-PZT Back Side Detail*

Appendix F: Transition Frequency Calculations

This appendix outlines the calculations of the frequencies in Table 6.1. These calculations are based on Chapter III of *Spectra of Diatomic Molecules* by Herzberg [65]. The values of constants come from Table 39 in the appendix of Herzberg.

By modeling a diatomic molecule as a quantum oscillator, we can describe its vibrational and rotational motion and calculate its quantized energy. The energy in wavenumbers, $\tilde{\nu}$, of the molecular states is approximated by the following expression:

$$\tilde{\nu}(v, J) \approx \omega_e \left(v + \frac{1}{2}\right) - \omega_e x_e \left(v + \frac{1}{2}\right)^2 + B_v J\left(J+1\right) - D_v J^2 \left(J+1\right)^2. \qquad \text{(F.1)}$$

(In this expression we have dropped higher-order terms in $\left(v + \frac{1}{2}\right)$ and $(J + 1)$. Higher-order terms can be found in Herzberg.)

v and J are the quantum numbers of vibration and rotation, respectively. ω_e is a constant term that is based on modeling the molecule as a classical anharmonic oscillator oscillating with infinitesimal amplitude. $\omega_e x_e$ is a constant term that indicates by how much ω_e deviates from the corresponding classical frequency. Both terms are given in Table F.1 for both deuterium and hydrogen.

Molecule	ω_e	$\omega_e x_e$	B_e	α_e
$\mathbf{D}_2$	3118.4	64.09	30.429	1.0492
$\mathbf{H}_2$	4395.2	117.99	60.800	2.993

Table F.1 *Deuterium and Hydrogen Constants* This table presents the values of the constants needed to calculate the energies of the molecular states as detailed above. All values are for the ground electronic state, and units for all entries are wavenumbers (cm^{-1}). All values are from Table 39 of the appendix of Herzberg [65].

B_v is a rotational constant; it is the mean value of a rotational constant for a molecule vibrating (and thus changing its rotational constant) in the vth vibrational state. Given a quantum number v,

B_v can be calculated using the following expression:

$$B_v \approx B_e - \alpha_e \left(v + \frac{1}{2} \right). \tag{F.2}$$

The approximation indicates that we have ignored higher-order terms in $\left(v + \frac{1}{2}\right)$. B_e is the rotational constant of the molecule in its equilibrium orientation, and α_e is a constant that quantifies the small deviation in the rotational constant that occurs due to the changing internuclear spacing of a vibrating molecule. Both B_e and α_e can be found in Table F.1. D_v is the mean rotational constant of the molecule. It includes the effects of inertia on a rotating object, and it depends on the vibrational frequency of the molecule. As with B_v, D_v can be calculated given v.

$$D_v \approx D_e + \beta_e \left(v + \frac{1}{2} \right) \tag{F.3}$$

The approximation again indicates that we have ignored higher-order terms in $\left(v + \frac{1}{2}\right)$. D_e is the rotational constant of the equilibrium, vibrationless state. This can be calculated using the following equation:

$$D_e = \frac{4B_e^3}{\omega_e^2}. \tag{F.4}$$

β_e is related to the deviation of the rotational constant of a vibrating molecule from that of a vibrationless state. β_e can be calculated in terms of previously defined constants.

$$\beta_e = D_e \left(\frac{8\omega_e x_e}{\omega_e} - \frac{5\alpha_e}{B_e} - \frac{\alpha_e^2 \omega_e}{24 B_e^3} \right) \tag{F.5}$$

To calculate the frequency values in Table 6.1, the energies of the ro-vibrational levels of interest were first calculated using Equation F.1. These energies in wavenumbers, $\tilde{\nu}$, were multiplied by the speed of light, c, to convert to frequencies, ν.

$$\nu = \tilde{\nu} c \tag{F.6}$$

Several frequency differences are displayed in Tables F.2 and F.3 for deuterium and hydrogen, respectively. The frequency differences that are most relevant for our experiment are recorded in Table 6.1.

D_2	$v=0$	$v=1$	$v=2$
$J=0$	0	89.6	175.5
$J=1$	1.8	91.4	177.1
$J=2$	5.4	94.8	180.4
$J=3$	10.7	100.0	185.4
$J=4$	17.8	106.8	192.0
$J=5$	26.6	115.3	200.2

Table F.2 *Deuterium Frequency Separation from the Ground State* This table presents the frequency spacing in THz between molecular energy levels in deuterium and the ground state, $|v=0, J=0\rangle$. The row indicates the rotational quantum number, J, and the column indicates the vibrational quantum number, v.

H_2	$v=0$	$v=1$	$v=2$
$J=0$	0	124.7	242.3
$J=1$	3.6	128.1	245.5
$J=2$	10.6	134.8	251.9
$J=3$	21.1	144.8	261.3
$J=4$	35.0	158.0	273.8
$J=5$	52.1	174.2	289.1

Table F.3 *Hydrogen Frequency Separation from the Ground State* This table presents the frequency spacing in THz between molecular energy levels in hydrogen and the ground state, $|v=0, J=0\rangle$. The row indicates the rotational quantum number, J, and the column indicates the vibrational quantum number, v.